Non Linear Finite Element Simulation of Complex Bulge Forming Processes

By

Bryan J. Mac Donald, B.Eng. M.Sc.

This thesis is submitted to Dublin City University as the fulfilment of the requirement for the award of the degree of

Doctor of Philosophy

Supervisor: Professor M.S.J. Hashmi, Ph.D. D.Sc.

School of Mechanical and Manfacturing Engineering
Dublin City University

June 2000

DECLARATION

I hereby certify that this material, which I now submit for assessment on the programme of study leading to the award of *Doctor of Philosophy*, is entirely my own work and has not been taken from the work of others save and to the extent that such work has been cited and acknowledged within the text of my work.

Signed: Date: 19/9/2000
Bryan Mac Donald
ID: 97971065

Acknowledgements

I would like to express my sincere gratitude to Prof. M.S.J Hashmi for his guidance and help over the last three years, for the opportunity to work in a stimulating research environment and for the chance to present work at international conferences.

I would also like to thank my students Arnaud Girard and Yannick Grenier for their assistance during the experimental verification of some of the finite element models

Finite Element Simulation of Complex Bulge Forming Processes

Bryan James Mac Donald B.Eng. M.Sc.

ABSTRACT

Bulge forming is a manufacturing process that is becoming increasingly important as a technology that can be used to produce seamless, lightweight and near-net-shape industrial components. The process is being increasingly applied in the automotive and aerospace industries where the demands for increased structural strength and decreased vehicle weight make it a very attractive manufacturing method.

This work is concerned with increasing knowledge of the deformation mechanisms during bulge forming processes using numerical simulation. A number of complex bulge forming operations which have not been satisfactorily analysed in published research were identified and subsequently analysed using commercial finite element software. A non-linear explicit solution method was used in each case. The processes chosen for simulation were: hydraulic bulge forming of cross joints, bulge forming using a solid bulging medium, bulge forming of bimetallic tubes and the behaviour of the die during these bulge forming processes. In each case a number of process parameters were varied and their effect on the process identified. Where possible the finite element results were validated against results from experimental trials. It was found that the simulations predicted the experimental results with accuracy, thus indicating that the models developed here can be used with confidence to predict the behaviour of bulge forming operations.

From the results of the finite element simulations it was concluded that when designing processes to bulge form cross joint components that compressive axial loading should be used in conjunction with pressure loading where possible, friction between the die and workpiece should be kept to a minimum where maximum branch height is required and greater tube thickness should be used when seeking to reduce stress and thinning behaviour in the formed component. The results also indicate that, where possible a solid bulging medium should be used as it results in much more favorable forming conditions, which can allow the realisation of greater branch heights. The simulations of bulge forming of bimetallic tubes showed that the relative thickness of the two metal layers has a significant effect on the shape of the final component. It was also found that varying the relative strength of the two metallic layers had a significant effect on the branch height obtained. The development of stress in the die during various bulge forming process was detailed at various stages during the process. It was found that generally a stress concentration moves towards the die bend as the process progresses. The effect of using different die materials was examined and it was concluded that certain materials are unsuitable for use as die materials due to the fact that their yield stress is exceeded during the forming process.

Contents

Section No. *Description* *Page No.*

Chapter 1 **Introduction**

Chapter 2 **Literature Survey**

Chapter 3 **Theoretical Background**

Chapter 4 **Hydraulic Cross Branch Forming**

Chapter 5 Bulge Forming Using a Solid Bulging Medium

Chapter 9 Conclusions

Appendix 1

Estimation of Failure Propagation During Bulge Forming

Appendix 2

Publications

Nomenclature

Symbol	Definition	Dimension
c	Sonic wave propagation velocity	m/s
f	Force	N
l	Element characteristic length	m
t	Time	seconds
v	Element volume	m^3
x	Velocity of specific node	m/s^2
B	Strain-displacement Matrix	-
C	Global damping matrix	-
D	Stress-strain matrix	-
E	Young's modulus	MPa
F	Concentrated Force	N
H	Displacement Interpolation Shape Matrix	-
I	Identity matrix	-
K	Global stiffness matrix	-
M	Global mass matrix	-
R	Load vector	-
T	Period	-
U	Virtual Displacement	m
$\overline{U}$	Displacement in global X direction	m
$\ddot{U}$	Nodal point velocities	m/s
$\ddot{U}$	Nodal point accelerations	m/s^2
$\overline{V}$	Displacement in global Y direction	m
$\overline{W}$	Displacement in global Z direction	m
Greek		
α	Number of hourglass mode	-
δ	Stress	N/m^2
ε	Strain	-

κ	Damping property parameter	-
ρ	Density	Kg/m^3
Γ	Hourglass shape vector	-

Subscripts

p	Plastic	-
Tan	Tangent	-
CR	Critical	-
S	Surface	-
V	Volume	-

Superscript

eff	Effective	-
i	Points in space	-
t	Time	seconds
B	Body	-
S	Surface	-
T	Transpose of a Matrix	-

List of Figures

Chapter 1 : Introduction

1.1. The Bulge Forming Process

Bulge forming is a widely used industrial process which is generally used to form complex components from tubular blanks. Components are formed by restraining the blank in a die bearing the desired shape and applying an internal hydrostatic pressure to the tube via a liquid or solid medium. Bulge forming by pressure loading alone is limited in the type and quality of components it can produce, as it leads to excessive thinning of the tube wall, which can result in ruptures. If a compressive axial load is applied to the ends of the tube in conjunction with the pressure load, then material can be pushed into the deformation zone during forming thus preventing excessive thinning of the walls. If this axial load is large enough to cause a reduction in length of the tube, then much greater expansion can also be obtained.

Many near-net shaped industrial parts are manufactured using the bulge forming process, such as : T-branches, cross branches, stepped hollow shafts, rear axle casing of cars, bicycle wheel hubs, metal bellows, nozzles etc. The products are all either asymmetric or axisymmetric. Figure 1.1. shows cross sectional views of an arrangement for the manufacture of cross branch tubular components.

The tubular blank is placed between two die halves and the tube ends are held by shouldered plungers which also act as a punch. The plungers compress the bulging medium and pressure builds up inside the tube. In the case of hydraulic bulge forming the liquid is pumped in through holes in the plungers in order to build up pressure. The plungers are then pushed inward to provide the axial compressive load. Due to the internal pressure and the compressive loading the branches begin to form. Simultaneous application of these loads helps to obtain large deformations. Prominence of either the pressure or compressive load will produce defective components. There are two main modes of defects from process instabilities during the bulge forming process. Defect by rupture occurs due to excessive thinning of the bulge area and is the result of a dominant pressure loading. Defect by buckling occurs in non-bulged areas when the axial compressive loading is excessive.

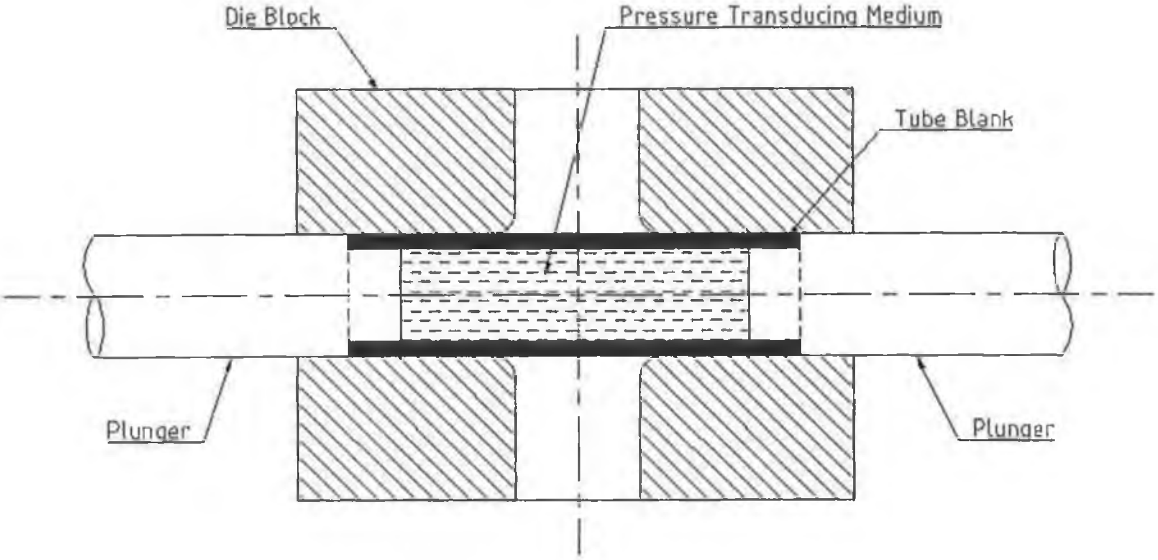

(a) Prior to forming with tube blank in position

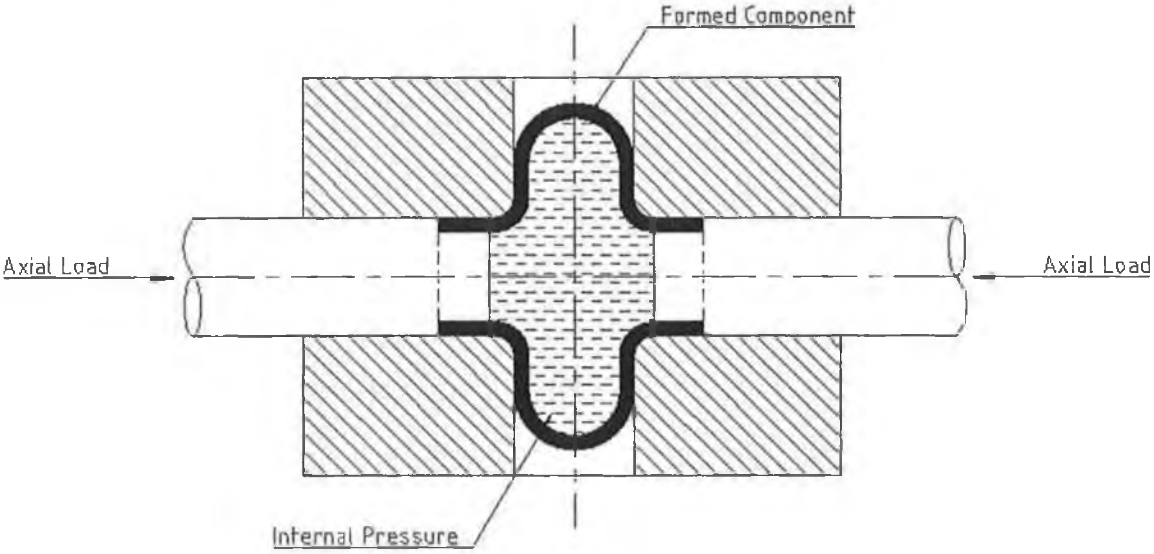

(b) Component formed with axial deformation

Figure 1.1. : A Bulge Forming Process

Obviously, a knowledge of the optimum loading conditions that would avoid these instabilities would enable higher deformations and result in a more efficient process. The bulge forming process is a highly complicated process to analyse theoretically and hence, to date, theoretical analysis methods for plastic deformation of bulge forming have resulted in a limited understanding of the process. Numerical analysis and simulation has the potential to provide a much deeper understanding of the process and hence allow for better design of process equipment and end products.

1.2. Finite Element Analysis and Metal Forming.

The finite element method came of age in the early 1960's with the replacement of analog with digital computers and the development of the first commercial finite element analysis codes. Linear static and limited dynamic analyses were available to analysts who could justify the expense. The introduction of the finite element method to plasticity problems dates back to the late 1960's when an elastic-plastic constitutive equation was incorporated in the standard solution routine that had been used in the solution of elasticity problems. At this early stage the application was confined to the contained elastic-plastic deformation where the plastic strain is of the order of 0.1%. The extension to the large strain regime was achieved in the late 1970's when limited nonlinear solvers were developed and made available. The 1970's also saw a large increase in computer speed and the power and more availability of finite element software.

The 1980's saw the usage of the finite element method for analysis of metal forming operations slowly begin to grow. Wagoner and Zhou [1] reviewed the number of papers in the field submitted to the conference series "Numerical Methods in Industrial Forming Processes" in the period 1977 to 1989. In the 1977 conference there were 2 papers analyzing sheet metal forming and this had grown to 22 by 1989. By 1989 it was stated that the ability to simulate general sheet metal forming operations reliably, accurately and consistently had yet to be demonstrated. At this stage all programs in use were based on the static implicit method, although some testing of explicit methods was reported. The 1980's also saw large improvements in computer power, graphics and pre and post-processing tools which made the finite element method more widely available and user friendly.

The early 1990's saw some significant advances with the development of benchmark tests for finite element simulation of metal forming processes. The first implementation of the benchmark tests showed considerable scatter between results from different commercial implicit finite element codes [1]. Contact was determined to be one of the main sources of error in analyses and renewed effort was placed on improving existing contact algorithms. The advantages of dynamic explicit programs, (i.e. faster computational speed for large problems, low storage requirements etc.) began to be recognized. The 1990's saw a large growth in research in the field. A recent review paper [2] reported that in the period from 1984 to 1994 there was a rapid increase in the use of finite element analysis to simulate metal forming operations. The growing popularity for the use of the explicit finite element method to solve complex metal forming problems was also noted. Some factors which are thought to have influenced this increase are the interdisciplinary nature of the field (which encompasses mechanics, materials, numerical methods, computer science etc.) and the setting up of a number of university/government/industry consortia (such as the 'Sheet Metal Forming Research Group' in Japan).

Traditionally finite element codes were based on Newton-Rhapson type algorithms which are incremental and iterative. In the simulation of metal forming we face a multiplicity of non-linearities : physical (viscoplacticity, damage), geometrical (large displacement and large deformation) and contact/friction. The combination of these non-linearity's results in convergence difficulties. In the 1970's when the first 2-dimensional forming analyses were carried out the traditional implicit direct solvers were used along with experimental explicit dynamic solvers. For such simple 2-dimensional analyses the implicit analysis methodology is more effective than explicit dynamic based methods. As a consequence, much of the development effort in subsequent years concentrated on implicit methods [3]. Based on the successes obtained with 2-dimensional analyses an extension of implicit methods to 3-dimensional problems appeared natural. However, the transition from 2 to 3-dimensional metal forming analysis introduces a number of difficulties which were initially not appreciated. The increased number of contact points inherent in 3-dimensional analysis causes a considerable reduction in time increment size and hence longer and more costly analysis. Also implicit solvers are incapable of dealing with wrinkling which is inherent in many metal forming analysis [3]. These difficulties led to a renewed interest in the application of the explicit dynamic based solution method to metal forming problems. In the explicit method the time step size is dictated by the stability limit of the operator and is not effected by the increased number of contact points. Also the explicit method has the advantage that loss of contact after loading beyond the critical point does not lead to unchecked growth of the solution. It has generally been concluded that for more complex models with larger, more refined meshes, the explicit method is much more effective than the implicit method. However, the implicit method is reasonably effective and can be faster than the explicit method in smaller problems.

Within the last number of years there has been a large growth in the use of the explicit method to analyse metal forming problems [4]. This has been primarily due to the advances made in explicit solvers in the mid to late 1990's such as improved and more robust contact algorithms. Also the 'coming of age' of computer graphics has result in more user-friendly pre and post processing tools which have allowed the generation and analysis of more complex models.

1.3. Summary of Chapter 1

This chapter introduces the bulge forming process and illustrates how further understanding of the process is required in order to optimise both process and product design. The history of the finite element method and it's application to analysis of metal forming problems is also described, and the different solution methods available are discussed.

Chapter 2 : Literature Survey

2.1. Introduction

The objective of this chapter is to examine the work of others who have performed similar or related analyses of bulge forming of tubular components. There are many experimental studies available in literature on simple bulge forming or bulge testing and in recent years a number of simulation studies have also been reported [5]. However, more complex bulge forming processes, particularly bulge forming of asymmetric components, have received little if any attention.

2.2 Analytical and Experimental Studies

The bulge forming process has been described in literature for many years. A patent filed by Grey et al. [6] with the United States patent office in 1939 described a bulge forming process for the manufacture of seamless metal fittings with branches such as T-branches and cross branches. The machine used allowed control of the hydraulic internal pressure and endwise axial load to avoid rupture of the blank. The process involved placing a tubular blank in between two die halves which were then clamped together. A compressive load was then applied to the ends of the tube via plungers which entered the ends of the die block. The internal pressure was applied via a liquid through a drilled hole in one of the plungers. This combination of axial load and internal pressure pushed the tube wall into the die recess thus forming the component. Although the process at this stage was by no means new, it was the first time that the deforming loads were related in such a manner that a satisfactory T-branch was produced.

Crawford [7] described an applied process whereby components were formed by pouring a soft metal (a bismuth-lead-tin alloy) into a copper tube and subsequently applying an endwise pressure to both the filler material and the tube while they were restrained in a die. This process produced well shaped components but had the disadvantage of requiring the filler material to be added before and removed after the process. This was more time consuming than using a liquid bulging medium, but had the advantage of a reduction in tooling costs due to the elimination of the need for pumps, seals etc. An improvement in the process was patented by Stalter [8] which increased productivity of the process and removed the disadvantages caused by shrinking of the filler material on pouring. Remmerswall and Verkaik [9] described a method of bulge forming axisymmetric conical products from deep drawn cylindrical blanks. Ogura and Ueda [10] described procedures to form axisymmetric and asymmetric components by simultaneous application of axial compressive load and hydraulic internal pressure. Al-Qureshi et al. [11] described an experimental process for axisymmetrically bulging thin walled metal tubes. A polyurethane rod was used to apply the internal pressure and the friction between the tube and the rod provided the axial load on the tube. In a separate presentation Al-Qureshi [12] experimentally compared bulge forming using a polyurethane rod with hydraulic bulge forming. It was found that greater circumferential expansion and longitudinal drawing was possible with the polyurethane method. It was concluded, however, that due to the complexity of analysing the polyurethane forming technique, that the more highly developed hydraulic forming method generally gave better results.

Woo [13] presented a limited theoretical method for analysing tube bulging under axial compressive load and internal hydraulic pressure. Experimental results showed reasonable agreement with theoretical results. Limb et al [14,15] reported experimental analysis of hydraulic bulge forming of tubes using combined axial load and internal hydraulic pressure. Both axisymmetric and asymmetric components were formed using various materials and blank geometry's. In a separate presentation Limb [16] also developed a theoretical analysis method and indicated the manner in which pressure and axial loads should be applied during the process.

Kandil [17] reported experimental analysis whereby tubes of different material were bulge formed axisymmetrically under hydraulic pressure only. The experimental results were used to derive empirical relationships between pressure, stress and the geometry of the die and tube. Sauer et al. [18] reported a theoretical and experimental analysis of axisymmetric tube bulging. In this case both pressure and axial load was used. They developed a theory to determine the bulge shape when load increments are specified on a step by step basis. Woo and Lua [19] extended earlier theoretical work [13] by introducing anisotropy of the tube material and considering bulge forming using pressure load alone. In a subsequent work Woo [20] presented an experimental technique of bulge forming closed ended deep vessels from deep drawn tubular blanks.

Lukanov et al. [21] presented an experimental technique of bulge forming of double T-branches from a singular tubular blank by careful control of internal hydraulic pressure. Superplastic forming of tee-joints from tubular blanks was reported by Ragab [22]. Pressurised heated air was used to bulge tubes of lead tin metal alloy. An approximate analysis was developed to predict the wall thickness of the formed component. Ueda [23,24] described a process of manufacturing differential gear casings for automobiles form a straight tubular blank by the liquid bulge forming technique with a flexible tool system.

Hashmi [25] presented an analysis for the prediction of wall thickness around the circumference of T-branches formed by bulge forming. Comparison with experimental results indicated that the analysis over-estimated the thinning of the wall. In a separate presentation Hashmi [26] reported an analytical method to predict height and thickness distributions of both axisymmetric and asymmetric bulged products. The analysis was based on the geometry of the forming bulge but did not take into account key parameters such as pressure, friction, bend radius etc. Later Hashmi and Crampton [27] compared experimental results with this analytical method and found that the method generally overestimates the thickness of formed components. Hutchinson et al. [28,29,30] experimentally established a formability zone for forming T-branches and cross-joints from a certain blank material and geometry and also examined the effects on the final product of changing various process parameters. It was found that lubrication, blank material and plunger geometry all have a considerable effect on bulge shape and size.

Filho and Al-Qureshi [31] presented an experimental method of forming tee joints from straight tubes using a urethane rod. The deformation was achieved by using repetitive loading and unloading cycles and by varying the length of the urethane rod between cycles. A theoretical expression for total forming load prediction was also developed and compared with experimental results.

Dohmann and Klass [32] described axisymmetric bulging of tubes with sliding dies. The dies push the tube ends giving the axial compressive forming load without friction between the die and tube. Hydraulic pressure was used as the internal forming load. Murata et al. [33] described the development of a new machine tool for axisymmetric tube bulging which initially puts a deflated rubber membrane into the work piece and while forming the internal pressure is applied on the membrane, which in turn applies pressure to the tube wall.

Thiruvarudchelvan and Travis [34] described experiments to axisymmetrically bulge copper tubes using a urethane rod. Urethane rods of different hardnesses were used and the friction between the rod and tube was varied using different lubrication methods. Thiruvarudchelvan [35,36] developed an approximate theory for predicting the initial yield pressure and final forming pressure required for bulging a metal tube using a urethane rod. The theory made use of experimentally determined friction characteristics and was compared with experimental results.

Dohmann and Hartl [37,38] reported on a flexible die system for tube bulging of both axisymmetric and asymmetric products. The die system has adjustable segments which can expand, displace or reduce the tube blank. The importance of process control for the quality of end products was also examined. Filho et al. [39] presented a theoretical analysis of bulge forming of a T-branch using an elastomer rod as the bulging medium. Equations were solved using the finite difference method to determine the axial compressive load required for the process. Sheng and Tonghai [40] reported on experimental research on forming of asymmetric components using bulge forming. In addition to internal pressure and axial load, a counter pressure was used on the formed component. It was found that this method improved the stress state in the formed component. An upper bound analysis was used to estimate power requirements. Tirosh et al. [41] described an upper bound analysis of axisymmetric bulging of tubes by combined internal pressure and axial compression. Using this formulation they experimentally attempted to determine an optimum loading pattern to give maximum bulging strain without early failure by buckling or necking.

During bulge forming of tubes an area of major concern is the onset of instability. In almost all experimental and analytical studies it was observed that excessive amounts of either the pressure or axial loads relative to the other, causes instability of the process resulting in excessive thinning leading to bursting or buckling. A great deal of research has been conducted in attempting to determine the onset of instability in tubes. Mellor [42] presented an analytical solution to determine the strain at instability of thin walled tubes. In his analysis it was assumed that the circumferential to axial stress ratio remains constant and positive throughout the straining process. In a subsequent work Jones and Mellor [43] experimentally showed that the theoretical solution in [42] was in good agreement with experimental results. Felgar [44] analysed instability of pressure vessels subjected to internal pressure and tensile axial load. Both thin and thick walled pressure vessels were examined for constant circumferential and axial stress ratio. When compared with experimental results, it was found that the theoretical prediction of instability pressure was accurate, but, the prediction of instability strains were in gross disagreement with experimental results. Weil [45] theoretically analysed tensile instability of thin walled cylinders of finite length. The analytical results showed that burst pressures increase progressively as the length/diameter ratio of the cylinders is reduced from infinity to lower values.

The above instability studies all considered a tensile axial loading of the cylinders. This type of loading results in positive (i.e. tensile) hoop and axial strains, which when illustrated on a strain diagram is signified by deformation in the first strain quadrant as shown in figure 2.1. During bulge forming by pressure and axial loading the forming regime is in a totally different strain quadrant. In this case the forming regime is due to tensile hoop strain but compressive axial strain. A typical example of a strain diagram during a bulge forming process is shown in figure 2.2.

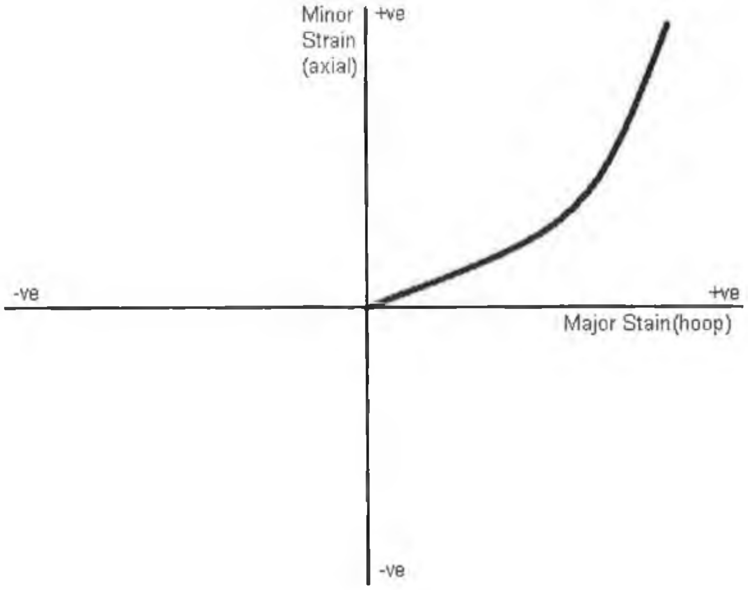

Figure 2.1 : Typical Strain Path During Tensile Axial Loading of Cylinders

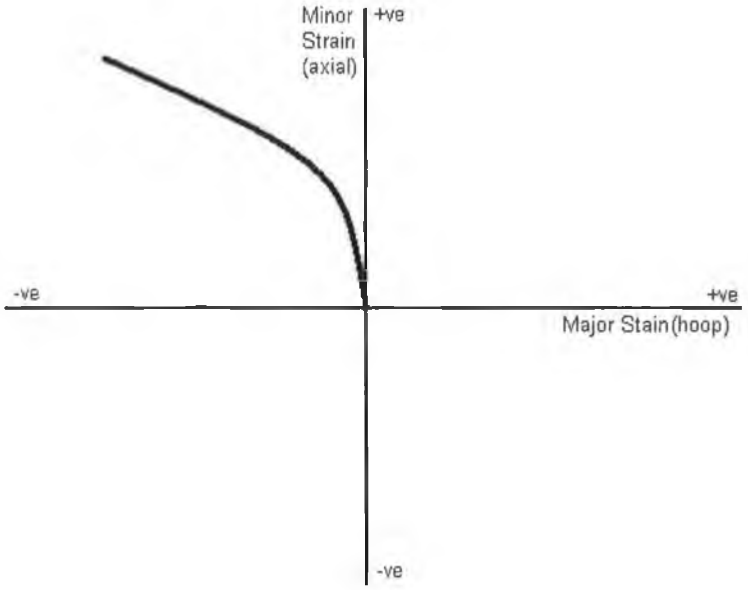

Figure 2.2. : Typical Strain Path During Axisymmetric Bulge Forming of Cylinders

Sauer et al [18] developed a theoretical necking criterion for axisymmetric bulging of thin walled tubes. It was found that the effective strain before necking depends on pre-strain in the material and circumferential stress/axial stress ratio at the point of necking. It was concluded that if the stress ratio could be maintained less than or equal to –1, infinitely large effective strain before necking may be attained. Manabe [46] experimentally tried to attain the so called "infinite strain" in axisymmetric bulge forming of thin-walled tubes. From the experiments it was discovered that it was possible to get products free of defects only in the stress ratio range from –0.2 to 0.

Eldred [47] reported a different kind of tube manipulation system suitable for manufacturing complex tubular components for the automobile and other industries. The process was patented as "vari-form" and uses internal hydraulic pressure applied to a pre-bent tube to create structural tubular components of varying cross section. A number of works have described a bulge forming technique used to form spherical vessels from an integral polyhedron [48, 49,50]. The polyhedron is made by joining flat pentagonal and hexagonal blank sheets of metal in a specific pattern. The polyhedron is then bulged by internal pressure to form a sphere. Manabe and Ozaki [51] reported a experimental method of axisymmetric bulge forming of braided thermoplastic composite tubes. The forming process took place at temperatures near the matrix melting point and the influence of different fibre orientations was investigated.

2.3. Simulation Studies

As mentioned in chapter 1, bulge forming of tubular components is a complex process that generally requires a three dimensional finite element simulation to properly analyse the process. Until very recently most applications of three dimensional finite element analysis to metal forming have been in the sheet metal forming sector. In comparison to sheet metal forming other metal forming process have received little attention. This is particularly true in the case of bulge forming where finite element analysis of the process incorporating the contact phenomenon between the die and the tube has received little attention, with only very particular arrangements having being considered.

A number of simulation works concerned with analysis of simple bulge forming of sheet metals or bulge testing have been reported. Numerical analysis of bulge forming of a circular sheet using the finite difference method has been reported by Woo [52], Yamada and Yokouchi [53], Wang and Shammamy [54], Ilahi et al. [55] and Ilahi and Paul [56]. The first finite element solution of bulge testing was reported by Iseki et al. [57]. An elastic-plastic material law and updated Langrangian formulation was used to formulate the problem. The results of the finite element analysis were compared with experimental measurements. It was found that at the pole of the bulge the results compared well, but at the periphery the comparison was not accurate. In a subsequent report, Iseki et al. [58] also analysed elliptical and rectangular metal diaphragms using the same formulation.

Kobayashi and Kim [59] formulated a finite element analysis technique using rigid-plastic material characteristics. The formulation used was verified by comparing results with those of Iseki et al. [57]. Kim and Yang [60] formulated a more general finite element solution method (also applicable to axisymmetric cases) using the same rigid plastic material model. They also compared their results with those of Iseki et al. [57]. Wifi [61] also analysed bulge forming by a generalised correction formulation of the finite element method and, again, compared findings with those of Iseki et al. [57]. All of these simulations modelled a circular sheet clamped at the edge. Although the illustrations in these works show a die with some edge radius, the simulations did not consider the peripheral boundary condition of the sheet with the die. Keck et al. [62] simulate the simple bulge test using an elasto-plastic formulation and took the peripheral boundary condition into account. It was found that simulation results agreed very well with the experimental results of Iseki et al. [57]. Lange et al. [63] used the same formulation to simulate bulging through elliptical dies with edge boundary conditions included in the model. Comparison with experimental test results showed good agreement.

Li et al. [64] used a finite element simulation to observe the influencesof various material parameters on bulge forming. Using the results an empirical relationship linking average limit thickness strain with material hardening and rate sensitivity parameters was obtained by regression fitting of the simulation results. Cronin et al. [65] used the ABAQUS general purpose finite element code to simulate simple bulge forming. The influence of varying mesh size and element type together with the variation of normal anisotropy of the material was investigated. From the simulation results it was found that beyond certain mesh density the results are unaffected, the continuum elements predicted better results than the shell elements and normal anisotropy of the sheet induces more uniform strain distributions on bulging. Predictions were verified by experimental results. Both of these works modelled the sheet as clamped at the periphery thereby disregarding the contact and friction conditions between the sheet and the die.

Bulge forming of a circular cup to a certain shape and heightwas simulated by Lee and Ma [66]. The simulation result predicted the shape and limiting height of the cup that can be formed from a particular blank geometry without failure. Experimental verification showed good agreement with predicted results. In this analysis all contact and interface boundaries were considered in the analysis. Ahmed and Hashmi [5] described a finite element simulation of bulge forming of a circular plate using the commercial finite element code ANSYS. An bilinear elasto-plastic material model was used and a contact algorithm was employed to model the contact region between the die and the plate. Two loading conditions were examined pressure loading only and combine pressure load and in-plane compressive load. The effect of changing blank thickness and blank radius were also examined. In a subsequent work Ahmed and

Hashmi [67] used a finite element simulation to examine the effect of restraining the bulge height during the process. Two methods of restraint were investigated : a restraining load applied as a pressure proportional to the main bulging pressure and using a die which physically obstructs the growth of the bulge after a certain height was achieved. It was found that the restraining load method does not significantly effect the shape of the bulge produced when compared to free forming. However, rigid restraint produced significantly different shaped bulges and delays the onset of instability. Ahmed and Hashmi [68] reported a finite element optimisation scheme to optimise bulge forming of a circular sheet applying pressure and in-plane compressive load. An attempt was made to maximise bulge height using pressure, in plane compressive load and die corner radius as design variables. The problem was constrained by specifying the maximum equivalent stress in the bulge within certain limits. Ahmed and Hashmi [69] also simulated bulge forming of a rectangular plate through a circular hole. It was found that dominant pressure loading produced a smooth bulge when compared to a dominant displacement loading.

Lange et al. [63] presented a simulation study of axisymmetric bulging of tubes. In this study it was possible to perform a two dimensional analysis by taking advantage of axisymmetry. The analysis was performed using a purposely developed implicit code and the effect of varying the ratio of pressure to axial load was studied. Bauer [70] reported a finite element simulation of a bulge forming process that produces a hollow camshaft from a pipe. A commercial explicit solver, LS-DYNA3D, was used for the simulations. In this case a three dimensional analysis was carried out and two different loading conditions were considered: pressure load with axial compression and pressure load alone. Comparison of simulated results with experimental measurements showed good agreement.

Dohmann and Hartl [71] described a flexible tool system used to manufacture a hollow camshaft from a tubular blank. The camshaft is manufactured by step-by-step bulge forming of the individual cams. Initially the tubular blank is positioned in the workpiece holder and the bulging medium is pumped in through a hole in the forming punch. The bottom of the tube is secured via a mandrel and is held in place via lateral jaws. The die segments are positioned between the mandrel and the workpiece holder and bear the required shape for the particular expansion step. After each expansion step the die segments and workpiece holder open and the tube is pushed down on the mandrel a distance corresponding to the interval between the cams. It is possible to have the cams at different angles to each other by swiveling the tool segments around the tube. A three dimensional finite element investigation was carried out using the ABAQUS commercial finite element software. In order to save computational time the length of the tube that is pushed into the tool without being formed was not modelled and by taking advantage of symmetry it was possible to model only half of the geometry.

Ahmed and Hashmi [72] simulated axisymmetric bulge forming of tubes using two different loading patterns. A pressure predominant loading and an axial compression predominant loading were used. A three dimensional model was used which modelled one quarter of the problem using symmetry. It was concluded that the pressure dominated loading resulted in smoother deformation while a dominant axial loading can result in instabilities (such as buckling) depending on the predominance of the compressive load. Ahmed and Hashmi [73] in a subsequent work used a finite element simulation to identify the locations and reasons for failure of a T-branch forming process. A three dimensional analysis was carried out using the commercial explicit solver LS-DYNA3D. It was found that the component either fails by rupture at the branch top due to a dominant pressure load or by buckling at the tube bend due to a dominant axial load. The manufacture of metal bellows was simulated by Ahmed and Hashmi [74] using a two dimensional analysis. Both solid and liquid bulging media were examined. The simulations indicated that although forming with a solid media is more difficult to optimise it generally produces bellows with less thinning when compared to the hydraulic process. In a subsequent presentation Ahmed and Hashmi [75] simulated bulge forming of T-branches from a straight tube. A three dimensional analysis was used and the effect of different loading patterns were investigated.

Neugebaur and Putz [76] describe the advantages of bulge forming for use as a manufacturing method in the automobile industry and briefly describe a three dimensional finite element simulation of an automobile component. No information is given on the simulation method used or the results obtained. Kleiner et al. [77] describe an internal high pressure forming method to form tubes from flat sheets of metal. Flat sheets are congruently put upon another and welded pressure tight. A tubular structure arises from internal high pressure forming. A finite element simulation of the manufacturing process was carried out using the finite element code INDEED. Simulation results were compared with experimental measurements and good agreement was found. A similar method and analysis was reported by Hein and Vollersten [78].

Doege et. al [79] describes a finite element optimisation scheme to determine optimised load paths for axisymmetric bulge forming processes. A specially developed algorithm is used in conjunction with the ABAQUS/explicit finite element analysis software. The algorithm avoids failure of the tube by adjusting the axial force and pressure boundary conditions using a fuzzy logic control. The calculated load path is optimised in such a way that every moment during the process as much axial force as possible is applied to the ends of the tube.

Ahmed and Hashmi [80] reported a finite element simulation of the manufacture of a box section elbow from a pre-bent cylindrical tube. The effect of fixing the ends of the tube and various loading patterns was examined. It was found that holding the tube ends during forming resulted in a better product than allowing the tube ends to move. Asnafi [81] and Asnafi and Skogsgardh [82] describe a finite element simulation of free bulging of axisymmetric tubes. An experimental analysis is also described and the finite element results are compared with theoretical and experimental analysis. Sokolowski et al. [83] describe how axisymmetric bulging of tubes, together with a finite element simulation can be used to determine tube formability and material characteristics.

Hashemi and Zheng [84] describe a finite element simulation of the manufacture of spherical pressure vessels from integral polyhedrons. The simulation take significant advantage of the symmetry of the polyhedron and a sub-modelling scheme is used. Zhang et al. [85] report a three dimensional finite element simulation of the manufacture of pressure vessel heads by bulge forming circular plates. Zhang et al. [86, 87] describe finite element simulations of the manufacture of spherical pressure vessels, similar to that of Hashemi and Zheng [84].

2.4. Summary of Literature Survey

From the literature cited and described the following points can be noted:

1. Many experimental studies have been carried out on axisymmetric and asymmetric bulging of tubular blanks. These studies have examined the effect of various process variables such as tube material, tube geometry and die configurations.
2. While a number of analytical studies are available concerning axisymmetric bulging of tubes, very few analytical studies concerning asymmetric tube bulging were found. The few studies available predict deformation, thickness and forming load, but do not take account of important process parameters such as internal pressure, material characteristics and friction.
3. Very few finite element simulation studies were found on bulge forming of asymmetric components. In particular, bulge forming of cross-joints has not been simulated.
4. No three dimensional finite element simulations of bulge forming using a solid bulging medium or bulge forming of non-homogenous tubes were found.
5. No simulation studies have considered the effects of the process on the die or the effect of die elasticity on the process.
6. Three dimensional finite element simulation has the potential to provide a deeper understanding of the process, particularly by illustrating the development of stresses and strains in the formed component. Understanding of this development will allow optimisation of the process and better design of process equipment.

Chapter 3 : Theoretical Background - Finite Element Method

3.1. Introduction

The objective of this chapter is to provide a basic theoretical outline of the numerical methods used to solve the problems as described in later chapters. This chapter is not intended as a text on the finite element method, rather as a description of how the method was utilised here, and hence the reader unfamiliar with the method is referred to the references section.

3.2. The Finite Element Method

The basic steps in any finite element analysis are:

1. Discretization:

   The problem domain is divided into a number of regularly shaped subdomains called finite elements. Each element contains a number of nodal points which have known coordinates relative to the global problem coordinate system. The shape of the element is defined in terms of the coordinates of these nodal points and interpolation or shape functions.

2. Determination of Element Behaviour

   An interpolation function is assumed for the variation of the unknown (i.e. displacement, temperature etc. depending on the analysis) across each element. For each element, coefficient matrices which describe the response characteristics of the element are determined. In the case of stress analysis this matrix corresponds to the element stiffness matrix.

3. Transformation of Element Behaviour to Global Axis

   The element stiffness matrices naturally lie parallel to the element local coordinate system. In order to solve the entire problem these matrices have to be transformed to align with the global coordinate system.

4. Assembly of Global Element Equations

   The transformed stiffness matrix for each element are now combined in order to determine the stiffness matrix for the entire problem domain. This forms a matrix equation defining the behaviour of the entire solution domain.

5. Application of Boundary Conditions

   In order for the problem to be solved, some of the nodal unknowns must be restrained and will not be arbitrary in value.

6. Solution for Nodal Unknowns

   The primary nodal unknowns are determined by solving a set of linear algebraic equations. In most problems the number of equations to be solved is very large thus special solution techniques are employed. After solution the values of the dependant variable at each node is known.

7. Calculation of Element Resultants

   Using the nodal values and interpolation functions secondary or derived quantities such as stresses and strains are determined.

3.2.1 General Theory

This section will outline the general theory involved in the finite element method drawing particularly from reference [88]. There are a number of methods available for determining the governing equations of equilibrium for the finite element method. One such method is to use the principle of virtual displacements to express the equilibrium of the body. This principle states that the internal virtual work in the body is equal to the external virtual work acting upon the body due to external forces. The internal virtual work is equal to the actual stresses going through the virtual strains. The external work is given by the actual forces going through the virtual displacements. For a three dimensional body with body forces f^B, Surface traction f^S, and concentrated forces F^i, resulting in virtual displacements U, virtual stress σ and virtual strain ε, the principle can be stated as:

$$\int_V \{\bar{\varepsilon}\}^T \{\sigma\} dv = \int_V \{\bar{U}\}^T \{f^B\} dv + \int_S \{\bar{U}\}^T \{f^S\} ds + \int_i \{\bar{U}\}^T F^i \qquad (1)$$

where:

$\{\bar{\varepsilon}\}^T = [\bar{\varepsilon}_{xx} \quad \bar{\varepsilon}_{yy} \quad \bar{\varepsilon}_{zz} \quad \bar{\gamma}_{xx} \quad \bar{\gamma}_{yy} \quad \bar{\gamma}_{zz}]$

$\{\sigma\}^T = [\sigma_{xx} \quad \sigma_{yy} \quad \sigma_{zz} \quad \sigma_{xy} \quad \sigma_{yz} \quad \sigma_{zx}]$

$\{\bar{U}\}^T = [\bar{U} \ \bar{V} \ \bar{W}]$ and $\bar{U}$, $\bar{V}$ and $\bar{W}$ are displacements in global directions

$\{f^B\}^T = [f_x^B \quad f_y^B \quad f_z^B]$ where superscript B indicates body

$\{f^S\}^T = [f_x^S \quad f_y^S \quad f_z^S]$ where superscript S indicates surface

$\{F^i\}^T = [F_x^i \quad F_y^i \quad F_z^i]$ where superscript i indicates points

As the problem domain is approximated by an assembly of finite elements which are interconnected at nodal points on the element boundaries, the displacements measured within each element are assumed to be a function of the displacements at the nodal points. Thus for element m,

$$u^{(m)}(x,y,z) = H^{(m)}(x,y,z)\hat{U} \qquad (2)$$

where $H^{(m)}$ is the displacement interpolation matrix or shape function for element m and $\hat{U}$ is a vector of the three global displacement components U_i, V_i and W_i at all nodal points (i.e. if there are N nodes then $\hat{U}$ will be of dimension 3N).

Using this assumption, equilibrium equations that correspond to the nodal point displacements of the assembly of finite elements can be constructed from equations (1) and (2):

$$\sum_m \int_{V(m)} \varepsilon^{(m)T} \sigma^{(m)} dV^{(m)} = \sum_m \int_{V(m)} \bar{U}^{(m)T} f^{B(m)} dV^{(m)} + \sum_m \int_{S(m)} \bar{U}^{S(m)T} f^{S(m)} dS^{(m)} + \sum_m \bar{U}^{iT} F^i \qquad (3)$$

From the assumption on displacements in equation (2) the corresponding element strains can be determined as:

$$\varepsilon^{(m)}(x,y,z)=B^{(m)}(x,y,z)\hat{U} \qquad (4)$$

where $B^{(m)}$ is the strain-displacement matrix for element m. The rows of $B^{(m)}$ are obtained by appropriately differentiating and combining rows of matrix $H^{(m)}$.

The stress within a finite element are related to the element strains and initial stresses by

$$\sigma^{(m)}=D^{(m)}\varepsilon^{(m)}+\sigma^{I(m)} \qquad (5)$$

where $D^{(m)}$ is a matrix which relates stress to strain in element m and $\sigma^{I(m)}$ is the element initial stresses. $D^{(m)}$ is essentially a matrix which contains the material behaviour of the element and may be isotropic or anisotropic and may vary from element to element. Using equations (2) , (4) and (5) we can rewrite equation (3) as:

$$\overline{U}^{T}\left[\sum_{m}\int_{V(m)}B^{(m)T}D^{(m)}B^{m}\,dV^{(m)}\right]\hat{U}=\hat{U}^{T}\left[\begin{array}{l}\left\{\sum_{m}\int_{V(m)}H^{(m)T}f^{B(m)}\,dV^{(m)}\right\}+\\ \left\{\sum_{m}\int_{S(m)}H^{S(m)T}f^{S(m)}\,dS^{(m)}\right\}-\\ \left\{\sum_{m}\int_{V(m)}B^{(m)T}\sigma^{I(m)}\,dV^{(m)}\right\}+F\end{array}\right] \qquad (6)$$

where $H^{S(m)}$ is the surface displacement interpolation matrix for element m, and is obtained from the volume displacement interpolation matrix, $H^{(m)}$, in equation (2) by substituting the element surface coordinates. F is a vector of the externally applied forces to the nodes of the finite element assembly. It may be noted that in equation (6) the nodal point displacement vector, $\hat{U}$, is outside the summation sign as it is independent of the element considered.

In order to obtain the equations for the unknown nodal point displacements from equation (6), the virtual displacement theorem is utilised by imposing unit virtual displacements in turn at all displacement components. This results in $\hat{U}^{T}$ = I (where ***I*** is the identity matrix) and by denoting $\hat{U}$ by $\boldsymbol{U}$, the equilibrium equation of the element assemblage corresponding to the nodal point displacements is:

$$KU=R \tag{7}$$

The matrix K is the global stiffness matrix and is given by:

$$K=\sum_{m}\int_{V(m)} B^{(m)T}D^{(m)}B^{(m)}\,dV^{(m)} \tag{8}$$

The load vector $R=R_B+R_S-R_I+R_C$, where R_B is the effect of element body forces:

$$R_B=\sum_{m}\int_{V(m)} H^{(m)T}f^{B(m)}dV^{(m)} \tag{9}$$

R_S is the effect of element surface forces and is given by:

$$R_S=\sum_{m}\int_{S(m)} H^{S(m)T}f^{S(m)}dS^{(m)} \tag{10}$$

R_I is the effect of element initial stresses and is given by:

$$R_I=\sum_{m}\int_{V(m)} B^{(m)T}\sigma^{I(m)}dV^{(m)} \tag{11}$$

and $R_C=F$ (i.e. the concentrated loads).

Equation (7) is a statement of the static equilibrium of the finite element mesh. In equilibrium considerations, applied forces may vary with time, in which case the displacements may also vary with time. In such a case equation (7) is a statement of equilibrium for a specific point in time. If in reality the loads are applied rapidly, inertia forces must be considered and a dynamic problem must be solved. Using d'Alembert's principle, the element inertia forces may be included as part of the body forces. In such a case equation (9) becomes:

$$R_B = \sum_m \int_{V(m)} H^{(m)T} \left[f^{B(m)} - \rho^{(m)} H^{(m)} \ddot{U} \right] dV^{(m)} \tag{12}$$

where $f^{B(m)}$ no longer includes inertial forces, $\ddot{U}$ gives nodal point accelerations and $\rho^{(m)}$ is the mass density of element m. In this case the equilibrium equations are:

$$M\ddot{U} + KU = R \tag{13}$$

where K is the global stiffness matrix, M is the global mass matrix and R and U are time dependant. The global mass matrix is given by:

$$M = \sum_m \int_{V(m)} \rho^{(m)} H^{(m)T} H^{(m)} dV^{(m)} \tag{14}$$

However, in a dynamic analysis some energy is dissipated during vibration, which in vibration analysis is usually taken account of by introducing velocity dependant damping forces. Introducing the damping forces as additional contributions to the body forces changes equation (12) as follows:

$$R_B = \sum_m \int_{V(m)} H^{(m)T} \left[f^{B(m)} - \rho^{(m)} H^{(m)} \ddot{U} - \kappa^{(m)} H^{(m)} \dot{U} \right] dV^{(m)} \tag{15}$$

where $\dot{U}$ is a vector of the nodal point velocities and $\kappa^{(m)}$ is the damping property parameter of element m. In this case the equilibrium equations become:

$$M\ddot{U} + C\dot{U} + KU = R \tag{16}$$

where C is the global damping matrix and can be written as:

$$C = \sum_m \int_{V(m)} \kappa^{(m)} H^{(m)T} dV^{(m)} \tag{17}$$

3.2.2. Non Linearities

In the above formulation it was assumed that the displacements of the finite element assembly are small, that the material is linearly elastic and that the boundary conditions remain unchanged during the application of loads. These assumptions have entered the equilibrium equation in the following manner:

(a) The fact that all integrations have been performed over the original volume of the finite elements implies that displacements must be small. This effects the stiffness matrix, K, and the load vector, R.

(b) The strain-displacement matrix, B, of each element was assumed to be constant and independent of element displacements.

(c) The assumption of a linear elastic material is implied in the use of a constant stress-strain matrix, D.

(d) The unchanged boundary conditions is implied by keeping constant constraint relations for the complete response.

These observations point to the different types of non-linearity that may arise in a finite element analysis:

(1) Non linearity due to large displacements, large rotations, but small strains.

(2) Non linearity due to large displacements, large rotations and large strains.

(3) Material non linearity.

(4) Non linearity due to contact.

3.2.3. Solution Methodology

There are many solution methods available for use with the finite element method, however, as the analysis in this work is primarily concerned with non linear analysis, this section will concentrate on solution methodology for non linear problems. The basic problem in a general non linear analysis is to determine the state of equilibrium of the body corresponding to the applied loads. Assuming that the external loads are described as a function of time, the equilibrium conditions of the finite element assembly can be written as:

$$ {}^{t}R - {}^{t}F = 0 \tag{18} $$

where ^{t}R gives the externally applied nodal point forces at time t and the vector ^{t}F lists the nodal point forces corresponding to the element stresses, where:

$$ {}^{t}R = {}^{t}R_B + {}^{t}R_S + {}^{t}R_C \tag{19} $$

$$ {}^{t}F = \sum_{m} \int_{tV(m)} {}^{t}B^{(m)T} \, {}^{t}\sigma^{(m)t} \, dV^{(m)} \tag{20} $$

It may be noted that in a dynamic analysis the vector ^{t}R would also include the inertial and damping forces.

Equation (18) must express the equilibrium of the system in the current defined geometry by taking account of all non linearities and must be satisfied throughout the complete history of load application. The solution process is carried out using a step by step incremental analysis. The basic approach in an incremental solution is to assume that the solution for the discrete time t is known and that the solution for a discrete time t+Δt is required, where Δt is a suitably chosen time increment. Thus, at time t+Δt equation (18) can be written as:

$$ {}^{t+\Delta t}R - {}^{t+\Delta t}F = 0 \tag{21} $$

Since the solution at time t is known it can be written that:

$$ {}^{t+\Delta t}F = {}^{t}F + F \tag{22} $$

where F is the increment in nodal point forces corresponding to the increment of element displacements and stresses from time t to time t+Δt. This vector can be approximated using a tangent stiffness matrix ^{t}K which corresponds to the geometric and material condition at time t.

$$ F \cong {}^{t}K\,U \tag{23} $$

where U is the vector of incremental nodal point displacements. By combining (21), (22) and (23) we get:

$$ {}^{t}KU = {}^{t+\Delta t}R - {}^{t}F \tag{24} $$

By solving this equation for U an approximation to the displacements at time t+Δt can be calculated:

$$ {}^{t+\Delta t}U \cong {}^{t}U + U \tag{25} $$

Having evaluated an approximation to the displacements corresponding to time t+Δt an approximation for stresses and corresponding nodal point forces at time t+Δt can be obtained. However, because of the approximation expressed in equation (24), such a solution may be subject to significant errors and may be unstable. In practice it is frequently necessary to iterate until equation (21) is satisfied to sufficient accuracy.

Different solution procedures exist for the solution of equation (24). In this work the explicit time integration method was used and will be briefly outlined. The most common explicit time integration operator used in non linear dynamic analysis is the central difference operator. The equilibrium of the finite element assembly is considered at time t in order to calculate the displacements at time t+Δt. Solution is sought for each time step for the equilibrium equation neglecting the effect of damping which may be expressed as:

$$ M\,{}^{t}\ddot{U} = {}^{t}R + {}^{t}F \tag{26} $$

where the nodal point force vector ^{t}F is evaluated on the basis of the methods used to formulate the material and geometric non linearity's. This involves the choice of element type, the kinematic description and the kinetic description, all of which are problem dependant. The solution for the nodal point displacements at time t+Δt is obtained using the central difference approximation for the accelerations as follows:

$$ \ddot{U} = \frac{1}{\Delta t^{2}} \left\{ {}^{t-\Delta t}U - 2\,{}^{t}U + {}^{t+\Delta t}U \right\} \tag{27} $$

Combining this with equation (26) gives:

$$ \frac{M}{\Delta t^{2}} \left\{ {}^{t+\Delta t}U \right\} = {}^{t}R - {}^{t}F - \frac{M}{\Delta t^{2}} \left\{ {}^{t-\Delta t}U - 2\,{}^{t}U \right\} \tag{28} $$

Thus, if ${}^{t-\Delta t}U$ and ${}^{t}U$ are known then ${}^{t+\Delta t}U$ can be determined from (28). A disadvantage in the use of this method is that for stability, the time step sizeΔt must be smaller than a critical time step size Δt_{CR} which is equal to T_n/π, where T_n is the smallest period in the finite element assembly.

3.3. LS-DYNA3D Theoretical Methods

3.3.1. Solution Methodology

LS-DYNA3D is a general purpose explicit dynamic finite element code for analysing highly non linear transient dynamic problems. Metal forming is a quasi-static process, therefore, a dynamic analysis process can be used for the simulation of metal forming processes if the kinetic energy of the process does not become too high relative to internal energy during the analysis. The equilibrium equation of a dynamic problem and the solution process using the central difference method was given above in equations (26), (27) and (28). As mentioned above, the time step sizeΔt and its relation to the critical time step size Δt_{CR} is of most importance. LSDYNA3D calculates the critical time step size from:

$$\Delta t = \frac{l}{C} \tag{29}$$

where l is the characteristic length of the smallest element and C is the sonic wave propagation velocity through the element material. For reasons of stability a scale factor of 0.9 is used to decrease the time step in equation (29). The time step used by LSDYNA3D is therefore given by:

$$\Delta t = 0.9\frac{l}{C} \tag{30}$$

l and ***C*** are calculated in a different manner depending on the element type concerned. In this work eight node solid elements were used for the analyses, in which ***l*** is the smallest distance between two neighbouring nodes of the smallest element in the model. The sound wave propagation speed is given by:

$$C = \sqrt{\frac{E(1-\nu)}{(1+\nu)(1-2\nu)\rho}} \tag{31}$$

3.2.2. Element Formulation

In this work an eight node hexahedron solid element was used for the analyses. Volume integration of the elements is carried out using Gaussian quadrature. Both reduced (one point) and full integration options are available. The biggest advantage to reduced integration is the substantial saving in computer time, however, this has to be balanced by the need to control the zero energy modes, called hourglassing modes, which may arise.

Hourglassing is a zero energy mode of deformation that oscillates at a frequency much higher than the structures global response. Hourglassing modes may result in stable mathematical states that are not physically possible. They typically have no stiffness and give a zigzag deformation appearance to the finite element mesh. The hourglass deformation mode in a two dimensional element is shown in figure 3.1. for illustration.

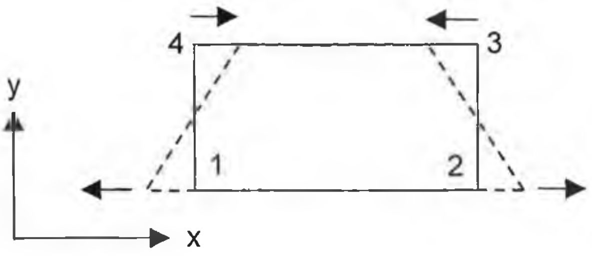

Figure 3.1. : Hourglass Deformation Mode

The origin and consequent implications of the hourglass deformation mode is described in elementary form, with reference to the above figure, by Halliquist and Benson [89]. Suppose nodes 1 and 3 are given a velocity of +1 in the x direction and nodes 2 and 4 are given a velocity of –1 in the x direction, then the element deforms but the velocity gradient of the element is zero. Because the velocity gradient is zero, the element does not develop stresses to oppose the velocities and the element may continue to deform in this mode without resistance.

One method of resisting hourglassing modes in to use a viscous damping or a small elastic stiffness capable of stopping the formation of the hourglass modes but having a negligible effect on the stable global nodes. The hourglassing resisting force for a particular node in a particular coordinate direction is dependant to the nodal velocity in that direction. The resisting force in solid elements is given by:

$$f_{i\alpha}^{k} = a_h h_{i\alpha} \Gamma_{ak} \tag{32}$$

where:

$$a_h = Q_{hg}\, \rho v_e^{2/3} \frac{c}{4} \tag{33}$$

$$h_{i\alpha} = \sum_{k=1}^{8} x_i^k\, \Gamma_{ak} \tag{34}$$

in which:

α = number of hourglass mode

$\Gamma_{\alpha k}$ = hourglass shape vectors

x_i^k = velocity of node k in i direction

v_e = element volume

c = speed of sound in material

Q_{hg} = a constant (usually set between 0.15 and 0.55 [reference 90])

Fully integrated elements are less susceptible to hourglass deformation but have the disadvantage of increased computing time. In addition fully integrated elements used in the solution of plasticity problems and other problems where Poisson's ratio approaches 0.5 lock up in the constant column bending modes. To preclude locking, an average pressure is used over the elements and consequently the zero energy modes are resisted by deviatoric stresses. In certain situations it has been noted [90] that the cost of using fully integrated elements can be justified by increased reliability and if used sparingly may actually increase the overall speed.

3.3.3. Material Model

LSDYNA3D has an extensive library of material models available to the user. In this work all simulations used a bilinear isotropic hardening plasticity model with no strain rate dependence. The yield stress is defined as:

$$\sigma_y = \sigma_o + E_p \varepsilon_p^{eff} \tag{35}$$

where:

σ_0 is the initial yield stress

E_p is the plastic hardening modulus and is given by $E_p = (E_{Tan}E)/(E - E_{Tan})$

ε_p^{eff} is the effective plastic strain

E_{Tan} is the tangent modulus

E is Young's modulus

3.3.4. Contact Algorithm

Unlike many implicit finite element formulations, elements are not used to define contact within LSDYNA3D. Contact is defined using contact surfaces. Contact occurs when one segment of a model's outer surface penetrates another segment. With eighteen different contact types available, contact surfaces within LSDYNA3D allow the user to represent a wide range of interactions between surfaces. To properly select a contact surface for a given model it is important to understand the different contact algorithms available. There are three different contact algorithms available: Single surface contact, Nodes to surface contact and Surface to Surface contact. In this work the surface to surface contact algorithm was used for all models and will be detailed below.

The surface to surface contact algorithm establishes contact when the surface of one body penetrates the surface of another. The algorithm establishes a fully symmetric contact so that the choice of contact and target surfaces are arbitrary. In order to define surface to surface contact, nodal components or part numbers are required for the contact and target surfaces. The surface to surface contact algorithm is generally used for bodies that have large contact areas and the contact surfaces are known, as in the processes analysed in this work. The algorithm is based on the penalty method.

The penalty method consists of placing normal interface springs between all penetrating nodes and the contact surface. The interface stiffness is chosen to be approximately the same order of magnitude as the stiffness of the interface element normal to the surface. Contact searching is performed in two steps: global and local searching. In a global search the bucket sort method is used. In the bucket sort algorithm, the three dimensional space occupied by the contact surface is divided into cubes (or "buckets"). Nodes can contact any segment in the same bucket or an adjoining bucket. After the global search has located possible contact, a local search checks for penetration. A node to segment algorithm is used to find the penetration. When a slave node penetrates a master surface, a restoring force $\boldsymbol{f_r}$, proportional to the penetration depth, $\boldsymbol{l}$, is generated to restore the node to the contact surface in the normal direction, $\boldsymbol{n}$. The restoring force may be expressed as:

$$f_r = -k\,l\,n \tag{36}$$

where k is the master surface stiffness which is independently calculated for each contact surface segment form the bulk modulus, the volume and the surface area of the element. The stiffness is expressed as:

$$k = \frac{(SFSI)K A^2}{V} \tag{37}$$

where K is the bulk modulus, A is the surface area and V is the volume of the element. The scale factor, **SFSI**, may be used to control the stiffness and is generally set to a default value of 0.1.

When a penetrating node stays in contact with the target, it may ether stick to the surface or slip along the surface. Friction is provided for stick-slip simulations by a tailored algorithm. The relative slip between the master and slave surfaces is calculated by recording the isoparametric co-ordinates and master segment number for every slave node that is in contact with the master surface. Any distance moved by the slave node is treated as a measure of strain and the radial return algorithm is used to return the tangential force to the yield surface.

As mentioned earlier, the penalty method is implemented in a symmetric manner. When the mesh grading varies along the contact surfaces, or the surfaces are subject to large distortions, the best choice of master surface may vary along the contact surfaces. The symmetry greatly increases the robustness of the contact algorithm by allowing each surface to act as both the master and slave surfaces.

3.3.5. Friction

Friction in LSDYNA3D is based on a Coulomb formulation. If f^* is the trial force, f_n is the normal force, k is the interface stiffness, μ is the coefficient of friction and f^n is the frictional force at time n, then:

$$f^* = f^n - \mu k \Delta e \tag{38}$$

where:

$$\Delta e = r^{n+1}(\xi_c^{n+1}, \eta_c^{n+1}) - r^{n+1}(\xi_c^{n}, \eta_c^{n}) \tag{39}$$

in which (ξ_c, η_c) are the contact point coordinates and $\boldsymbol{r}$ represents a master segment that has a unique normal whose direction depends continuously on the points of the corresponding master surface segment.

The frictional force at time n+1 (i.e. f^{n+1}) needs to be determined. This is given by:

$$f^{n+1} = f^* \quad \text{if} \quad |f^*| \le F_y \qquad \text{or} \qquad f^{n+1} = \frac{F_y f^*}{|f^*|} \quad \text{if} \quad |f^*| \ge F_y \tag{40}$$

$$\text{where : } F_y = \mu |f_n| \tag{41}$$

An exponential function smooths the transition between the static and dynamic coefficients of friction where v is the relative velocity between the slave node and the master segment:

$$\mu = \mu_d + (\mu_s - \mu_d)e^{-c|v|} \tag{42}$$

where:

$$v = \frac{\Delta e}{\Delta t} \tag{43}$$

where Δt is the time step size and c is the decay constant.

The interface shear stress that develops as a result of Coulomb friction can be very large and in some cases can exceed the ability of the material to carry the stress. In order to help avoid this situation a further limit is placed on the value of the tangential force:

$$f^{n+1} = \min\left(f^{n+1}_{Coulomb}, \kappa A_{Master}\right) \tag{44}$$

where, A_{Master} is the area of the master segment and κ is the viscous coefficient.

3.4. Summary of Chapter 3

This chapter presents the theoretical methods utilised in the following analyses and explains how they are implemented in the software used to perform the analyses.

Chapter 4 : Hydraulic Cross Branch Forming

4.1 Introduction

This chapter details the modelling procedures used to simulate the forming of cross branches from straight tubes using the hydraulic bulging method. The results from the simulations are presented and analysed.

4.2 Modelling

The most important step in any finite element simulation is the idealisation and modeling of the problem. In the case of metal forming analysis good modeling of the deforming body is of most importance in order to achieve an accurate solution. Asymmetric forming of tubes is a complicated process. In order to properly represent the problem and to be able to detect unusual deformations such as wrinkling or buckling a three-dimensional analysis is required. In this case the ANSYS pre-processor was used to develop the finite element model and the LS-DYNA3D explicit solver was used to solve the problem. The ability of LS-DYNA to successfully model large strain process such as those encountered in metal forming operations has been well demonstrated.

Simulations were carried out to bulge a copper cylindrical tube of 24.12 mm diameter and 107mm length into a cross-joint. The diameter of the branches was equal to that of the main tube. The geometry of the die and blank were modelled to be consistent with the geometry used by Hutchinson [30] in his experiments. By taking advantage of symmetry it was possible to model one eighth of the problem. The geometries used for the die and blank are shown in figures 4.1 and 4.2. In this case the die is a particularly difficult part to model satisfactorily particularly at the region where the die main body and die recess blend together. This region is indicated in figure 4.3, which shows a rendered solid model of one eighth of the die model. The difficulty in modelling this region arises from the fact that it is doubly curved and that the blending radius is varying from a known radius at one end to an infinite radius at the other (see figure). Unfortunately, the ANSYS pre-processor used for this analysis was not capable of developing such surfaces, so it was decided to use a separate solid modelling package to develop the die model.

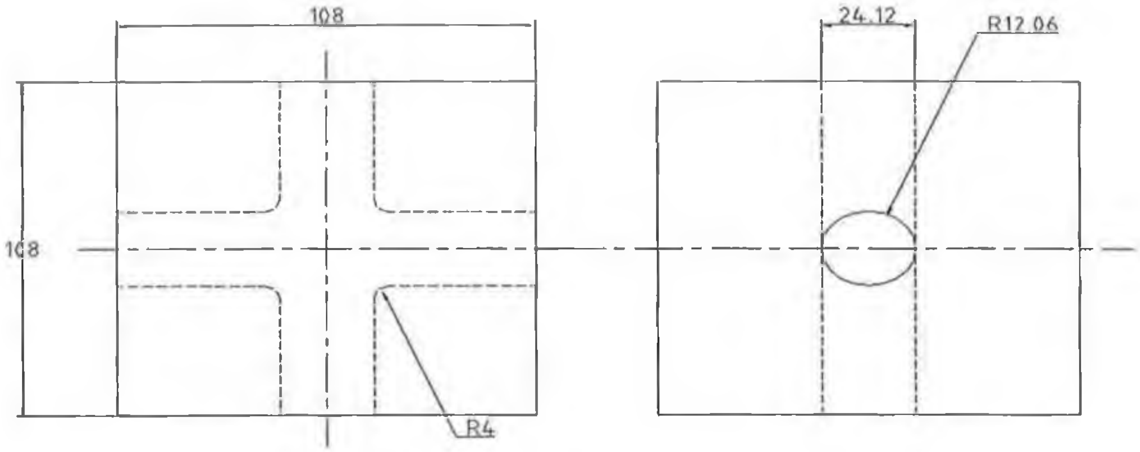

Figure 4.1. : Die Geometry

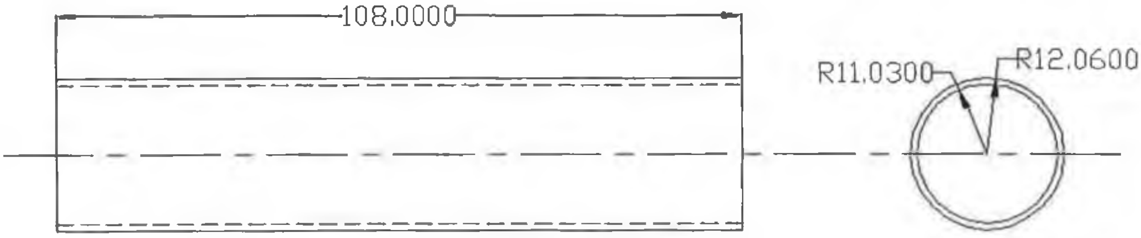

Figure 4.2. : Blank Geometry

The solid model was developed using Autodesk's Mechanical Desktop package. The modelling of the required geometry was easily achieved by extruding half-tubes from defined profiles, joining the two half-tubes to form a x-branch and then removing the required portion of the lower tube to make a quarter tube. The blending region was generated by defining a volume fillet between the two tube volumes. The model geometry was transferred to ANSYS using the IGES translation capabilities which was available in both packages. IGES (Initial Graphics Exchange Specification) is a neutral format used to exchange geometric models between dissimilar CAD and CAE systems. All the entities transferred from the Mechanical Desktop model are supported by the IGES input translator in ANSYS, however, the solid model reconstructed by ANSYS from the IGES data had a number of problems.

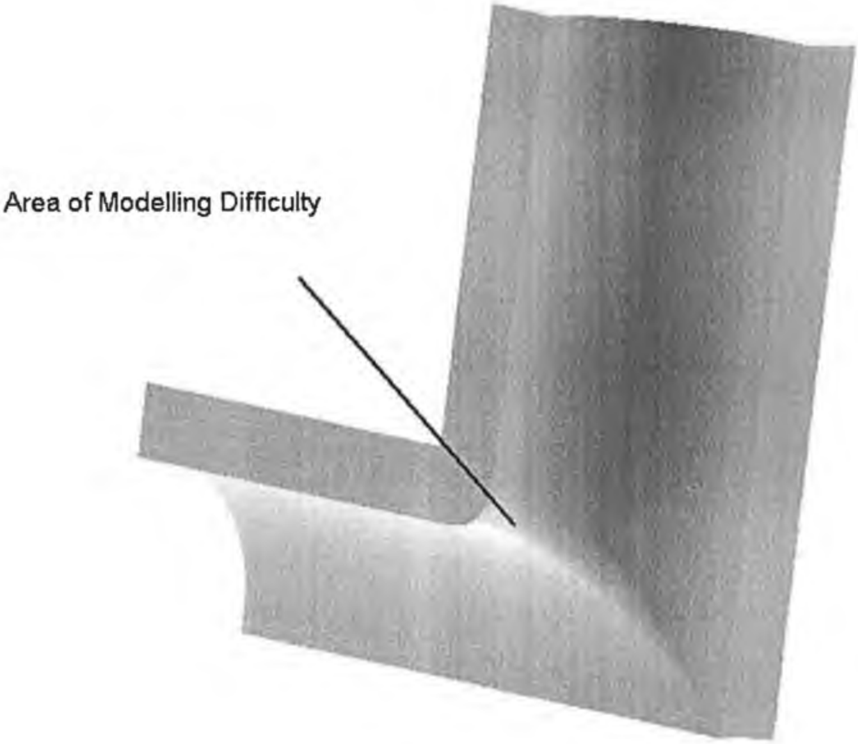

Figure 4.3. : Cut away View of One Eighth of the Die.

Upon checking of the model many unwanted lines and surfaces were found which would later pose problems when trying to mesh the die model. ANSYS is equipped with a suite of topological and geometric tools designed specifically for interactive repair of imported models. Using these tools is was possible to identify many duplicate lines and keypoints and merge them to a specific tolerance. After all necessary cleaning operations were complete the die model was satisfactory and consisted of three volumes : one volume described the die upper half of the die main body, one described the die recess and a third volume described the blending region.

Early analyses identified a phenomenon which required extension of the die model and hence generation of further volumes. It was noticed in these analyses that the edge nodes at symmetry edges of the model deformed in a very unusual manner. It was discovered to be a contact problem, in that at the edges there was no die node to harbour tube nodes to form a contact pair. In order to overcome this problem the die edges were extended a little further from the tube edges. After this the problem of edge deformation disappeared. The blank was built in one volume by defining a quarter cylinder with the required dimensions. Figure 4.4. shows the discretized finite element model of the entire problem. The die consists of 296 elements with one element height defining the die thickness. The blank comprised of 1140 elements with two layers of elements across its thickness. The total amount of nodes in the model is 2528. Both the die and the tube were modeled using eight node three dimensional explicit dynamic solid elements. Where possible, in order to reduce computational time, reduced integration was used, where the elements have one integration point at their centroid.

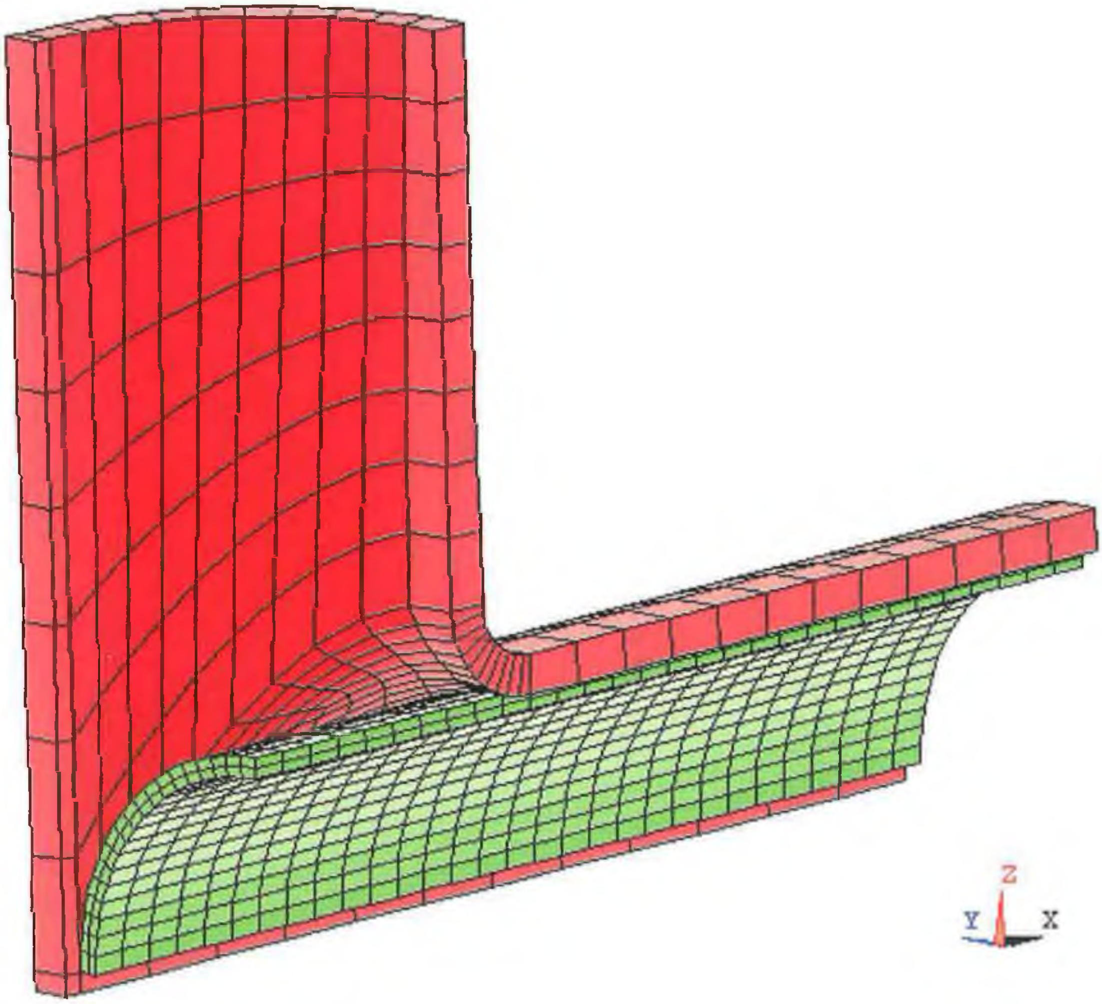

Figure 4.4. : Finite Element Model of One Eighth of the Problem

The material properties used for the tube are shown in table 4.1. A bilinear linear elasto-plastic material model was assumed for the tube, as illustrated in figure 4.5. This simplistic material model does not allow for strain rate effects, however, the impact of using such a model is not thought to be significant as copper at room temperature is not particularly strain rate sensitive and in the actual process strain rate generally does not exceed 10/sec.

Young's Modulus, E	124 GPa
Tangent Modulus, E_{tan}	0.112 GPa
Poisson's Ratio, ν	0.3
Density, ρ	8.9×10^{-6} Kg/mm^3
Yield Strength, σ_y	0.16 GPa
Failure Strain, ε_f	0.45

Table 4.1. : Material Data Used for Tube Material Model [30]

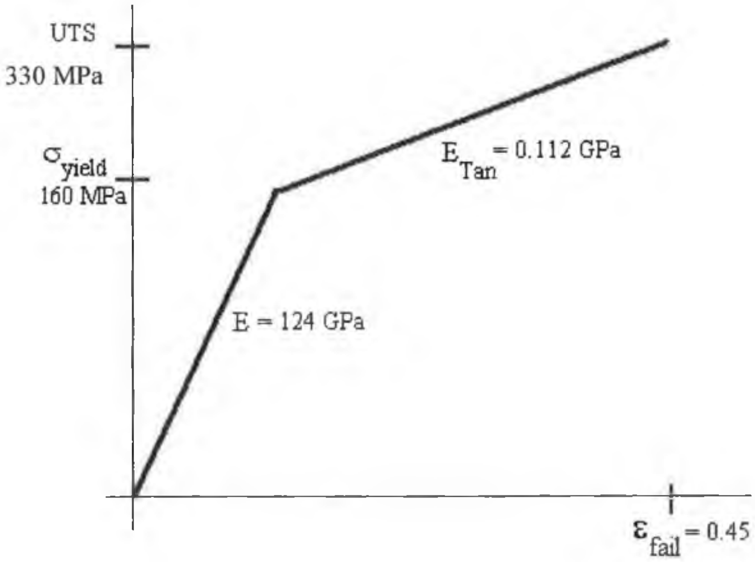

Figure 4.5. : Material Model Used for Tube Material

The die was modelled as a linear-elastic material model approximating tool steel. The interface between the die and the tube was modeled using the automatic surface to surface contact algorithm described in chapter 2. The algorithm uses the material properties of both contacting surfaces to calculate the stiffness of the contact elements. An elastic coulomb friction law was assumed and a coefficient of friction of 0.15 was assigned. This was taken as representative of values measured experimentally [30].

4.3. Boundary Conditions, Loading and Solution

Since one eighth of the model was developed by taking advantage of symmetry, the tube nodes at the symmetry edges were restrained in the appropriate directions. The die was constrained as a rigid body. The pressure load was applied as a surface load on the inner tube surface and the axial load was applied as a prescribed displacement of the nodes at the edge of the tube end. In the actual forming process the tube ends are placed over a punch. In this case the punch was not modelled, instead the nodes of the tube under the punch were constrained in the radial and circumferential directions, which is equivalent to the punch being in position.

The first simulation of the forming process was carried out using pressure loading only. The loading pattern for the first simulation is shown in figure 4.6. In this case the tube ends were free to move. The second simulation was performed on the same finite element model using pressure load and axial displacement as shown in figure 4.7. This loading pattern was developed in order to maximise bulge height. It was found from earlier simulations that it is important to apply the majority of the pressure load before the axial displacement becomes too great. It is also important to allow for a pressure increase during the application of the remainder of the axial load. This ensures that what occurs in the actual forming process (i.e. an increase in pressure, due to the decrease in internal volume as a result of the thickening of the main tube) is realistically modeled.

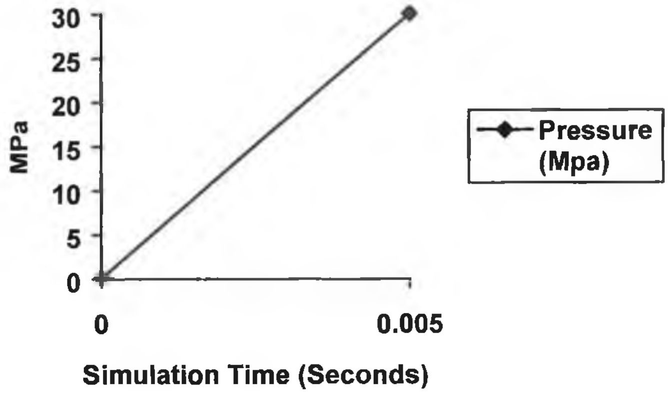

Figure 4.6 : Loading Pattern 1

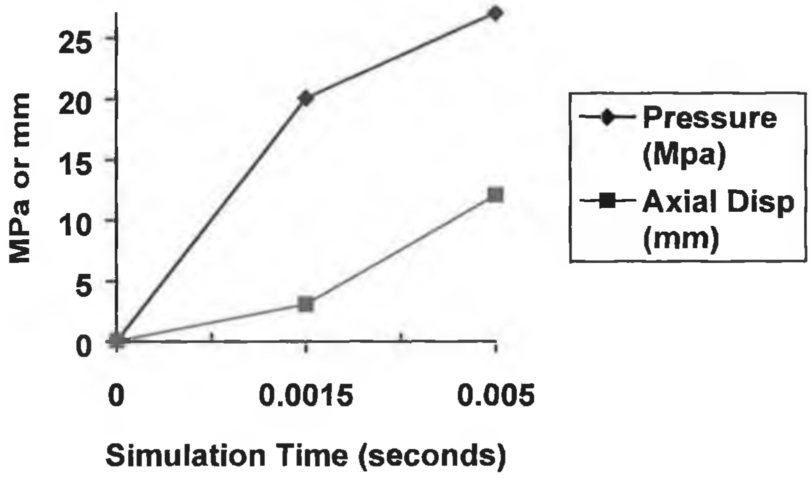

Figure 4.7 : Loading Pattern 2

The third simulation was carried out to examine the effect of friction. This simulation used the same loading pattern as the second simulation and a zero coefficient of friction was assigned. The fourth simulation was carried out to examine the effect of changing the blank wall thickness and also utilised loading pattern two. In order to determine the effect of die blend radius on the process two further simulations were run in which required different die models. The models were built in the manner described previously but the die blend radius was modelled as 3mm and 5mm respectively and both simulations utilised loading pattern two.

In order to reduce computational time it was required to set the simulation time for the analysis to 0.005 seconds. Clearly this is much shorter than actual real time for the process, however, the kinetic energy of the process during deformation was checked during each analysis to ensure that it was negligible. The brick elements used in the model were reduced integration elements. Reduced integration elements though prone to hourglass deformation are computer time efficient and generally give better results for metal forming analysis. The level of hourglass energy in each analysis was measured to ensure that it was within acceptable limits: defined by the developers of LSDYNA as being less than 10% of the internal energy of the process [42].

4.4. Results and Analysis

4.4.1. Pressure Load Only

The first simulation was run with a high pressure in order to determine the critical pressure for the process. The point of rupture is assumed when a node in the highly stressed area (i.e. the branch top) is steeply stressed or strained to beyond the ultimate tensile stress or failure strain for the material model. Figure 4.8 shows the distribution of stress in the bulged tube produced by the first loading pattern at the point just before rupture.

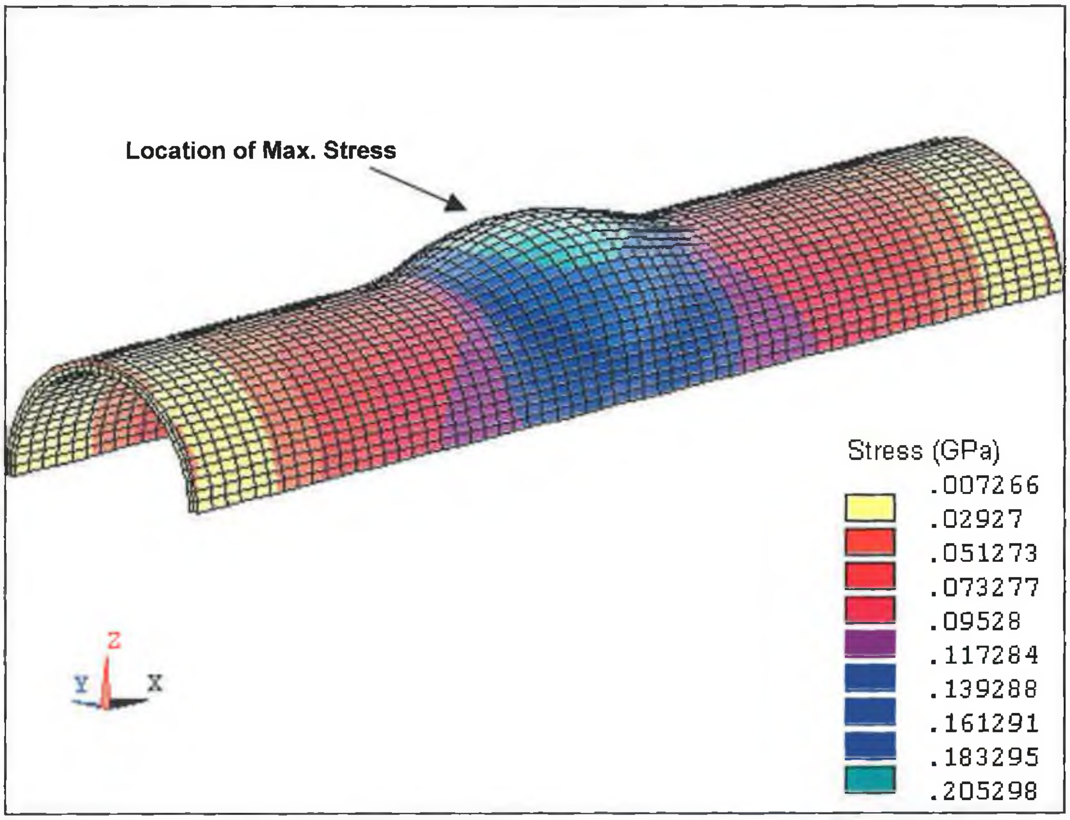

Figure 4.8 : Von-Mises Stress in the deformed Cross-branch by loading pattern 1.

This simulation time at this point was 3.25 milliseconds and the pressure at this stage was 20Mpa. The branch height obtained by this load was 4mm. The bulged region has stressed considerably with a relatively uniform distribution. The highest stressed region is at the branch top. The maximum stress developed in this region is 205 MPa. In comparison the highest stress in the main tube is approximately 46% of this value.

Figure 4.9 shows the development of von-Mises and principal stresses in the central node of the cross-branch top surface. After a simulation time of 3.25 all stress values began to increase sharply as the bulge ruptured, thus all results after this time were ignored. The stress development was steady and relatively stable until a simulation time of 0.002 seconds, which corresponds to the beginning of deformation. It can be seen that after the onset of deformation that the ratio of the first (hoop) and second (axial) principal stresses was relatively constant in agreement with the pressure load which was raised uniformly throughout the simulation.

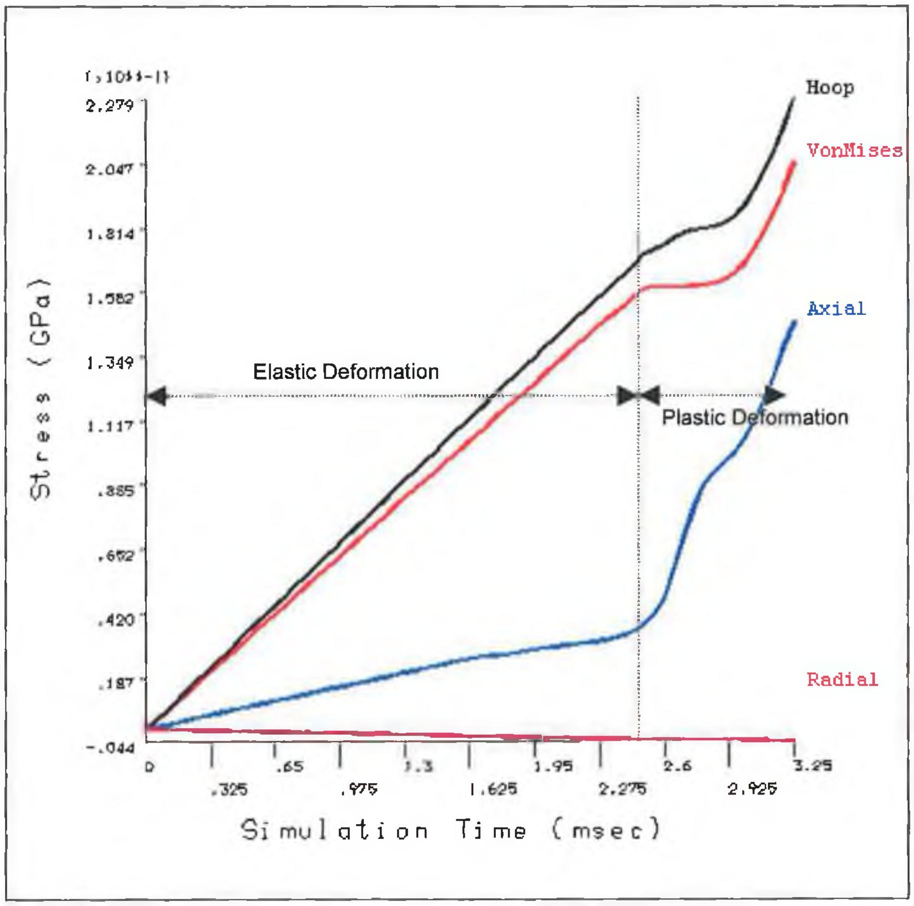

Figure 4.9. : Development of Stress at the Top Central Node of the Cross-branch

Figure 4.10 shows the distribution of thickness strain in the deformed cross branch. It can be seen from the figure that the bulged region has thinned considerably while the main tube has experienced little deformation. Upon closer examination it was found that the bulge top has thinned down to approximately 63% of the original thickness, while the main tube has not thinned significantly. Clearly this amount of thinning combined with the low branch height would not produce a useful component.

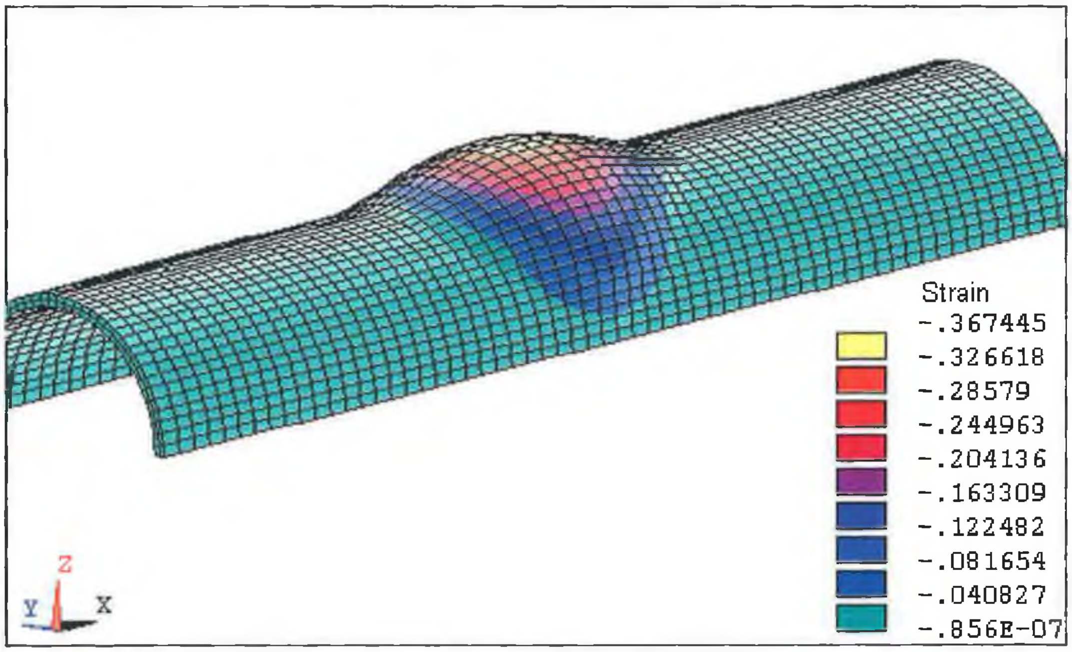

Figure 4.10. : Distribution of Thickness Strain in the Deformed Tube

4.4.2. Combined Pressure and Axial Loading

As mentioned previously, the second simulation was run with combined internal pressure and axial compressive loading in order to increase bulge height. The development of the bulge is detailed in figures 4.11. to 4.15. which show the distribution of stress at various times during the simulation. Using the symmetry expansion capabilities of the ANSYS post-processor it was possible to view the entire upper half of the cross branch. It can be seen from the figures that the bulge initially develops as a hump at the center of the tube. As the pressure increases then the bulge begins to become more regular. By the time 40% of the final load has been applied the bulge is well developed and develops in a regular fashion as illustrated in figures 4.14. and 4.15. It can be seen from the figures that the location of maximum stress does not change as the bugle grows.

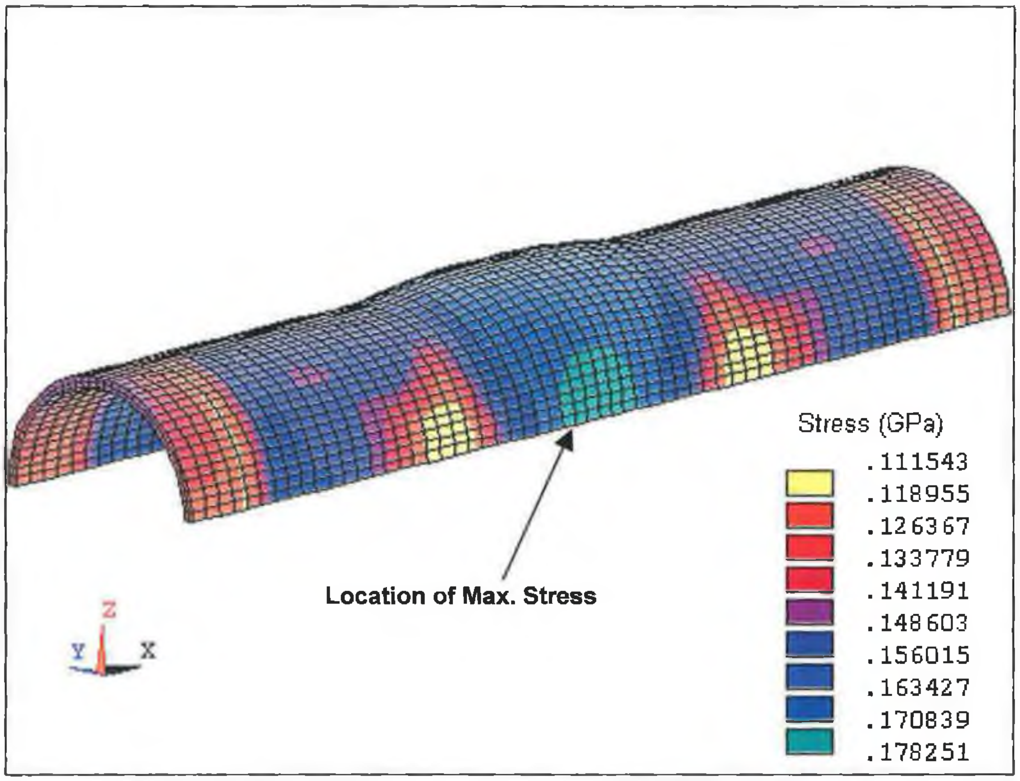

Figure 4.11. : Distribution of von-Mises Stress in the Tube at 10% of Final Load

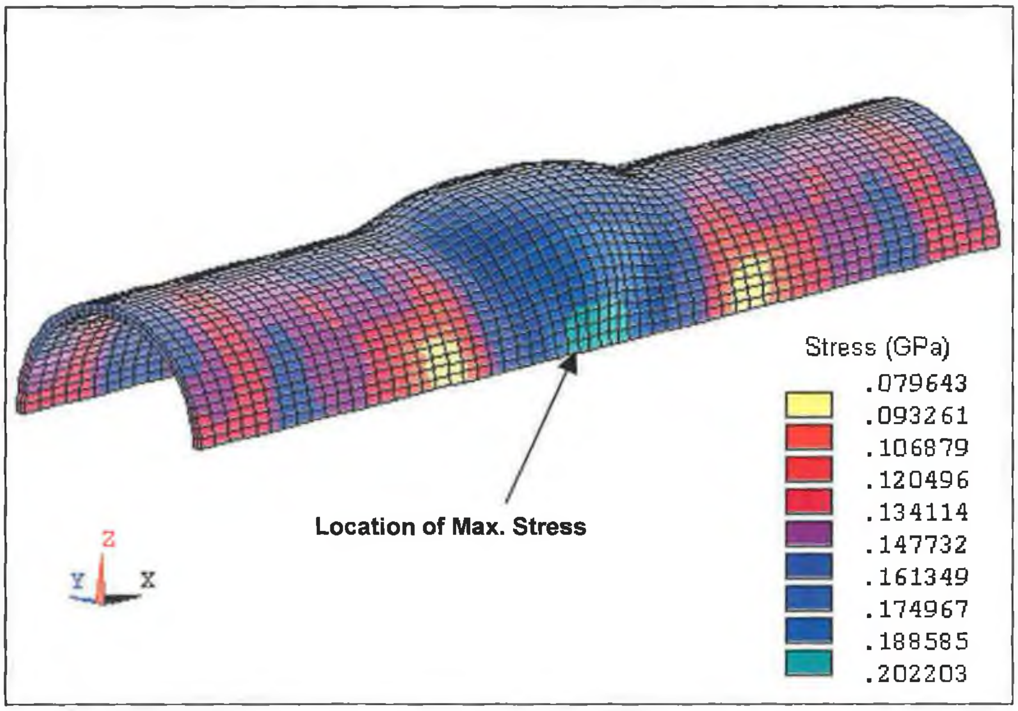

Figure 4.12. : Distribution of von-Mises Stress in the Tube at 20% of Final Load

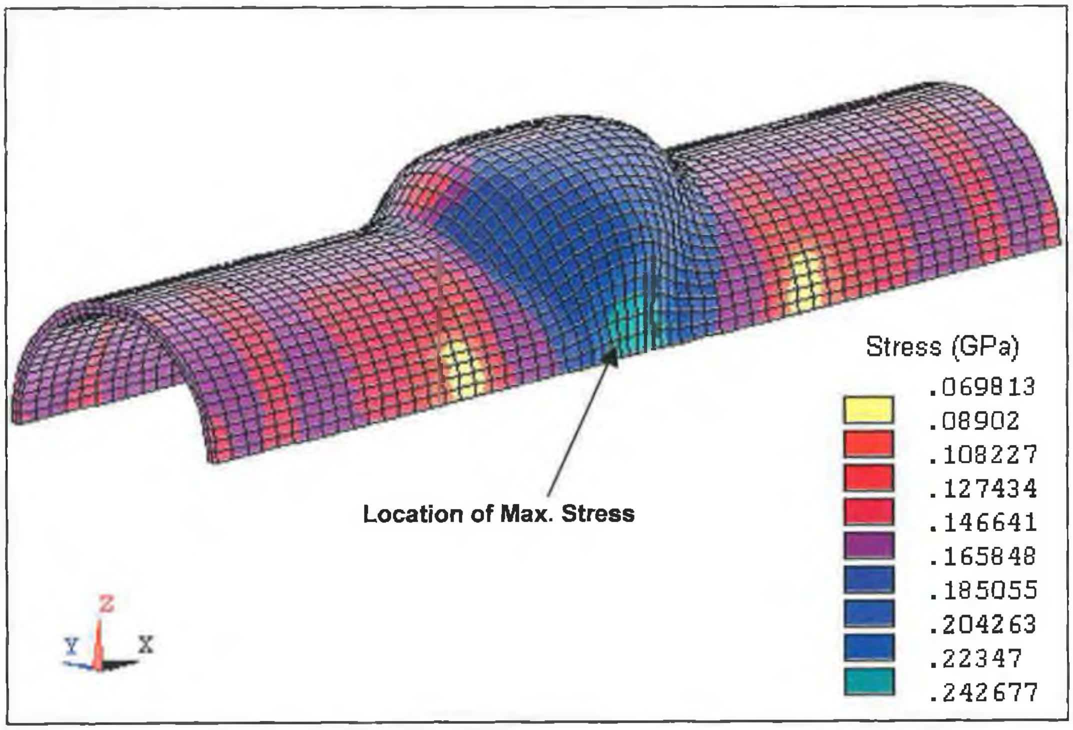

Figure 4.13. : Distribution of von-Mises Stress in the Tube at 40% of Final Load

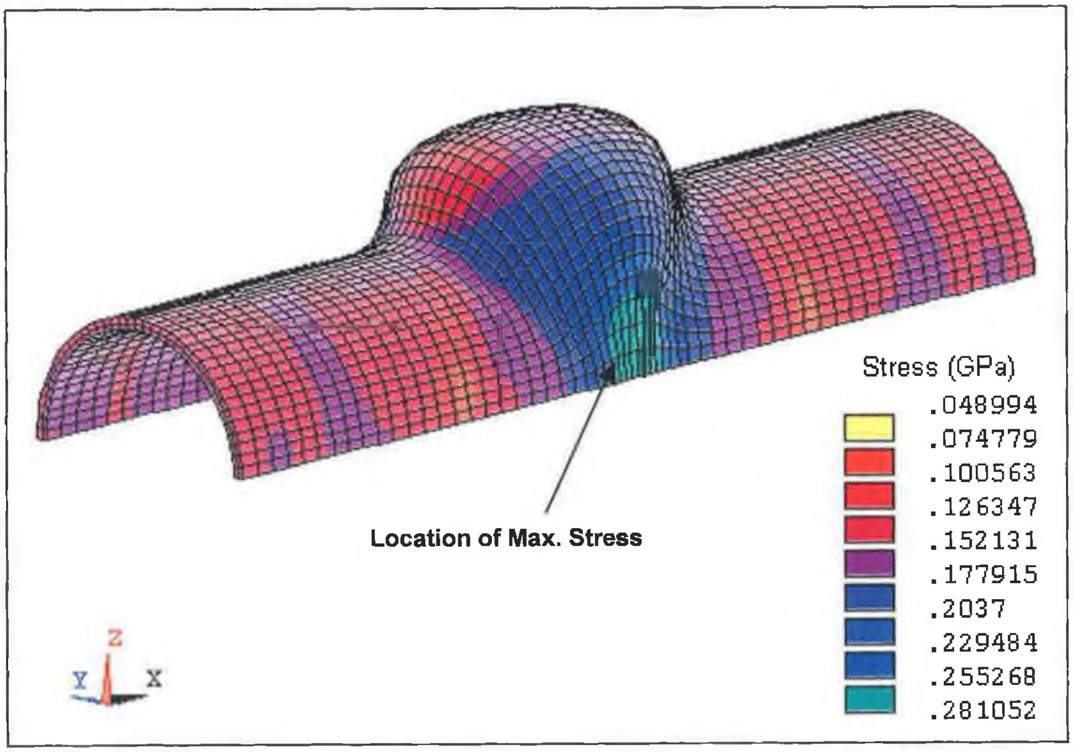

Figure 4.14. : Distribution of von-Mises Stress in the Tube at 70% of Final Load

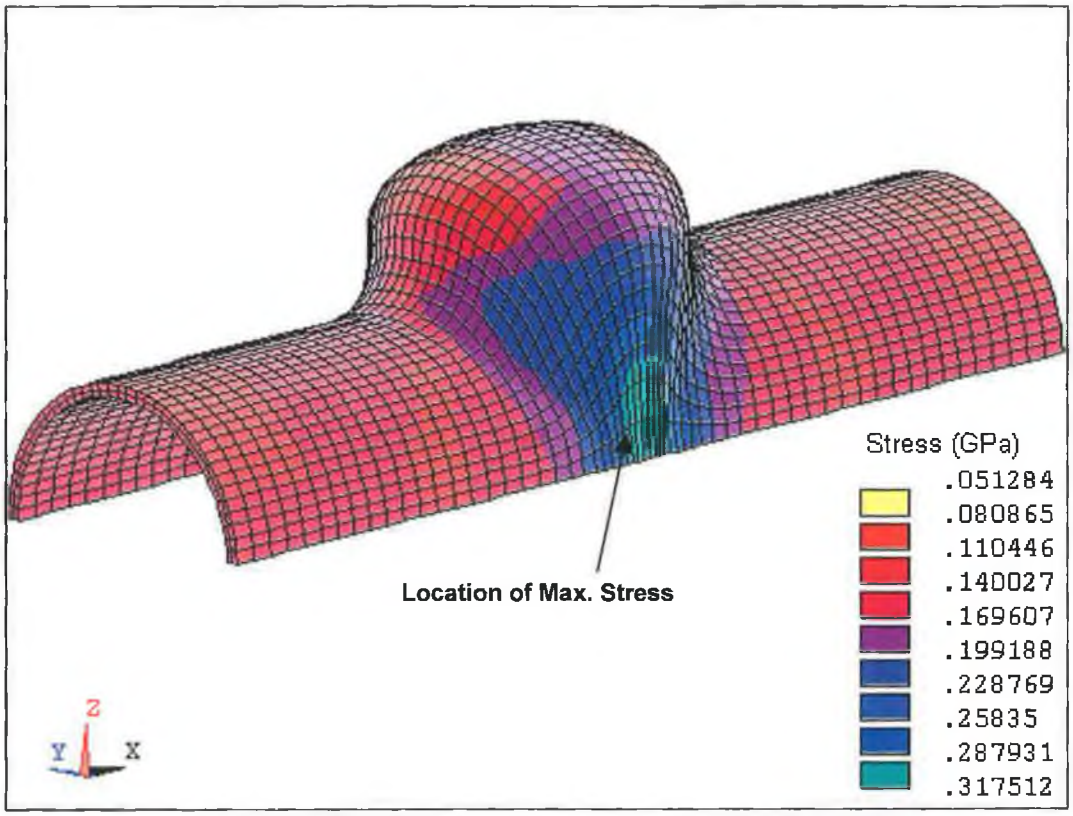

Figure 4.15. : Distribution of von-Mises Stress in the Tube at Final Load by Loading Pattern Two.

Figure 4.15. shows the distribution of stress in the bulged tube at full load. It can be seen from the figure that the cross branch has taken on a topospherical shape. The maximum branch height obtained was 12mm. The maximum stress was 317 MPa located in the region as indicated in the figure.

An investigation of thickening and thinning behaviour in the deformed tube showed that the branch top has thinned to 84% of the original thickness. This thin region does not extend too far down the branch and, in fact, encompasses the part which would be cut off to form the finished component. There is some thickening of the main tube in the region of high stress, as indicated previously, due to the axial compressive load. There is also some thickening in the main tube ahead of the punch. From the above information it is clear that this cross branch would be an acceptable component, but may require some machining to remove the material build up in the main tube.

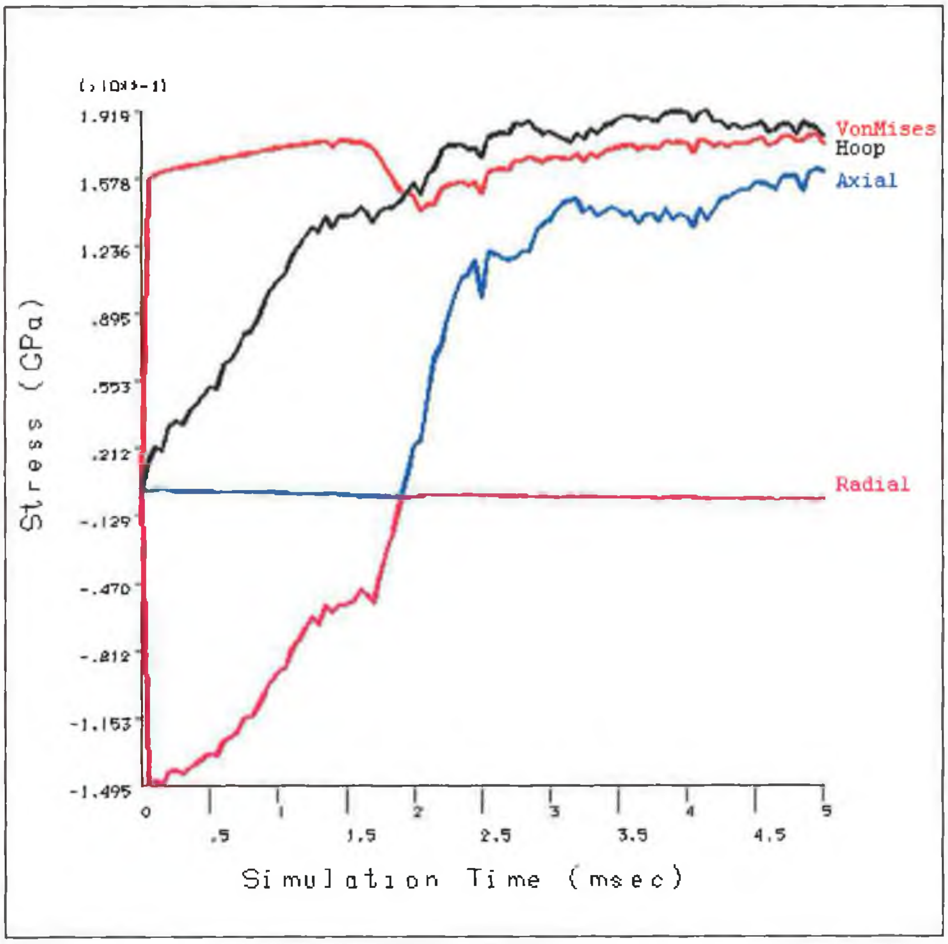

Figure 4.16. : Development of Stress at the Top Central Node of the Cross-branch by loading pattern two.

Figure 4.16. shows the development of von-Mises and principal stresses at the central node of the cross-branch top surface during the second simulation. It is evident from the figure that the development of stress in the early part of the simulation closely resembles the bi-linear stress-strain relationship of the material, which indicates a reliable solution. The hoop stress was always tensile, while the axial stress was compressive until the bulge began to develop and became tensile as soon as deformation of the bulge began, at a simulation time of approximately 2 milliseconds. The radial stress in the branch top was highly compressive until the bulge began to develop, at which point it became much less significant. It can be seen from the figure that the development of axial and hoop stresses was slightly erratic after the bulge began to form, this is thought to be a feature of the numerical calculation : most likely operation of the contact algorithm.

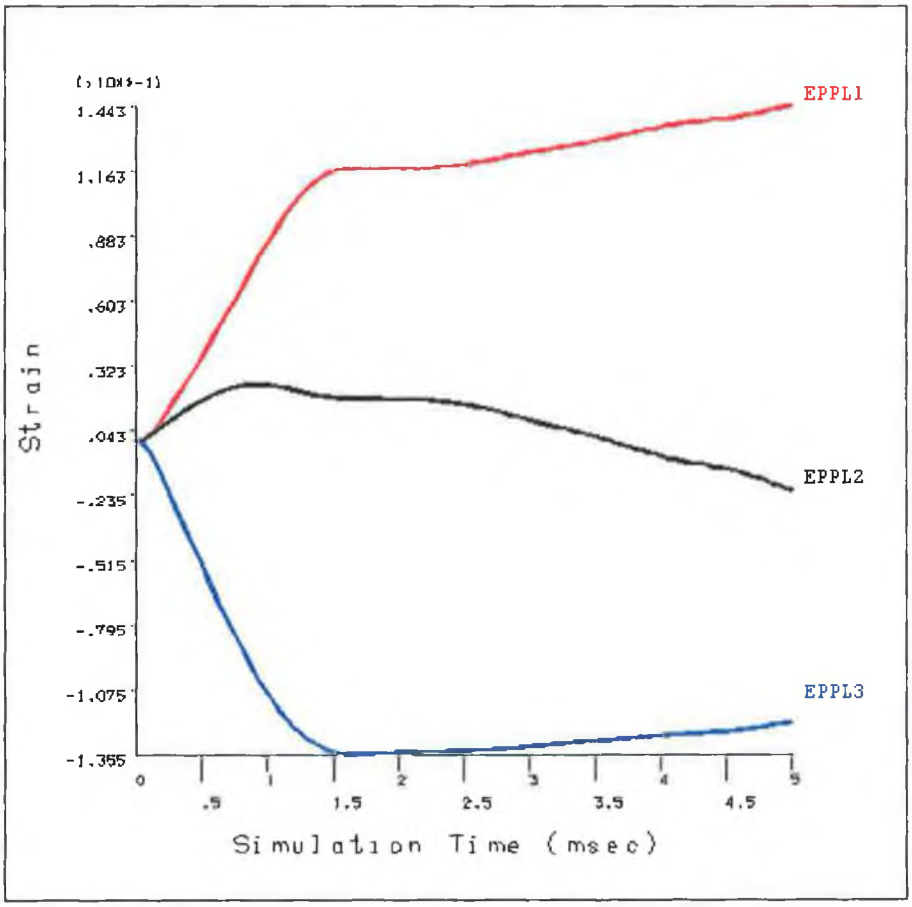

Figure 4.17. : Development of Principal Strains at the Top Central Node of the Cross Branch by loading pattern 2

The development of principal strains in the top central node of the cross branch is shown in figure 4.17. Hoop strain (EPPL1) was positive for the entire simulation while axial strain (EPPL2) was positive for the first two thirds of the simulation, before turning negative. Radial strain (EPPL3), as expected, was negative throughout the entire simulation. In order to get a clearer view of the deformation mechanisms in the branch top, figure 4.18. shows the strain path of the top central node of the cross branch in principal planes. It can be seen from the figure that the branch begins to form due to biaxial tension (in the first quadrant), due to the dominant pressure loading in the first two thirds of the simulation. After this time the axial loading becomes more prominent and the deformation mechanism is due to tension in the hoop direction and compression in the axial direction (in the second quadrant). It appears that the application of increasing compressive axial load moved the state of deformation to the second quadrant. Hoop tension appears to be dominant and the slope of the curve suggests that the elements at the branch top are elongating faster in the hoop direction than they are compressing in the axial direction. This would suggest that further loading in the same manner would rupture the branch in the axial direction of the tube. This mode of rupture has been evident in experimental studies [30].

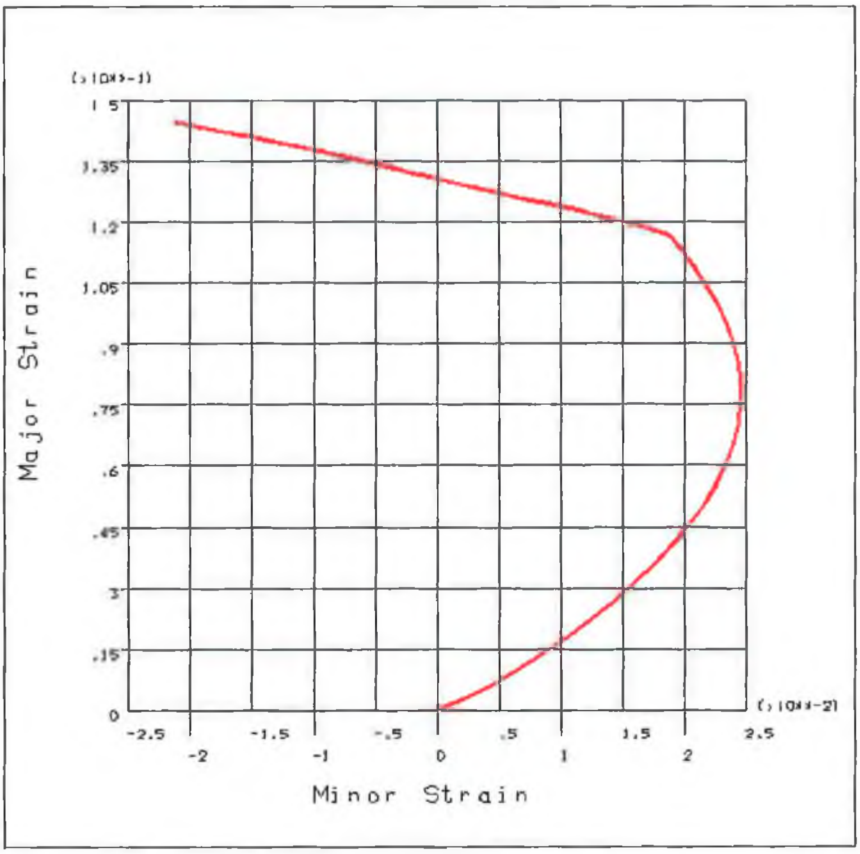

Figure 4.18. : Strain Path at the Top Central Node of the Cross-branch by loading pattern two (major strain = hoop and minor strain = axial).

4.4.3. The Effect of Increasing Friction

The third simulation was run with the objective of determining the effect of friction between the die and tube on the process. The same finite element model and loading pattern was used as in the second simulation. The distribution of stress in the bulged tube at full load is shown in figure 4.19. The cross branch has again taken on a topospherical shape. The maximum branch height obtained in this simulation was 10.5mm. This was 1.5mm lower than the height obtained in the second simulation.

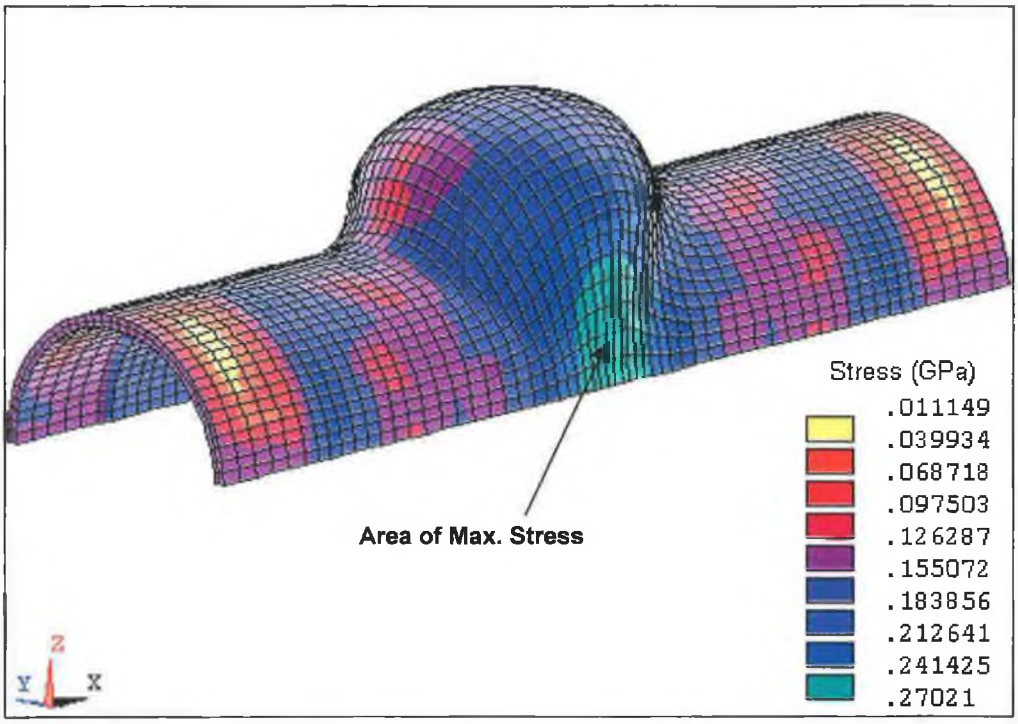

Figure 4.19. : Von-Mises Stress in the deformed Cross-branch (with increased friction).

It can be seen from figure 4.19. that the maximum stress was 270 MPa located in the same region as in the previous simulation. In this case the maximum stress is approximately 15% less than that experienced in the second simulation and the region in which the maximum stress occurs is less concentrated. It can also be seen, by comparing figures 4.15 and 4.19, that the stress gradient in the main tube is much higher for the low friction case.

An investigation of thickening and thinning behaviour showed that, as was observed in the previous simulation, the main ahead of the punch has thickened slightly. In this simulation it has increased by 33% of the original thickness. The branch top has also thinned down to approximately 78% of the original thickness. When compared with the previous simulation it appears that increasing friction appears to increase thickening ahead of the punch and also increasing thinning of the branch tops. This would appear to be a direct consequence of the increased difficulty of moving material into the deformation zone.

Figure 4.20 shows the development of stress in the central node of the cross-branch top surface during the third simulation. The stress development was relatively stable until a simulation time of 4 milliseconds, at which point it became more erratic. At this point in the simulation the compressive axial loading is becoming more important and this erratic behaviour may indicate some stick-slip movement in the main tube due to the increased friction. As with the previous simulation, the hoop stress was always tensile while the axial stress was compressive until deformation of the bulge began and then became tensile. When compared with figure 4.16, it can be seen that increasing the friction for the third simulation resulted in the final hoop stress in the branch top increasing to a value closer to the ultimate tensile stress of the material. This would seem to indicate that increased friction results in increased hoop stress at the branch top.

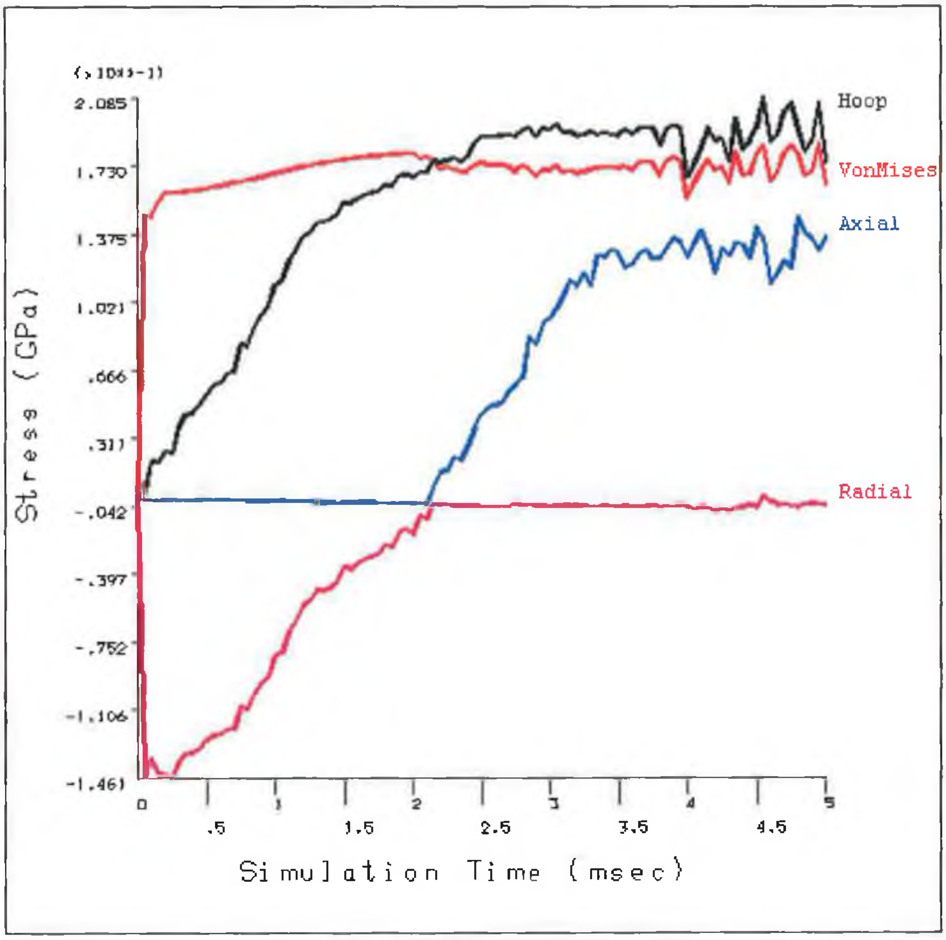

Figure 4.20. : Development of Stress at the Top Central Node of the Cross-branch (with increased friction)

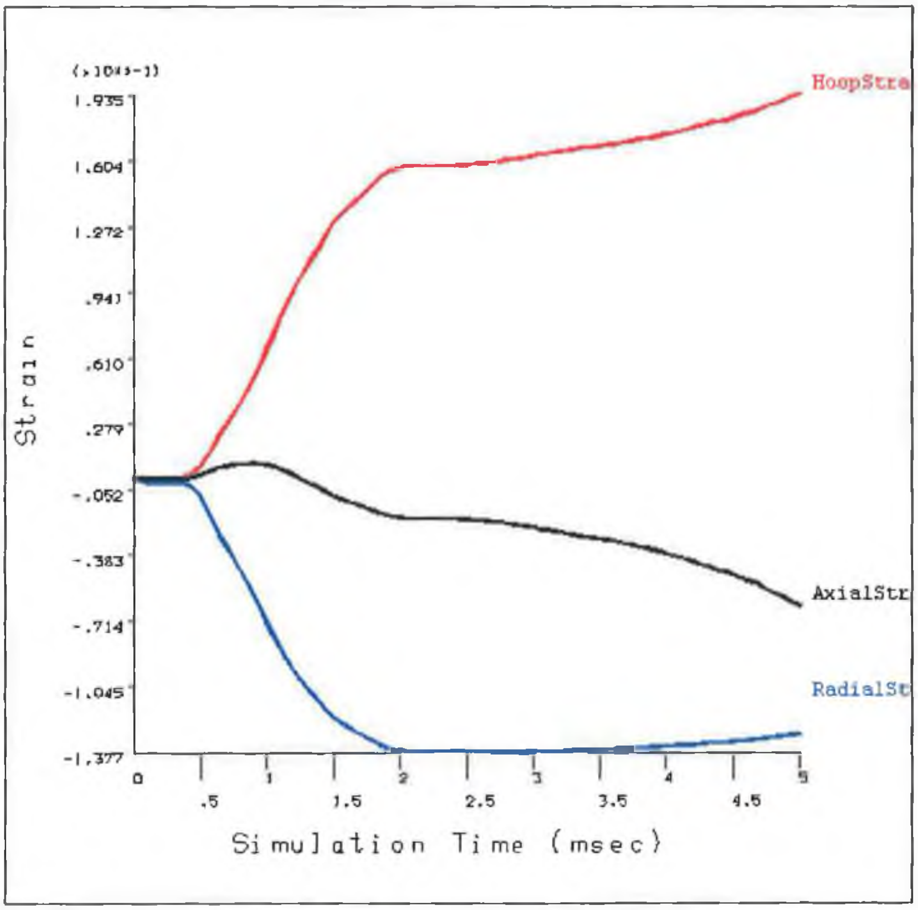

Figure 4.21. : Development of Principal Strains at the Top Central Node of the Cross-branch (with increased friction)

The development of principal strains at the top central node of the cross branch is shown in figure 4.21. Hoop strain was positive for the entire simulation while axial strain was positive for a brief period, before turning negative. Radial strain, as expected, was negative throughout the entire simulation. When compared with figure 4.17. it can be seen that the main effect of increased friction on the development of strain appears to have been a reduction in the period where axial strain was positive. In the previous simulation, axial strain was tensile for the majority of the simulation, whereas in this case it became compressive very quickly. In order to get a clearer view of the deformation mechanisms in the branch top, figure 4.22. shows the strain path of the top central node of the cross branch in principal planes. It can be seen from the figure that the branch begins to form due to biaxial tension (in the first quadrant), due to the dominant pressure loading in the first two thirds of the simulation. After this time the axial loading becomes more prominent and the deformation mechanism is due to tension in the hoop direction and compression in the axial direction (in the second quadrant). It appears that the application of increasing compressive axial load moved the state of deformation to the second quadrant. Hoop tension appears to be dominant and the slope of the curve suggests that the elements at the branch top are elongating faster in the hoop direction than they are compressing in the axial direction. This would suggest that further loading in the same manner would rupture the branch in the axial direction of the tube. This mode of rupture has been evident in experimental studies [30].

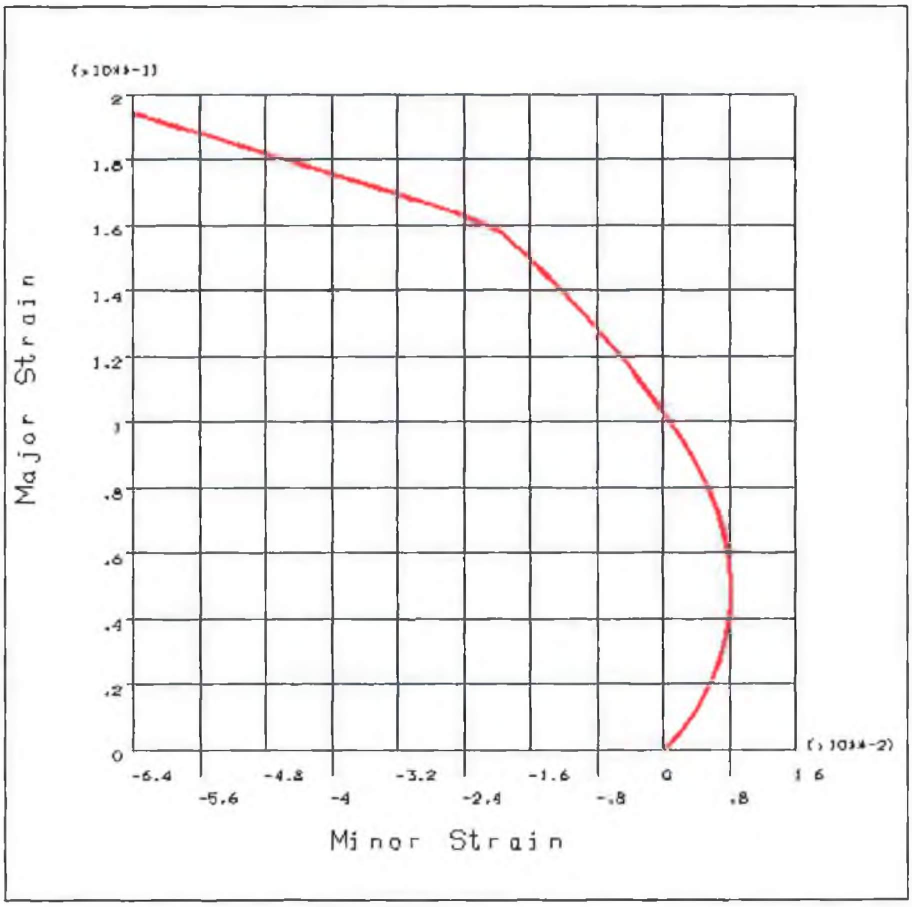

Figure 4.22. : Strain Path of the Top Central Node of the Cross-branch (with increased friction)

4.4.4 <u>The Effect of Changing the Blank Thickness</u>

The fourth simulation was run in order to determine the effect of increasing the blank thickness on the process. For this simulation the blank thickness was increased from 1.03mm to 1.37mm. The same model was used for the die as used in the previous simulations and loading pattern 2 was utilised again. A coefficient of friction of 0.15 was assigned. The distribution of stress in the bulged tube at full load is shown in figure 4.23. The cross-branch has again taken on a topospherical shape. The maximum branch height obtained in this simulation was 10mm. This was 2mm lower than the height obtained in the second simulation. It can be seen from the figure that the maximum stress was 307 MPa in the same region in which the maximum stress was observed in the previous two simulations in which a thinner tube was used. In this case the maximum stress is approximately 95% of that experienced in the second simulation, thus indicating that the use of a thicker tube results in a sight reduction in stress in the formed component. It can also be seen, by comparing figures 4.15 and 4.23, that the stress in the bulged region is higher in the simulation for the thinner tube, however, the main tube has stressed more in the simulation for the thicker tube.

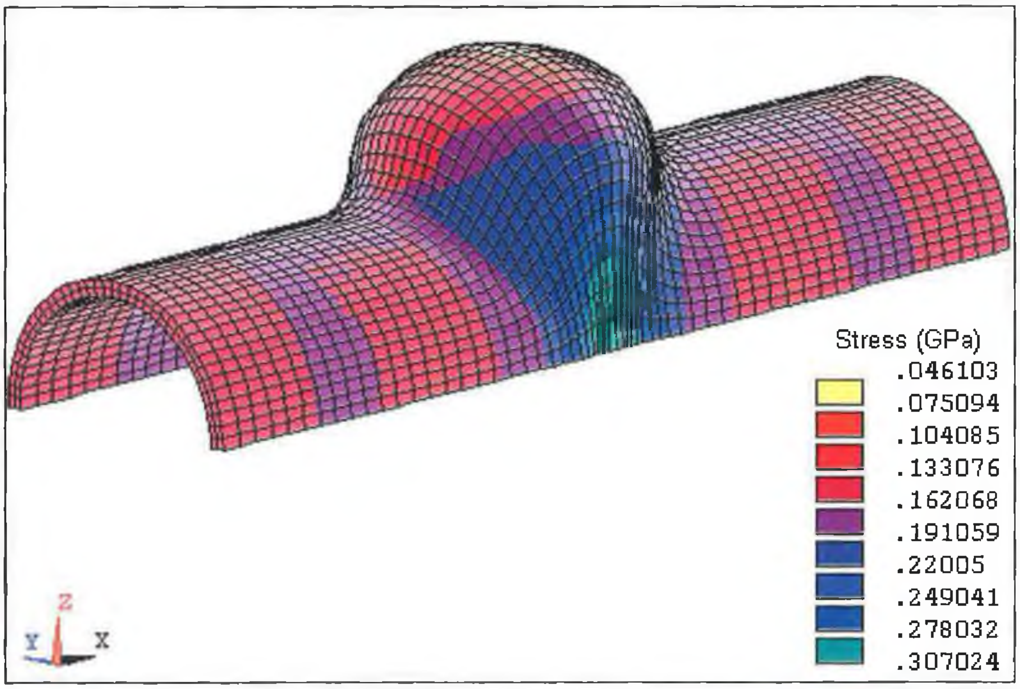

Figure 4.23. : Stress in the deformed Cross-branch (blank thickness = 1.37mm).

An investigation of thickening and thinning behaviour showed that the main tube ahead of the punch has not thickened significantly in this case. The branch top has experienced slightly less thinning behaviour than in the second simulation and has thinned down to approximately 86% of the original thickness. Again, the thinned region does not extend too far down the branch and corresponds to the portion that would be removed to form the finished component. By comparing results from simulations 2 and 4, it appears that increasing the blank thickness and using the same load pattern results in less thinning of the branch top and less thickening of the main tube ahead of the punch.

Figure 4.24 shows the development of stress in the central node of the cross-branch top surface during the fourth simulation. When compared with figure 4.16, it can be seen that using a thicker tube seems to result in a more erratic stress development pattern, indicating that stick-slip deformation and stop-start deformation in the tube is more prominent for the thicker tube. As experienced in the previous two simulations : the hoop stress was always tensile while the axial stress was compressive until deformation of the bulge began and then became tensile. It seems from the development of hoop stress up to a simulation time of 2.5 milliseconds, that the application of the majority of the pressure load early in the simulation has increased the stress and, subsequent axial loading has eased the tension in the bulge.

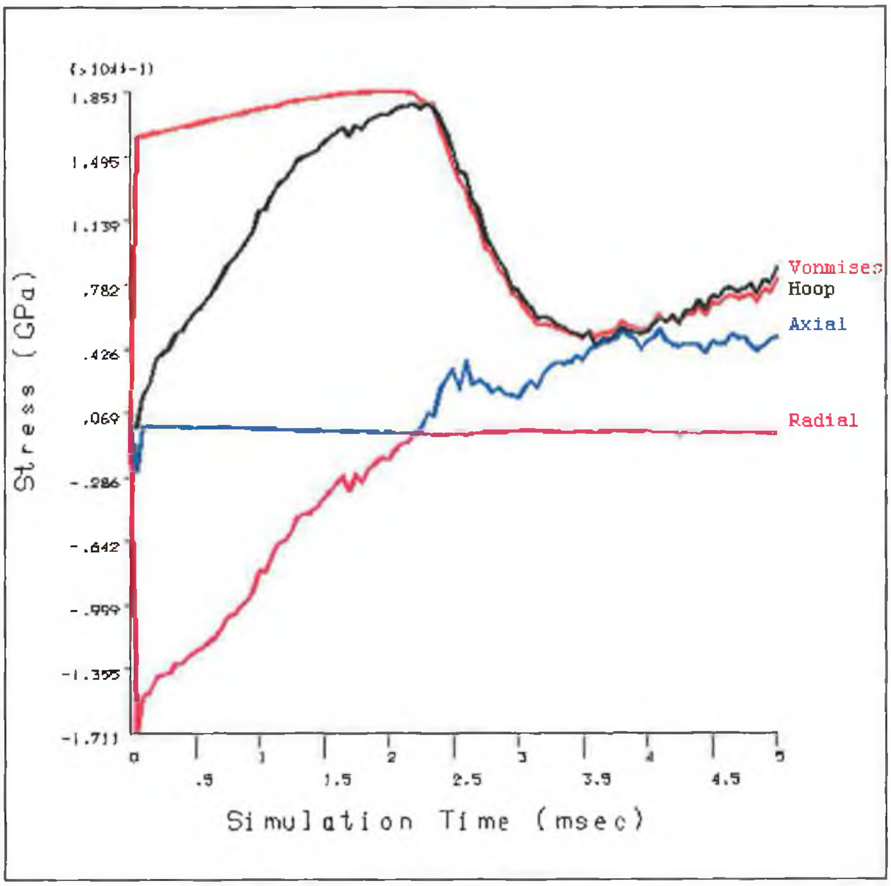

Figure 4.24. : Development of Stress in the Top Central Node of the Cross-branch (blank thickness = 1.37mm)

After a simulation time of 3.5 milliseconds the hoop stress begins to pick up again, indicating that pressure loading is beginning to become dominant again. This would seem to suggest that a greater pressure load could have been applied earlier in the simulation in order to increase deformation and bulge height. It was found from previous experience that applying a higher pressure to the thicker tube could indeed result in greater bulge height.

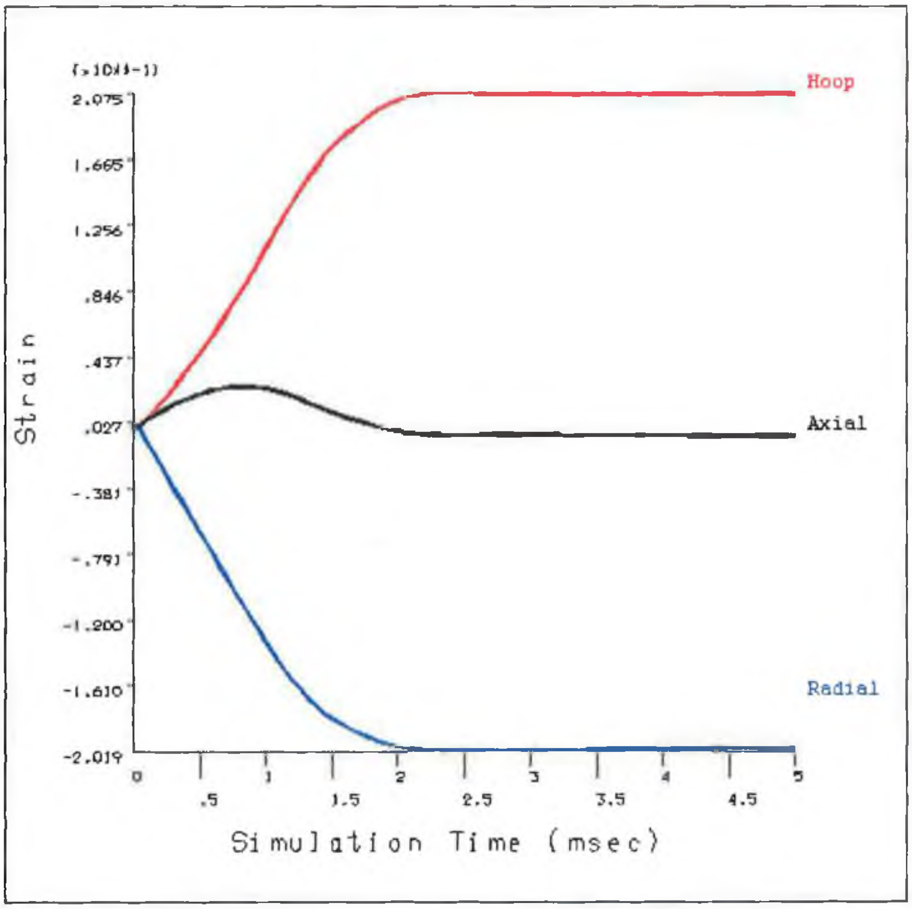

Figure 4.25: Development of Strain in the Top Central Node of the Cross-branch (blank thickness = 1.37mm).

The development of principal strains in the top central node of the cross branch is shown in figure 4.25. Hoop strain was positive for the entire simulation while axial strain was positive for a brief period, before turning negative. Radial strain, as expected, was negative throughout the entire simulation. When compared with figure 4.17. it can be seen that the effect of increased blank thickness on the development of strain appears to have been a reduction in the period where axial strain was positive. In the simulation for the thinner tube, axial strain was tensile for the majority of the simulation, whereas in this case it became compressive very quickly. However, the axial strain becomes less compressive in this case, compared to the simulation of the thinner blank.

In order to get a clearer view of the deformation mechanisms in the branch top, figure 4.26. shows the strain path of the top central node of the cross branch in principal planes. It can be seen from the figure that biaxial tension was the deformation mechanism for most of the simulation, after which the curve moved to the second quadrant, which indicates that deformation is governed by tension in the hoop direction and compression in the axial direction. From the slope of the curve in the second quadrant it appears that hoop strain is dominant until almost the very end of the simulation, when axial compression appears to become briefly dominant.

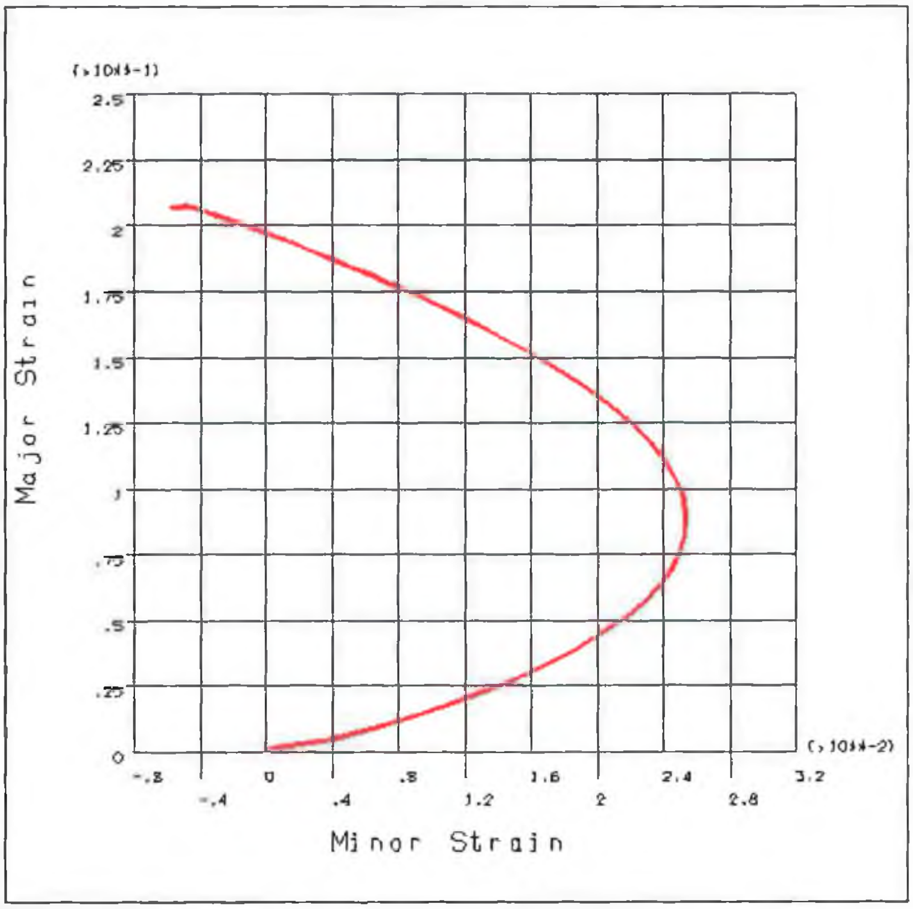

Figure 4.26. : Strain Path for the Top Central Node of the Cross-branch (blank thickness = 1.37mm)

This would seem to indicate that further loading in the same manner would result in buckling of the tube. This would agree with experimental experience [30], particularly in this case as the same loading pattern was used as was used for the thinner tubes in previous simulations. Obviously the thicker tube can withstand a greater pressure and requires increased pressure if the simulation was to be continued. Failure to provide increased pressure results in the dominance of axial loading and possible buckling defects in the final product.

4.4.5. The Effect of Changing the Die Radius

In order to examine the effect changing the die blend radius has on the process, two further simulations were run in which the die blend radius was changed from 4mm to 3mm and 5mm respectively. The same loading pattern and contact conditions were used as in the previous simulations. A coefficient of friction of 0.15 was used between the die and the tube. Figure 4.27 shows the distribution of stress in the deformed cross branch at full load for a die blend radius of 3mm.

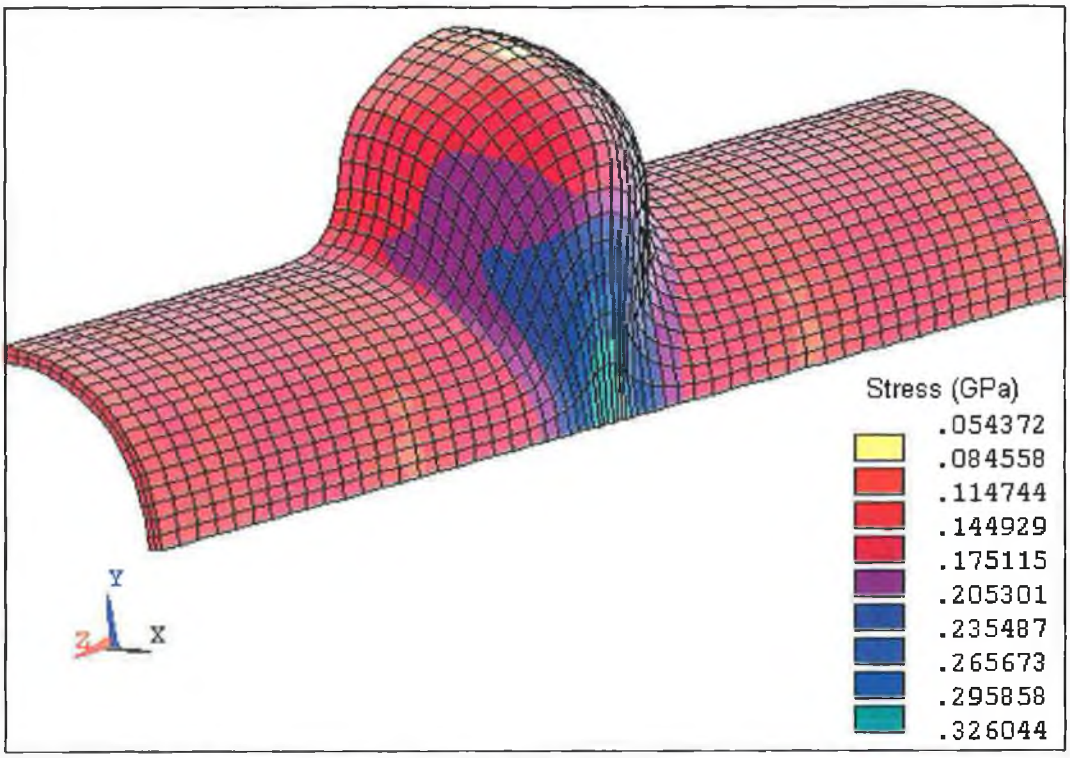

Figure 4.27. : Distribution of Stress in the deformed Cross-branch (die blend radius = 3mm)

The bulge height at this point was 11mm. This was 1mm lower than the height obtained in simulation two, which utilised the original die blend radius of 4mm. The reduction in die blend radius appears to have caused the shape of the branch top to change significantly. In simulation two the branch top took on a smooth and regular topospherical shape, in this case the branch top is not regular and is slightly pointed. It can be seen from the figure that the change in die radius has not affected the location of maximum stress. The maximum stress obtained was 326 MPa, which was slightly greater than the value obtained from simulation two. When comparing the two stress distributions it can be seen that there is higher stress in the region around the die bend for the smaller die blend radius. It may also be noticed that the smaller die radius produces slightly lower stress in the branch tops.

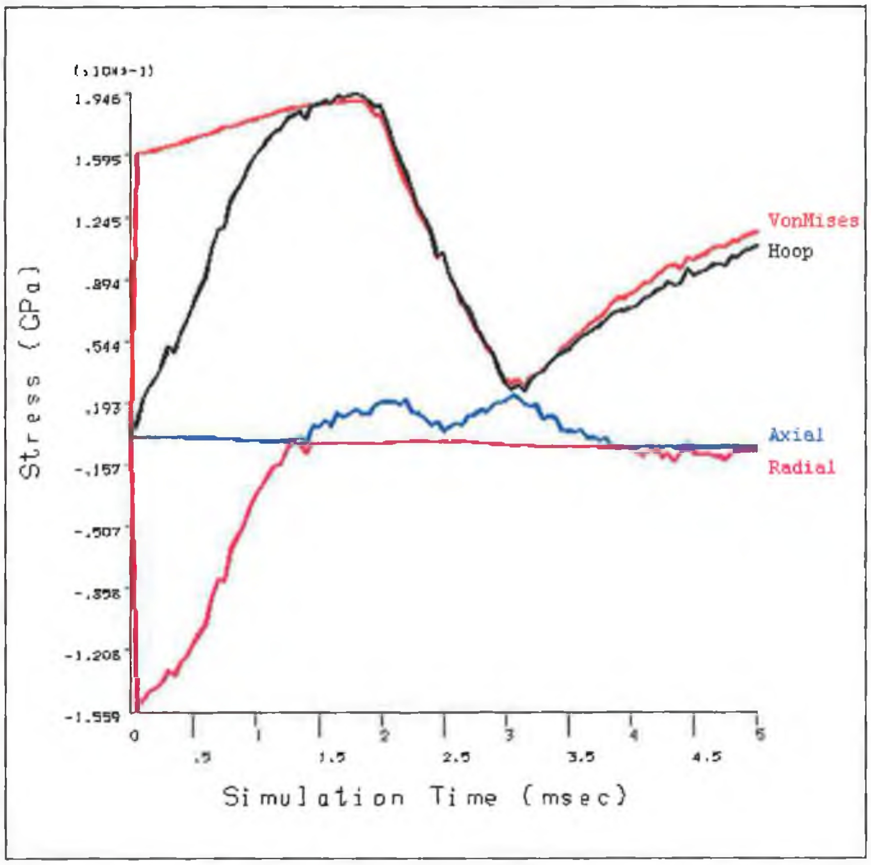

Figure 4.28. : Development of Stress at the Top Central Node of the Cross-branch (die blend radius = 3mm)

The development of principal and von-Mises stress at the top central node of the cross-branch during the simulation is shown in figure 4.28. The stress development was, again, slightly erratic indicating some stop-start deformation in the main tube ahead of the punch. As with the previous simulations, the hoop stress was always tensile while the axial stress was compressive until deformation of the bulge began and then became slightly tensile. It can be seen that the hoop stress is dominant through most of the process. The hoop stress begins to drop off at a simulation time of 1.7 milliseconds as the axial load begins to increase due to material being pushed around the die bend into the bulging zone. After a simulation time of 3 milliseconds the hoop stress begins to increase again as the bulge begins to deform further. The development of axial stress is highly erratic and it can be noticed that the hoop stress never develops to the magnitudes experienced in previous simulations. It is thought that this was due to difficulty in pushing material around the small die radius into the deformation zone of the forming bulge.

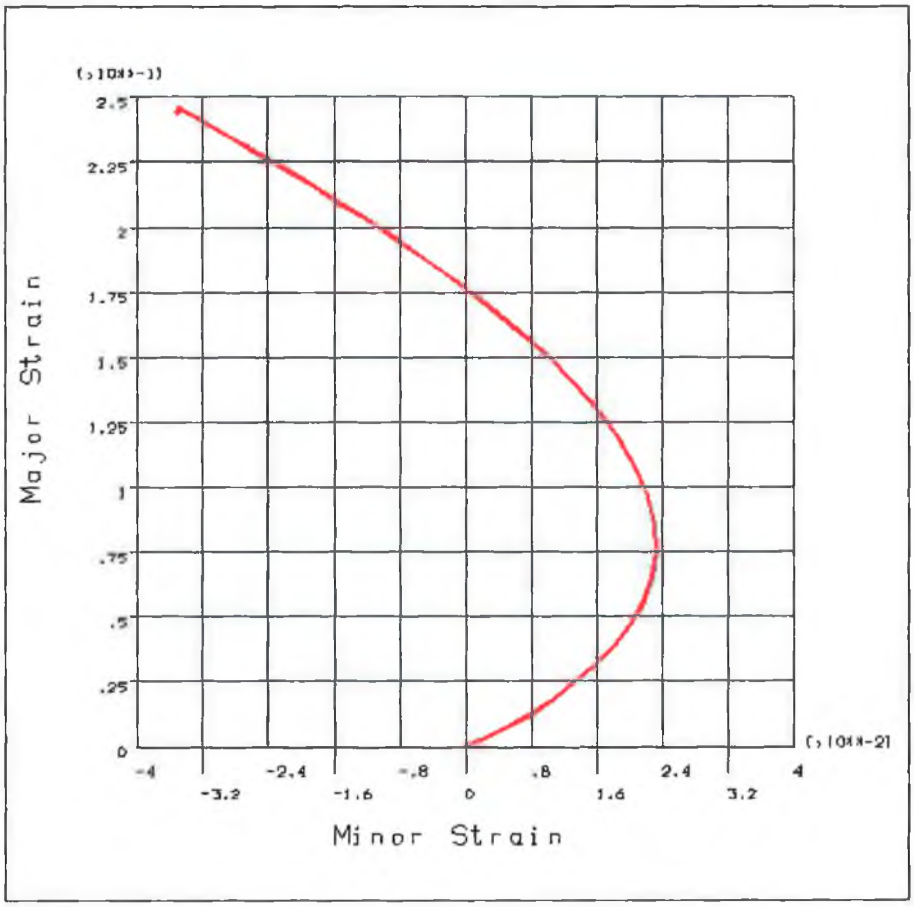

Figure 4.29. : Strain Path for the Top Central Node of the Cross-branch (die blend radius = 3 mm)

Figure 4.29. shows the strain path of the top central node of the cross branch during the simulation for a die radius of 3mm. Similar to what was experienced in previous simulations, a brief period of biaxial tension was followed by hoop tension and axial compression for the majority of the simulation. Hoop tension appears to be dominant and the slope of the curve suggests that the elements at the branch top are elongating faster in the hoop direction than they are compressing in the axial direction. This would suggest that further loading in the same manner would rupture the branch in the axial direction of the tube, as has been evident in experimental studies [30].

An investigation of thickening and thinning behaviour showed much less thinning behaviour than in previous simulations. The branch top had thinned to 95% or the original thickness while the area around the die bend had thickened to approximately 108% of the original thickness.

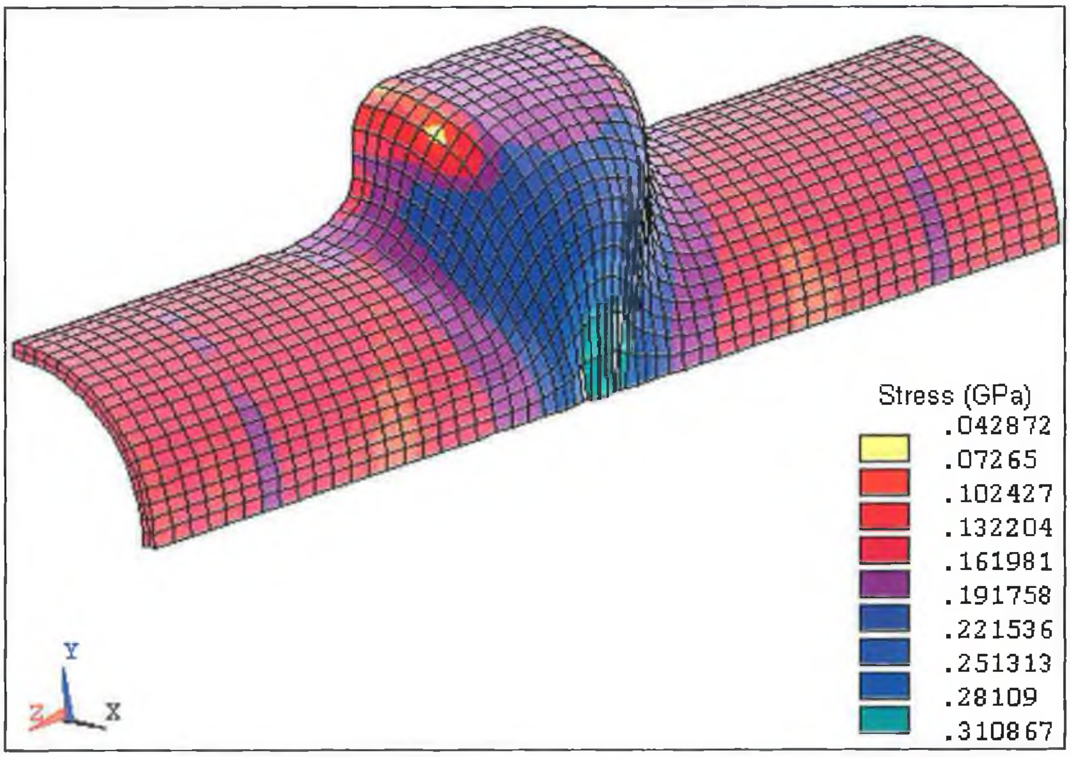

Figure 4.30. : Distribution of Stress in the deformed Cross-branch (die blend radius = 5 mm)

The distribution of stress in the formed component with a die blend radius of 5 mm is shown in figure 4.30 In this case the ultimate tensile stress of the material was exceeded in the hoop direction after a simulation time of 3.25 milliseconds, which corresponded to 75% of the load application, thus, all results after this time were ignored. The maximum bulge height at this point was 8.9mm. This was approximately 3mm lower than that obtained in simulation two, which utilised the original die blend radius of 4mm. It can be seen from the figure that the location of maximum stress is in the area expected, as found in previous simulations. The maximum stress obtained was 310 MPa, which was slightly lower than the value obtained from simulation two. It can be noticed from figure 4.30. that a significantly different branch shape was obtained in this simulation. In all the simulations which utilised the original die blend radius of 4mm, a topospherical branch shape was obtained. In this case, however, a flat branch top was obtained. When comparing the two stress distributions it can be seen that there is less stress in the region around the die bend for the larger die blend radius. It may also be noticed that the larger die radius produces slightly lower stress in the branch tops.

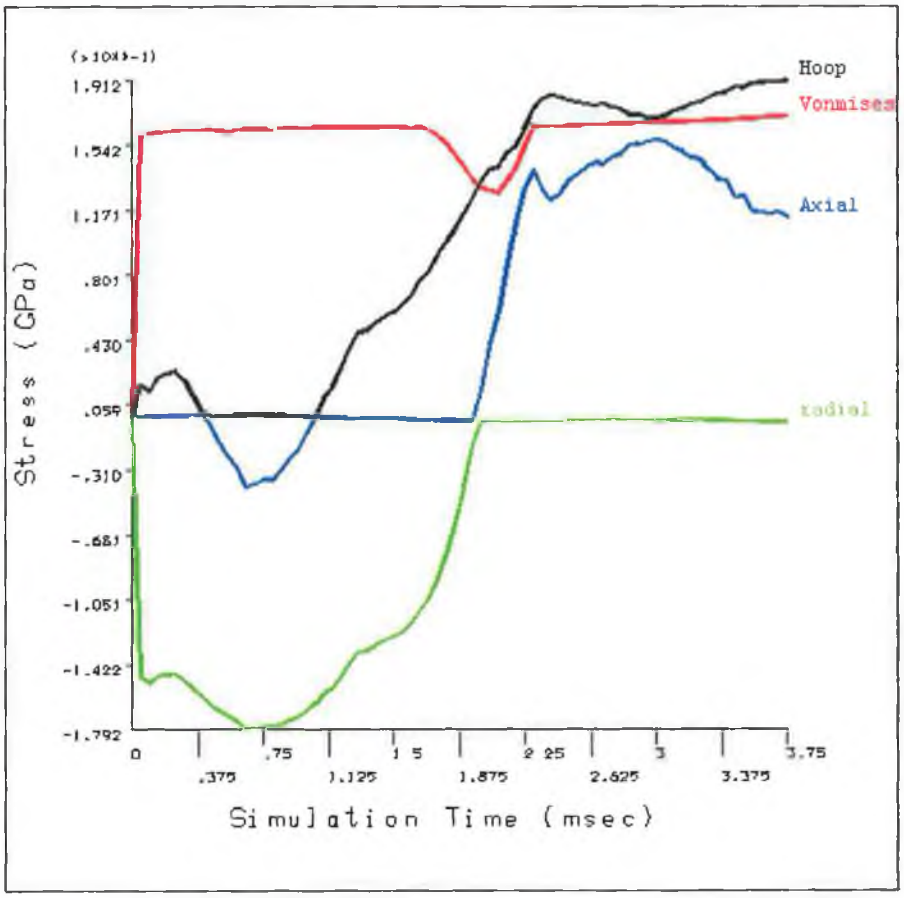

Figure 4.31. : Development of Stress at the Top Central Node of the Cross-branch (die blend radius = 5 mm)

The development of principal and stress at the top central node of the cross-branch during the simulation is shown in figure 4.31. The development of stress here is much less erratic when compared with figure 4.16, thus indicating that a larger die blend radius results in a less erratic stress development in the bulged component. The development of stress is markedly different from that experienced in previous simulations. The hoop stress drops off after a brief period of tension and then picks up again at a simulation time of 1 millisecond. The axial stress is compressive initially but becomes highly compressive for a brief period as the hoop stress drops off. The axial stress becomes tensile after a simulation time of 1.9 milliseconds. This seems to indicate that the larger die blend radius makes it more difficult for the bulge to grow initially as there is less contact with die wall which results in a dominance of axial load. Upon investigation it was found that at the end of the simulation the formed branch was not in contact with the die wall. This indicates that a larger pressure load could be used with the larger die radius in order to expand the bulge further. Subsequent simulations verified that this was indeed possible.

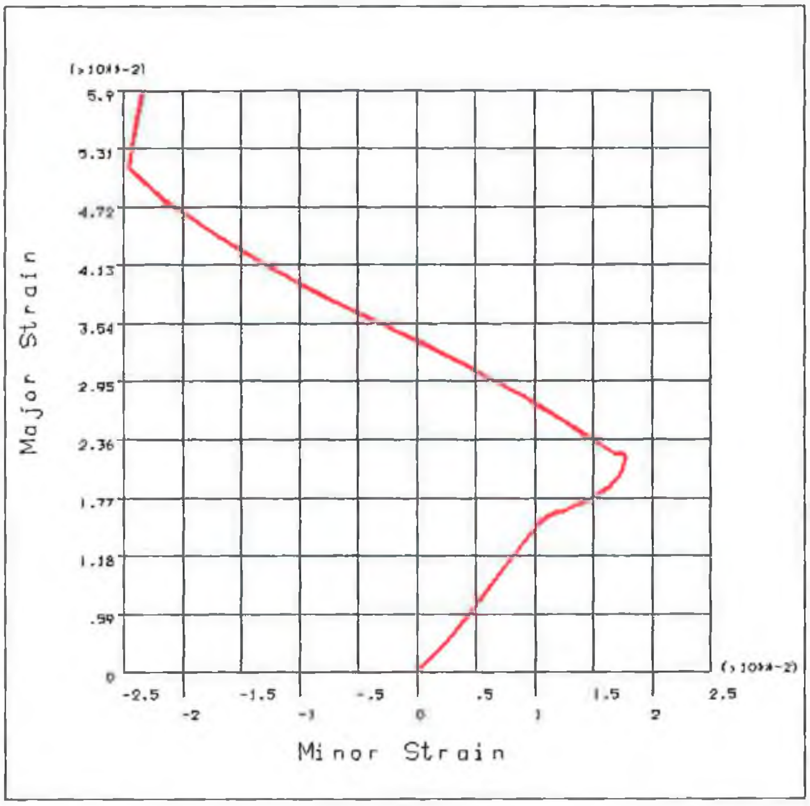

Figure 4.32. : Strain Path for the Top Central Node of the Cross-branch (die blend radius = 5 mm)

Figure 4.32. shows the strain path of the top central node of the cross branch during the simulation for a die radius of 5mm. In keeping with the complex development of stress, the strain path is slightly different to those obtained in previous simulations. Similar to what was experienced previously, a brief period of biaxial tension was followed by hoop tension and axial compression for the majority of the simulation. Following this, the curve turns back towards the biaxial tension quadrant, as hoop strain begins to pick up again and axial strain becomes less compressive. Again, hoop tension appears to be dominant and the slope of the curve suggests that the elements at the branch top are elongating faster in the hoop direction than they are compressing in the axial direction. This would suggest that further loading in the same manner would rupture the branch in the axial direction of the tube, as has been evident in experimental studies [30].

4.4.6. Validation of Finite Element Model

As mentioned previously the geometry, material model and loading patterns used here were chosen to be consistent with the geometry used by Hutchinson [30] in his experimental work. As part of his investigation Hutchinson measured the thickness at different heights of the cross branch. The thickness was measured along the plane of axial symmetry of the tube, corresponding exactly with the plane of symmetry of the finite element model used here. Those experimental findings, along with the results from simulations two and three from the finite element simulation are presented in figure 4.33. It can be seen from the figure that the branch height predicted by the second simulation is exactly the same as that measured experimentally. Simulation three, which utilised a higher friction between the die and the tube, predicted a lower branch height than that obtained experimentally.

The thickness at the branch top is predicted reasonably accurately by both simulations. There is, however, some differences observed at the branch root. The thickness at this area predicted by the simulations is lower than those measured experimentally. It is thought that the simulation results may not be truly representative at this point due to the fact that solid elements were used to model the tube. The deformation mechanism in this region is due to translation and bending. The solid elements used do not have any rotational degree of freedom and thereby have no stiffness in bending. Only translational movement is accounted for in the finite element solution and possible bending in this region has not been considered. This results in relatively less stress than would actually occur and consequently less thickening behaviour than measured experimentally.

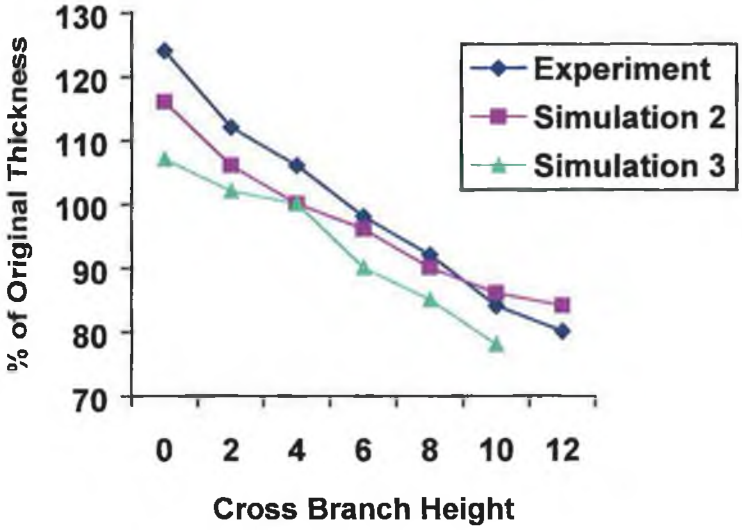

Figure 4.33. : Comparison of simulation results with experimental work of Hutchinson [30]

4.4.7. Summary of Results from Hydraulic Bulge Forming Simulations

Simulation Number	Blank Thickness	Loading Pattern	Coeff. of Friction	Max. Branch Height	Maximum Stress	Thinning Behaviour (% of original thickness)
1	1.03mm	1	0.15	4 mm	205 MPa	63% at branch top
2	1.03mm	2	0.15	12 mm	317 MPa	84% at branch top
3	1.03mm	2	0.3	10.5mm	270 MPa	78% at branch top
4	1.37mm	2	0.15	10mm	307 MPa	86% at branch top
5 (3mm die radius)	1.03mm	2	0.15	11mm	326 MPa	95% at branch top

6 (5mm die radius)	1.03mm	2	0.15	8.9mm	310 MPa	97% at branch top

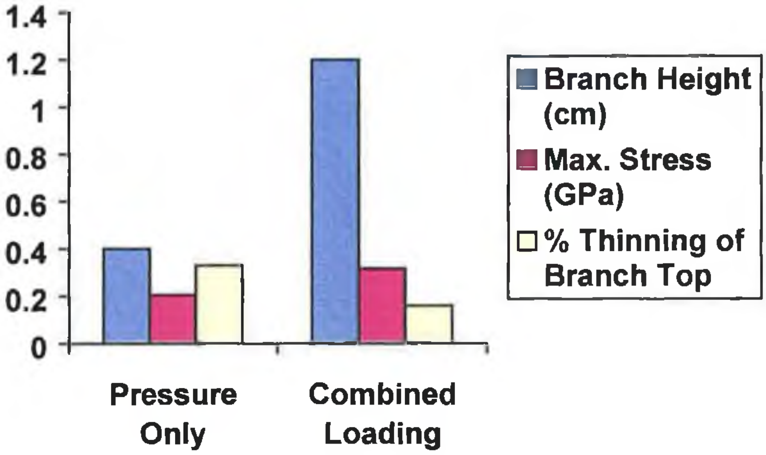

Figure 4.34. : The Effect of Using Different Loading Patterns.

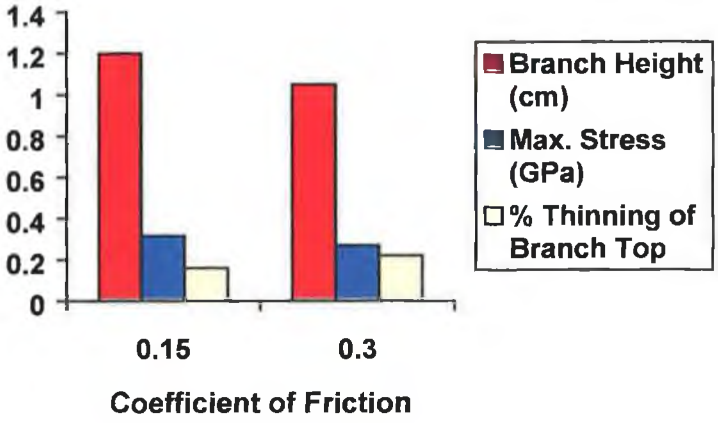

Figure 4.35. : The Effect of Changing Friction between the Die and the Tube

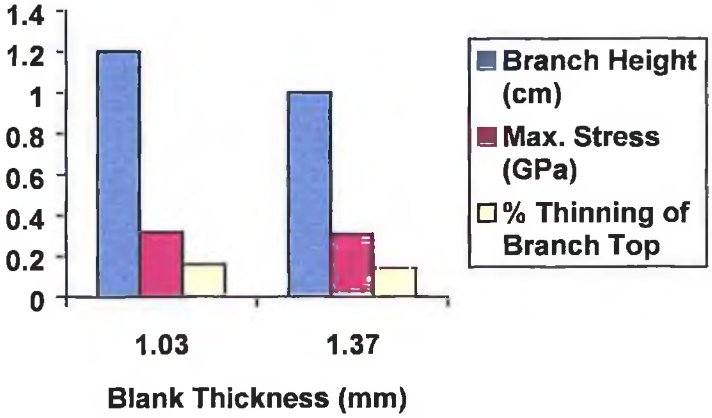

Figure 4.36. : The Effect of Changing the Blank Thickness

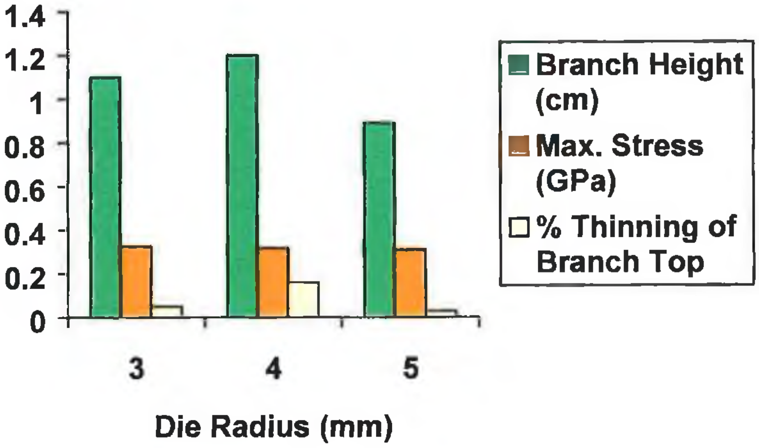

Figure 4.37. : The Effect of Changing Die Radius

Chapter 5 : Bulge Forming Using a Solid Bulging Medium

5.1 Introduction

This chapter details the modelling procedures used to simulate the bulge forming using a solid bulging medium. The manufacture of cross branches from straight tubes using lead as a bulging medium and axisymmetric bulge forming of tubes using urethane as a bulging medium is simulated. The results from the simulations are presented and analysed.

5.2. Cross Branch Forming Using a Solid Bulging Medium

5.2.1. Modelling

In order to simulate bulge forming of cross branches from straight tubes using a solid bulging medium the same die and tube model was used that was developed to simulate hydraulic bulge forming in the previous section. The bulging medium was modelled as a quarter cylinder placed inside the tube, with the outside diameter of the bulging medium being equal to that of the inside diameter of the tube. Initially the 1.03mm tube thickness was used. The length of the bulging medium was modelled slightly shorter than that of the tube. This accurately modelled the actual situation which facilitates insertion of the punch into the tube.

Figure 5.1. shows the discretized model used for the simulations. The die, the tube and the bulging were modelled using eight-node solid elements. A total of 2875 elements describe the model. The interfaces between the die and the tube, and between the bulging medium and the tube, were modelled using an automatic surface to surface contact algorithm. An elastic coulomb friction law was assumed and a coefficient of friction of 0.15 was assigned between the die and the tube. The coefficient of friction between the bulging medium and the tube was varied in order to determine its effect on the process. The material properties for the die and tube were the same as those used in the hydraulic analysis described in the previous section. The material parameters for the bulging medium were chosen to approximately represent lead. Soft metals such as

lead are widely used as a bulging medium in industrial applications and are capable of producing far more deformation than elastomers

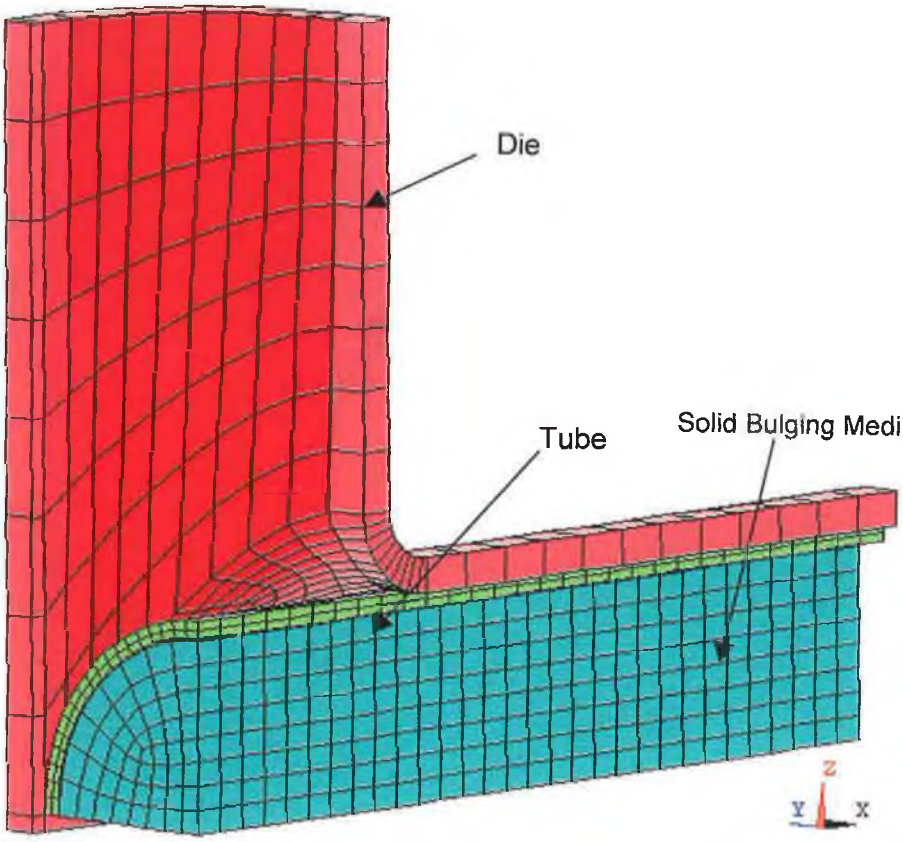

Figure 5.1. : Finite Element Model Used for Solid Bulging Medium Analysis

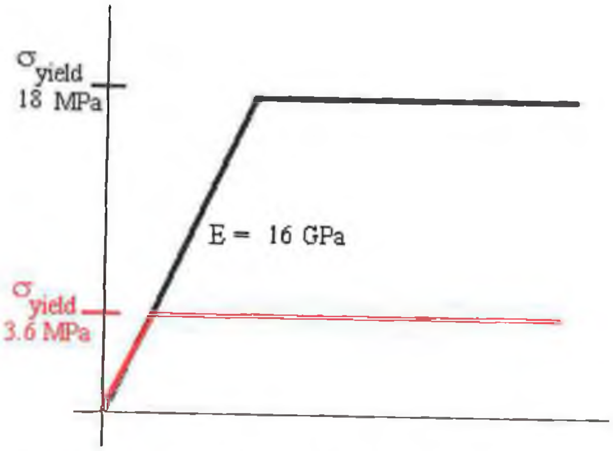

Figure 5.2. : Material Models Used for Bulging Media

An analysis was carried out specifically to examine the effect the strength of the bulging medium had on the process. In this case the yield strength of the bulging medium was reduced to 20% of the initial value. This value was chosen in order to gain a significant difference in the results to allow analysis of the effect of varying this parameter. The material models used for the bulging media are illustrated in figure 5.2.

5.2.2 Boundary Conditions, Loading and Solution

As one eighth of the problem was modelled by taking advantage of symmetry the tube and bulging medium nodes were constrained in the appropriate directions. The die was constrained as a rigid body. The internal pressure was generated by applying a prescribed displacement to the nodes at the end of the filler material. The axial deformation in the main tube was generated by applying a prescribed displacement to the nodes at the edge of the tube end. In the actual forming process the axial loads on the filler and tube are applied by a shouldered punch where the length of the shoulder controls the amount of deformation of the filler material prior to axial deformation of the tube. In this case the punch was not modelled, instead the nodes of the tube under the punch were constrained in the radial and circumferential directions, which is equivalent to the punch being in place.

The first simulation was run by applying a compressive axial displacement to the filler material only, in order to produce an internal pressure loading. The loading pattern for this simulation is shown in figure 5.3. The second simulation was run by applying simultaneous and equal compressive axial displacement to both the tube and the filler material. This resulted in both pressure and compressive axial loading being applied to the tube simultaneously. The loading pattern used for the second simulation is shown in figure 5.4.

From experience gained in the second simulation it was thought that greater branch height could be obtained by experimenting with load application. With this in mind a simulation was run in which the axial displacement of the filler medium began independently some time before axial load was applied to the tube. This effectively modelled a realistic situation where a shouldered punch is used to apply the axial displacement to both the tube and filler material. The length of the shouldered portion of the punch effectively determines the amount of displacement that is applied to the filler material before the tube begins to move. The loading pattern used here is described in figure 5.5.

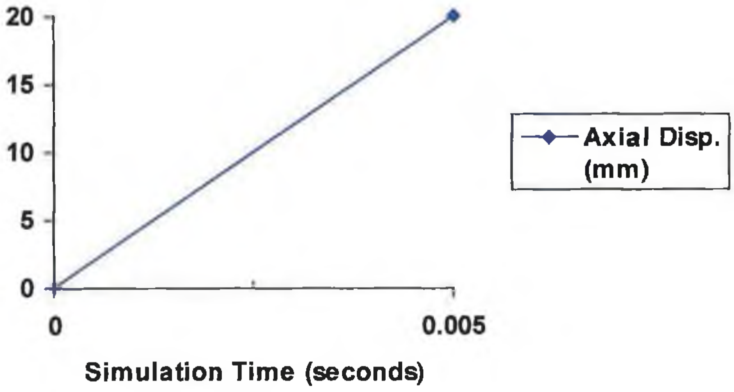

Figure 5.3. : Loading Pattern Three : Displacement to Filler Material Only

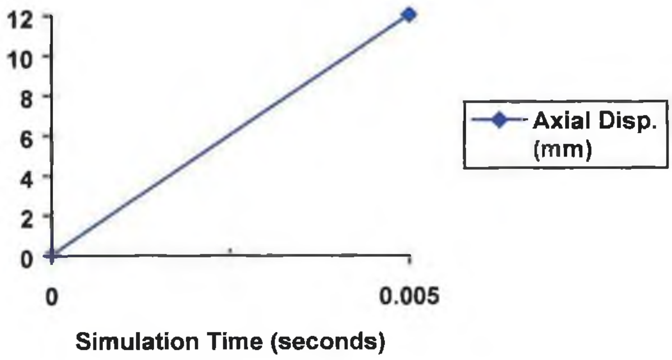

Figure 5.4. : Loading Pattern Four : Simultaneous Displacement to Filler and Tube

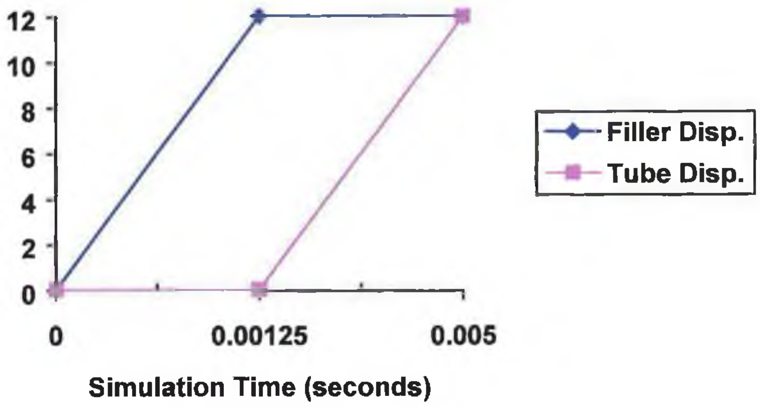

Figure 5.5 : Loading Pattern Five : Non- Simultaneous Displacement to Filler and Tube

In order to gain a better understanding of the process a number of simulations were carried out in which process parameters were varied. In all simulations the axial load was applied simultaneously to the filler material and tube. The first simulation was carried out using a zero coefficient of friction between the bulging medium and the tube. In subsequent simulations the coefficient of friction was varied between zero and 0.5.

5.2.3. Simulation Results and Analysis

5.2.3.1. Pressure Load Only

As mentioned in above, the first simulation was run by applying a compressive axial displacement to the filler material only, in order to produce an internal pressure loading. Figure 5.6 shows the distribution of Von-Mises stress in the bulged tube produced by the first loading pattern at the point just before rupture. The simulation time at this point was 1.55 milliseconds and this corresponded to an axial displacement of approximately 4mm of for the filler material. The branch height obtained by this load was 5.25mm. It can be noticed by comparing this result with the height obtained by hydraulic pressure loading only in section 4.4.1. that using a solid bulging medium allows a greater branch height for this type of loading.

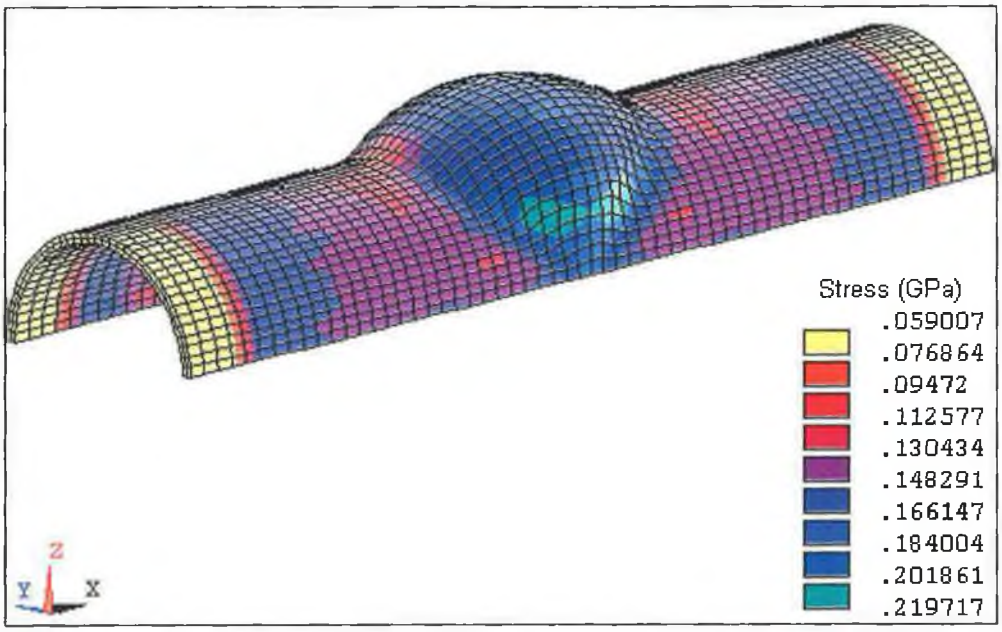

Figure 5.6. : Distribution of von-Mises Stress in the Formed Component by loading pattern 3

The bulged region has stressed considerably with a relatively uniform distribution. The highest stressed region is at the branch sides as indicated on the figure. The maximum stress developed in this region is 219 MPa. In contrast to what was experienced during simulation of hydraulic bulging, it can be seen that the main tube has stressed considerably also. This is due to friction between the filler material and the tube causing material to be pulled into the bulging zone and accounts for the greater branch height obtained by using the solid bulging medium.

Figure 5.7 shows the development of Von-Mises stress and principal stresses at the central node of the cross-branch top surface. After a simulation time of 1.55 all stress values began to increase sharply as the bulge ruptured, thus all results after this time were ignored. The stress development was steady and relatively stable and closely resembled the bilinear material model for the tube. The hoop stress is clearly dominant throughout the process, but axial stress plays a more prominent role here than in the case for hydraulic bulging, due to friction between the filler material and the tube.

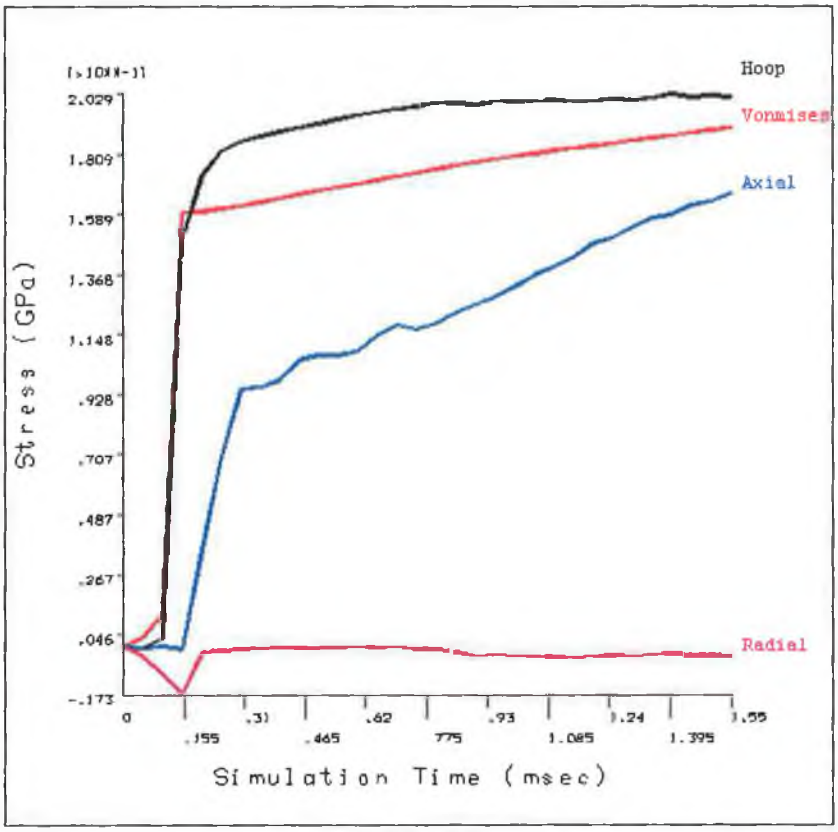

Figure 5.7. : Development of Stress at the Top Central Node of the Cross Branch by loading pattern 3

Figure 5.8. shows the strain path of the top central node of the cross branch during the simulation. It can be seen that after an initial period of almost pure hoop tension the bulge is formed by biaxial tension. It can be seen from the slope of the curve that the elements are expanding more quickly in the hoop direction than they are in the axial direction. This indicates that failure will occur, with further loading, due to a rupture of the branch in the axial direction of the tube, as has been evident in experimental studies [30].

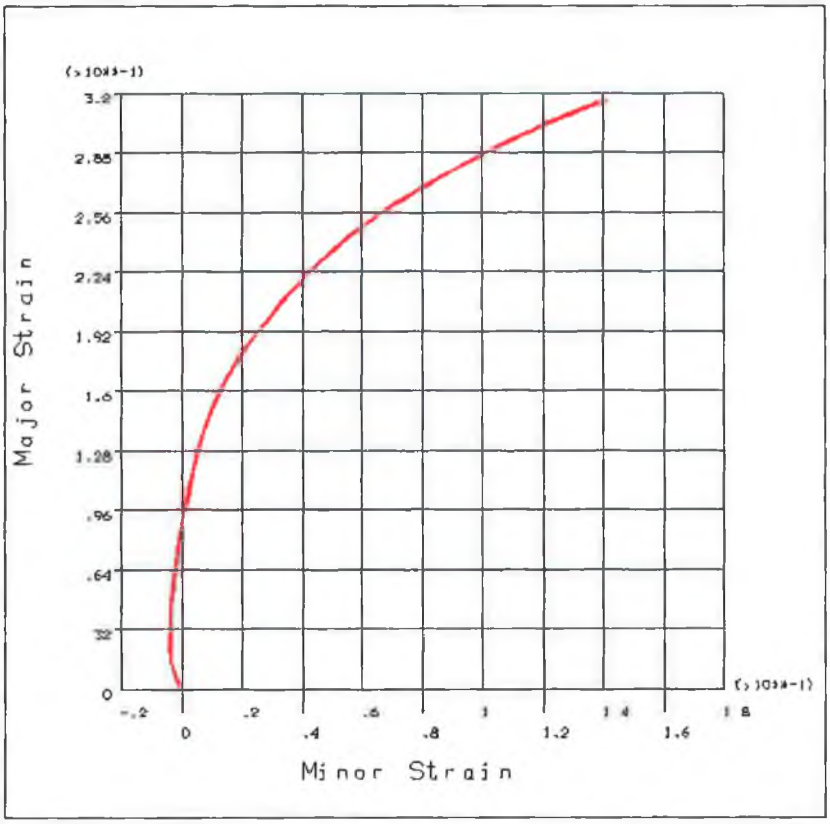

Figure 5.8. : Strain Path for the Top Central Node of the Cross-branch by loading pattern 3

An investigation of thinning behaviour showed that the branch top had thinned to 70% of the original thickness. It should be noted that the simulation of hydraulic bulge forming with pressure load only showed that the branch top thinned to 66% of the original thickness. This indicates that for an internal pressure load only the solid medium bulging method is capable of producing a greater branch height with less thinning of the branch top for the same tube and die geometry. Clearly this is a result of friction between the tube and the filler material causing some material to be pulled from the main tube into the deformation zone, thus allowing for an increase in branch height and a reduction in thinning behaviour. The low branch height, however, would mean that this cross branch would not be a very useful component and the next section will investigate combining an axial compressive load to the tube with the internal pressure load in order to increase branch height and produce a more useful component.

5.2.3.2. Simultaneous Tube and Bulging Medium Axial Displacement

The second simulation was run by applying simultaneous and equal compressive axial displacement to both the tube and the filler material. This resulted in both pressure and compressive axial loading being applied to the tube simultaneously. Figure 5.9. shows the distribution of Von-Mises stress in the deformed tube due to this loading condition. The maximum branch height at this point was 10mm. It should be noted that this was 2mm lower than the branch height obtained in simulation two of hydraulic bulging, which utilised the same friction conditions between the tube and die and the same axial displacement applied to the tube.

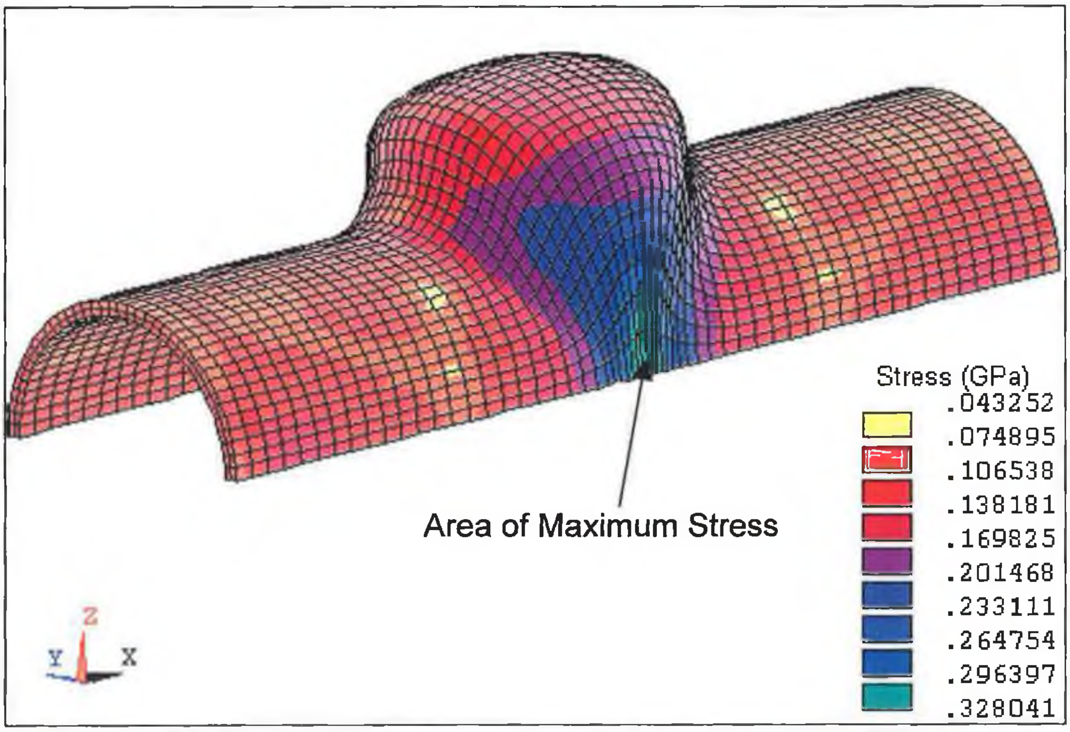

Figure 5.9. : Distribution of von-Mises stress in the deformed tube by loading pattern 4 (solid medium bulging).

It can be seen that the region of maximum stress is in the area expected given the experience gained of simulation hydraulic bulging in the previous section. In this case, however, the area in which the maximum stress occurs is much more concentrated and the stress gradient is more regular than in the simulations of hydraulic bulging in the previous section.

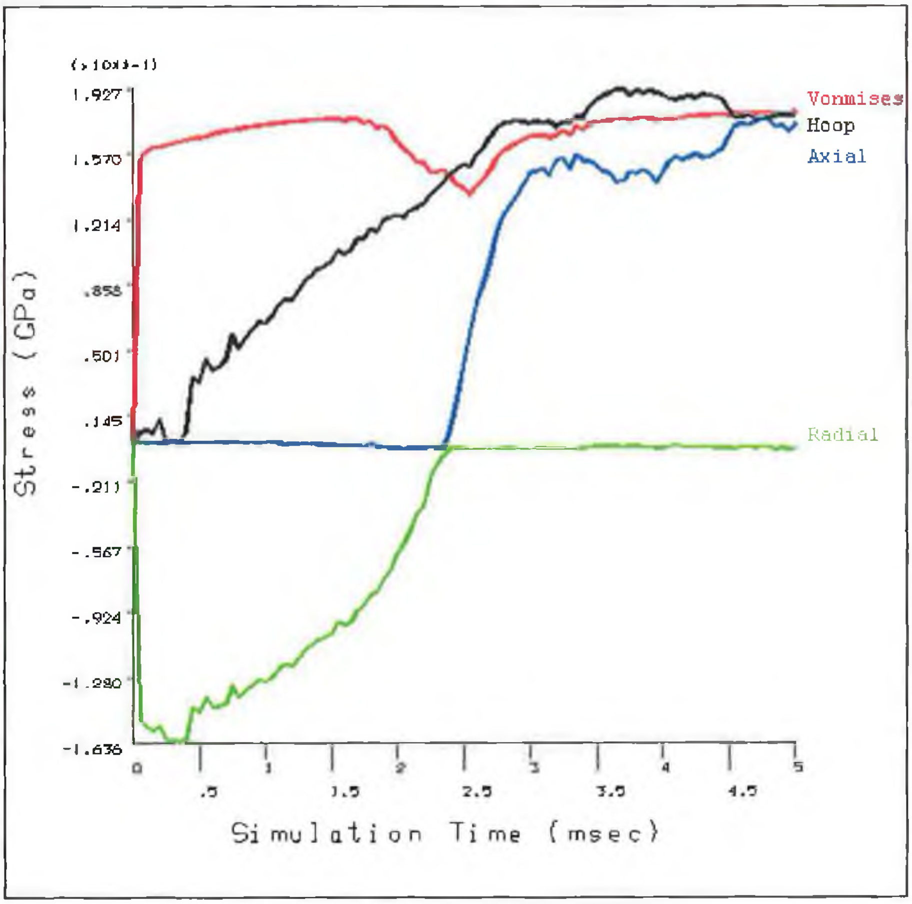

Figure 5.10. : Development of Stress in the Top Central Node of the Cross Branch by loading pattern 4.

Figure 5.10 shows the development of Von-Mises and principal stresses in the top central node of the cross branch during the simulation. It can be seen, by comparing the above figure with figure 4.17, that the stress development for the solid medium bulging method is much less erratic than for the hydraulic method. The stress development is similar to what was experienced previously in the simulations of hydraulic bulge forming, the hoop stress was always tensile, while the axial stress was compressive until the bulge began to develop and became tensile as soon as deformation of the bulge began.

The radial stress in the branch top was highly compressive until the bulge began to develop, at which point it became much less significant, however in this case the radial stress becomes much more compressive than in the previous simulations. There is some slight erratic behavior in the development of axial stress early in the simulation. This is thought to be due to friction between the solid medium and the tube, which is pulling the tube material towards the deformation zone in a start-stop fashion.

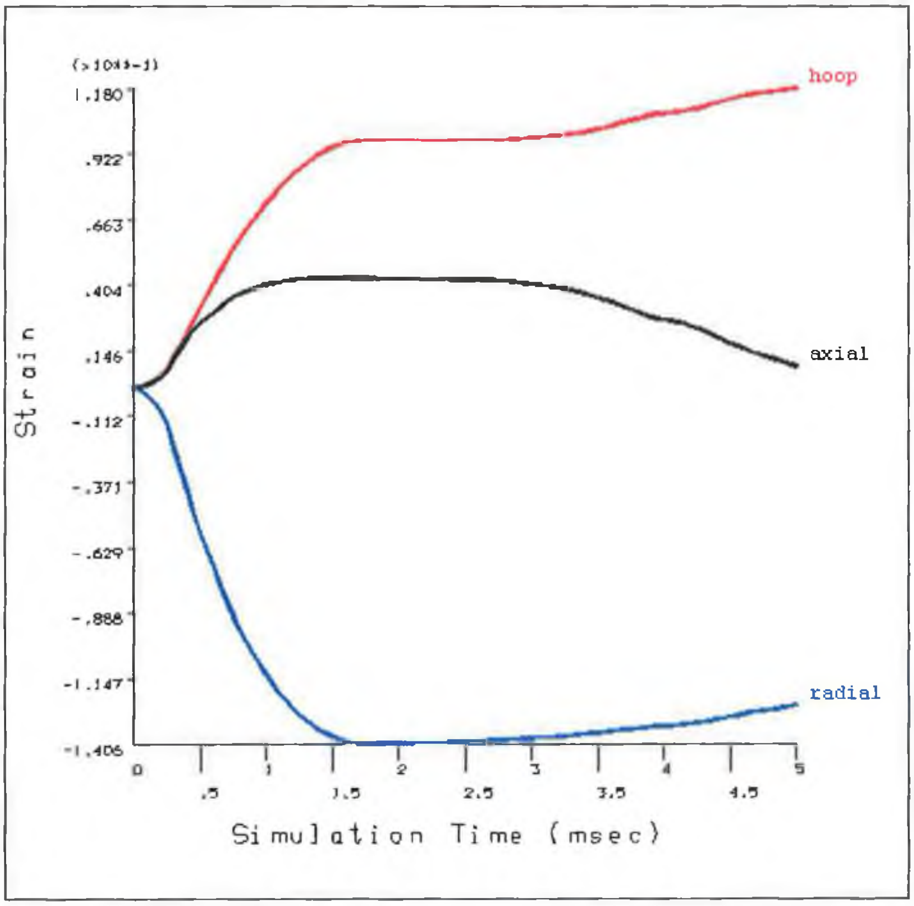

Figure 5.11. : Development of Strain in the Top Central Node of the Cross Branch by loading pattern 4.

The development of principal strains in the top central node of the cross branch is shown in figure 5.11. Hoop strain was positive for the entire simulation while axial strain was positive for the majority of the simulation, before beginning to turn negative in the final few milliseconds. Radial strain, as expected, was negative throughout the entire simulation. In order to get a clearer view of the deformation mechanisms in the branch top, figure 5.12. shows the strain path of the top central node of the cross branch in principal planes. It can be seen from the figure that the majority of the branch is formed due to biaxial tension. Towards the end of the simulation axial strain turns towards the compressive direction. It appears that the application of increasing compressive axial load is moving the state of deformation to the second quadrant. Hoop tension appears to be dominant and the slope of the curve suggests that the elements at the branch top are elongating faster in the hoop direction than they are expanding in the axial direction. This would suggest that further loading in the same manner would rupture the branch in the axial direction of the tube, as has been reported in experimental studies [30].

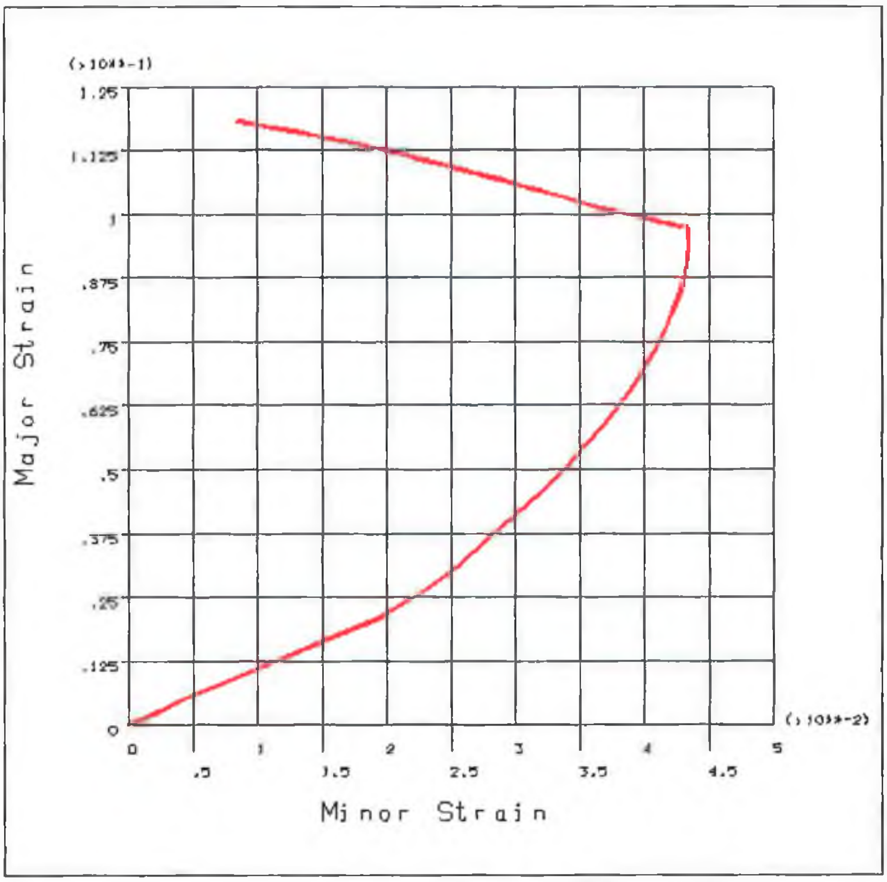

Figure 5.12. : Strain path of the top central node of the cross branch in principal planes by loading pattern 4.

An investigation of thickening and thinning behaviour showed that the branch top had not thinned significantly while the region around the die bend had thickened to approximately 105% of the original thickness. When compared to the previous simulations of hydraulic bulge forming it is clear that the solid medium bulging method results in a component which exhibits little thinning of the branch top and a small amount of thinning around the bulge root, both of which are desirable features for the final component.

5.2.3.3. Non-Simultaneous Tube and Bulging Medium Axial Displacement

From experience gained in the previous simulation it was felt that greater branch height could be obtained by experimenting with load application. With this in mind a simulation was run in which the axial displacement of the filler medium began independently some time before axial load was applied to the tube. This effectively modelled a realistic situation where a shouldered punch is used to apply the axial displacement to both the tube and filler material. The length of the shouldered portion of the punch effectively determines the amount of displacement that is applied to the filler material before the tube begins to move.

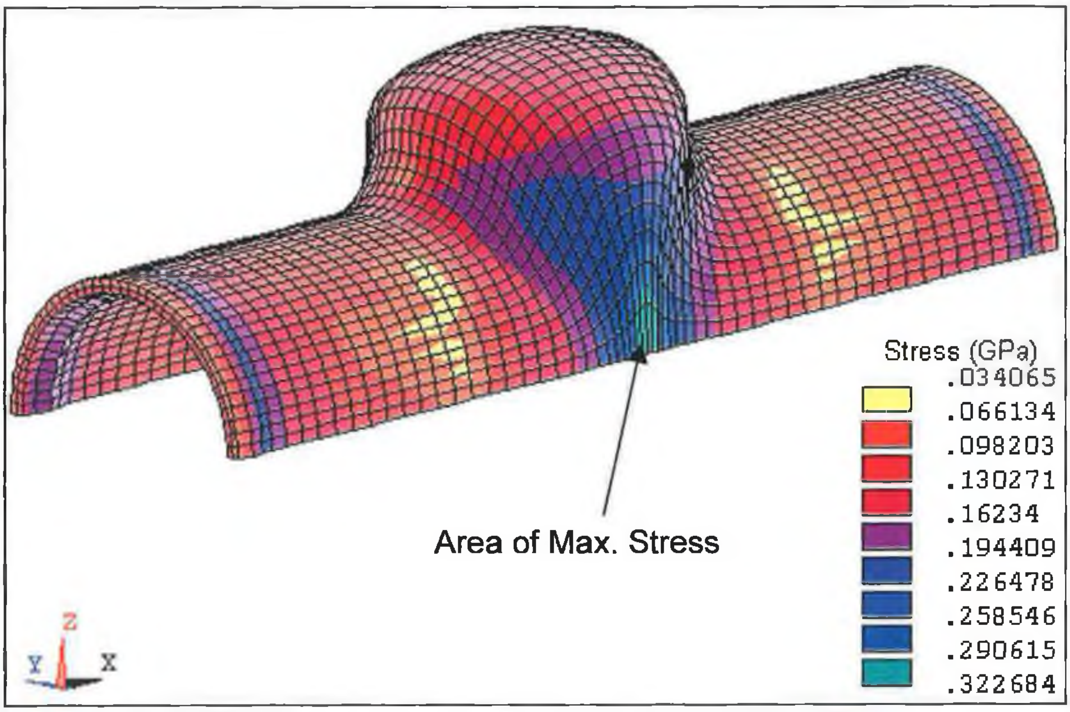

Figure 5.13. : Distribution of von-Mises Stress in the formed component by loading pattern 5.

The loading pattern used here is described in detail in the previous chapter. Figure 5.13 shows the distribution of Von-Mises stress in the formed component by loading pattern five. The branch height obtained by this loading pattern was 12mm, which is 2mm higher than the previous simulation and equal to that obtained by the simulation of hydraulic bulge forming. The highest stress has occurred in the expected region and is even more concentrated than in the previous simulation. The stress values are not significantly different from the previous simulation apart from the area in front of the punch which has thickened and consequently stressed higher than expected. Obviously the fact that this loading pattern produces a higher branch height with little effect on the stress in the tube makes this loading pattern much more attractive for solid medium bulging of cross branches.

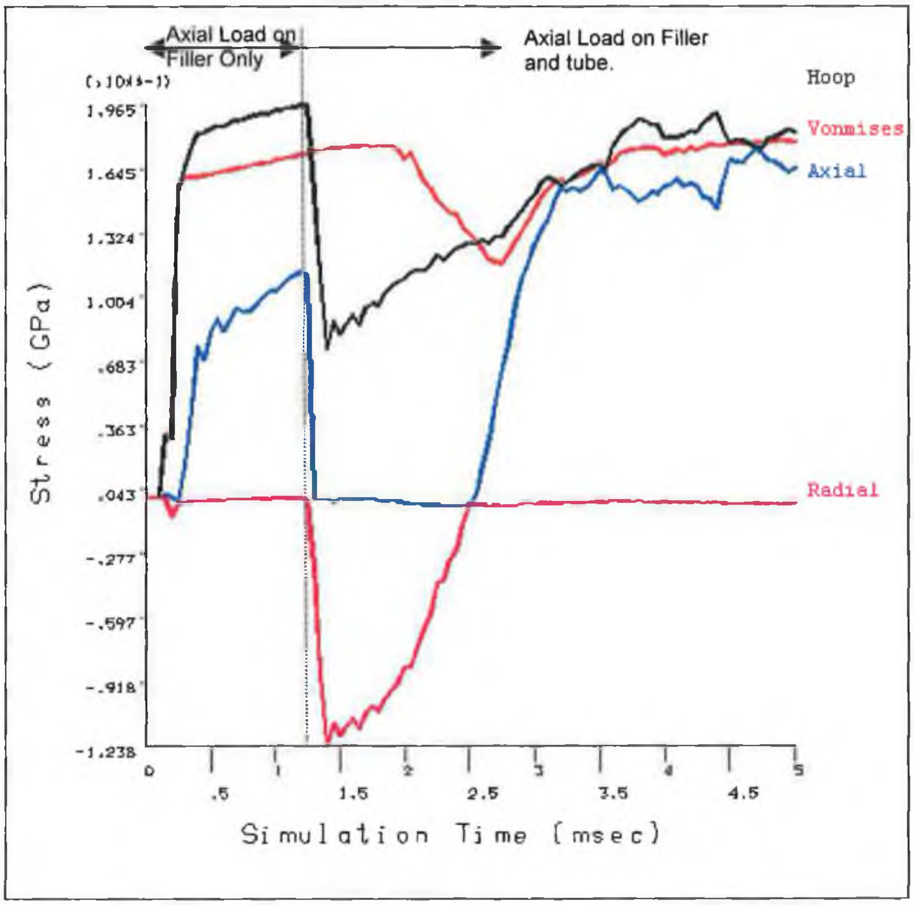

Figure 5.14. : Development of Stress at the Top Central Node of the Cross Branch by loading pattern 5.

Figure 5.14 shows the development of Von-Mises and principal stresses at the top central node of the cross branch during the simulation. The stress development is rather different to what was experienced in previous simulations. It can be seen from the figure that hoop and axial stress become tensile and radial stress is minimal for the first 1.5 milliseconds of the simulation. This corresponds to the period where axial load was applied to the filler material only, thus inducing an internal pressure load on the tube. After this time an axial load was also applied to the tube, thus pushing more material into the deformation zone and causing hoop and axial stress in the branch top to drop off.

Hoop stress begins to pick up again very rapidly while axial stress doesn't begin to pick up until a simulation time of 2.5 milliseconds. It can be seen from the figure that the development of stress is much more erratic than in the previous simulation, indicating more stop-start deformation due to friction between the die and the tube and between the tube and the filler material.

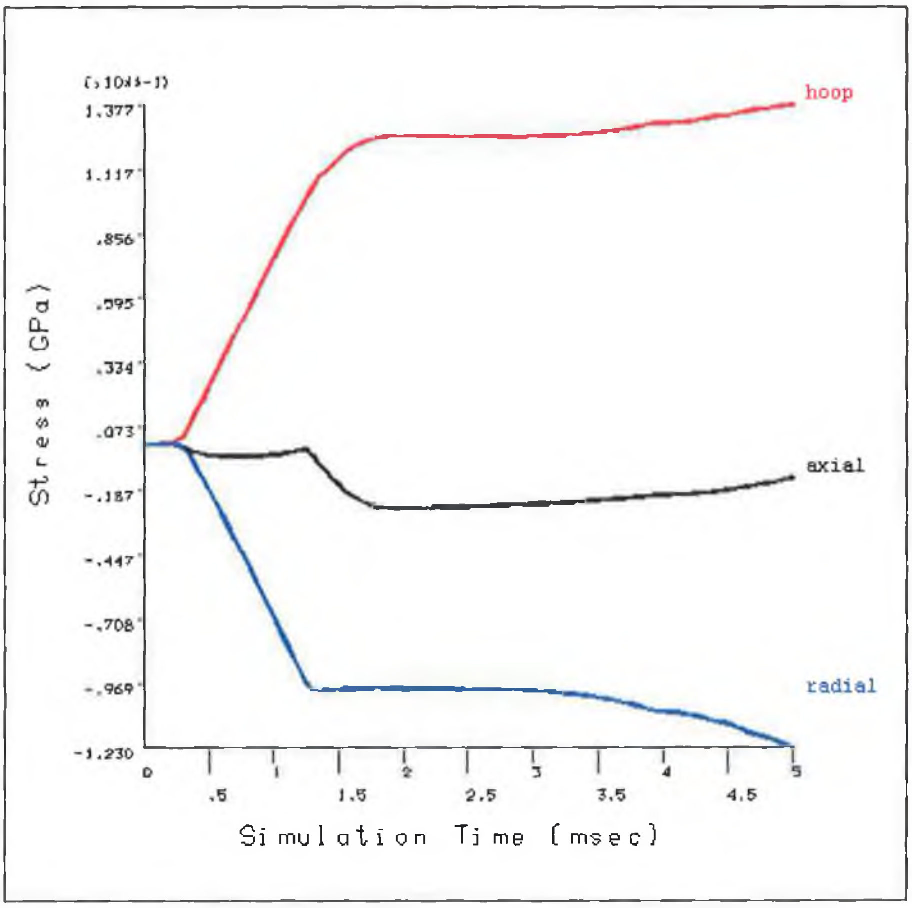

Figure 5.15. : Development of Principal Strains in the Top Central Node of the Cross Branch by loading pattern 5.

The development of principal strains in the top central node of the cross branch is shown in figure 5.15. Hoop strain was positive for the entire simulation while axial strain was positive until a simulation time of 1.5 milliseconds before turning negative for the remainder of the simulation. Radial strain, as expected, was negative throughout the entire simulation. It can be noticed that towards the end of the simulation axial strain begins to turn positive again, while radial strain begins to become even more compressive. In order to get a clearer view of the deformation mechanisms in the branch top, figure 5.16. shows the strain path of the top central node of the cross branch in principal planes. It can be seen from the figure that the majority of the branch is formed due to biaxial tension. Towards the end of the simulation axial strain turns towards the compressive direction.

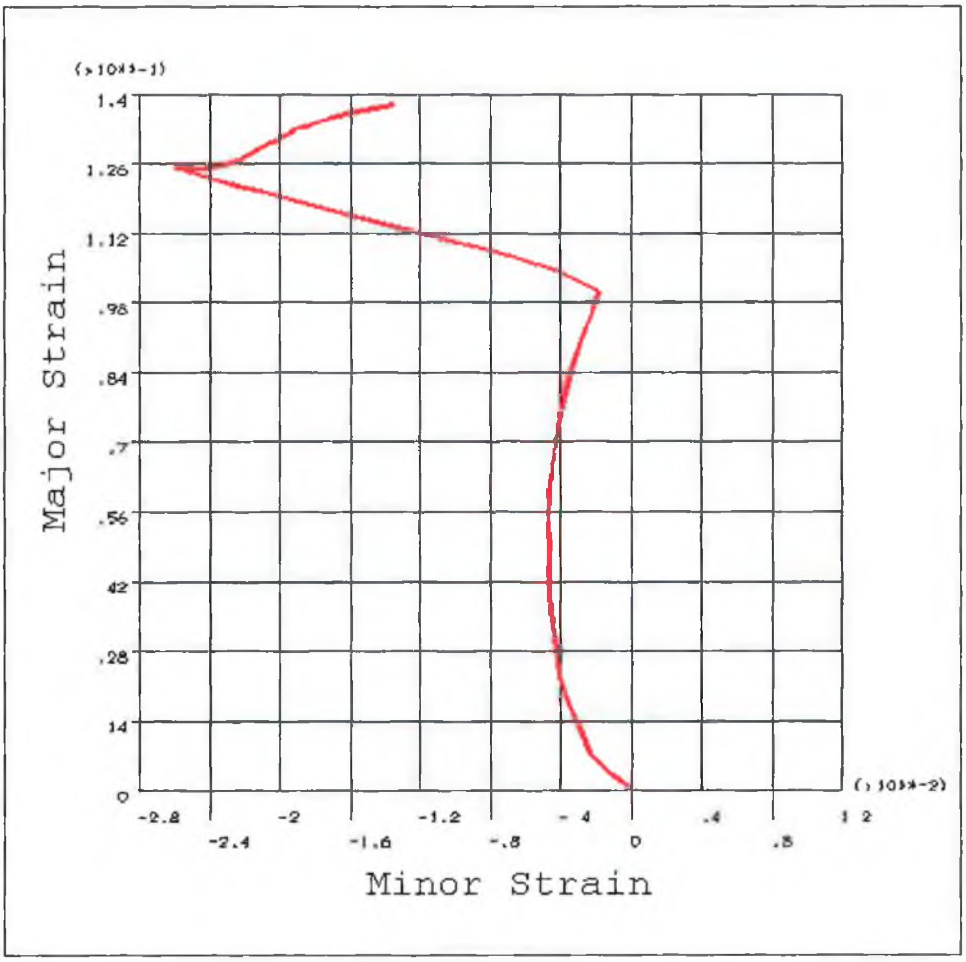

Figure 5.16. : Strain path of the top central node of the cross branch in principal planes by loading pattern 5.

It appears that the application of increasing compressive axial load is moving the state of deformation to the second quadrant. Hoop tension appears to be dominant and the slope of the curve suggests that the elements at the branch top are elongating faster in the hoop direction than they are expanding in the axial direction. This would suggest that further loading in the same manner would rupture the branch in the axial direction of the tube, as has been reported in experimental studies [30].

An investigation of thickening and thinning behaviour in the deformed tube showed that the branch top had thinned to 88% of the original thickness and the area around the die bend had thickened to 110% of the original thickness. As mentioned earlier the main tube ahead of the punch had thickened considerably upon investigation it was found that this region had thickened to approximately 160% of the original thickness. This region was, however, very localised and could be controlled by a change in punch design and the appropriate boundary conditions used in the finite element simulation.

5.2.3.4. The Effect of Friction Between the Tube and Filler Material

The effect of varying the friction between the bulging medium and the tube was investigated by carrying out four simulations which used friction factors of 0, 0.15, 0.3 and 0.5 respectively. Each simulation used loading pattern four. The maximum branch height produced in each case was around 11mm and decreased with increasing friction, with a difference of only ±1mm between each simulation. The maximum stress at point A in each case varied between 300 MPa and 328 MPa with the level decreasing with increasing friction. The maximum stress in the branch top varied between 185 MPa and 200 MPa and again decreased with increasing friction. An examination of the thinning behaviour of the branch top showed that for a friction factor of 0 the branch top had thinned to 90%, of the original thickness. The simulations for increased friction exhibited almost no thinning of the branch top. The thickening behaviour of the main tube, ahead of the punch, varied from 120% to 102% of the original thickness. Lower friction values produced less thinning of the branch top and more thickening of the main tube.

The development of stress was also influenced by the level of friction between the bulging medium and the tube. Figure 5.17 shows the development of stress in the top central node of the cross branch during simulation 2 (friction = 0.15). The stress development is quite erratic indicating some stick-slip behaviour between the bulging medium and the tube. When compared with figure 5.18, which shows the development of stress by simulation 3 (friction = 0.3) it can be seen that increasing friction results in a much smoother development of stress in the bulge.

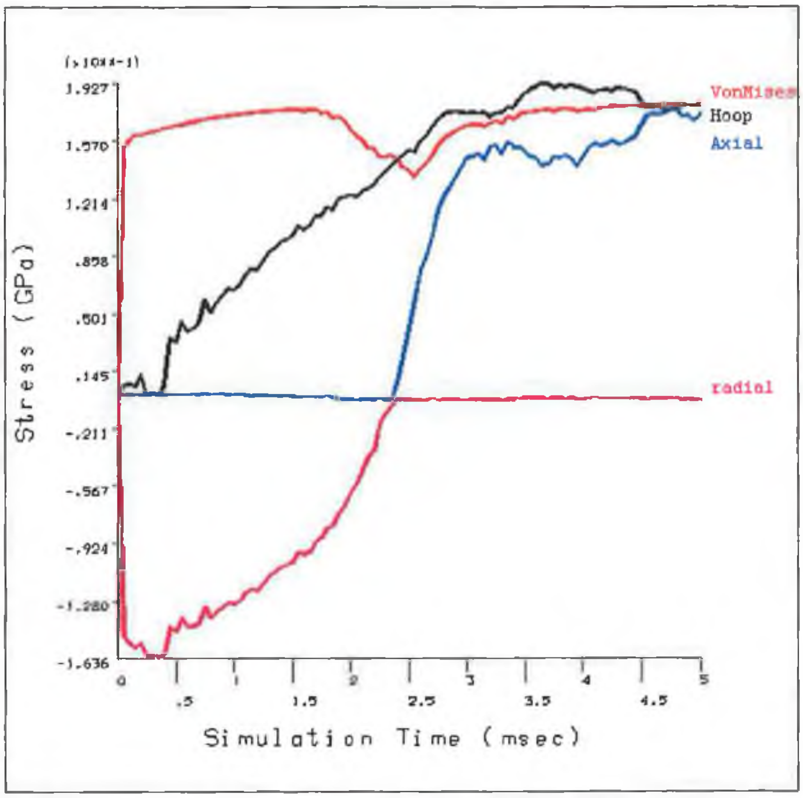

Figure 5.17. : Development of Stress at the Top Central Node of the Cross Branch During Simulation 2 (Friction = 0.15)

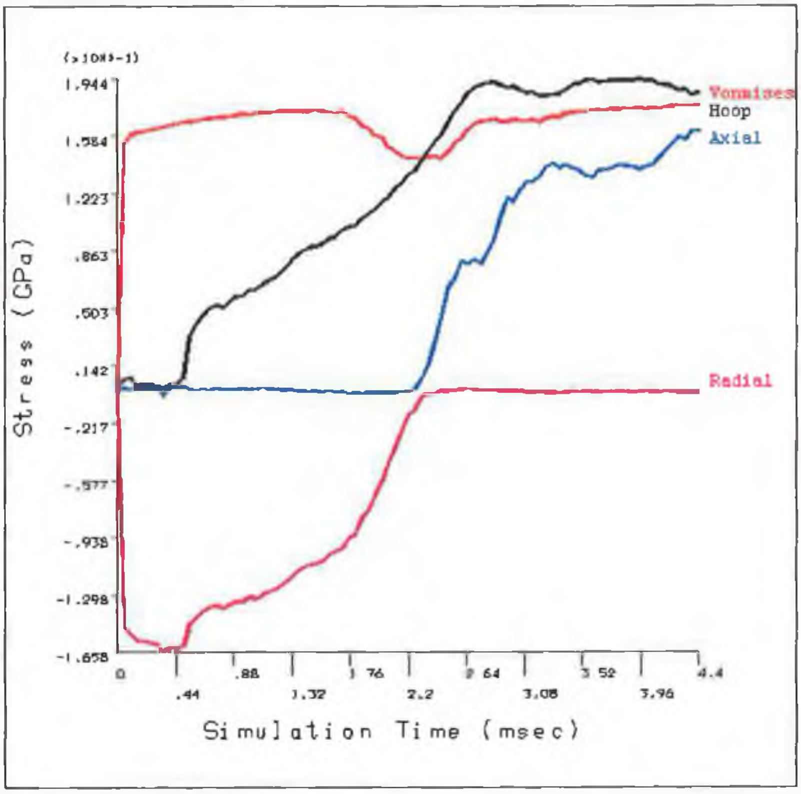

Figure 5.18. : Development of Stress at the Top Central Node of the Cross Branch During Simulation 3 (Friction = 0.3)

5.2.3.5. Comparison with Hydraulic Bulging

In the previous chapter hydraulic bulge forming of cross branch components was simulated using the same blank geometry and material properties as used in this analysis. In order to compare the solid medium bulging process with the hydraulic bulging process, results from the previous chapter were compared with results here.

In order to compare stress conditions a further simulation was run to bulge a component to the same height as that experienced in the simulation of the hydraulic process (11.5mm). Figures 5.19 and 5.20 show the distribution of von-Mises stress in the formed components using hydraulic and solid bulging processes respectively. When the stress distributions were compared it was noticed that the solid medium bulging process produced less stress in the formed component.

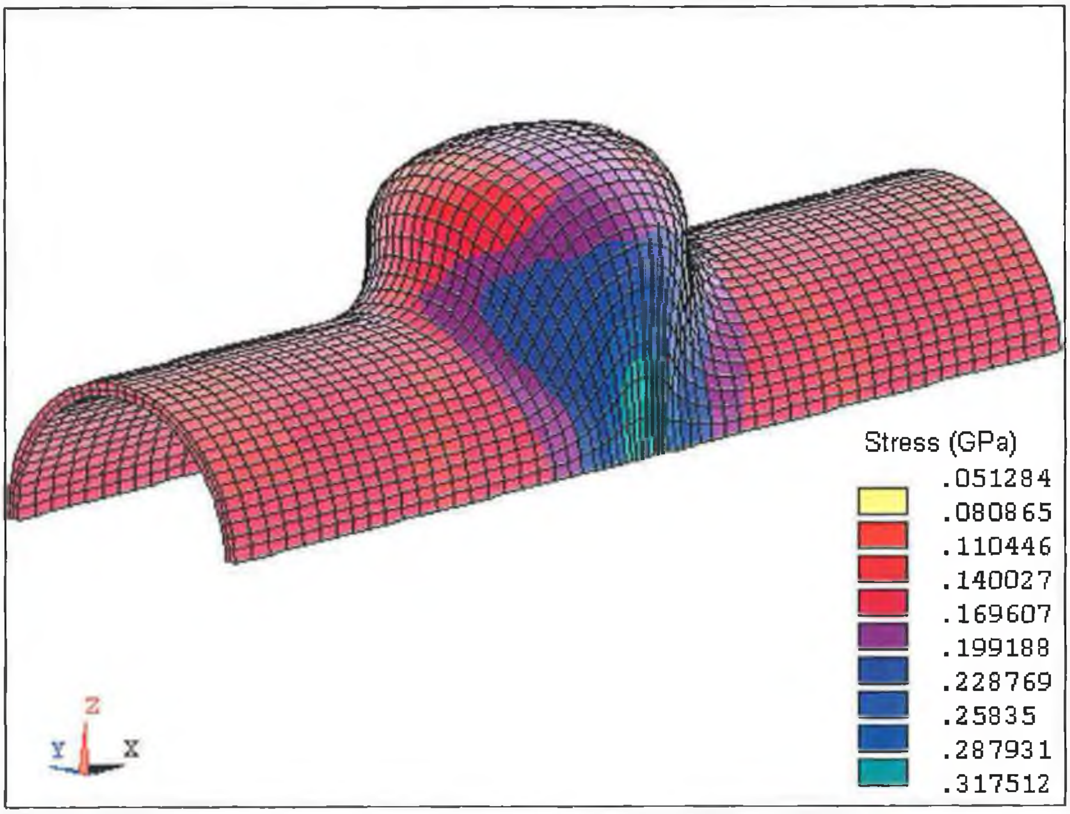

Figure 5.19 : Distribution of von-Mises Stress in Hydraulically Bulged Cross Branch (height = 11.5mm)

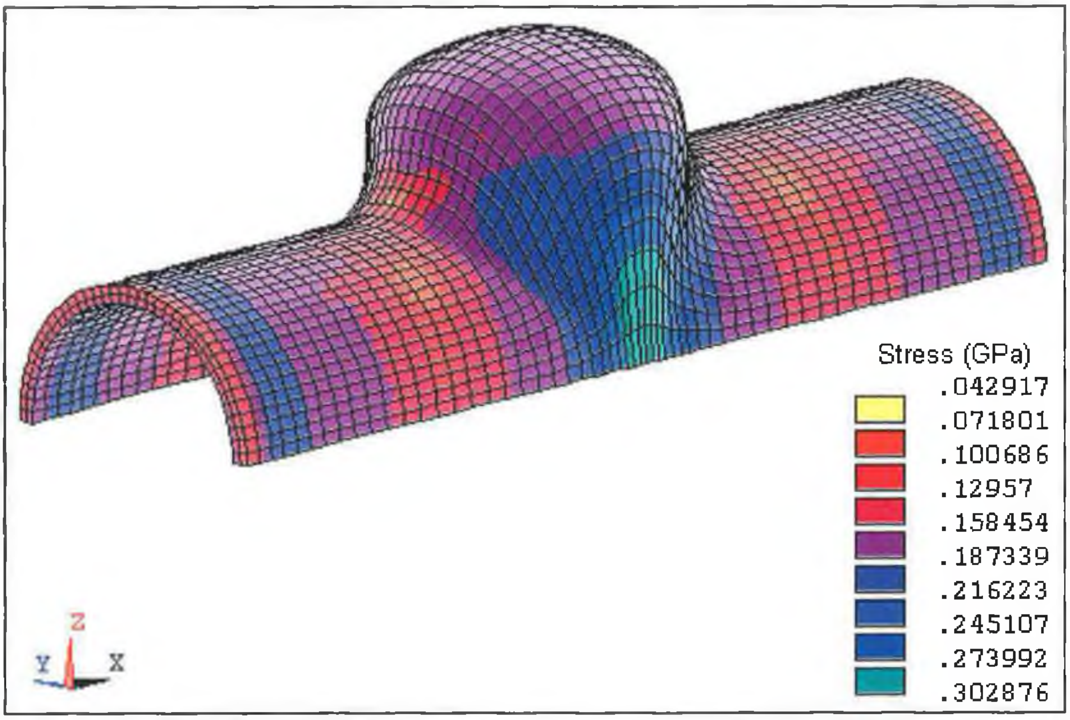

Figure 5.20 : Distribution of von-Mises Stress in Solid Medium Bulged Cross Branch (height = 11.5mm)

The distribution of stress in the formed component was quite similar in the area around the point of maximum stress for both simulations. The main tube has stressed a great deal more in the simulation for solid medium bulging. This is due to friction between the bulging medium and the tube causing greater axial stress to be imparted on the tube than was present in the hydraulic simulation. An important advantage of the solid medium process noticed during the comparison was that it can produce the same branch height as the hydraulic process but with far less reduction in length of the unbulged tube. This is again due to friction between the bulging medium and the tube causing material to be pulled into the bulging zone. This phenomenon has been well documented in experimental investigations [11,12,31].

Upon investigation it was found that the tube bulged using the hydraulic bulge forming method had a branch top thickness of 85% of the original thickness. In comparison, the tube bulged using the solid bulging medium had only thinned down to 98% of the original thickness. This again is thought to be due to friction between the filler material and the die causing more material to be pulled into the deformation zone.

5.2.3.6. The Effect of Varying the Strength of the Filler Material

As mentioned earlier, a further simulation was carried out where the strength of the filler material was reduced in order to determine its effect on the process. Figure 5.21. shows the distribution of Von-Mises stress in the deformed tube at the end of the simulation. The bulge height at this point was 12.5mm. It should be noted that this is 2.5mm higher than that obtained in the simulation detailed in section 5.4.2. which utilised the same finite element model and loading pattern but used the increased strength filler material. It appears that the use of a reduced strength filler material results in a significant increase in bulge height.

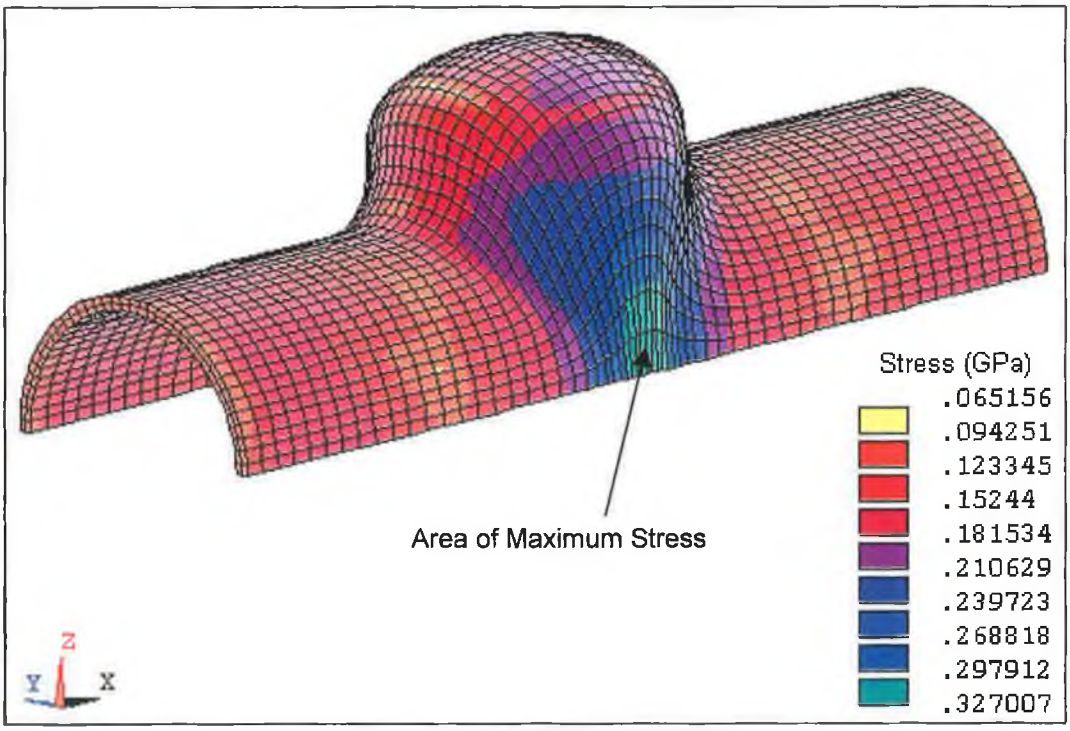

Figure 5.21. : Distribution of von-Mises Stress in the Deformed Tube with Reduced Strength Bulging Medium

The maximum stress obtained was 327 MPa, which is not significantly different from that obtained in the simulation in section 5.2.3.2. The distribution of stress in both simulations is quite similar. In this case the area of maximum stress is less concentrated and the branch top has stressed more than in the simulation in section 5.2.3.2.

The development of von-Mises and principal stresses in the top central node of the cross branch during the simulation is presented in figure 5.22. When compared with the previous simulation, which utilised the same model and loading conditions, but had increased bulging media strength, it can be seen that the development of stress in this case is generally much less erratic. The increase in hoop stress, which occurs in both simulations around a simulation time of 2.5. milliseconds, is much more pronounced in this case than in the previous simulation. It can be seen by comparing the figures that the level of hoop stress experienced at the branch top throughout the simulation is much greater for the softer bulging medium.

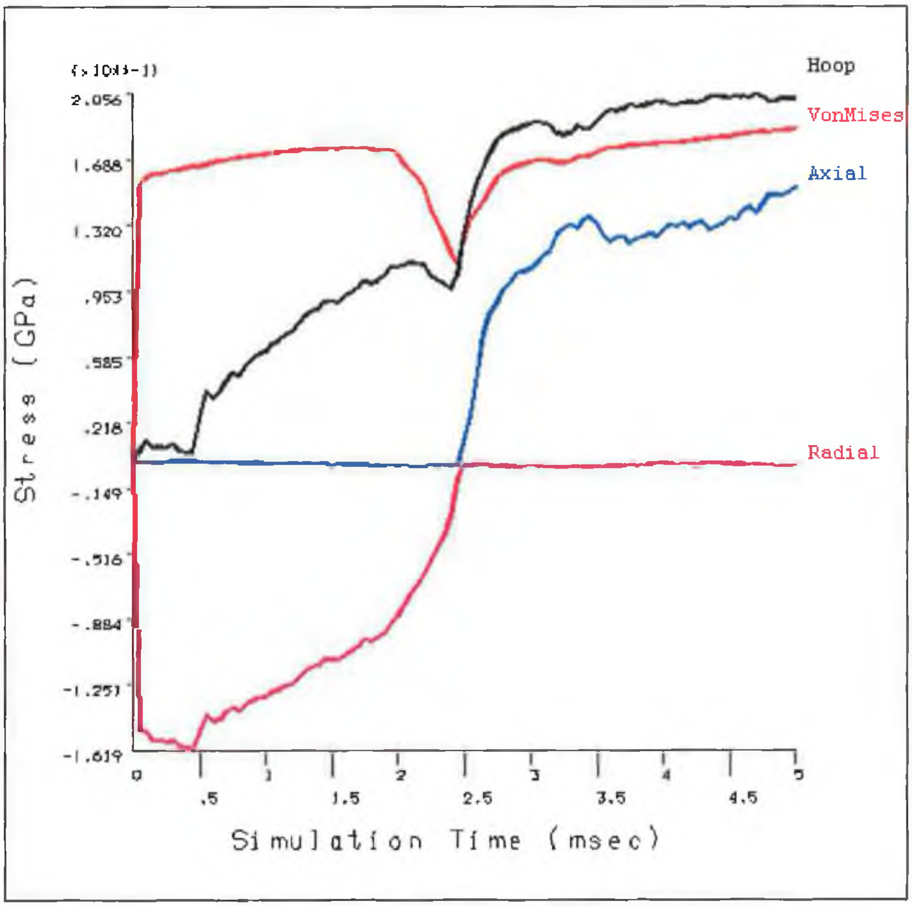

Figure 5.22. : Development of Stress in the Top Central Node of the Cross Branch with Reduced Filler Material Strength.

The development of principal strains in the top central node of the cross branch is shown in figure 5.23. Hoop strain was positive for the entire simulation while axial strain was positive for the majority of the simulation, before beginning to turn negative in the final few milliseconds. Radial strain, as expected, was negative throughout the entire simulation. When compared with figure 5.11. which shows the development of principal strains in the node for the same loading conditions but with increased bulging media strength, it can be seen that the use of a softer bulging media appears to result in increased hoop strain, particularly towards the latter half of the simulation. In the previous simulation hoop strain developed rapidly at first and then levelled off for the remainder of the simulation, as illustrated in figure 5.11. In this case hoop strain increases rapidly, levels off for a short period and then begins to increase again. In a similar manner, the axial strain in this case turns negative much quicker than in the previous simulation.

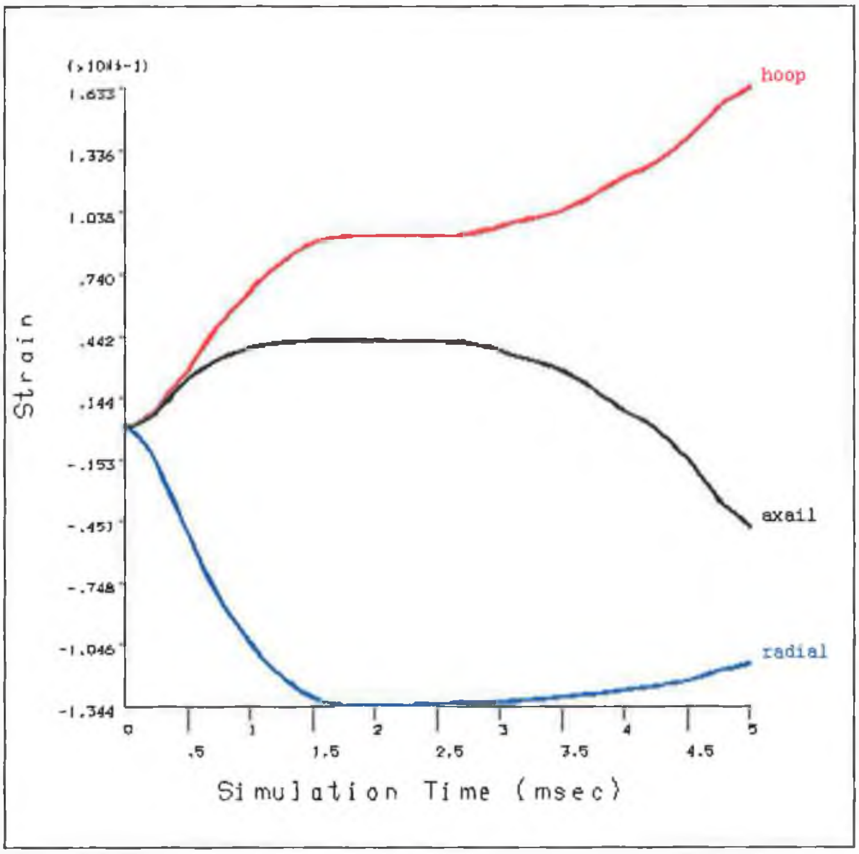

Figure 5.23. : Development of Principal Strains in the Top Central Node of the Cross Branch with Reduced Filler Material Strength.

In order to get a clearer view of the deformation mechanisms in the branch top, figure 5.24. shows the strain path of the top central node of the cross branch in principal planes. It can be seen from the figure that the majority of the branch is formed due to biaxial tension. Towards the end of the simulation axial strain turns towards the compressive direction. This is very similar to what was experienced in the previous simulation, where the stronger bulging medium was used. In this case, however, the period of biaxial tension is much shorter than in the previous simulation and the state of deformation quickly begins to move to the second quadrant. As experienced previously, hoop tension appears to be dominant and the slope of the curve suggests that the elements at the branch top are elongating faster in the hoop direction than they are expanding in the axial direction. This would suggest that further loading in the same manner would rupture the branch in the axial direction of the tube, as has been reported in experimental studies [30].

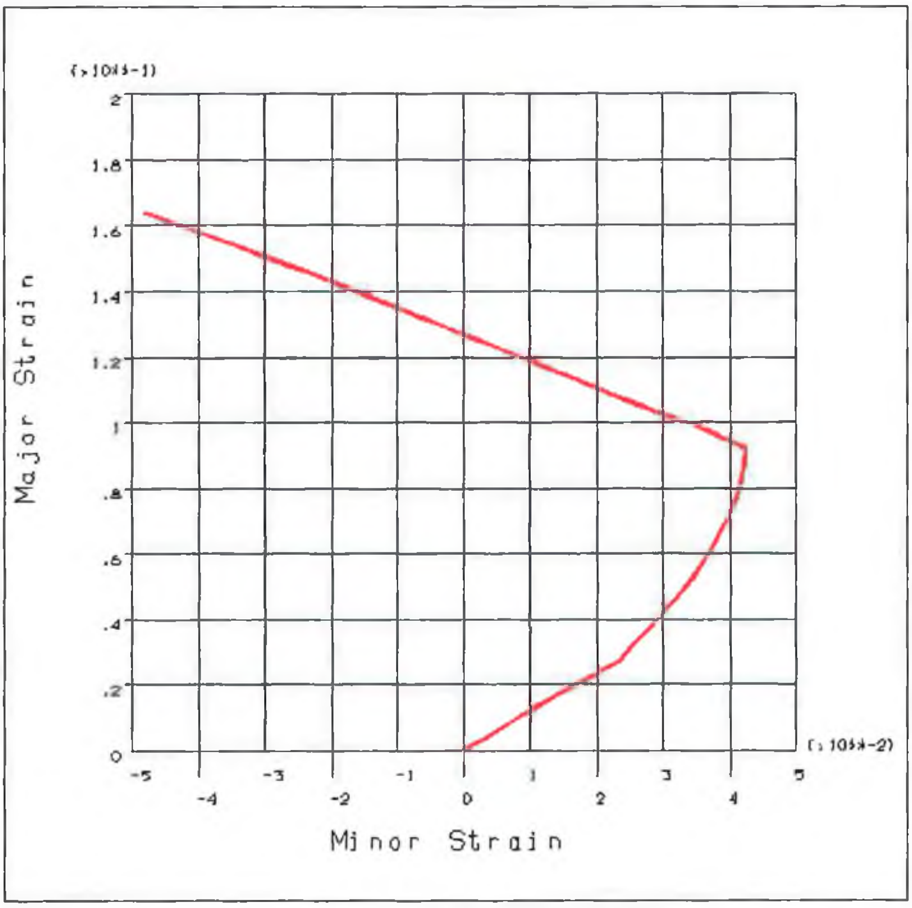

Figure 5.24. : Strain path of the top central node of the cross branch in principal planes.

5.2.3.7. Summary of Results

Simulation Number	Loading Type	Yield Strength of filler material	Tube/filler friction coeff.	Max. Branch Height	Maximum Stress	Thinning Behaviour (% of original thickness)
1	Pressure Only	18 MPa	0.15	5.25 mm	219 MPa	70% at branch top
2	Combined Simultaneous	18 MPa	0.15	10 mm	328 MPa	99% at branch top
3	Combined Non-Simultaneous	18 MPa	0.15	12 mm	322 MPa	88% at branch top
4	Combined Simultaneous	18 MPa	0	11 mm	328 MPa	90% at branch top
5	Combined Simultaneous	18 MPa	0.3	10.5 mm	311 MPa	99% at branch top
6	Combined Simultaneous	18 MPa	0.5	10 mm	300 MPa	99% at branch top
7	Combined Simultaneous	3.6 MPa	0.15	12.5 mm	327 MPa	95% at branch top

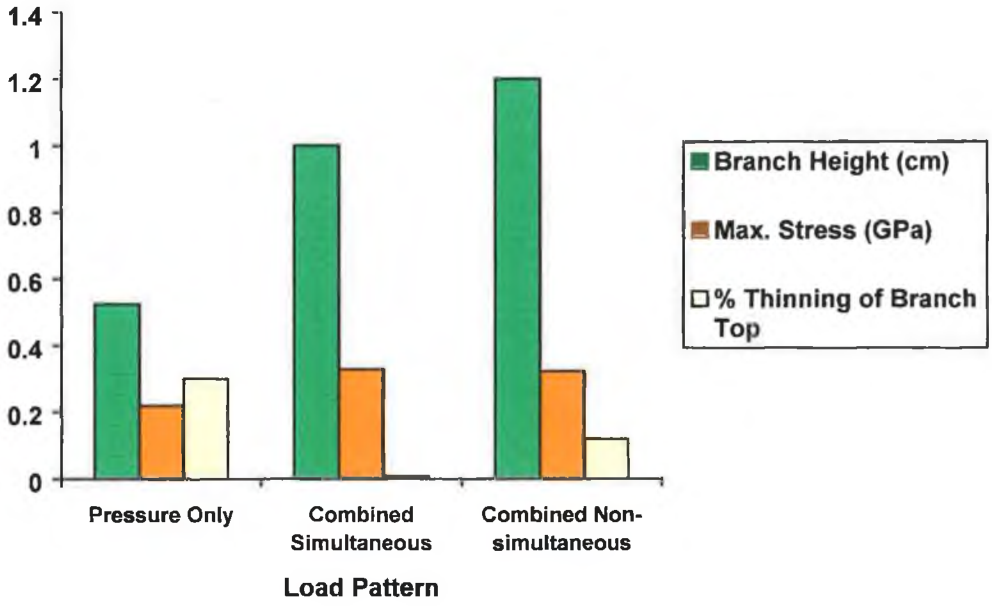

Figure 5.25. : The Effect of Using Different Loading Patterns

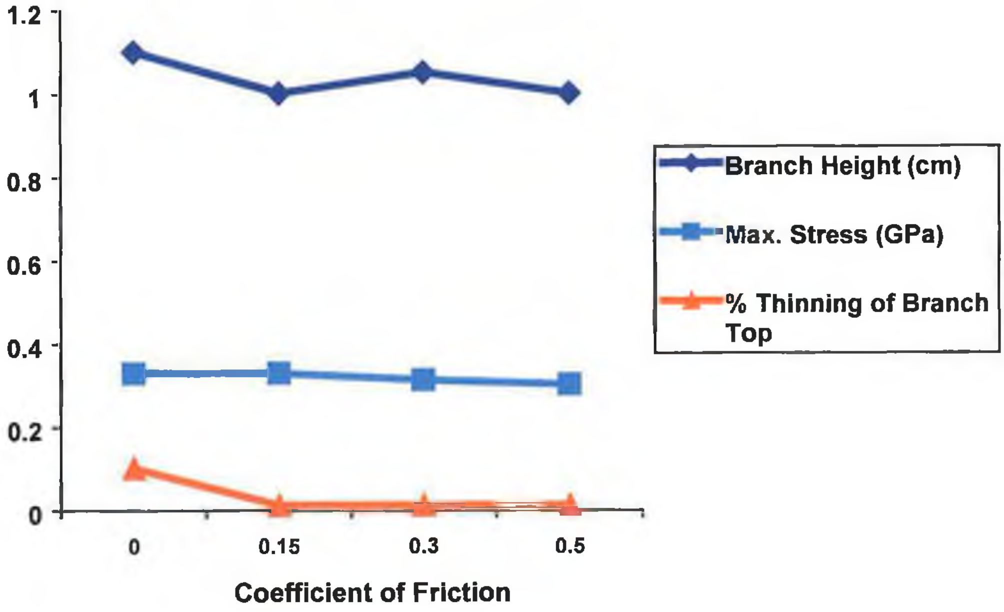

Figure 5.26. : The Effect of Varying Friction Between the Tube and The Bulging Media

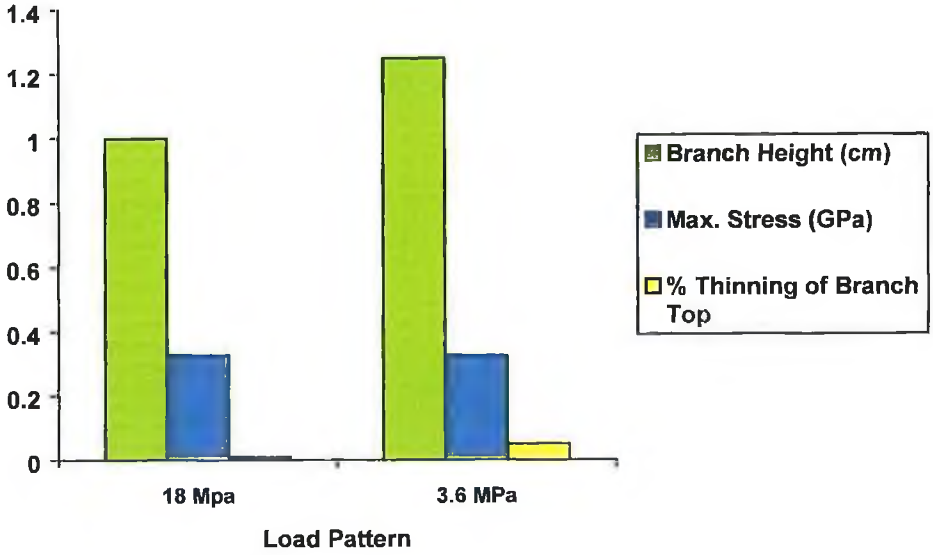

Figure 5.27. : The Effect of Varying the Relative Strength of the Bulging Media

5.3. Axisymmetric Bulge Forming of Tubes Using a Solid Bulging Medium

As it was not possible to validate the previous simulations of cross branch forming using a solid bulging medium during the course of this work, it was decided to design an experiment to axisymmetrically bulge tubes using a urethane rod as the bulging medium. The experimental apparatus was designed according to guidelines given by Thiruvarudchelvan [34,35,36]. A urethane rod of Shore Hardness 95A and diameter 38mm was used to bulge an annealed copper tube of diameter 42mm and wall thickness of 1.2mm. Figure 5.28 shows the arrangement used for the experimental procedure.

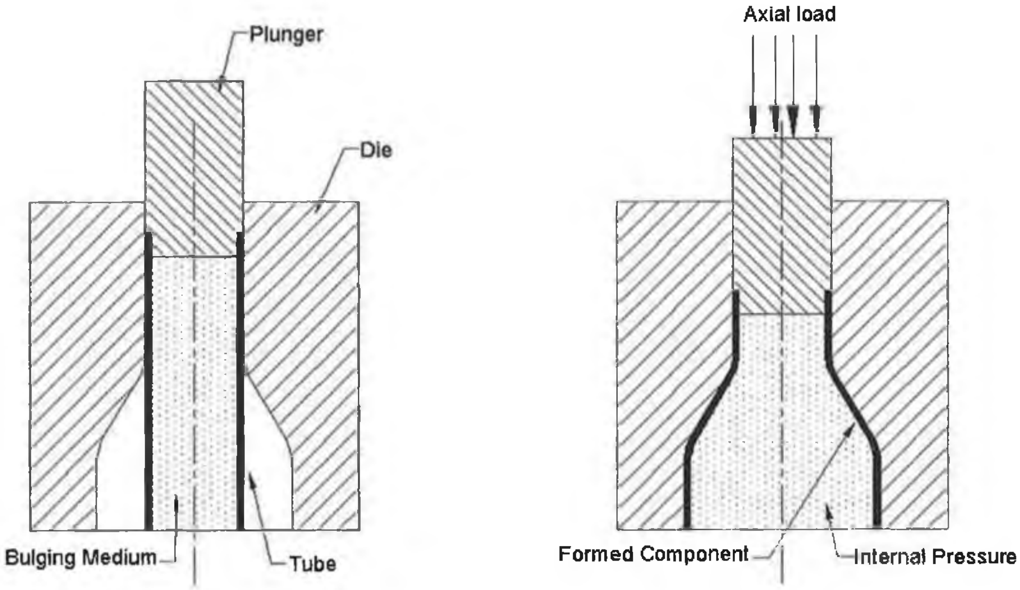

(a) Prior to Forming *(b) Forming Complete*

Figure 5.28. : Arrangement for Axisymmetric Bulge Forming Using a Urethane Rod

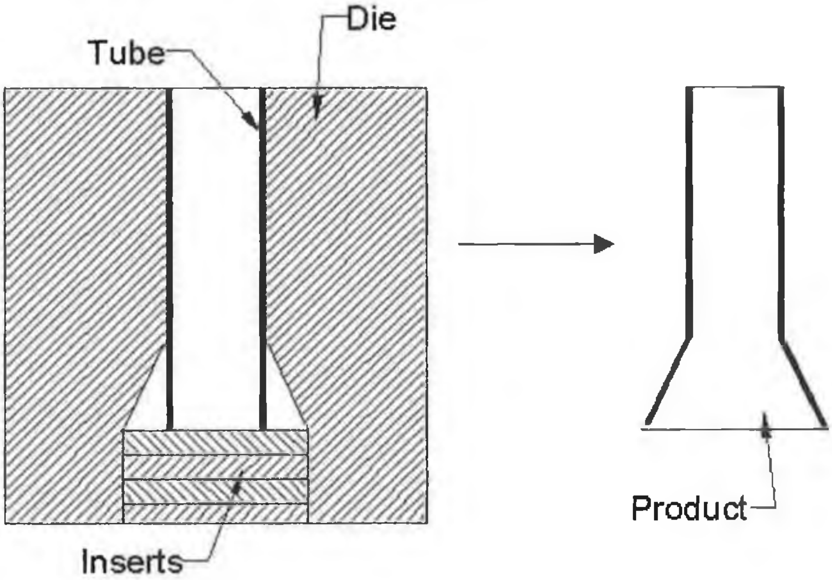

Figure 5.29. : Use of Inserts in Experimental Tests

The experimental apparatus was designed so that a number of different products could be manufactured by placing inserts into the bottom of the die. This is illustrated in figure 5.29. Figure 5.30 details the experimental apparatus used to validate the finite element model results. A hydraulic press was used to apply the compressive axial load to the urethane via a plunger. The load was applied at a constant speed throughout the forming process.

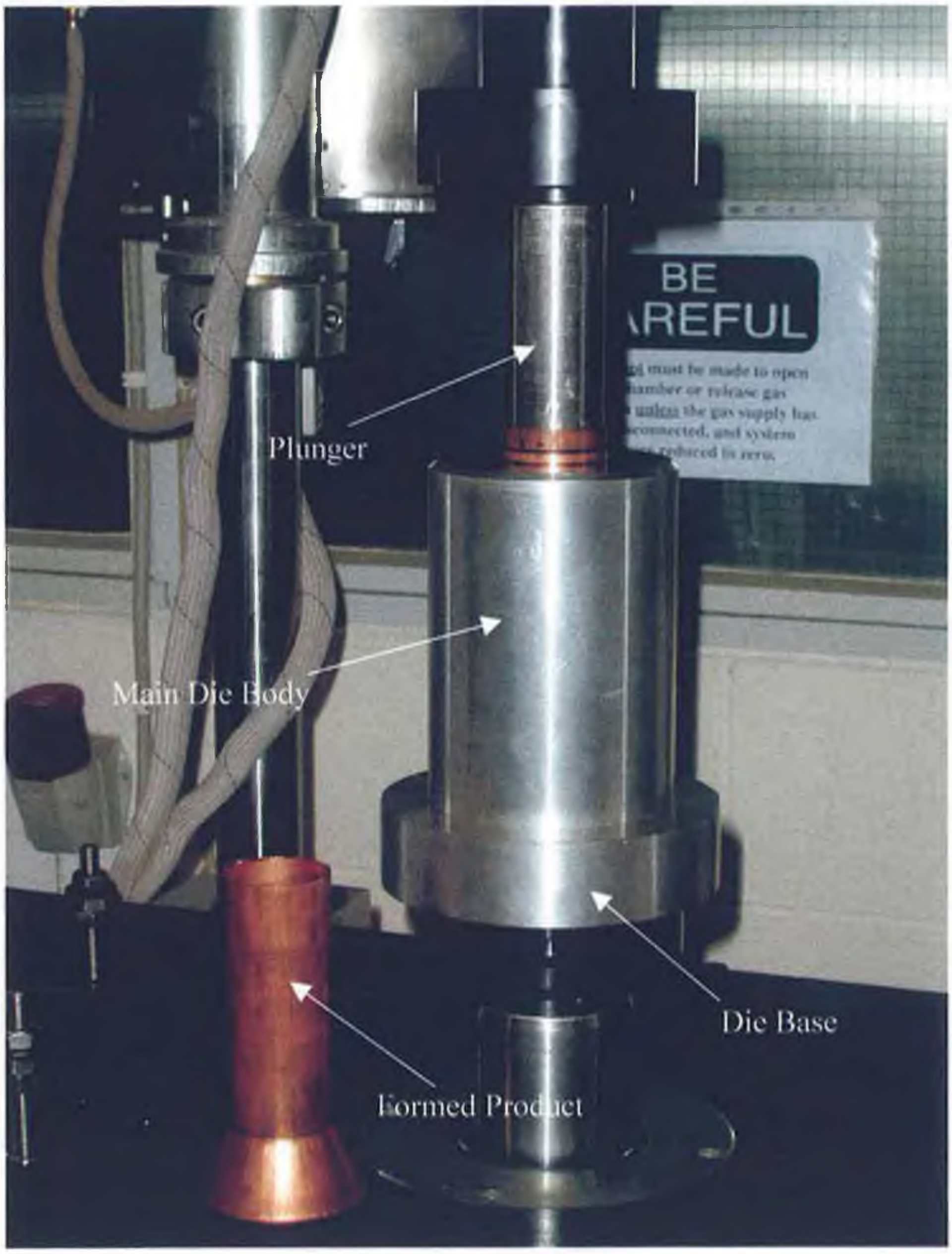

Figure 5.30. : Experimental Apparatus Used to Validate the Finite Element Results

5.3.1. Modelling

In order to simulate bugle forming of tubes using a urethane rod a finite element model was built according to the geometry of the experimental apparatus as described above. By taking advantage of symmetry it was possible to model one quarter of the die-tube-rod assembly and still obtain a full three dimensional solution. The bulging medium was modelled as a quarter cylinder placed inside the tube, with the outside diameter of the bulging medium being equal to that of the inside diameter of the tube.

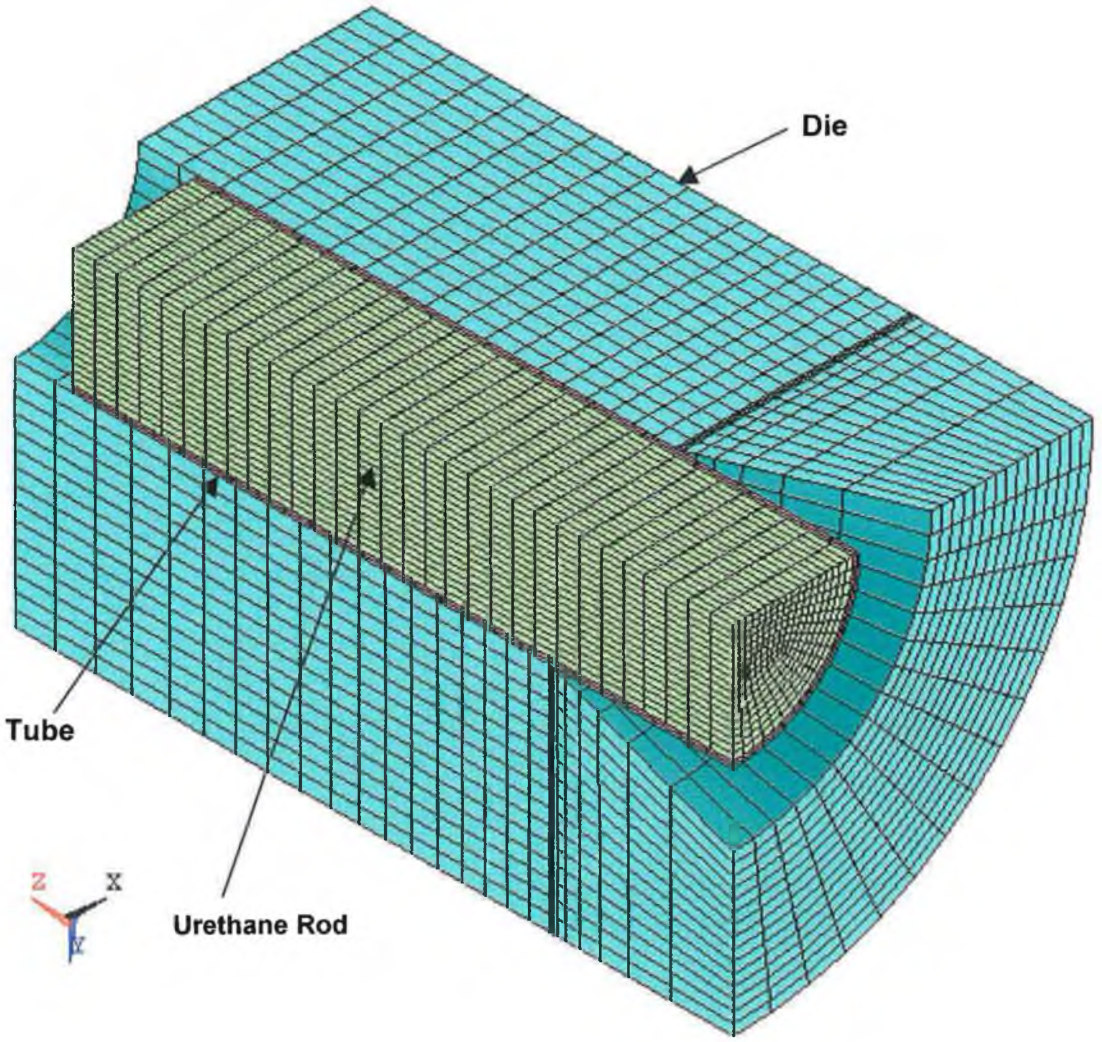

Figure 5.31. : Finite Element Model Used for Analysis of Bulging Using Urethane

Figure 5.31. shows the discretized model used for the first simulation. This simulation modelled the situation where a number of inserts were used in the die to produce a product with conical bulge, as shown in figure 5.32.

Figure 5.32. : Product with Conical Bulge

The die, the tube and the urethane were modelled using eight-node solid elements. The interfaces between the die and the tube, and between the urethane and the tube, were modelled using an automatic surface to surface contact algorithm. An elastic coulomb friction law was assumed and a coefficient of friction of 0.15 was assigned between the die and the tube. The coefficient of friction between the bulging medium and the tube was varied in order to determine its effect on the process. The material properties for the die were assigned to be consistent with the aluminium material used in the experimental tests. The material properties for the tube were determined from a compression test performed on the tube material. A compression test was also carried out to determine the material properties of the urethane rod. A linear elastic material model was used for the die and a bilinear elasto-plastic material model was used for the tube. A Mooney-Rivlin material model was assumed for the urethane rod. This material model has previously been used with success to predict the behaviour of hyperelastic materials such as urethane [90]. The Mooney-Rivlin constants were evaluated from the experimental test on the urethane material with the aid of a module of the Ansys preprocessor which is specially designed for calculating the constants.

A subsequent simulation was run to simulate the manufacture of a different product, where one of the inserts is removed and the resultant product is a conical shape with an expanded cylindrical portion attached. This required the development of an extended finite element model. The finite element model used for this simulation is shown in figure 5.33. and the resultant product is shown in figure 5.34.

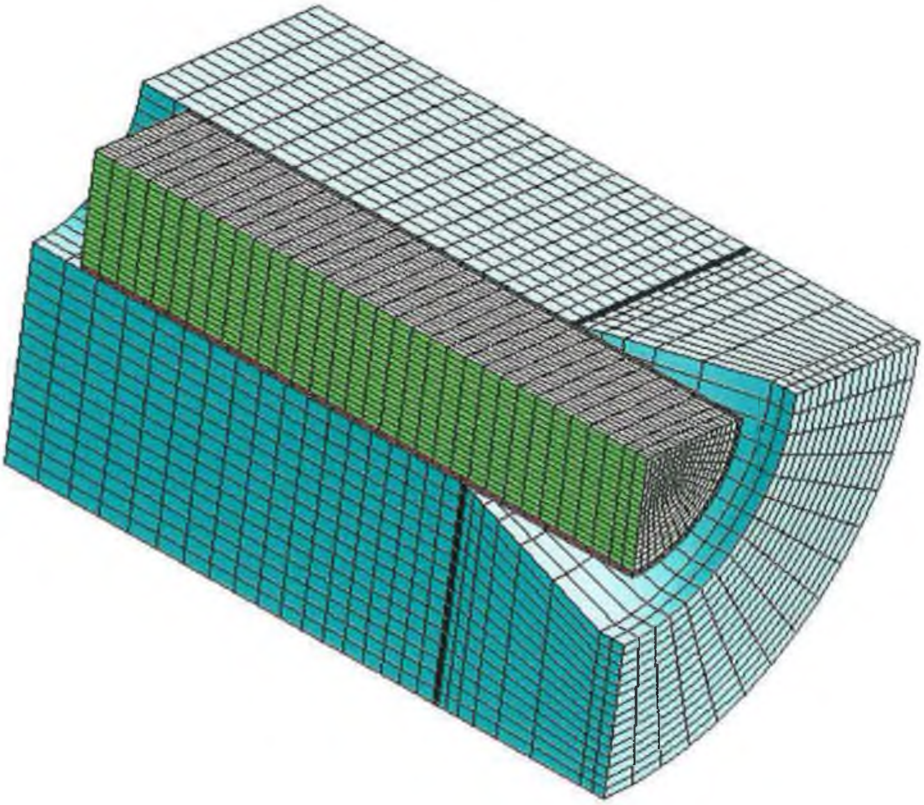

Figure 5.33. : Finite Element Model Used for Second Product.

Figure 5.34. : Geometry of Second Product

5.3.2. Boundary Conditions, Loading and Solution

Since one quarter of the model was developed by taking advantage of symmetry, the tube, die and urethane nodes at the symmetry edges were restrained in the appropriate directions. The assembly was also constrained in the Z-direction at the base in order to model the die base. The forming load was applied as prescribed displacement of the nodes at the urethane rod end. The displacement in each case was assigned to be equal to the displacement of the rod measured during the experimental tests.

The first simulation of the forming process was carried out produce a conical bulge, as mentioned earlier. The loading pattern for the first simulation is shown in figure 5.35.

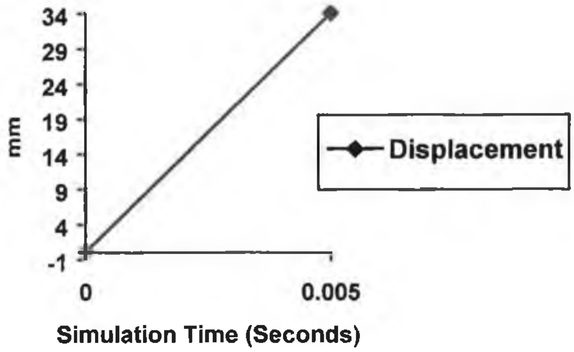

Figure 5.35. : Loading Pattern to Produce Conical Bulge

The second simulation was run to simulate the manufacture of a different product, where one of the inserts is removed and the resultant product is a conical shape with an expanded cylindrical portion attached as shown in figure 5.34. The loading pattern used for this simulation is shown in figure 5.36.

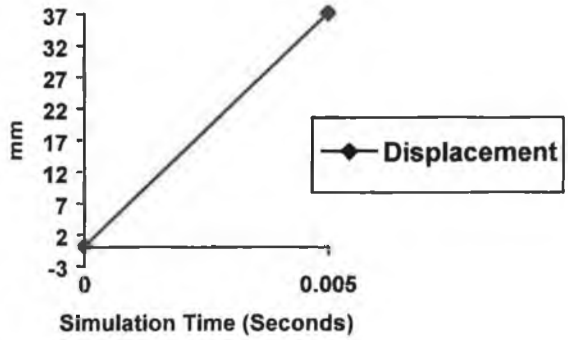

Figure 5.36. : Loading Pattern Used for Second Product.

5.3.3. Results and Analysis

5.3.3.1. First Product – Conical Bulge

Figures 5.37 to 5.41 show the distribution of von-Mises stress in the deformed tube at 20%, 40%, 60%,80% and 100% of full load application. It can be seen from the figures that the bulge initially begins as a hump at the part of the tube near the die bend.

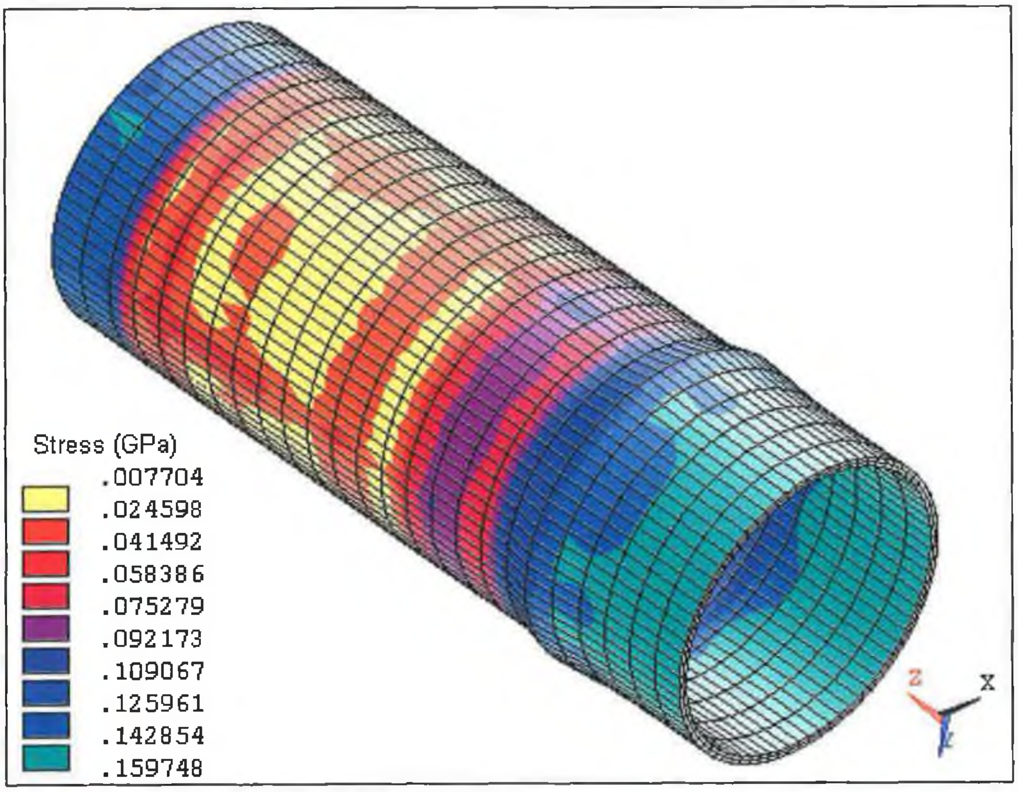

Figure 5.37. : Distribution of von-Mises Stress in the Deformed Tube at 20% of Full Load

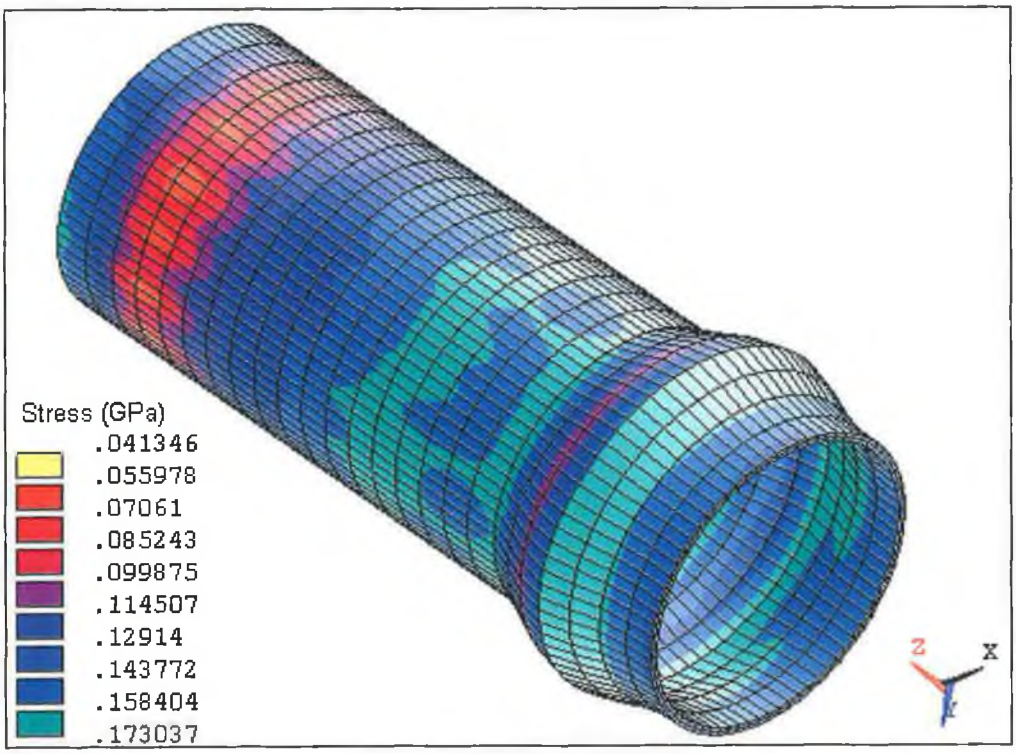

Figure 5.38. : Distribution of von-Mises Stress in the Deformed Tube at 40% of Full Load

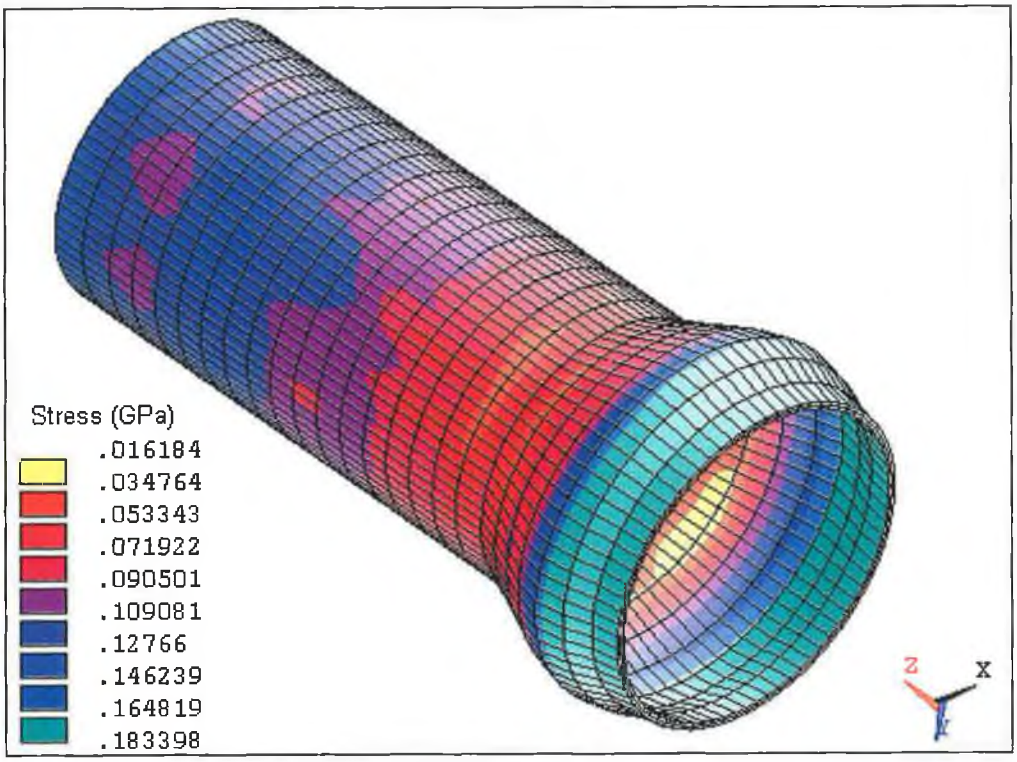

Figure 5.39. : Distribution of von-Mises Stress in the Deformed Tube at 60% of Full Load

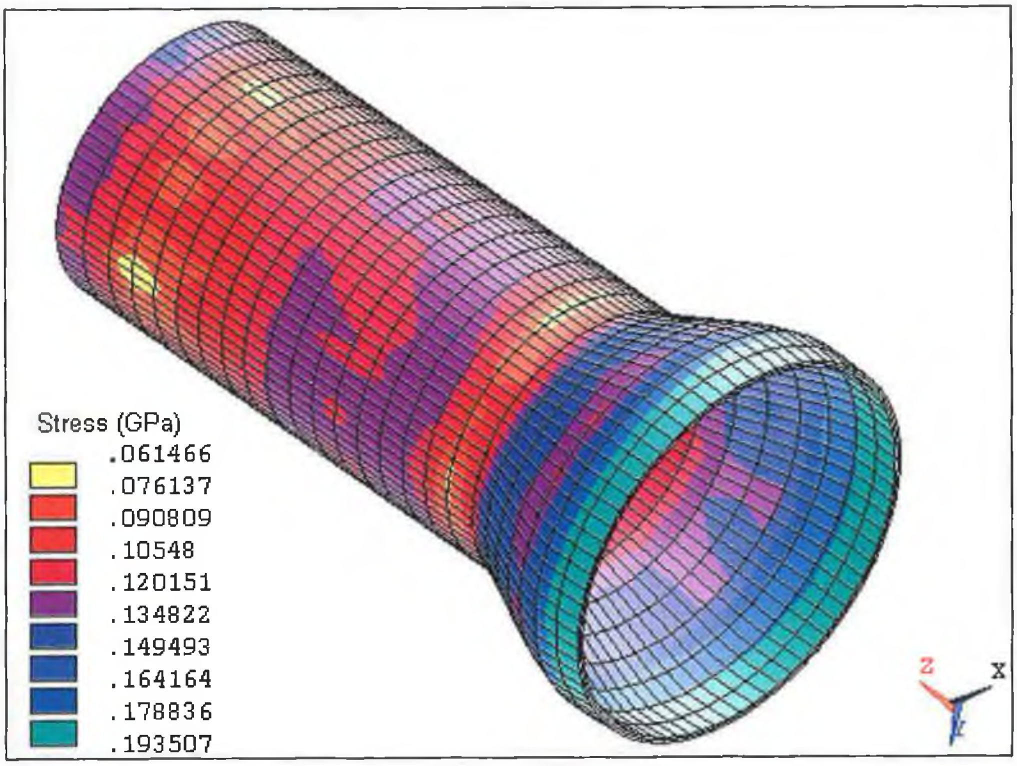

Figure 5.40. : Distribution of von-Mises Stress in the Deformed Tube at 80% of Full Load

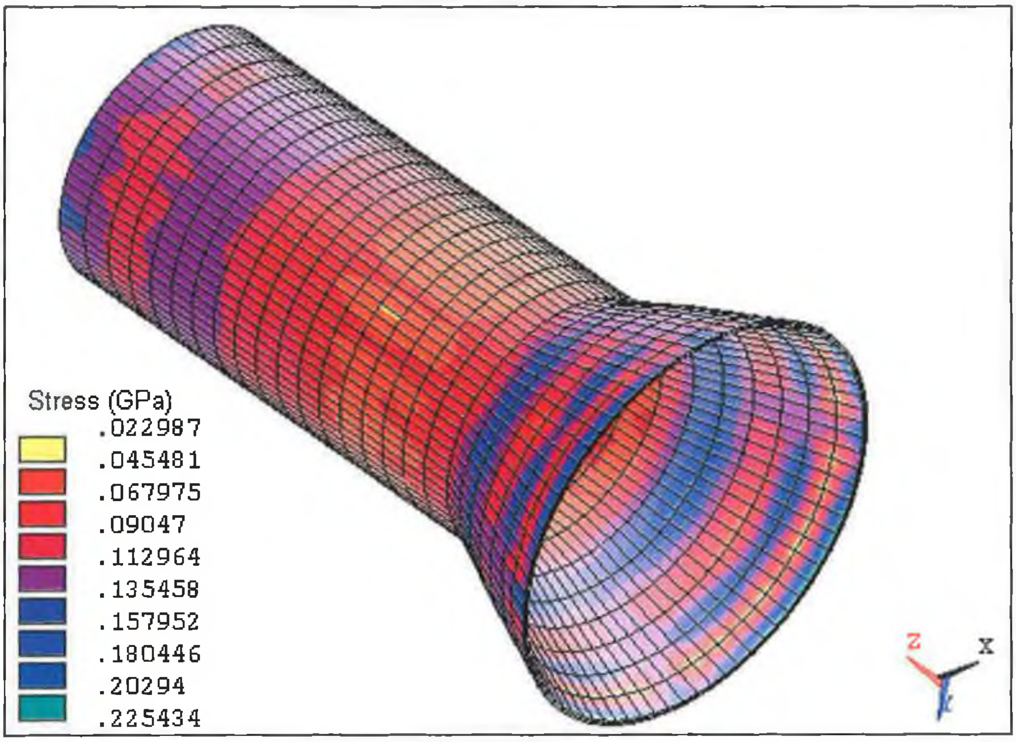

Figure 5.41. : Distribution of von-Mises Stress in the Deformed Tube at Full Load

As the process continues the bulge grows and moves further down the tube and begins to fill the die cavity. By the time 80% of the loading has been applied the bulge is almost fully formed and during the remaining 20% of the simulation the bottom-most part of the tube comes in contact with the die wall. At full load the tube is almost in complete contact with the die wall. This is in agreement with experimental tests in which the same loading pattern was used.

Figure 5.42 shows the development of von-Mises and principal stresses in a node at the outer surface of the bottom of the tube during the deformation process. It can be seen that the stress development is highly erratic due to the friction between the urethane rod and the tube and between the tube and the die. Despite the erratic nature of the results it can be seen that the development of von-Mises stress approximately follows the bilinear material model used for the tube material. The bulge initially develops due to an increase in hoop stress and is aided towards the latter half of the simulation by an increase in axial stress. Axial stress is mildly compressive for most of the simulation but becomes tensile towards the end of the simulation as the bulge begins to grow more rapidly in this region.

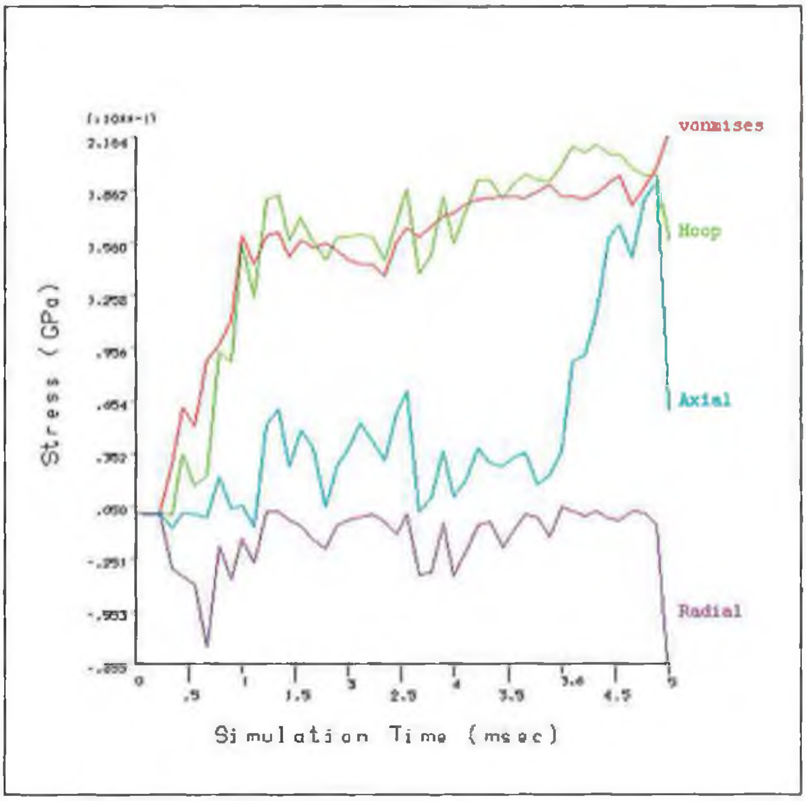

Figure 5.42. : Development of Stress at the Tube End during the Process

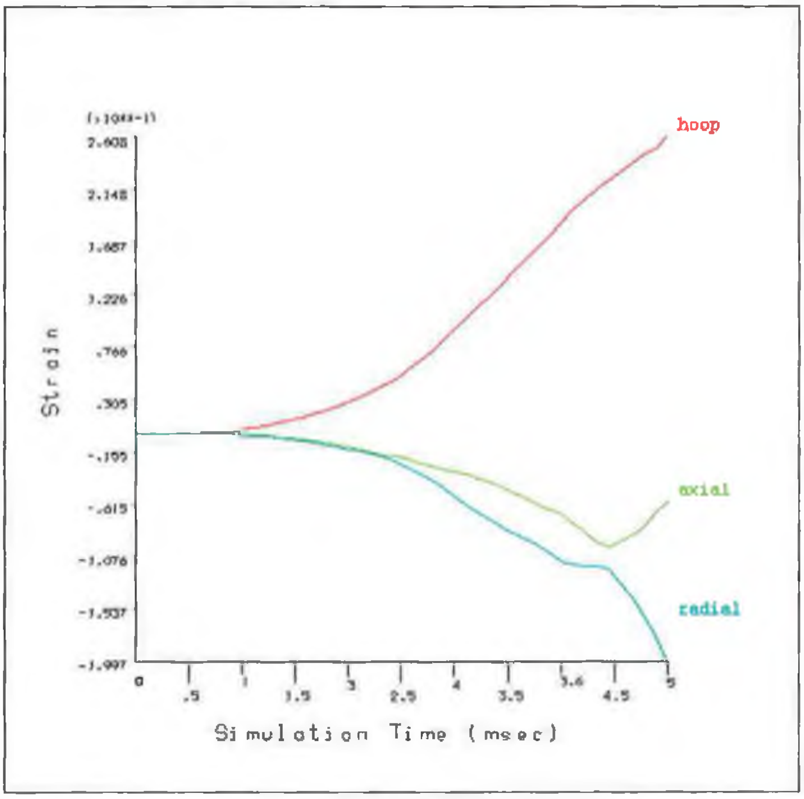

Figure 5.43. : Development of Principal Strains during the Process

The friction between the tube and the urethane rod causes the initial compressive axial stress and is favourable as it helps to push material into the bulging zone. Radial stress is highly compressive early in the simulation but falls off rapidly as the bulge begins to form. It can be seen that all stresses begin to become more compressive at the end of the simulation when the tube comes into full contact with the die wall.

The development of strain in the same node during the process is shown in figure 5.40. It can be seen from the figure that hoop strain was positive for the entire simulation, while axial and radial strains were compressive. The compressive axial strain is evidence of the favourable friction conditions between the die and the urethane rod causing material to be pushed into the bulging zone during the forming process. In order to get a clearer view of the deformation mechanisms : the strain path of the node during the process is shown in figure 5.44. It can be seen from the figure that the majority of the bulge is formed due to compressive axial strain and tensile hoop strain. The slope of the graph indicates that hoop strain is dominant.

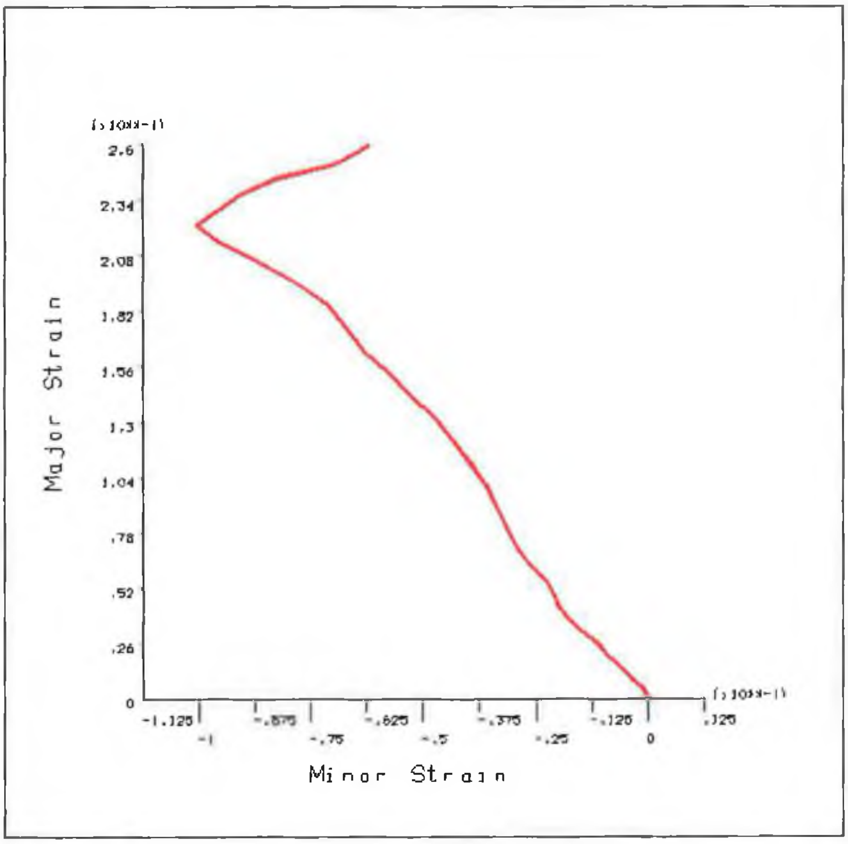

Figure 5.44. : Strain Path of a Node at the Tube End during the Process.

Towards the end of the simulation the direction of the curve changes and turns towards the first quadrant as the tube comes in contact with the die wall.

In order to validate the results of the finite element simulation an experiment was performed using the same geometry, materials and loading conditions as the finite element model, as explained earlier. The resultant geometry was cut longitudinally in order to facilitate measuring thickness along the deformed tube. In order to compare results figure 5.45. shows a graph of thickness versus distance from the tube end for both the experimental and finite element results. It can be seen from the figure that the thickness distribution is predicted reasonably accurately by the simulation. In general the simulation tends to predict slightly greater thinning than the experimental analysis. It is thought that this may be a consequence of difficulty in accurately modelling the friction conditions between the tube and the urethane. Slightly higher friction would help in pulling more tube material into the bulging zone and hence reduce thinning of the bulged region. Experimenting with altering the friction conditions used in the simulation or using a different friction model may help to improve the results. It should be pointed out, however, that the percentage accuracy of the current simulation results, from figure 5.45, is over 95%. Given this results efforts to further improve the model may not be justified in terms of time and cost.

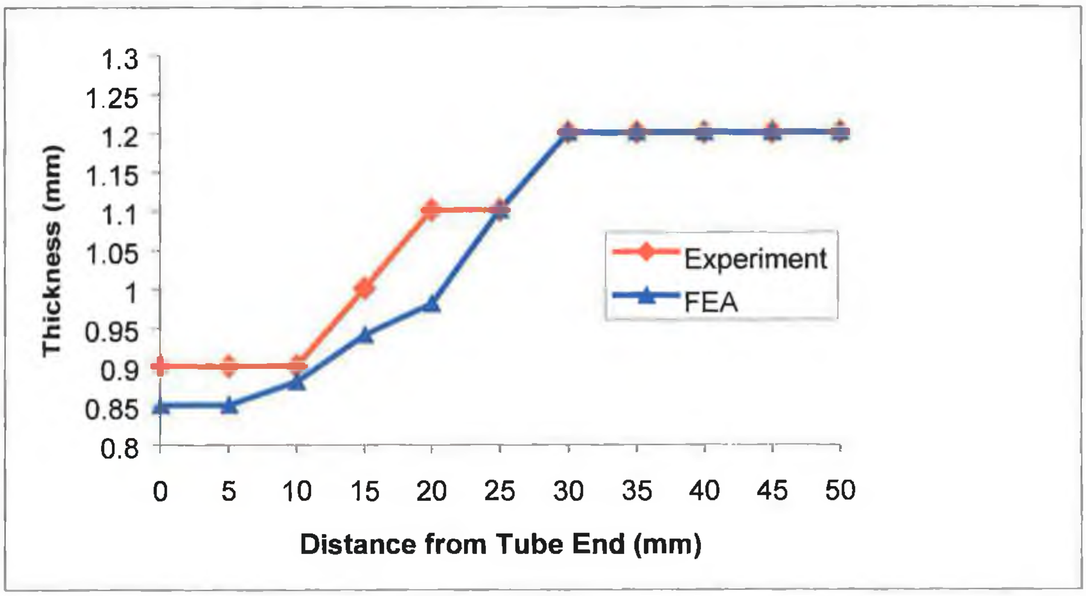

Figure 5.45. : Comparison of Experimental and Simulation Results.

5.3.3.2. Second Product – Conical Bulge with Extension

Figures 5.46 to 5.50 show the distribution of von-Mises stress in the deformed tube at 20%, 40%, 60%,80% and 100% of full load application. It is interesting to note that the bulge develops in almost exactly the same manner as in the previous simulation up to 60% of load application. In this case however the stress levels at each stage are much higher than in the previous simulation. After 60% load application the bulge develops more rapidly in this case. At 80% of load application the bulge resembles the final product in the previous simulation. The remaining 20% of the simulation pushes the tube firmly against the die wall and establishes the cylinder at the end of the bulge. Figure 5.48 shows a side view of the fully deformed tube, clearly showing the formation of the cylinder at the end of the conical section.

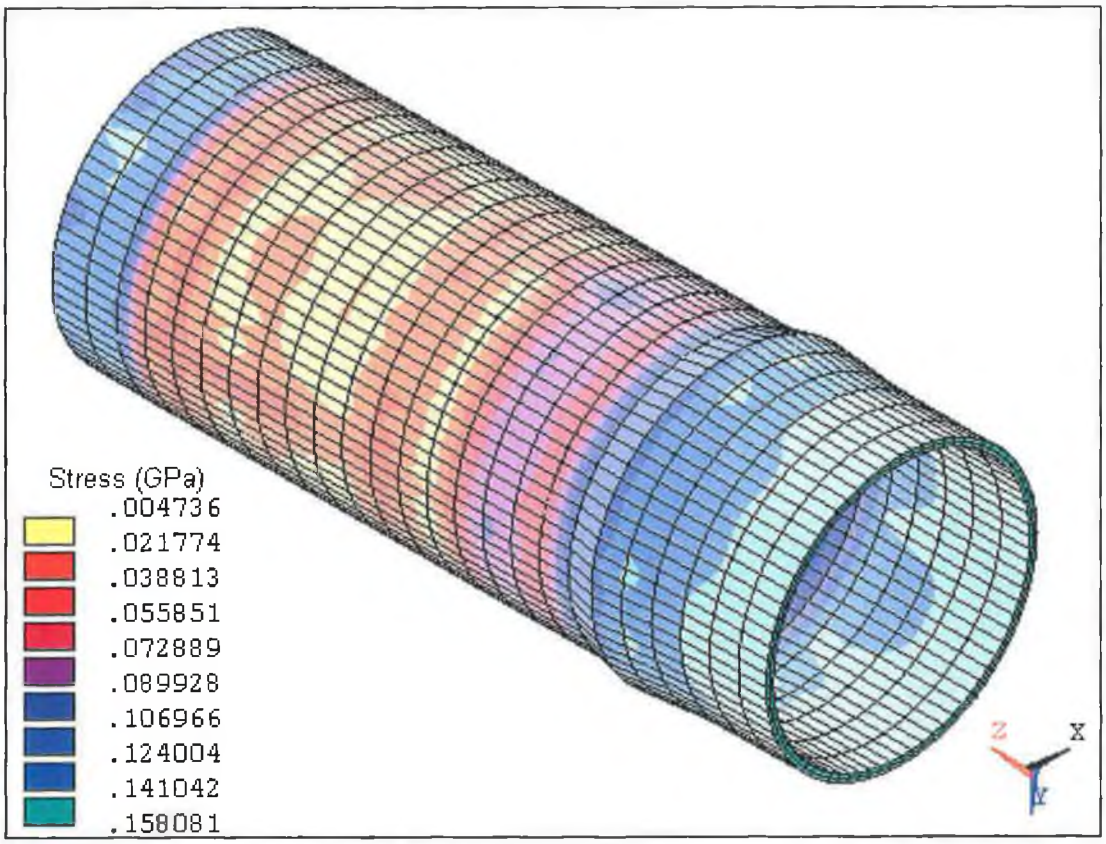

Figure 5.46. : Distribution of von-Mises Stress in the Deformed Tube at 20% of Full Load

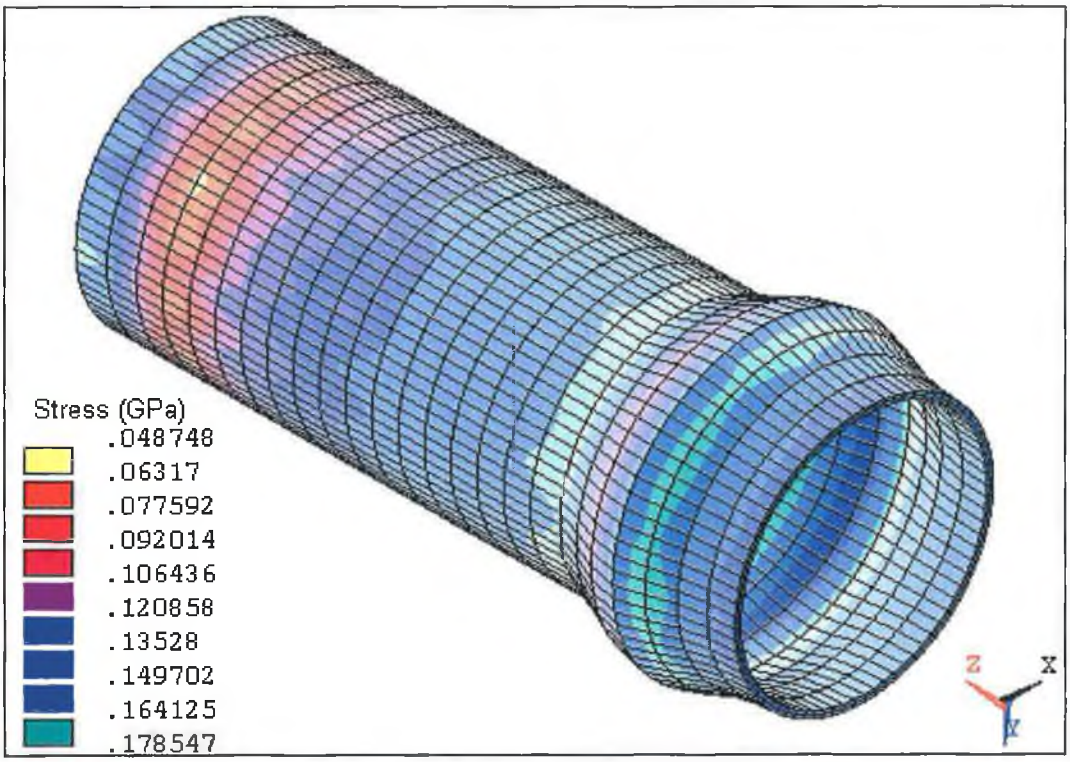

Figure 5.47. : Distribution of von-Mises Stress in the Deformed Tube at 40% of Full Load

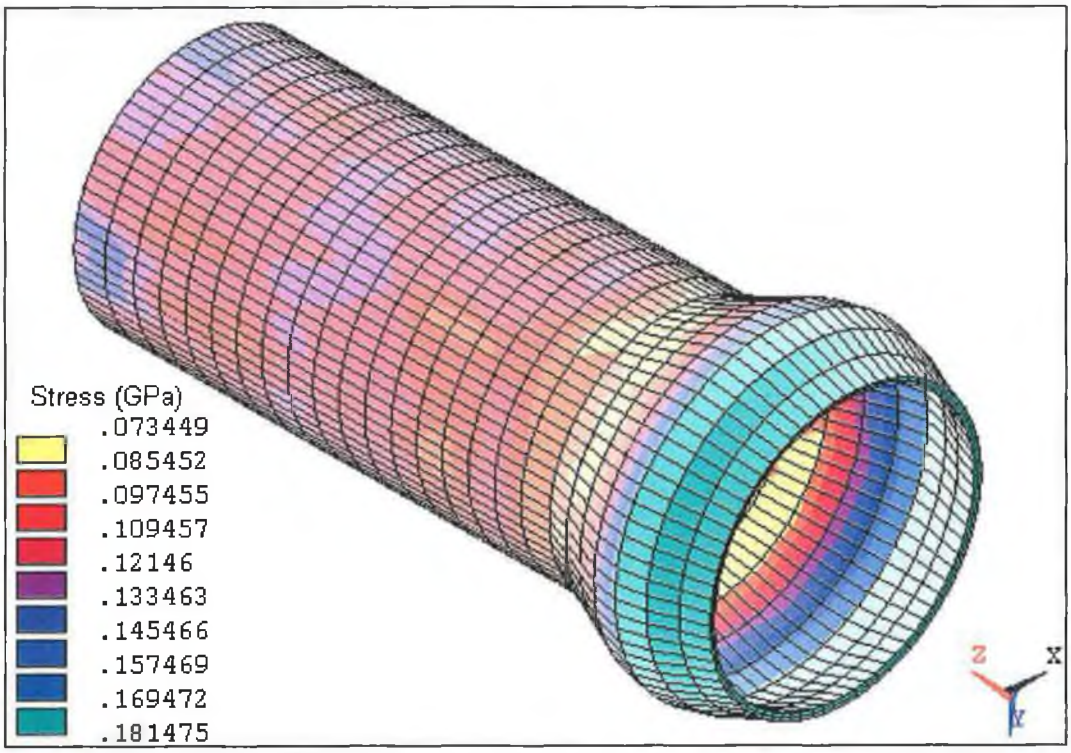

Figure 5.48. : Distribution of von-Mises Stress in the Deformed Tube at 60% of Full Load

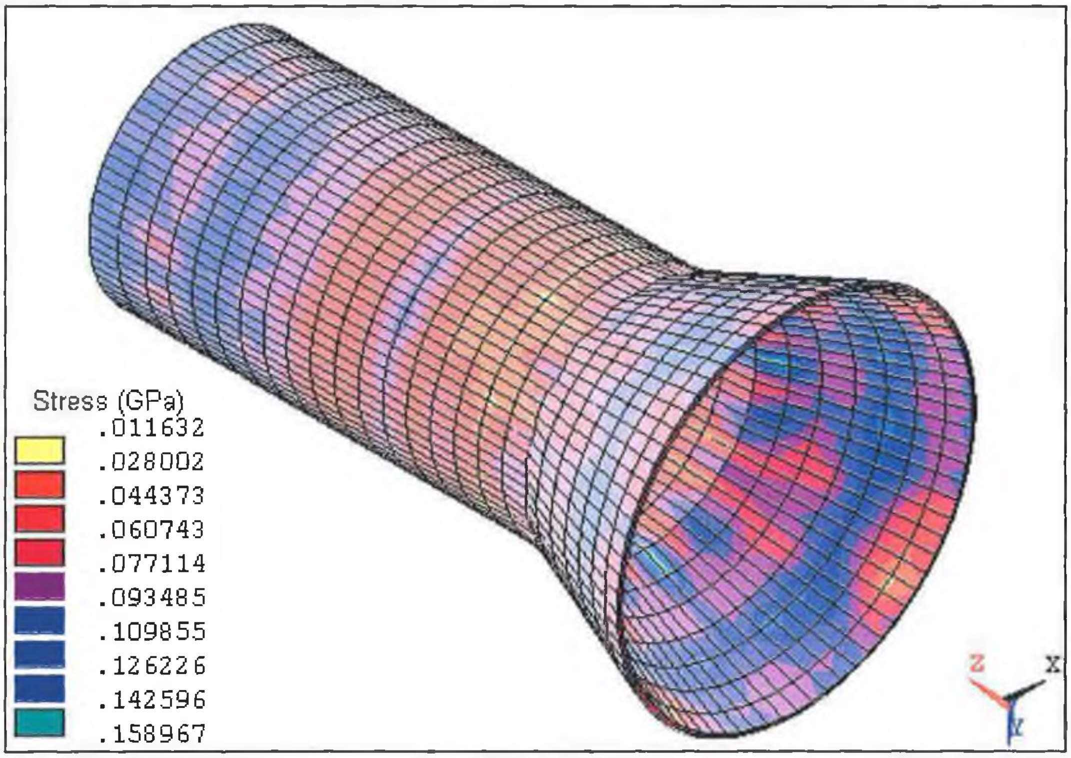

Figure 5.49. : Distribution of von-Mises Stress in the Deformed Tube at 80% of Full Load

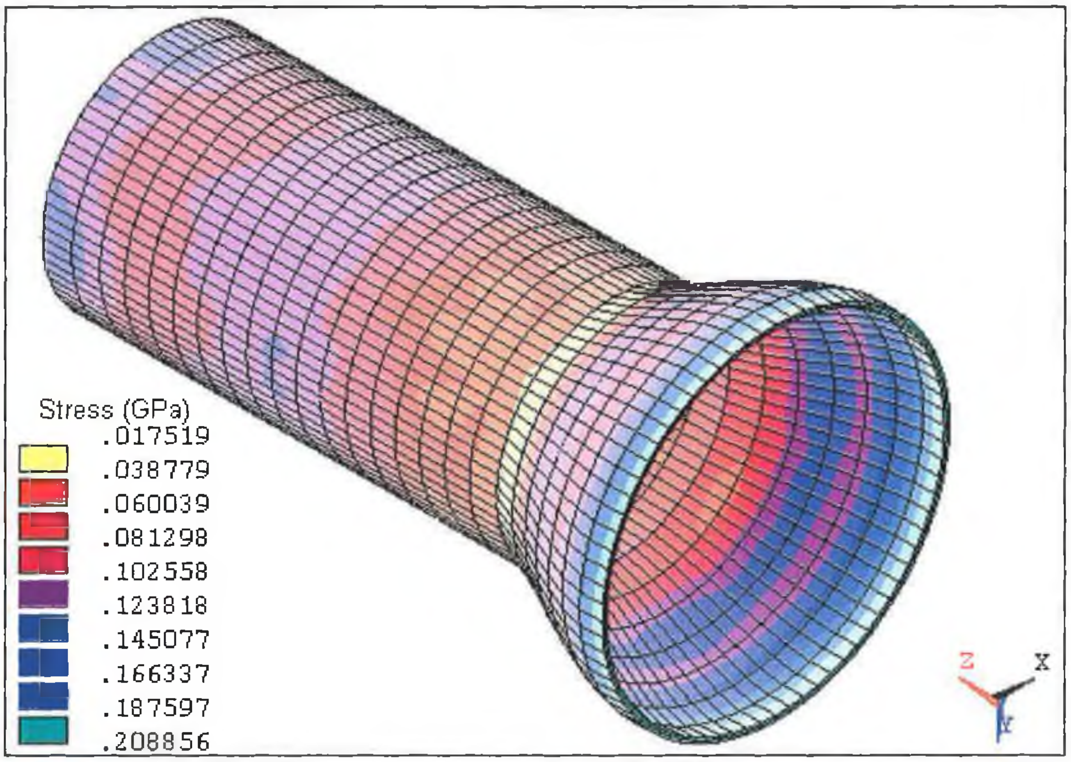

Figure 5.50. : Distribution of von-Mises Stress in the Deformed Tube at Full Load

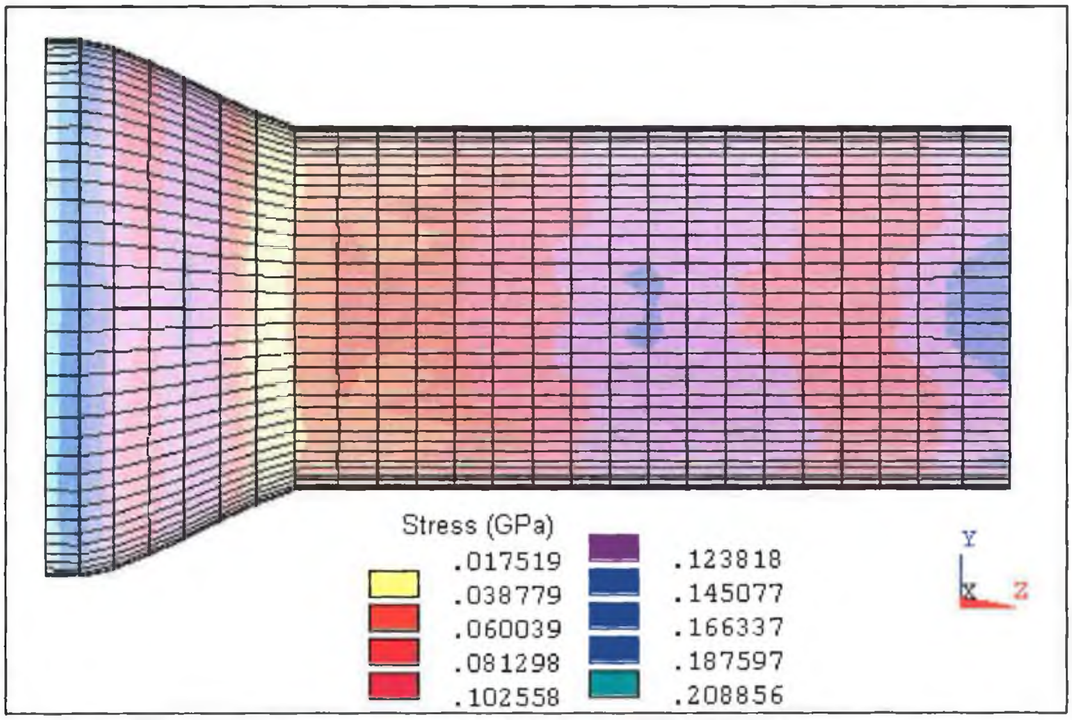

Figure 5.51. : Alternative View of the Fully Deformed Tube

The figures provide a valuable insight into the development of the bulge and help to explain why some defects were encountered during the experimental process. It can be seen from figure 5.48 that the bulge at this stage consists of a hump in the tube. It can be appreciated that if too great an axial load was provided to the tube at this point that the tube would buckle easily. This result was evident in experimental tests where too much friction between the tube and urethane rod was used. Figure 5.52 shows an example of a tube that failed in this manner.

Figure 5.53 shows the development of von-Mises and principal stresses in a node at the outer surface of the bottom of the tube during the deformation process. It can be seen that the stress development is again erratic due to the friction between the urethane rod and the tube and between the tube and the die. The development of stress here is less erratic than in the previous simulation. The bulge initially develops due to an increase in hoop stress and is aided towards the latter half of the simulation by an increase in axial stress. Axial stress varies between being compressive and tensile for most of the simulation but becomes continuously tensile towards the end of the simulation as the bulge begins to grow more rapidly in this region.

Figure 5.52. : Buckling Failure of a Tube due to High Tube-Rod Friction

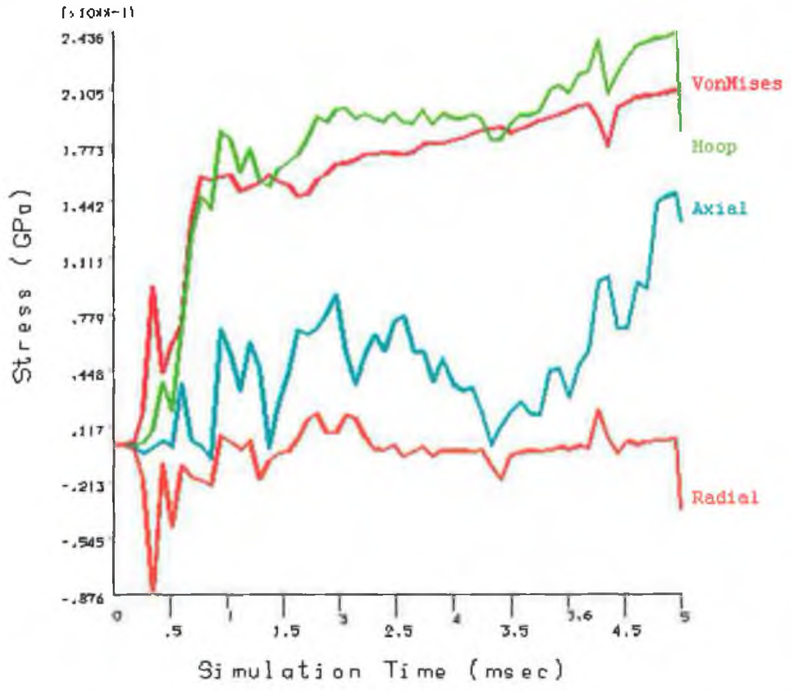

Figure 5.53. : Development of Stress at the Tube End during the Process

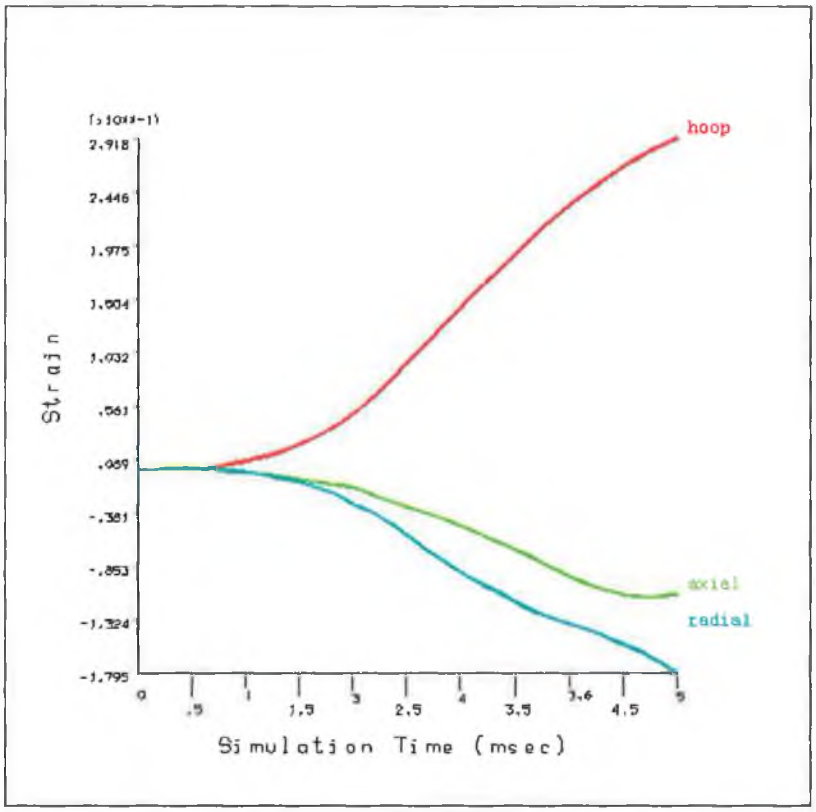

Figure 5.54. : Development of Principal Strains during the Process

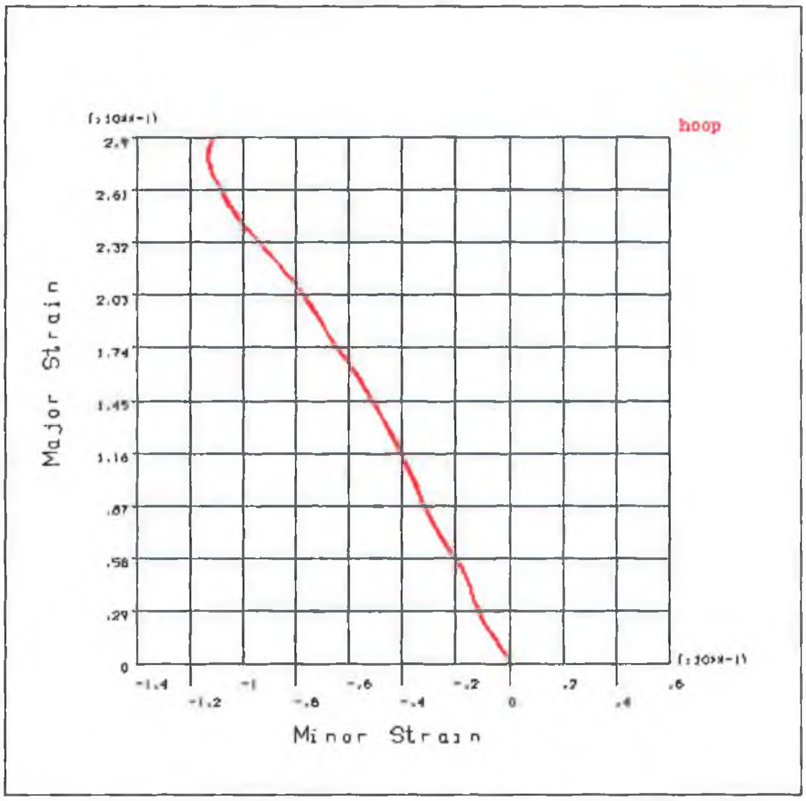

Figure 5.55. : Strain Path of a Node at the Tube End during the Process.

It can be seen again that all stresses begin to become more compressive at the end of the simulation when the tube comes into full contact with the die wall in the region of the node under consideration.

The development of strain in the same node during the process is shown in figure 5.54. It can be seen from the figure that hoop strain was positive for the entire simulation, while axial and radial strains were compressive. The development of strain here is much more regular than in the previous simulation. The compressive axial strain is again evidence of the favourable friction conditions between the die and the urethane rod. In order to get a clearer view of the deformation mechanisms : the strain path of the node during the process is shown in figure 5.55. It can be seen from the figure that the bulge is formed due to compressive axial strain and tensile hoop strain. The slope of the graph indicates that hoop strain is dominant. Towards the end of the simulation the direction of the curve begins to change as the tube comes in contact with the die wall.

Similar to the previous simulation, an attempt to validate the results of the finite element simulation was made by conducting an experiment test utilising the same geometry, materials and loading conditions as the finite element model. Figure 5.56. shows a graph of thickness versus distance from the tube end for both the experimental and finite element results.

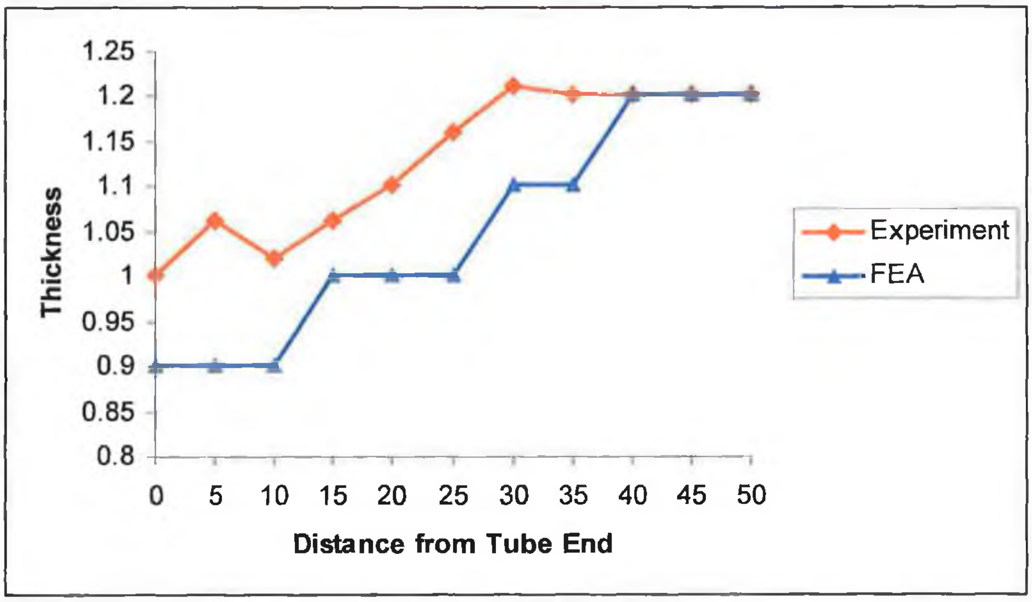

Figure 5.56. : Comparison of Experimental and Simulation Results

It can be seen from the figure that the thickness distribution is predicted reasonably accurately by the simulation, the maximum percentage error being approximately 10%. As in the previous simulation the finite element model tends to predict slightly greater thinning than the experimental analysis. Again this may be a consequence of difficulty in accurately modelling the friction conditions between the tube and the urethane. In this case, with reference to figure 5.45., it can be seen that the thickness predicted is much less accurate at the point 5mm from the tube end. This region is the blend between the conical region and the short cylinder at the end of the tube. It is thought that the simulation results may not be truly representative at this point due to the fact that solid elements were used to model the tube. The deformation mechanism in this region is due to translation and bending. The solid elements used do not have any rotational degree of freedom and thereby have no stiffness in bending. Only translational movement is accounted for in the finite element solution and possible bending in this region has not been considered. This results in relatively less stress than would actually occur and consequently less thickening behaviour than measured experimentally.

5.4. Summary of Chapter 5

This chapter presents the results from simulations of bulge forming of both asymmetric and axisymmetric components using a solid bulging medium. The results of the axisymmetric analysis have been validated against experimental results in order to have confidence in the modelling procedures used here.

Chapter 6 : Bulge Forming of Coated Bimetallic Tubes

6.1. Introduction

This chapter details the modelling procedures used to simulate cross branch bulge forming of coated bimetallic tubes. The results from the simulations are presented and analysed.

6.2. Modelling

Simulations were carried out to bulge a cylindrical tube of 1.3mm thickness, 24.12mm diameter and 107mm length into a cross joint. The diameter of the branch was equal to that of the main tube. This was the same geometry used in the previous simulations of cross branch forming. The same die model was used here as in the previous simulations. The tube was modelled as two separate volumes. Initially the inner layer of material was 1mm thick and the outer layer, or coating, was 0.3mm thick. A number of simulations were carried out whereby the thickness of the outer layer was increased while still keeping the same overall tube thickness.

The inner tube material properties were determined from a compression test on annealed copper. The material parameters for the coating were chosen to approximately represent stainless steel. In both cases a bilinear elasto-plastic material model was used as illustrated in figure 6.1.

By taking advantage of symmetry and providing the correct boundary conditions and loading on the resulting segment of the geometry, it was possible to model one eighth of the problem and obtain a proper three dimensional solution. The finite element model presented in figure 6.2 was used to simulate the bulge forming process.

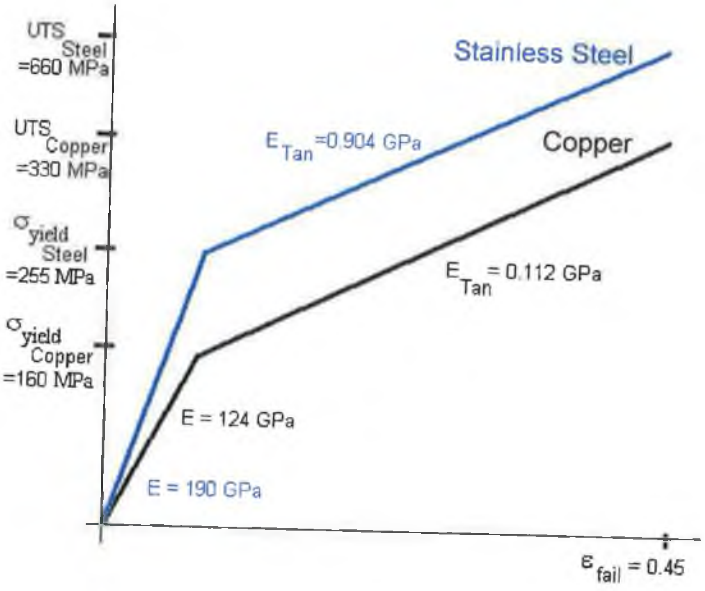

Figure 6.1. : Material Model's Used in the Bimetallic Tube Analysis

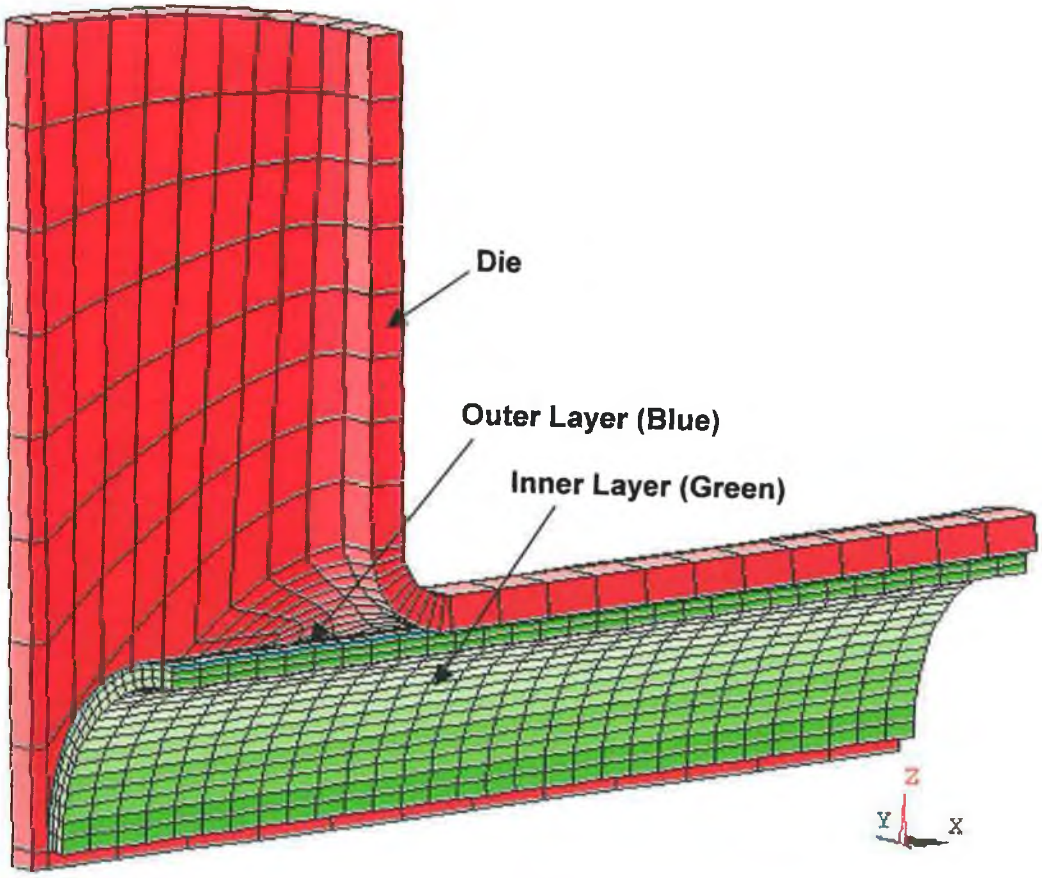

Figure 6.2. : Finite Element Model Used in the Bimetallic Tube Analysis

The bimetallic tube was modelled in two separate volumes. The inner tube describes the main copper tube while the outer tube describes the stainless steel coating. Both tubes were modelled using eight-node explicit solid elements. The interface between the two tubes was modelled using a tiebreak surface to surface contact algorithm which effectively bonded the two volumes to each other. The algorithm uses the user-specified tensile, f_n, and shear, f_s, failure stresses to calculate the failure criterion for the bond. In this case values in excess of the UTS of stainless steel were used in order to ensure that the bond remained intact throughout the process. Failure of the connection is defined to occur when:

$$\left(\frac{|f_n|}{f_{n,fail}}\right)^{m_1}+\left(\frac{|f_s|}{f_{s,fail}}\right)^{m_2}\geq 1$$

This is illustrated in figure 4 below:

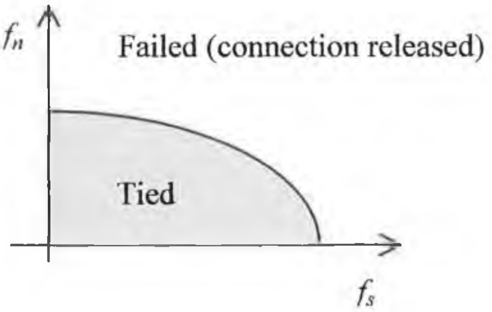

Figure 6.3 : Method Used to Determine Failure of Tied Surface to Surface Contact

The interface between the die and the tube was modelled using an automatic surface to surface contact algorithm. The algorithm uses the material properties of both contacting surfaces to calculate the stiffness of the contact elements. An elastic coulomb friction law was assumed and a coefficient of friction of 0.15 was assigned between the die and the tube.

6.3. Boundary Conditions, Loading and Solution

Since one eighth of the model was developed by taking advantage of symmetry, the tube nodes at the symmetry edges were restrained in the appropriate directions. The die was constrained as a rigid body. The pressure load was applied as a surface load on the inner tube's inner surface and the axial load was applied as a prescribed displacement of the nodes at the edge of both tube ends.

The first simulation of the forming process was carried out using pressure loading only. The loading pattern for the first simulation is shown in figure 6.4. The second simulation was performed on the same finite element model using pressure load and axial displacement as shown in figure 6.5.

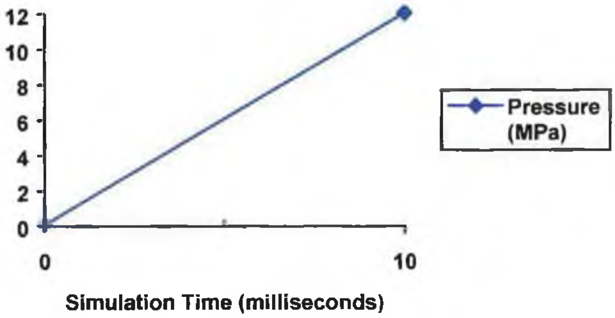

Figure 6.4. : Loading Pattern 1

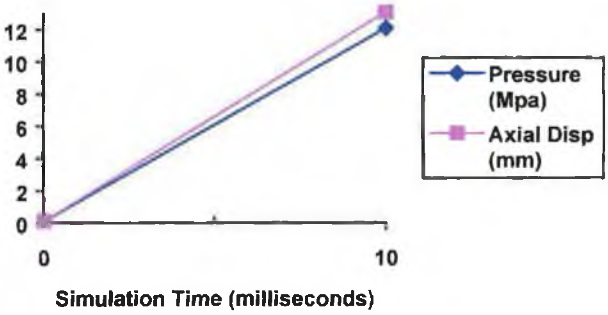

Figure 6.5. : Loading Pattern 2

6.4. Results and Analysis

6.4.1. Pressure Load Only

The first simulation was run with a linearly increasing pressure load, as shown in figure 6.4, in order to determine the critical pressure load for the process. The point of rupture is assumed when a node in the highly stressed area becomes steeply stressed beyond the ultimate tensile strength of the material. In this case the ultimate tensile stress of the steel outer layer was exceeded after a simulation time of 9 milliseconds. The branch height obtained at this point was 6.3mm. It can be seen from figure 6.6. that the bulged region has stressed considerably with the greatest stress concentration at the branch top and the main tube under the branch. The main tube outside the bulged region has remained relatively unstressed.

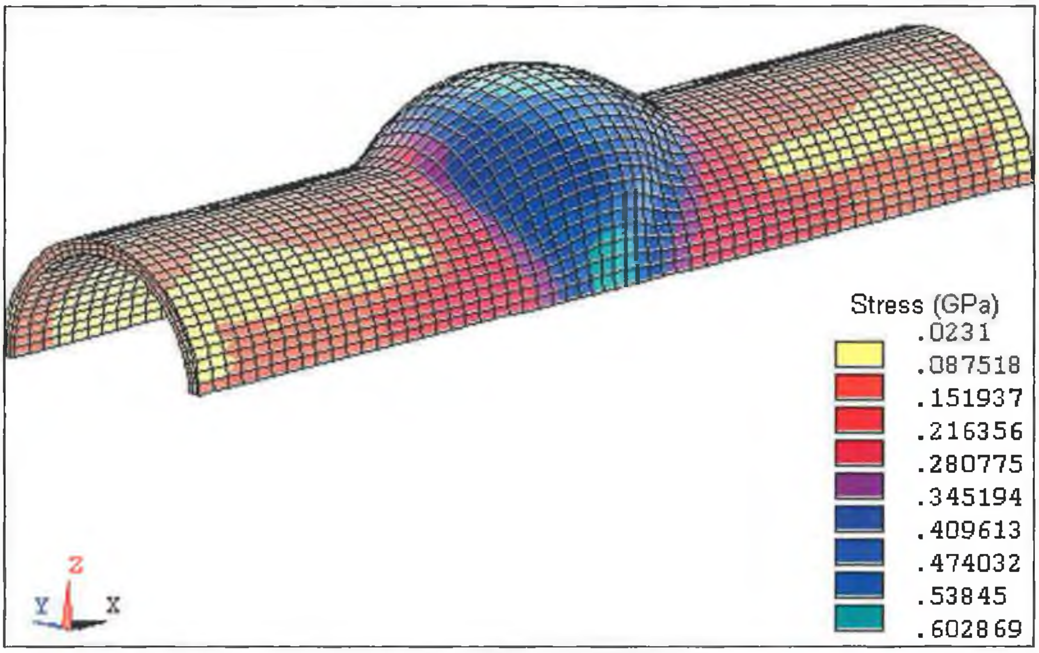

Figure 6.6. : Distribution of von-Mises Stress in the Deformed Bimetallic Tube

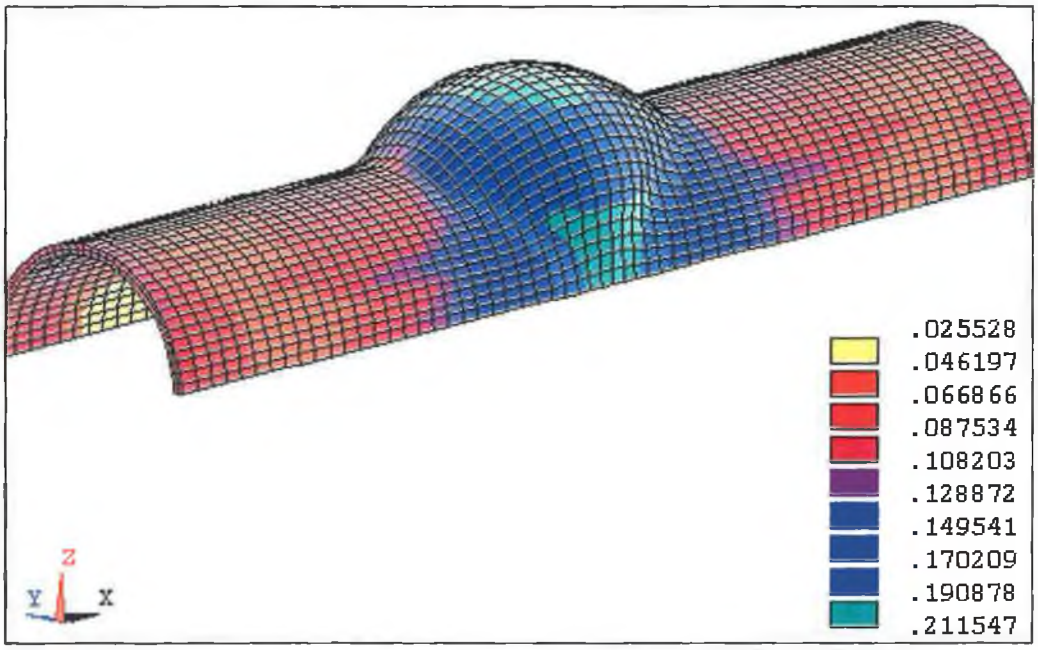

Figure 6.7. : Distribution of von-Mises Stress in the Deformed Inner Tube

Upon investigation it was noted that the maximum stress is located in the outer stainless steel tube and that the inner copper tube has not stressed considerably. In order to illustrate this point clearly figure 6.7. shows the distribution of von-Mises stress in the inner copper tube. It can be clearly seen that the outer tube has stressed a great deal more than the inner tube. The ratio of maximum stress of the outer tube to that of the inner tube was 1.56. This result was expected, given the material properties of both tubes, as illustrated in figure 6.1. and the strain levels predicted at maximum deformation.

Figures 6.8. and 6.9. show the development of principal stresses in the top central node of the inner and outer tubes respectively during the deformation process. It can be seen that in each case the development of stress was regular in accordance with the application of load. There is some slightly erratic behaviour early in the simulation which corresponds to the beginning of deformation and may also be influenced by friction between the outer tube and the die wall.

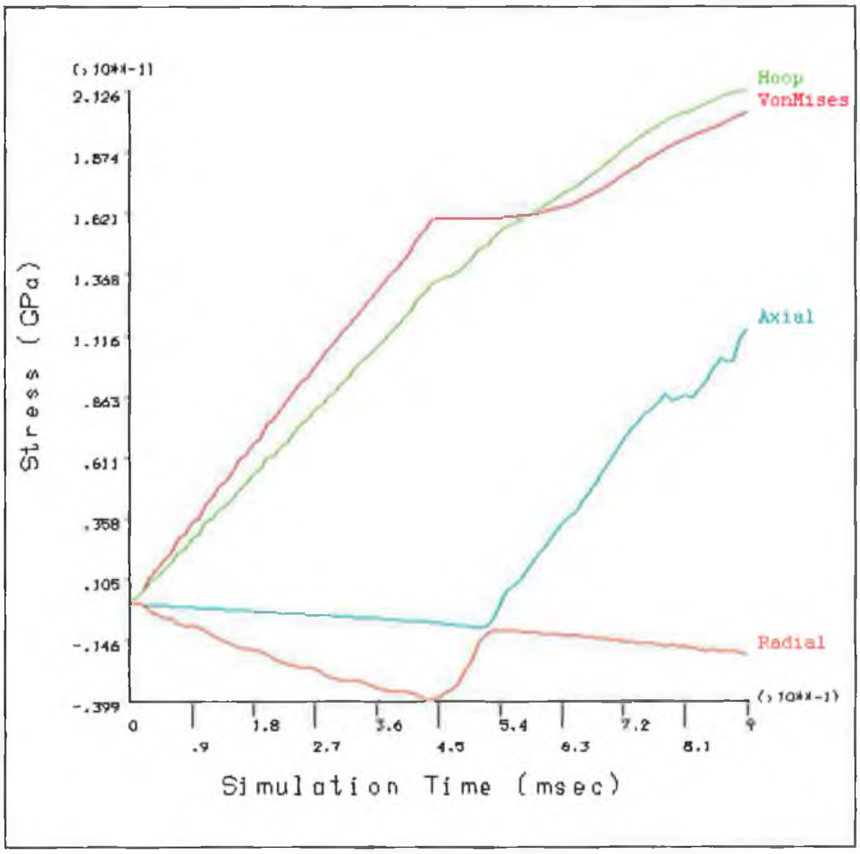

Figure 6.8. : Development of Stress in the Top Central Node of the Inner Tube

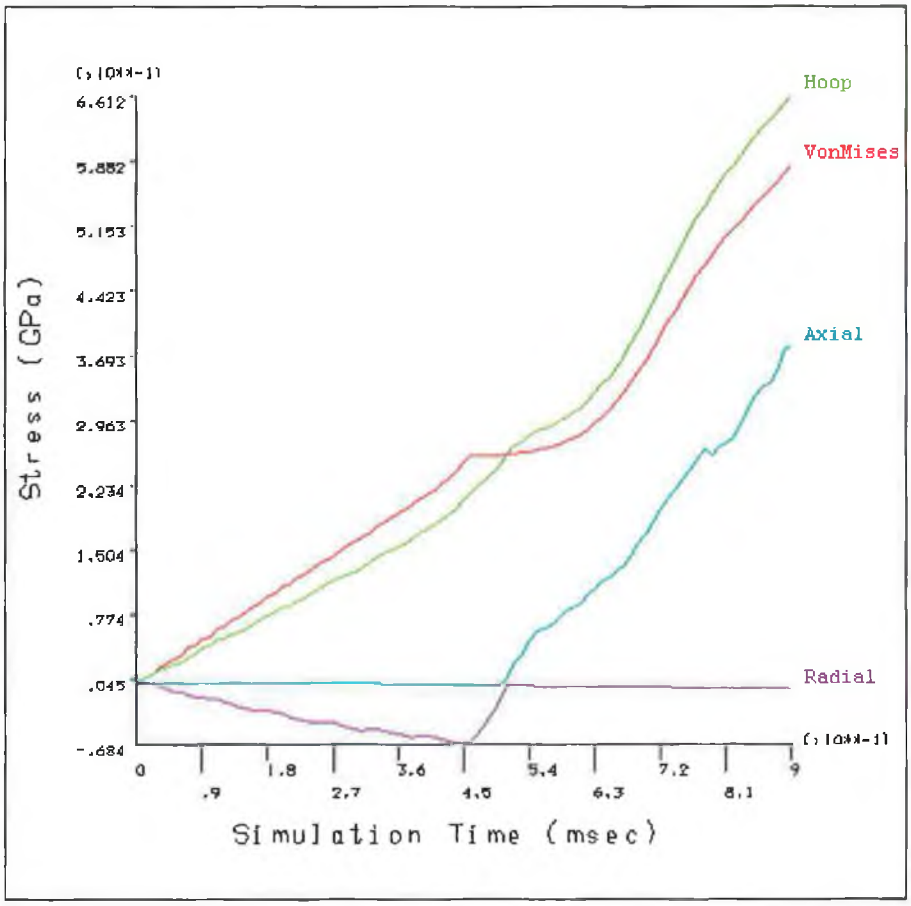

Figure 6.9. : Development of Stress in the Top Central Node of the Outer Tube.

6.4.2. Combined Internal Pressure and Axial Load

The second simulation utilised the loading pattern shown in figure 6.5 which combined pressure loading and compressive axial loading. Figure 6.10 shows the distribution of von Mises stress in the deformed tube at a simulation time of 5.7 milliseconds. After this point, stress levels began to rise sharply beyond the ultimate tensile strength of the material, leading to the failure of the outer tube. It can be seen that the maximum stress occurred at the outer tube under the branches, as indicated in figure 6.10. It was at this point the outer tube failed upon subsequent loading. Figure 6.11 shows the distribution of von Mises stress in the inner copper tube in the fully deformed state. It can be clearly seen, by comparing figures 6.10 and 6.11, that the outer tube has stressed to a much greater extent than the inner tube.

The maximum branch height at this time was 5 mm. This was 1.3 mm lower than that experienced in the previous simulation which utilised pressure load alone. This objective of using combined pressure and axial loading was to increase branch height, but the results indicate that combined loading results in earlier failure of the outer tube and hence lower possible branch heights.

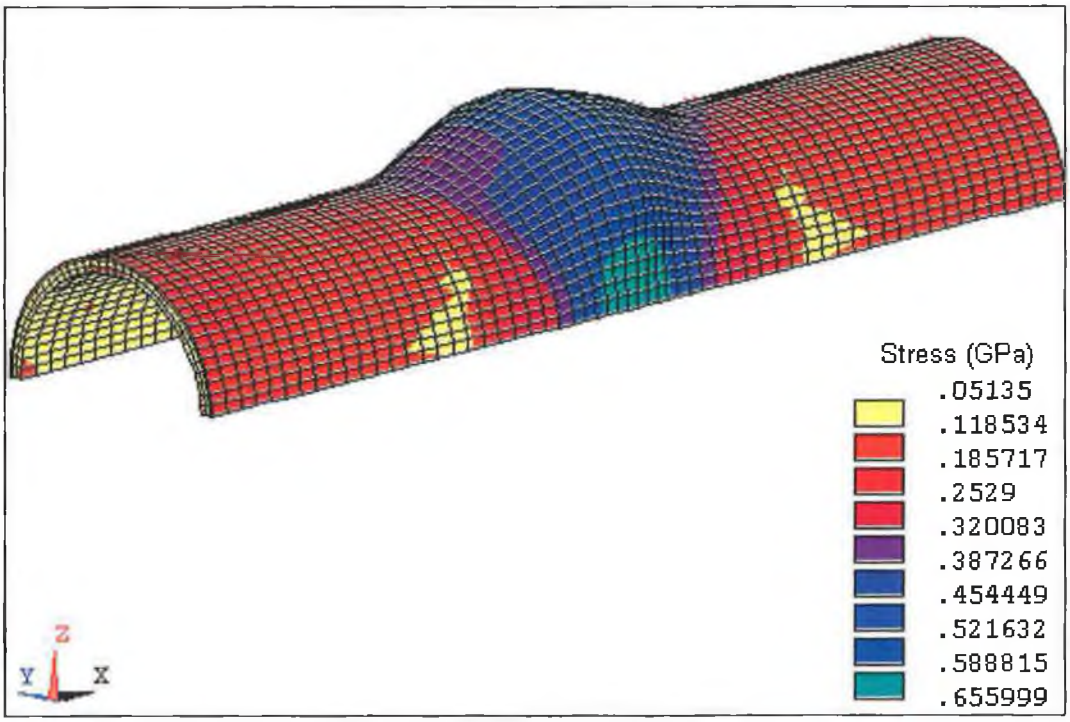

Figure 6.10 : Distribution of von-Mises Stress in the Deformed Bimetallic Tube with Combined Loading.

In order to investigate the failure mechanisms at work here figure 6.12 shows the development of stress in the central node of the highly stressed area of the outer tube, as indicated in figure 6.10. As mentioned earlier, after a simulation time of 5.7 milliseconds stress levels exceeded the ultimate strength of the material, so all results after this time were ignored. It can be seen from the figure that the stress state the causes the failure is a combined tensile hoop stress and highly compressive radial stress. It can be seen that the development of stress was regular in accordance with the application of load. There is some slightly erratic behaviour during the simulation which correspond to the beginning of deformation and may also be influenced by friction between the outer tube and the die wall.

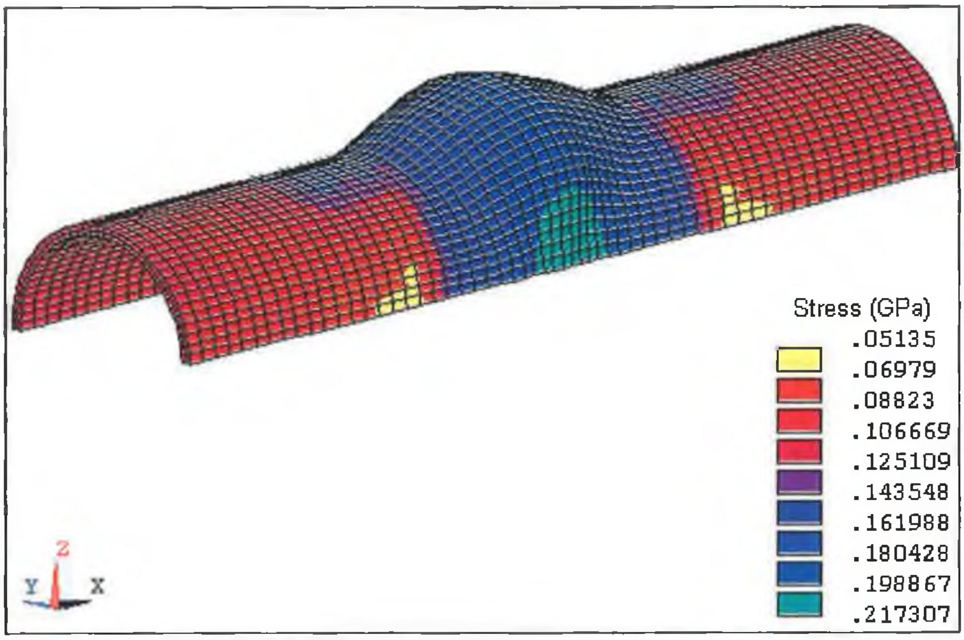

Figure 6.11. : Distribution of von-Mises Stress in the Deformed Inner Tube

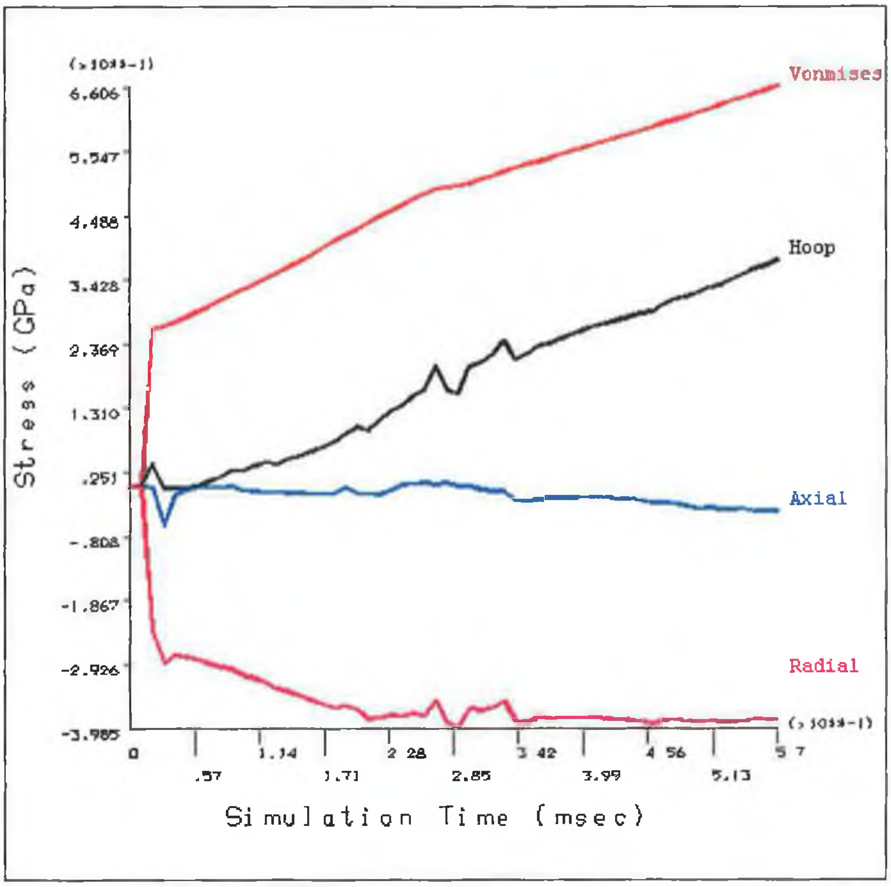

Figure 6.12. : Development of Stress in the Central Node of the Highly Stressed Area of the Outer Tube.

Figure 6.13. shows the development of strain in the central node of the highly stressed area. It can be seen from the figure that radial strain is highly compressive, indicating that the tube has thinned considerably at this point. Hoop strain is highly tensile and axial strain is slightly tensile. This indicates that the mode of failure appears to be due to excessive thinning of the outer tube due to combined tensile hoop and axial strain.

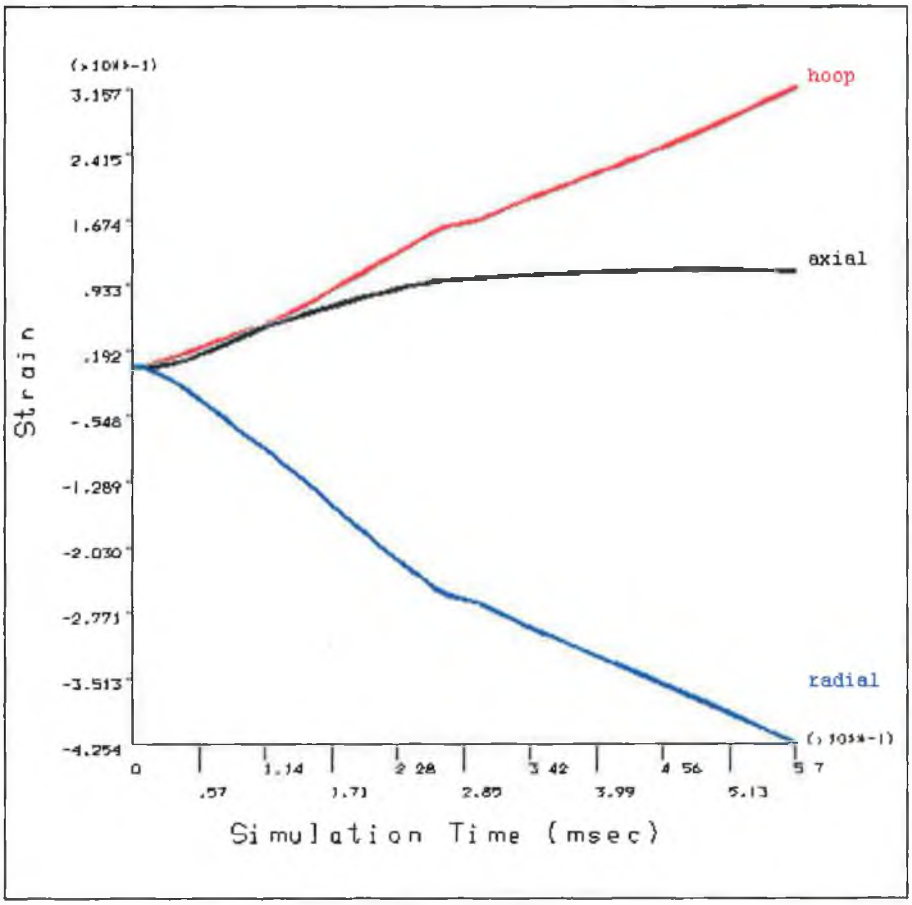

Figure 6.13. : Development of Principal Strains in the Central Node of the Highly Stressed Area.

This simulation did not continue to the point where the compressive axial load could have much effect on the process. If the simulation had continued and the axial load was allowed to develop, then it is possible that material could be pushed into this zone and thus reduce the thinning behaviour that resulted in failure. The thickness of the outer tube appears to be highly influential to the failure of bimetallic tubes in this manner. In order to investigate whether this is true, the following simulations investigate the effects increasing the thickness of the outer tube.

6.4.4. Outer Tube Thickness Increased to 0.65mm

In order to determine the effect of the relative thickness of the two tubes on the process, the outer tube thickness was increased to 0.65 mm. The overall tube thickness remained the same as in the previous simulations. The same material properties and loading conditions were used as in the previous simulation. Figure 6.14. shows the distribution of von-Mises stress in the deformed bimetallic tube at the point just before failure of the outer tube. The simulation time at this point was 8 milliseconds and the maximum branch height was 7mm. It can be seen from the figure that the branch top has taken on a slightly concave shape. This shape is unusual and appears to be unique to bimetallic tubes.

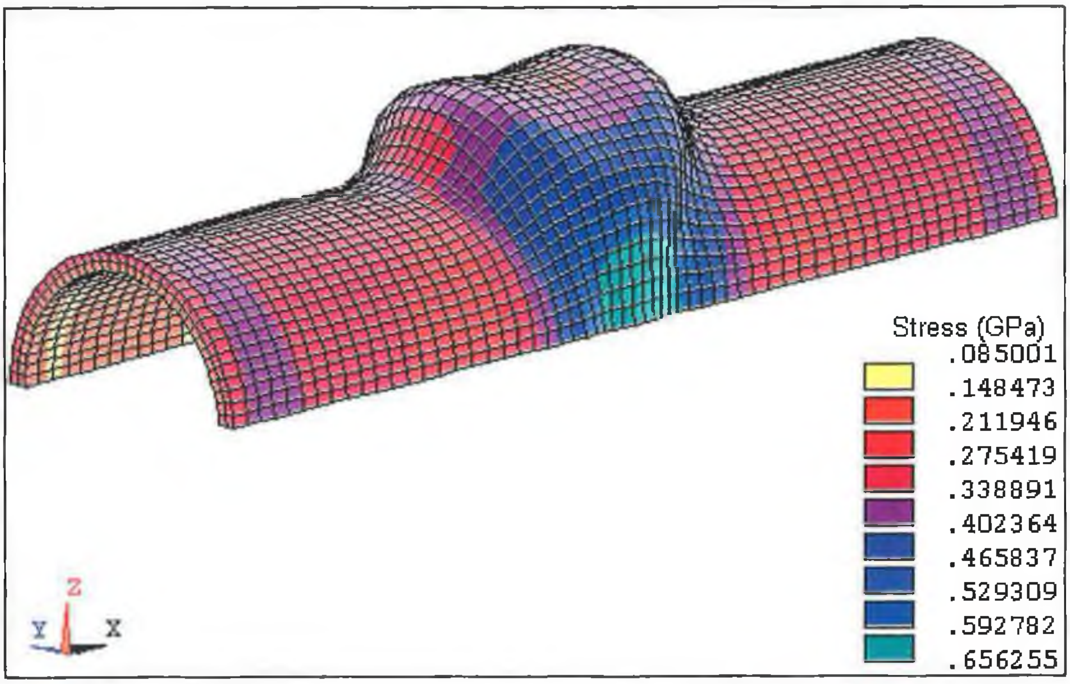

Figure 6.14. : Distribution of von-Mises Stress in the Deformed Bimetallic Tube with Increased Outer Tube Thickness.

Figure 6.15 shows the distribution of von-Mises stress in the inner tube in the fully deformed state. It can be seen that, as expected, the maximum stress in the inner tube is much less than that experienced in the outer tube.

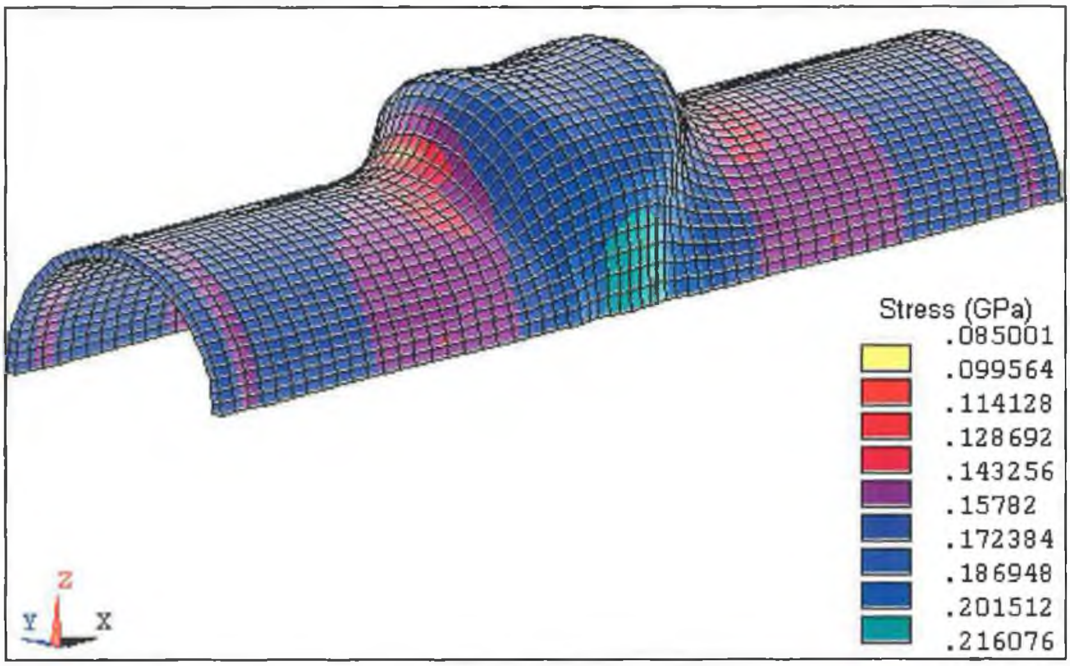

Figure 6.15. : Distribution of von-Mises Stress in the Deformed Inner Tube

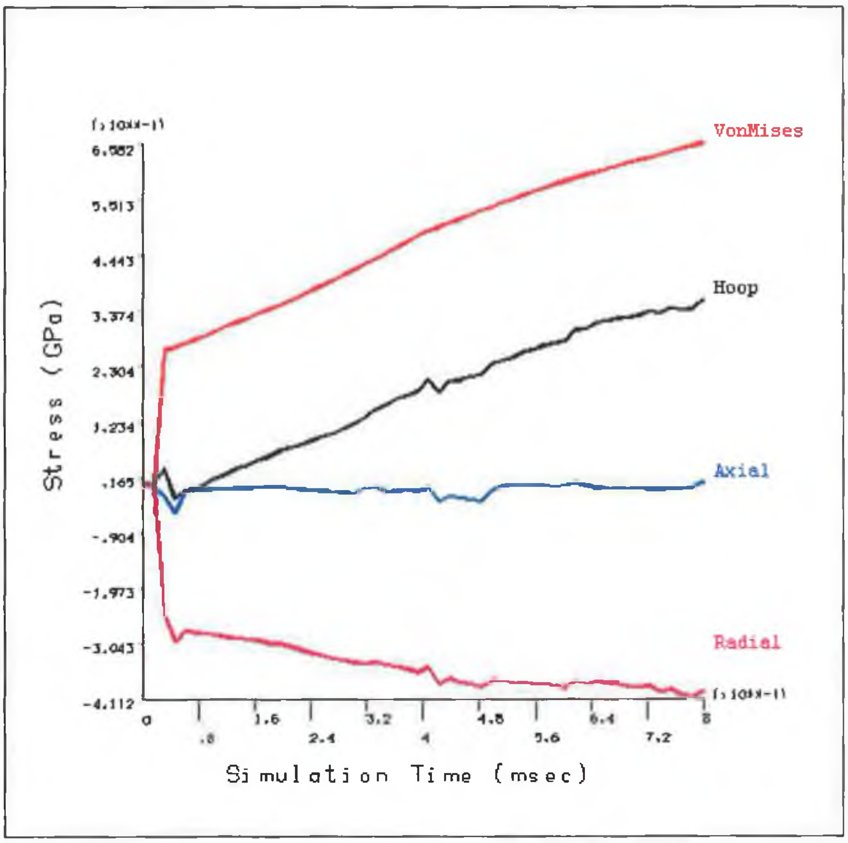

Figure 6.16. : Development of Stress in the Central Node of the Highly Stressed Area of the Outer Tube

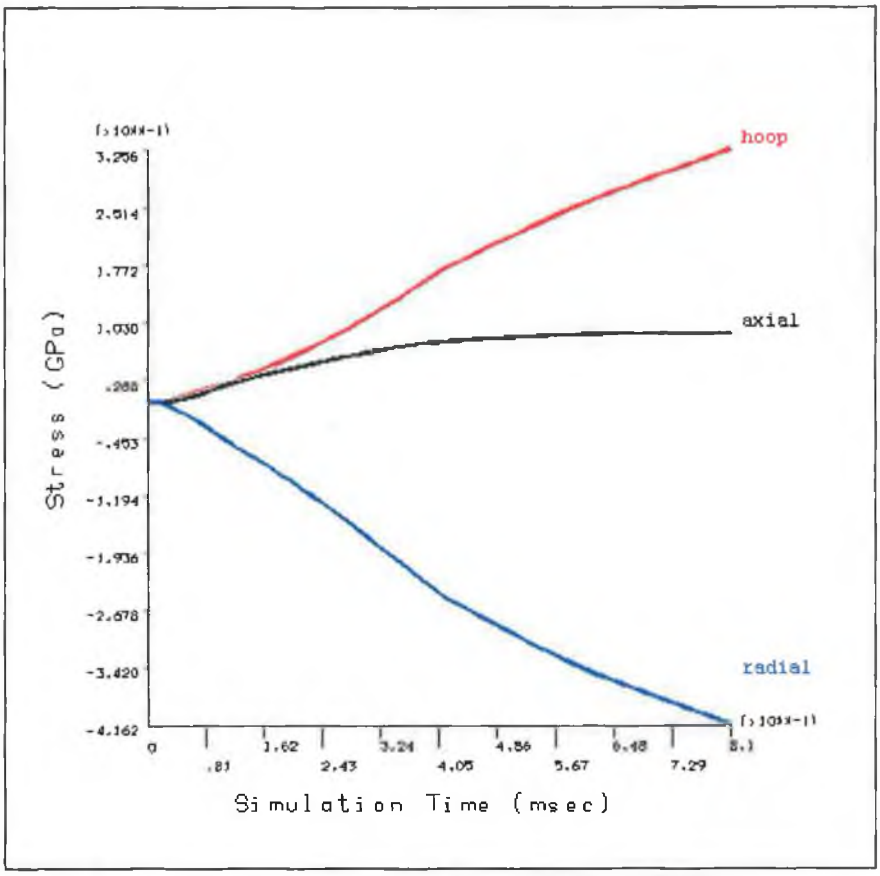

Figure 6.17. : Development of Principal Strains in the Central Node of the Highly Stressed Area.

In order to investigate the failure mechanisms at work here, figure 6.16 shows the development of stress in the central node of the highly stressed area of the outer tube, as indicated in figure 6.14. As mentioned earlier, after a simulation time of 8 milliseconds stress levels exceeded the ultimate strength of the material, so all results after this time were ignored. It can be seen from the figure that the stress state the causes the failure is a combined tensile hoop stress and highly compressive radial stress. Similar to the previous simulation it can be seen that the development of stress was regular in accordance with the application of load. There is some slightly erratic behaviour during the simulation which correspond to the beginning of deformation and may also be influenced by friction between the outer tube and the die wall.

The development of strain in the central node of the highly stressed area is shown in figure 6.17. It can be seen from the figure that radial strain is highly compressive, indicating that the tube has thinned considerably at this point. Hoop strain is highly tensile and axial strain is slightly tensile. This indicates that the mode of failure appears to be due to excessive thinning of the outer tube due to combined tensile hoop and axial strain. In such a case the inner tube would be exposed and the component would be of no use. It appears that the axial load has little effect on reducing the thinning behaviour of the outer tube. The contact algorithm used between the inner and outer tube effectively bonded the two tubes to each other. This meant that the compressive axial load was unable to move material into the thinning area of the outer tube without moving material into the bulging region of the inner tube. Making more material available for expansion of the inner tube increased the resultant pressure on the outer tube and effectively increased the thinning behaviour.

It was thought that a different loading pattern may produce a better shaped component. In order to investigate whether this was true a further simulation was run where the internal pressure was increased from 12MPa to 18MPa. The distribution of von-Mises stress in the resultant component just before failure of the outer tube is shown in figure 6.18.

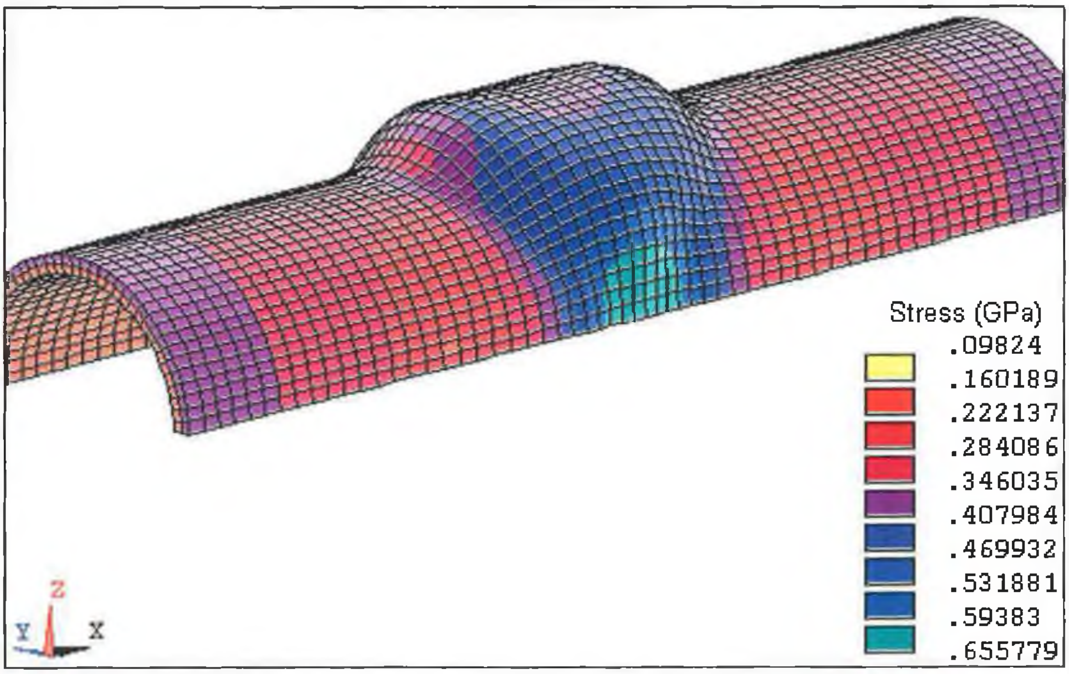

Figure 6.18. : Distribution of von-Mises Stress in the Deformed Tube with Increased Pressure Load.

It can be seen from the figure that the use of an increased pressure load produced a far more regularly shaped component with a flat branch top. The branch height however was significantly reduced from 8mm to 4.5mm as a result of the increased pressure load.

6.4.4. Outer Tube Thickness Increased to 1mm

In order to examine if increasing the thickness of the outer tube further would have any beneficial effects on the process, a further simulation was run where the thickness of the outer layer was increased to 1mm and the thickness of the inner tube reduced to 0.3mm.

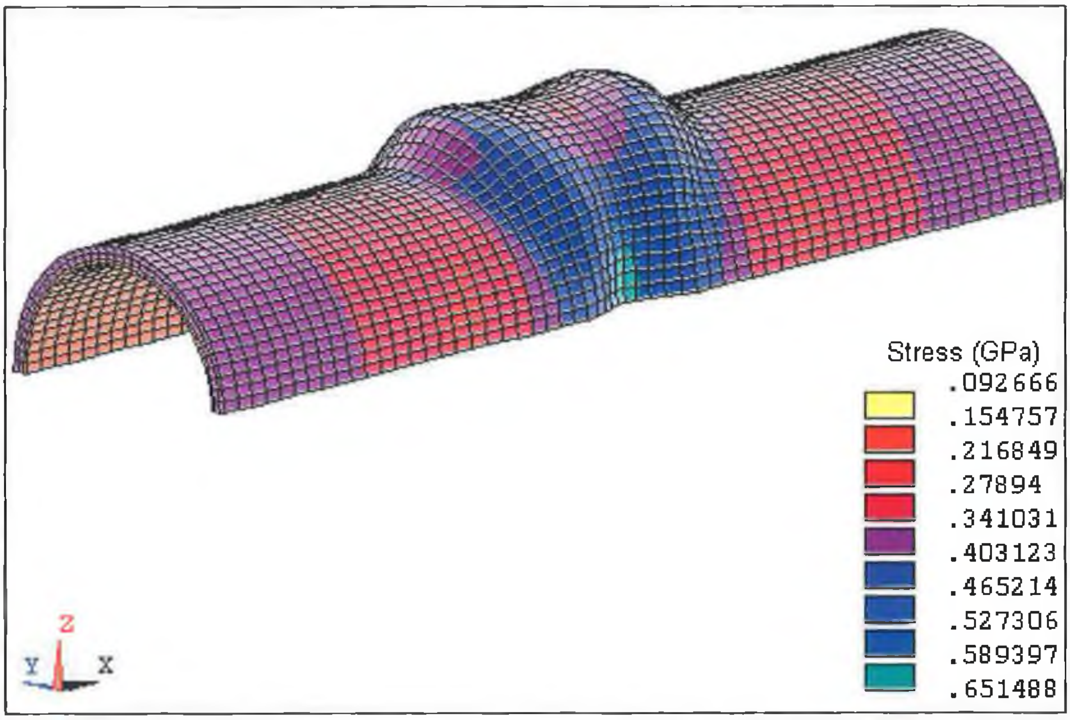

Figure 6.19. : Distribution of von-Mises Stress in the Deformed Bimetallic Tube with Outer Tube Thickness Set to 1mm.

It was found that rather than improving the height or shape of the resultant product that increasing the thickness of the outer layer actually resulted in a defective component. The distribution of von-Mises stress in the deformed tube at the final acceptable result is shown in figure 6.19. The simulation time at this point was 5 milliseconds and the maximum branch height was 4 mm. After this point stress values exceeded the ultimate strength of the material and consequently all results were ignored. It can be seen from the figure that the component has buckled. Buckling defects in components formed by bulge forming are usually the result of compressive axial load being too high relative to internal pressure. In this case the loading conditions used were the same as in the previous two simulations where thinner outer stainless steel tubes were used. Obviously, in this simulation, the thick outer steel tube makes up most of the bimetallic tube volume, so it is important that enough internal pressure is provided to ensure that the outer tube bulges satisfactorily. In this case enough pressure was supplied to bulge a copper tube but not a thick steel tube. This resulted in a dominance of axial load which resulted in the buckling defect.

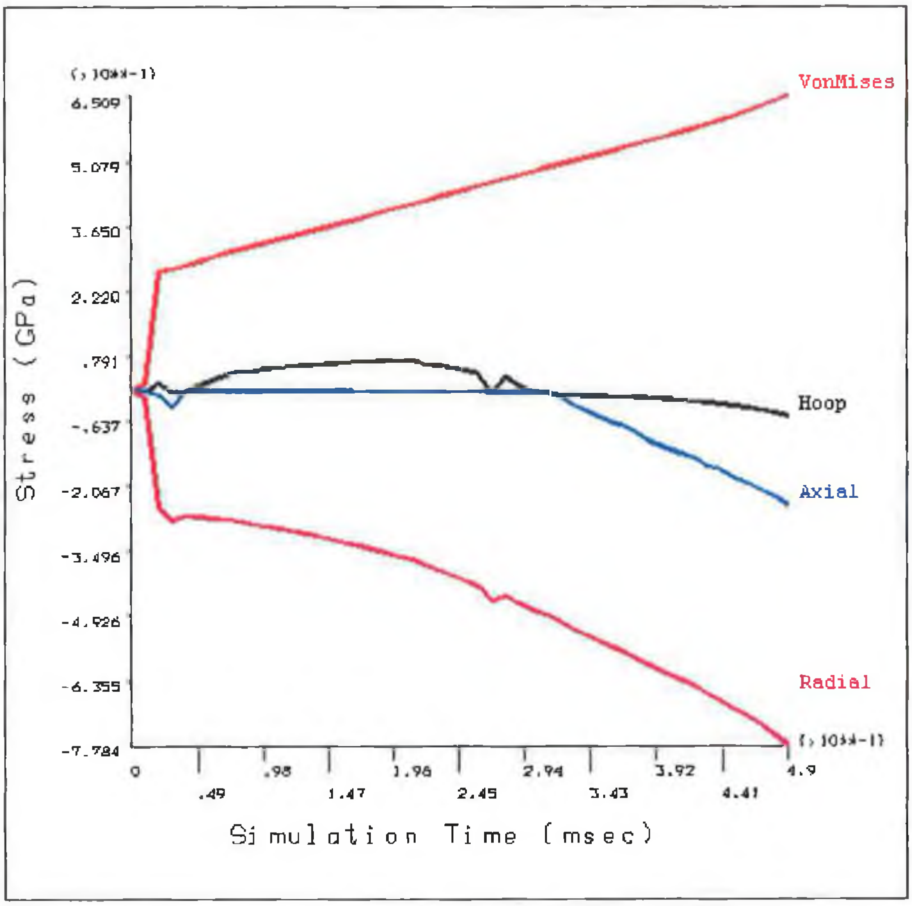

Figure 6.20. : Development of Stress in the Central Node of the Highly Stressed Region

In order to investigate the failure mechanisms at work here, figure 6.20 shows the development of stress in the central node of the highly stressed area of the outer tube, as indicated in figure 6.19. As mentioned earlier, after a simulation time of 5 milliseconds stress levels exceeded the ultimate strength of the material, so all results after this time were ignored. It can be seen from the figure that the development of stress is markedly different to what was experienced in the previous simulations. Hoop stress is only slightly tensile for most of the simulation and becomes compressive as the buckle begins to form. Axial stress is much more prevalent than in previous simulations, being compressive for most of the simulation and becoming significantly compressive as the buckle defect develops. Radial stress is much more compressive than in the previous simulations. This is due to the buckle forming in towards the centre of the tube and the internal pressure attempting to push the material back out. In the previous simulations the radial stress was relived by the bulge forming, in this case however, the bulge never forms significantly so the radial stress continues to grow rather than reduce or plateau.

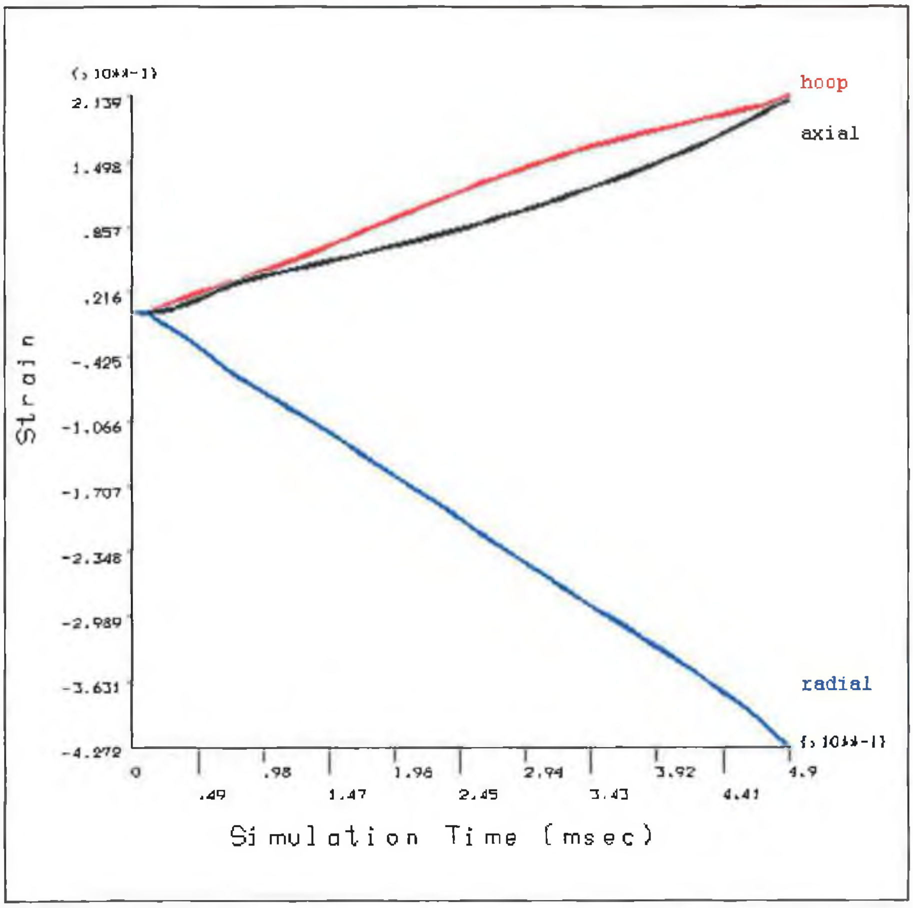

Figure 6.21. : Development of Principal Strains in the Central Node of the Highly Stressed Area

The development of strain in the central node of the highly stressed area is shown in figure 6.21. It can be seen from the figure that radial strain is highly compressive, indicating that the tube has thinned considerably at this point. Hoop strain and axial strain are both moderately tensile indicating that the elements at in this area have been pulled in both the axial and hoop direction.

As in the previous simulation, it was thought that an increased pressure load may have resulted in a defect free component. In order to investigate this the simulation was rerun with the pressure load increased from 12 MPa to 24 MPa. The distribution of von-Mises stress in the resultant component just before failure of the outer tube is shown in figure 6.xx.

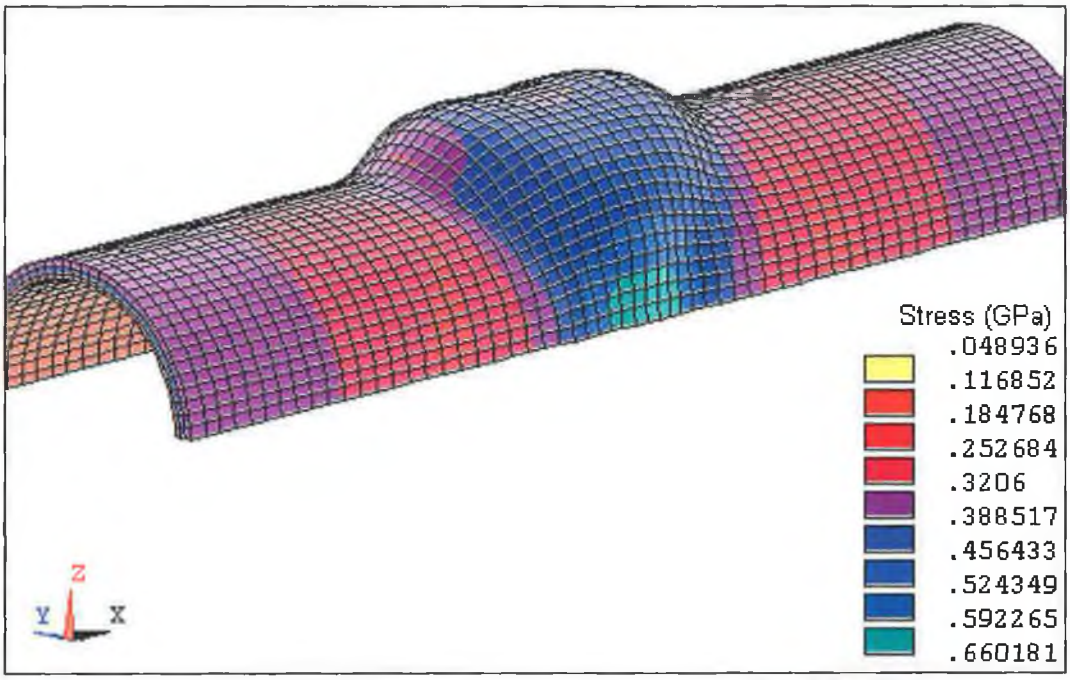

Figure 6.22. : Distribution of von-Mises Stress in the Deformed Tube with Increased Pressure Load.

It can be seen from the figure that the use of an increased pressure load produced a far more regularly shaped component with a flat branch top. The branch height was unaffected by the increased pressure and remained at 4mm.

6.4.5. <u>The Effect of Changing the Relative Strength of the Tubes</u>

A further simulation was run to investigate the effect on the process of varying the relative strength of the tubes. In order to accomplish this the same finite element model was used as in the seconds simulation (outer tube thickness = 0.3mm) but the material properties of the outer tube were changed. The Young's Modulus and Tangent Modulus as before were used, but the yield stress was reduced to be closer to that of the inner copper tube. Figure 6.23. illustrates the stress strain curve for the new outer tube material.

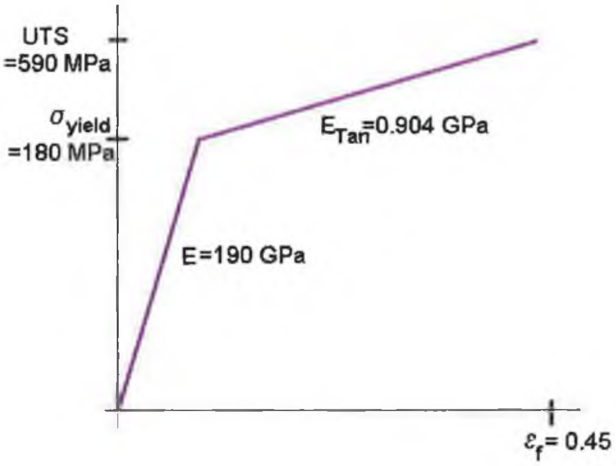

Figure 6.23. : New Material Properties of Outer Tube

Figure 6.24. shows the distribution of von-Mises stress in the deformed tube at the point just before the ultimate tensile stress in the outer tube was exceeded. The branch height at this point was 6mm. This was 1mm higher than the height obtained in the second simulation which use the same model and loading conditions, but the increased strength outer tube. This indicates that using two materials of similar yield stress in the bimetallic tube results in higher branch heights.

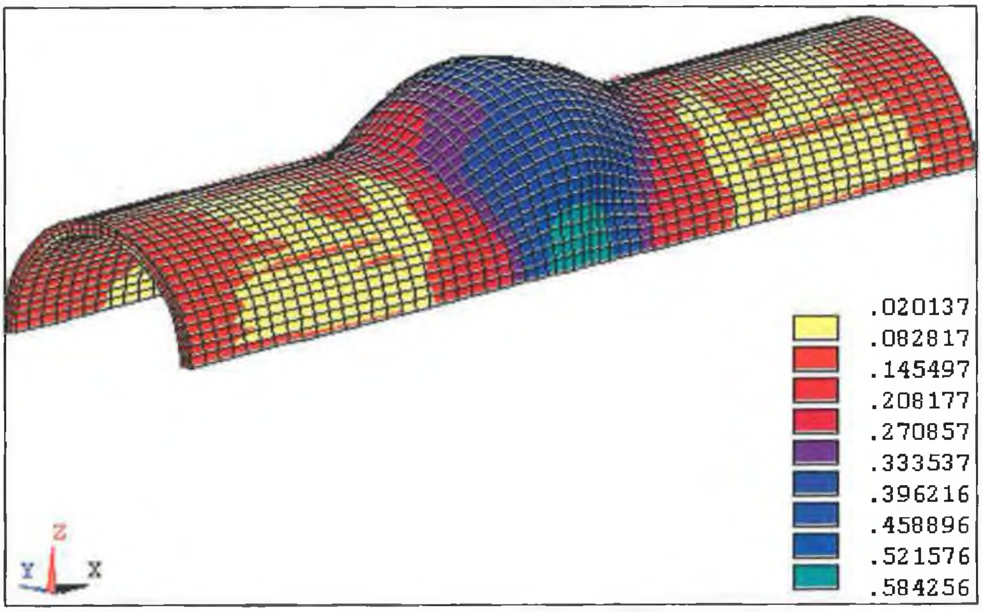

Figure 6.24. : Distribution of von-Mises Stress in the Deformed Bimetallic Tube

The location of maximum stress is in the region expected and corresponds with previous simulations. When we compare the above figure with figure 6.10 which shows the distribution of stress in the deformed tube in the second simulation we can see that the distribution of stress in this case is much less regular. In the previous simulation the main tube has a very regular stress distribution. In this case the stress distribution in the main tube is very erratic and appears to be a consequence of the earlier yielding of the outer tube. The stress distribution in the fully deformed inner tube is show in figure 6.25. The stress distribution here is much more regular than in the outer tube. There is no significant difference between the distribution here and that experienced in the previous simulation, as illustrated in figure 6.11.

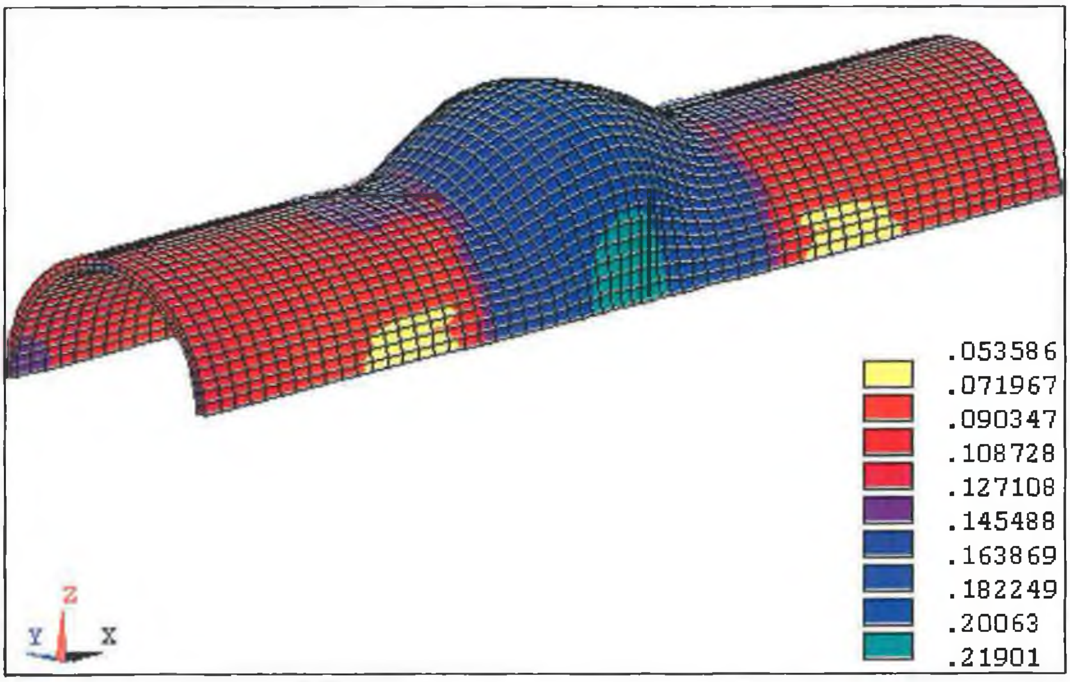

Figure 6.25. : Distribution of von-Mises Stress in the Deformed Inner Tube

Figure 6.26 shows the development of stress in the highly stressed area of the outer tube where failure eventually occurred. After a simulation time of 5.7 milliseconds stress levels exceeded the ultimate strength of the material, so all results after this time were ignored. It can be seen from the figure that the stress state the causes the failure is a combined tensile hoop stress and highly compressive radial stress. It can be seen that the development of stress was regular in accordance with the application of load.

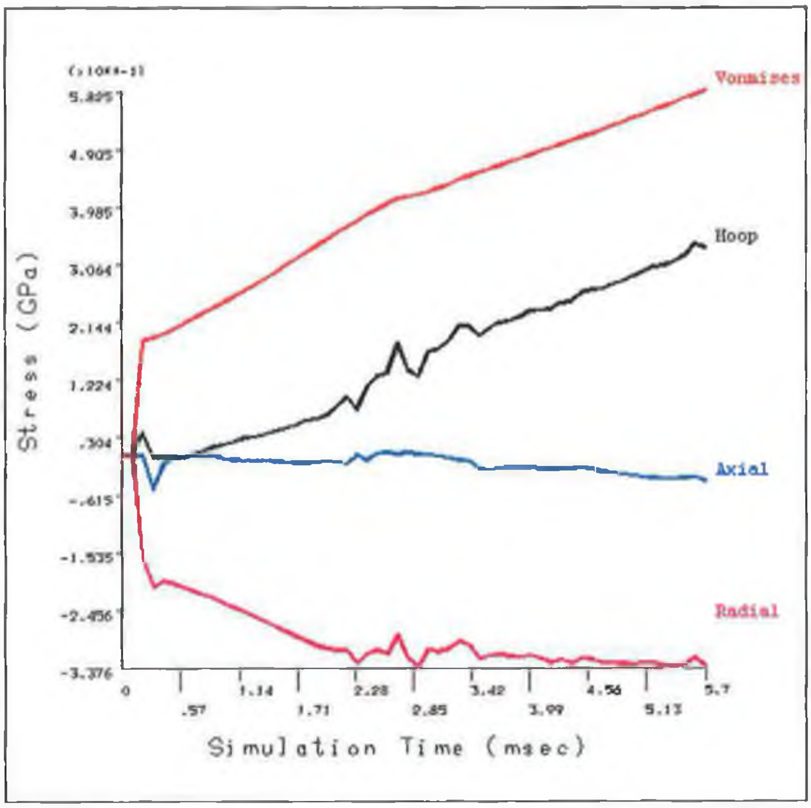

Figure 6.26. : Development of Stress in the Central Node of the Highly Stressed Area

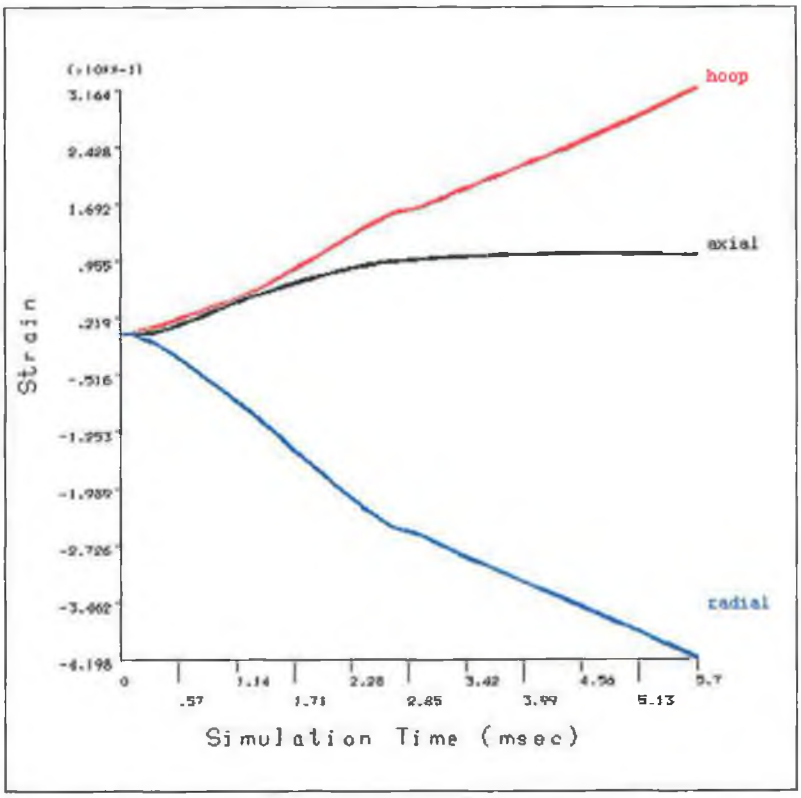

Figure 6.27. : Development of Strain in the Central Node of the Highly Stressed Area

There is some slightly erratic behaviour during the simulation which correspond to the beginning of deformation and may also be influenced by friction between the outer tube and the die wall. The development of stress here is very similar to that obtained in simulation two and as indicated in figure 6.12.

Figure 6.27. shows the development of strain in the central node of the highly stressed area of the outer tube. It can be seen from the figure that radial strain is highly compressive, indicating that the tube has thinned considerably at this point. Hoop strain is highly tensile and axial strain is slightly tensile. This indicates that the mode of failure appears to be due to excessive thinning of the outer tube due to combined tensile hoop and axial strain. As with previous simulations, the simulation did not continue to the point where the compressive axial load could have much effect on the process. As explained previously this is thought to be an effect of the contact conditions between the two tubes.

6.5. Summary

This chapter presents the results from the simulation of bulge forming of cross branches from bimetallic tubes. The effect of different loading conditions, changing the relative thickness of the two tubes and changing the relative strength of the tubes was investigated and the results analysed. The results are summarised in the figures below.

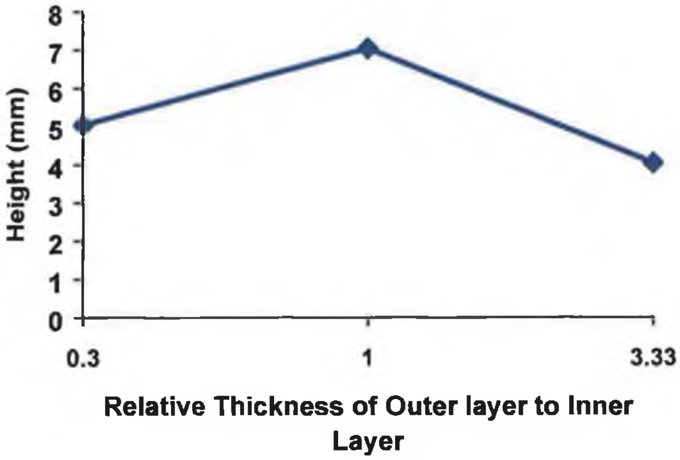

Figure 6.28. : The effect of varying the relative thickness of the bimetallic layers on bulge height.

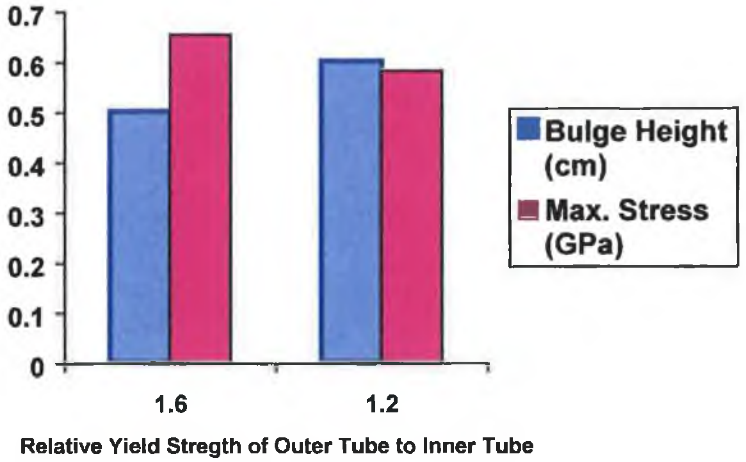

Figure 6.28. : The Effect of Varying the Relative Strength of the Tubes

Chapter 7 : The Behaviour of the Die During Bulge Forming Operations

7.1 Introduction

This chapter details the modelling procedures and the results from three dimensional finite element simulations of bulge forming with particular emphasis on the state of stress and strain in the die during the forming process. By analyzing the stress distributions in the die some important considerations for optimizing the design of the die are outlined.

7.2. Hydraulic Cross Branch Forming

7.2.1. Modelling

In order to properly represent the die it was necessary to build a more extensive model than was used in the analysis of hydraulic cross branch forming detailed in chapter 3. In that analysis the die was modeled as a rigid body so all that was necessary to model was the portion which would be in contact with the tube. In this analysis we are interested in the stress and strain distribution over the entire die and we wish to constrain the die exactly as it would be in the actual situation. The die was modelled to be consistent with that used by Hutchinson [30]. The inner die geometry and tube geometry were the same as those used in chapter three. Figure 7.1. shows the finite element model used to analyse the die behaviour. The tube is modelled as detailed in chapter four using eight node brick elements. Because of the complex geometry of the die it was necessary to use tetrahedral elements to properly model the geometry. Generally speaking tetrahedral elements are not recommended for use with the LS-DYNA solver, however, in order to check the accuracy of the results a number of analysis were run with this model in order to compare results with the analysis in chapter three. The same loading conditions were used as in chapter four and the same tube deformations and stresses were obtained. It was thus concluded that the use of tetrahedral elements would give reasonably accurate results in this case.

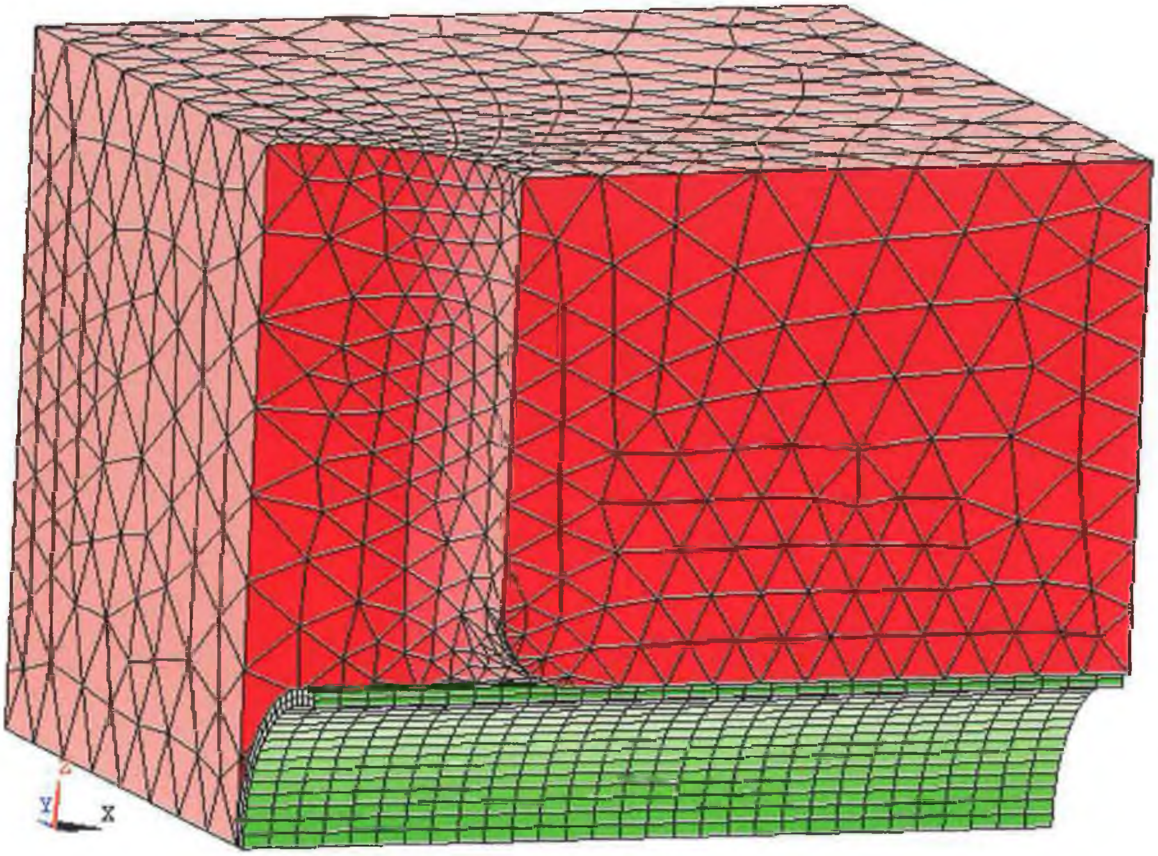

Figure 5.1. : Finite Element Model Used for the Die Analysis

In the previous analysis as detailed in chapter four the die was modelled as a rigid body and thus no stresses or strains were calculated for the die. In this case a linear elastic material model was used for the die. The die was assigned the material properties of steel EN21, again to be consistent with that used by Hutchinson [30]. The tube was assigned an elasto-plastic material model for annealed copper as detailed in chapter three.

7.2.2 Boundary Conditions, Loading and Solution

By taking advantage of symmetry it was possible to model one eighth of the entire die-tube assembly and still obtain a proper three dimensional solution. As a result of this the die and tube were constrained in the appropriate directions with symmetry boundary conditions. The die was further constrained to model the die clamping force that would be present in the process : this corresponded to constraining all nodes on the front and back faces of the die (as viewed from figure 7.1).

In order to allow a direct comparison with the results obtained in chapter four the same loading conditions and patterns were used as detailed in chapter three. The pressure load was applied as a surface load on the inner tube surface and the axial load was applied as a prescribed displacement of the nodes at the edge of the tube end. The first simulation of the forming process was carried out using pressure loading only. The loading pattern for the first simulation is shown in figure 7.2. The second simulation utilised pressure load and axial displacement as shown in figure 7.3.

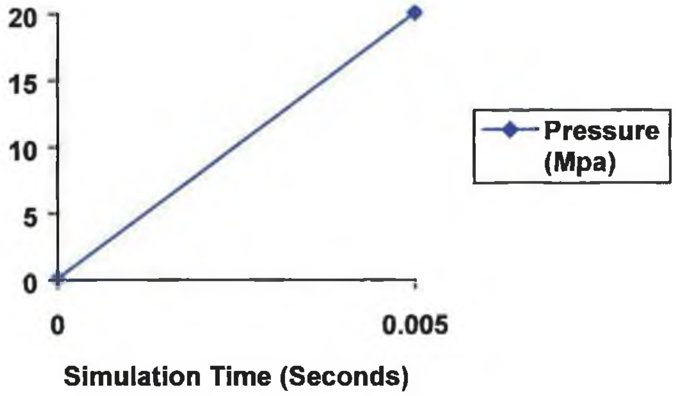

Figure 7.2. : Loading Pattern 1

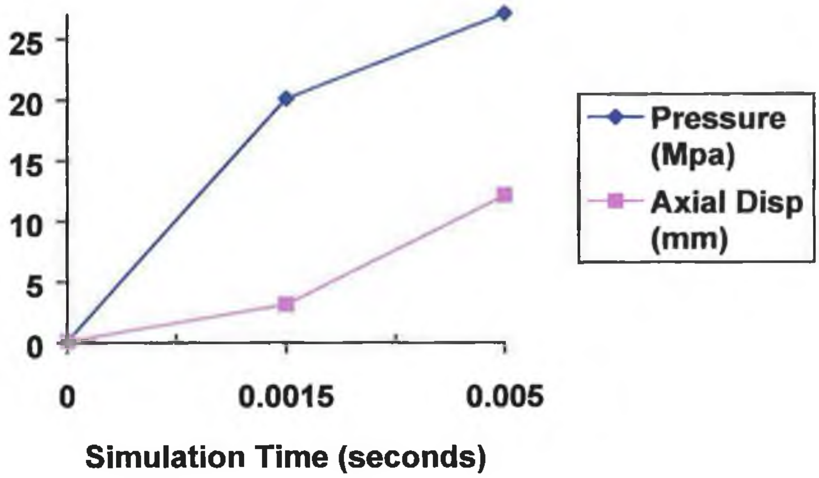

Figure 7.3. : Loading Pattern 2

7.2.3. Simulation Results and Analysis

7.2.3.1. Pressure Load Only

The first simulation was run with pressure load only applied to the tube according to loading patter one. At full load the branch height was 4mm and the maximum stress in the tube was 205 MPa at the branch top. This corresponded directly with the result obtained in chapter four, in which a rigid body model was used for the die. In order to examine the development of stress in the die during the process, figures 7.4. to 7.7 show the distribution of von-Mises stress in the die at 25%, 50%, 75% and 100% of full load. Using the symmetry expansion capability of the ANSYS post processor, the results are shown for one half of the die assembly.

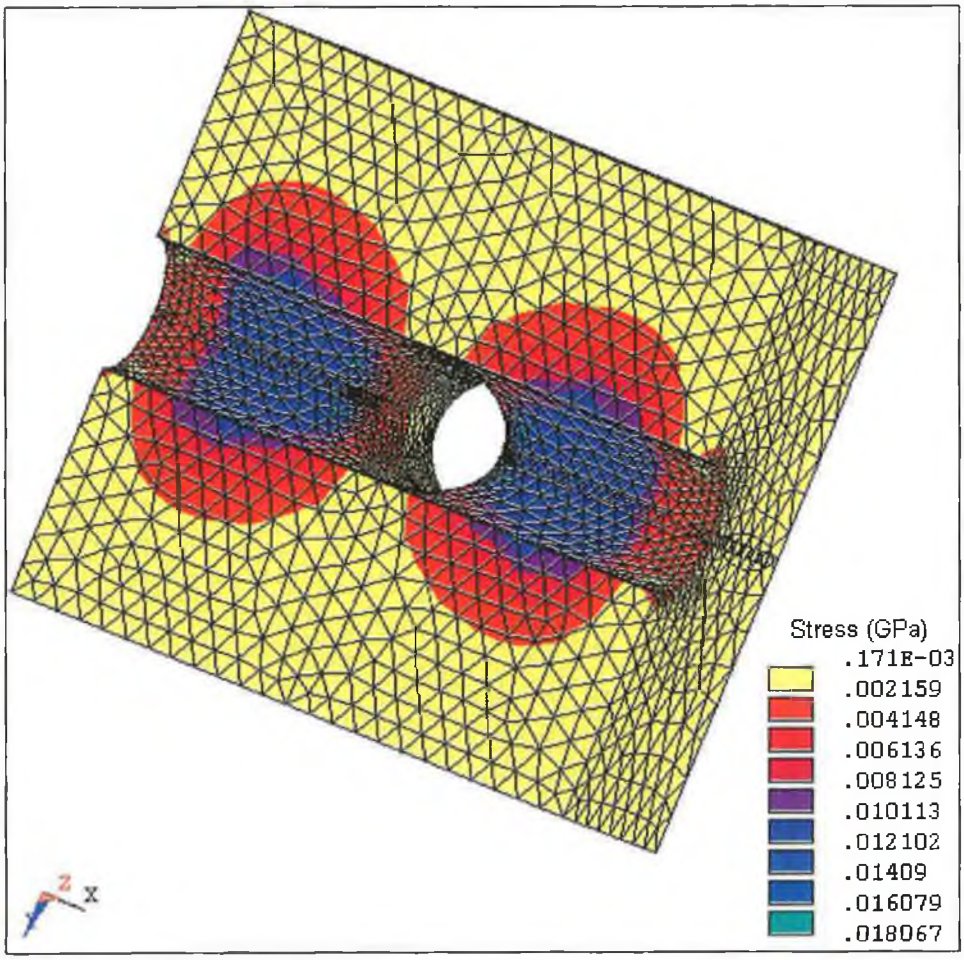

Figure 7.4. : Distribution of von-Mises Stress in the Die at 25% of Full Load

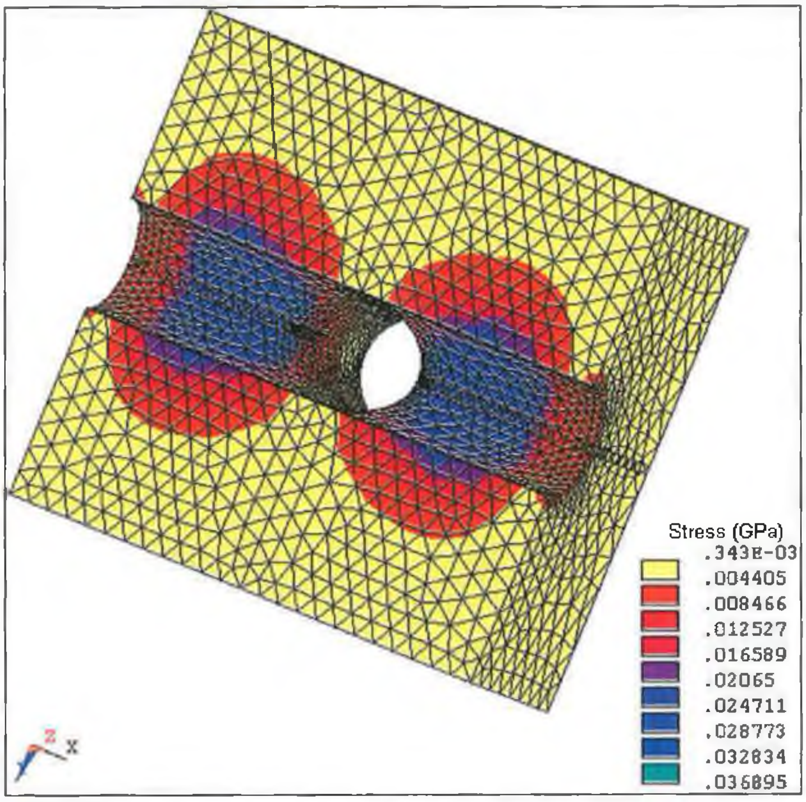

Figure 7.5. : Distribution of von-Mises Stress in the Die at 50% of Full Load

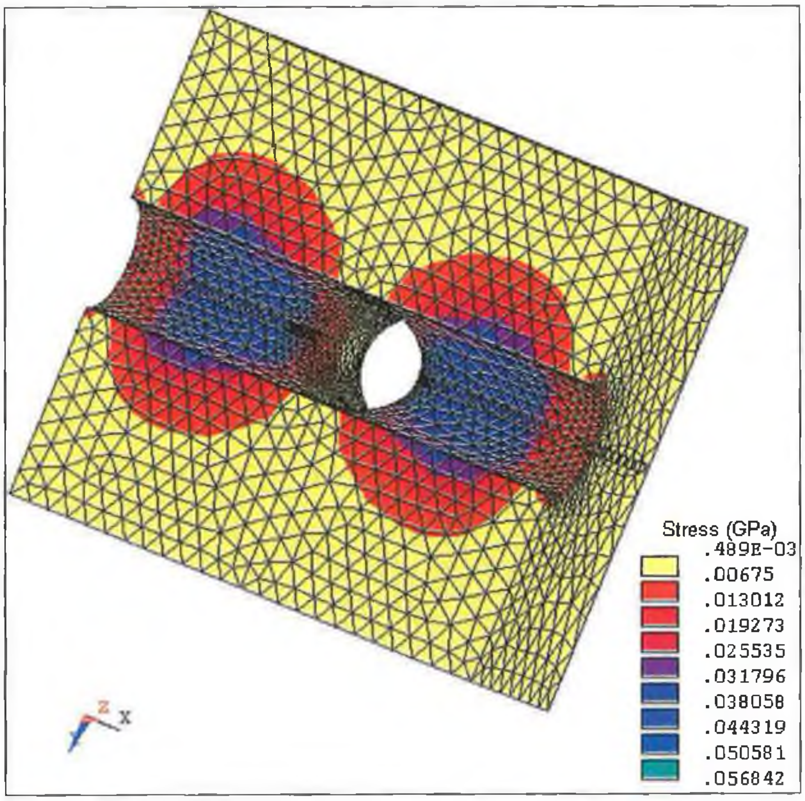

Figure 7.6. : Distribution of von-Mises Stress in the Die at 75% of Full Load

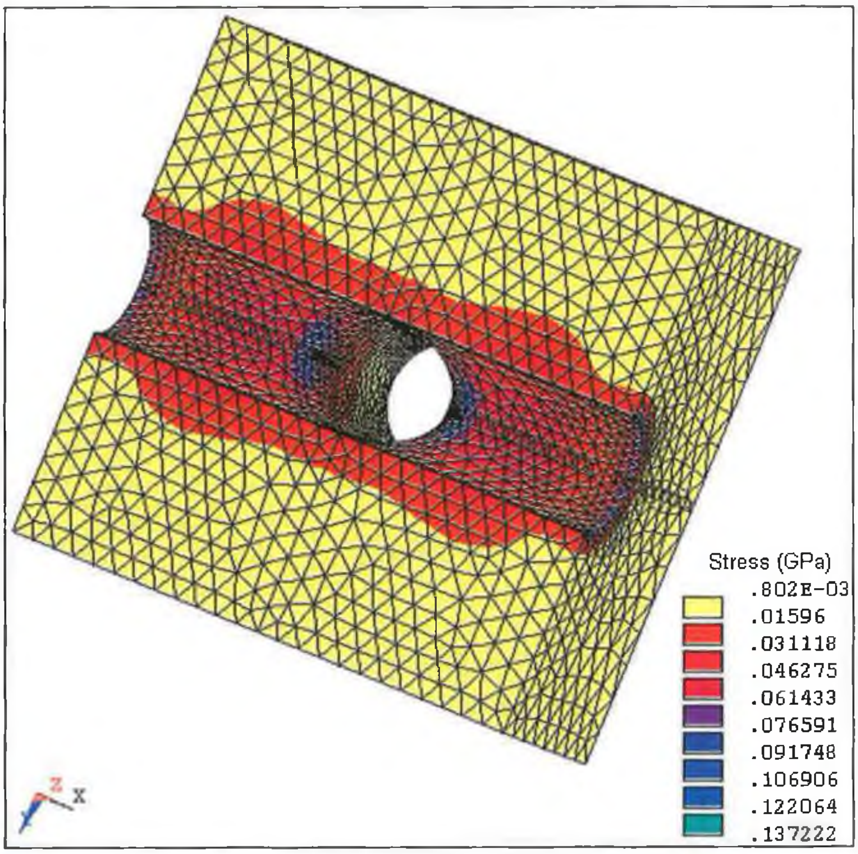

Figure 7.7 : Distribution of von-Mises Stress in the Die at 100% of Full Load

It can be seen from figure 7.4. that the application of internal pressure to the tube immediately forces it against the die wall, with the maximum amount of stress being experienced by the die in the main die body where there is maximum contact between the die and the tube. It can be seen from figures 7.5. and 7.6. that stress develops in a regular fashion in this region as the internal pressure on the die increases. Once the tube yields and the bulge begins to form, just after the application of 75% of full load, the stress state changes. The maximum stress is now located at the die bend as the tube tries to move into the die recess, as indicated in figure 7.7. In order to provide a clearer view of the state of stress in the die at full load figure 7.8 shows the distribution of stress for one eighth of the die. It can be clearly seen from the figure that the maximum stress experienced by the die is at the two extremities of the die blend radius. There is also a region of high stress at the edge of the die near the tube end. This is due to the internal pressure still pushing the tube against the die at this point. Nearer the die bend the pressure of the tube on the die is reduced due to material being pulled into the bulging zone by the formation of the bulge.

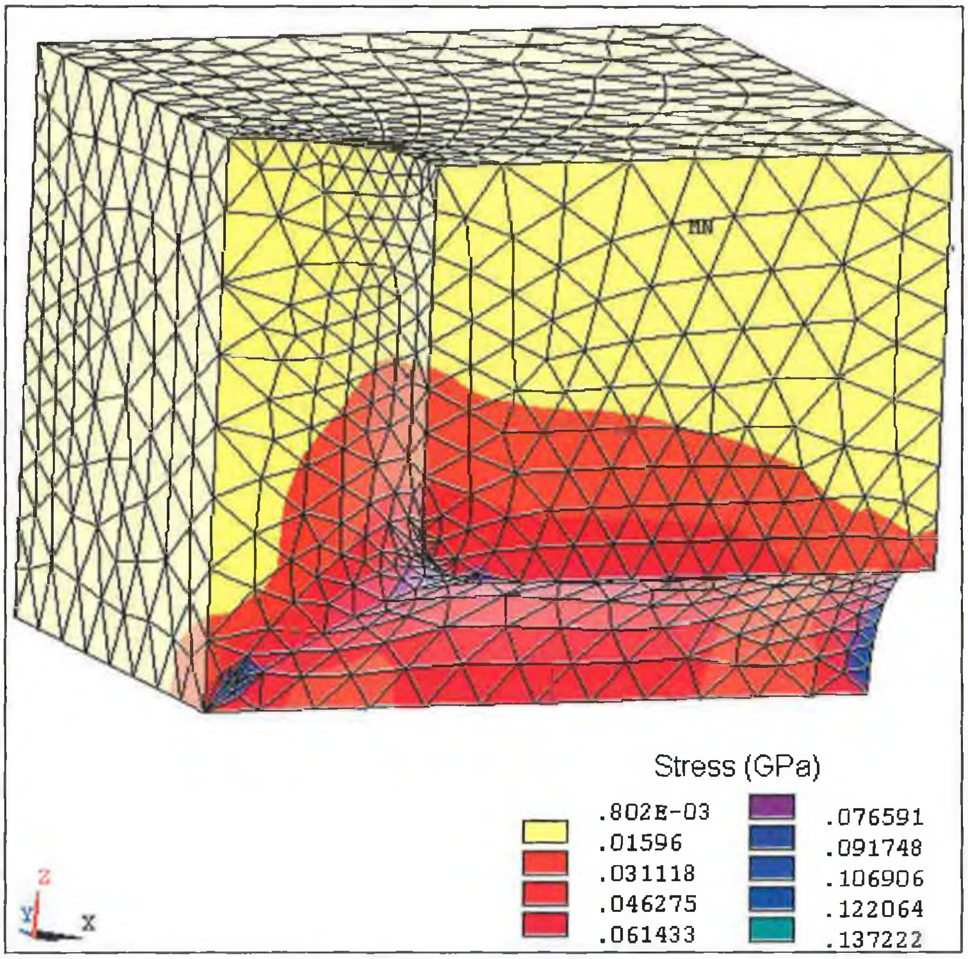

Figure 7.8. : Distribution of von-Mises Stress in the Die at Full Load

It can be seen from figure 7.8 that the maximum stress experienced by the die is 137 MPa. This is well below the yield point for steel EN21 so no permanent deformation of the die would be expected due to this loading. In order to investigate the deformation of the die during the process figure 7.9 shows the distribution of equivalent strain at full load. It can be seen from the figure that the maximum strain occurs at the region of greatest stress. In order to get a better insight into the deformation of the die, figure 7.10. shows the amount of elastic deformation of the die in millimeters. It can be seen that the maximum deformation is 0.004425 mm which is not significant and thus it can be concluded that there will be no significant deformation of the die during the process when this type of loading is used.

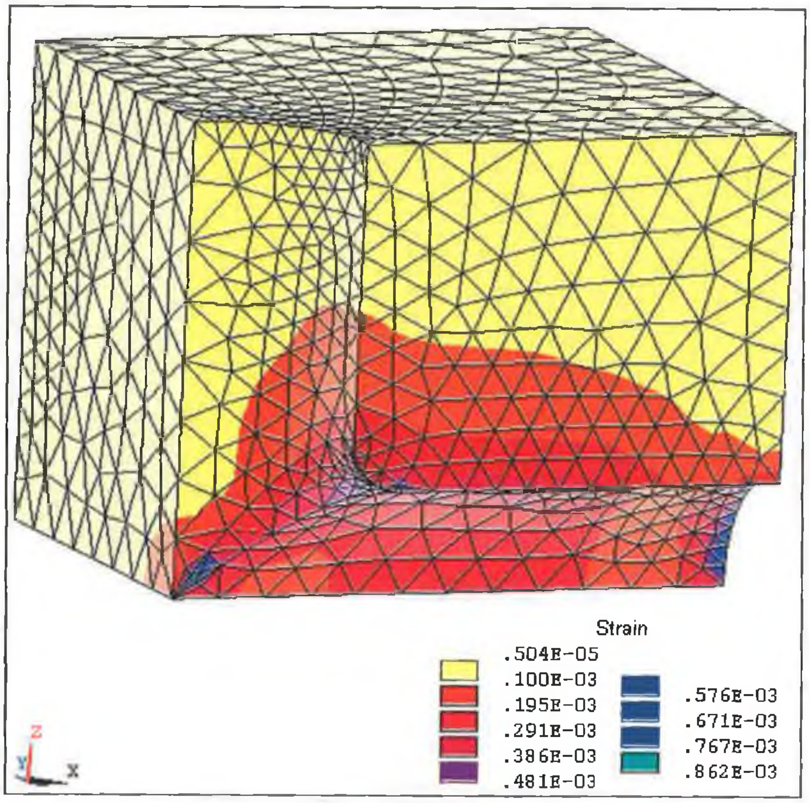

Figure 7.9. : Distribution of Equivalent Strain in the Die at Full Load

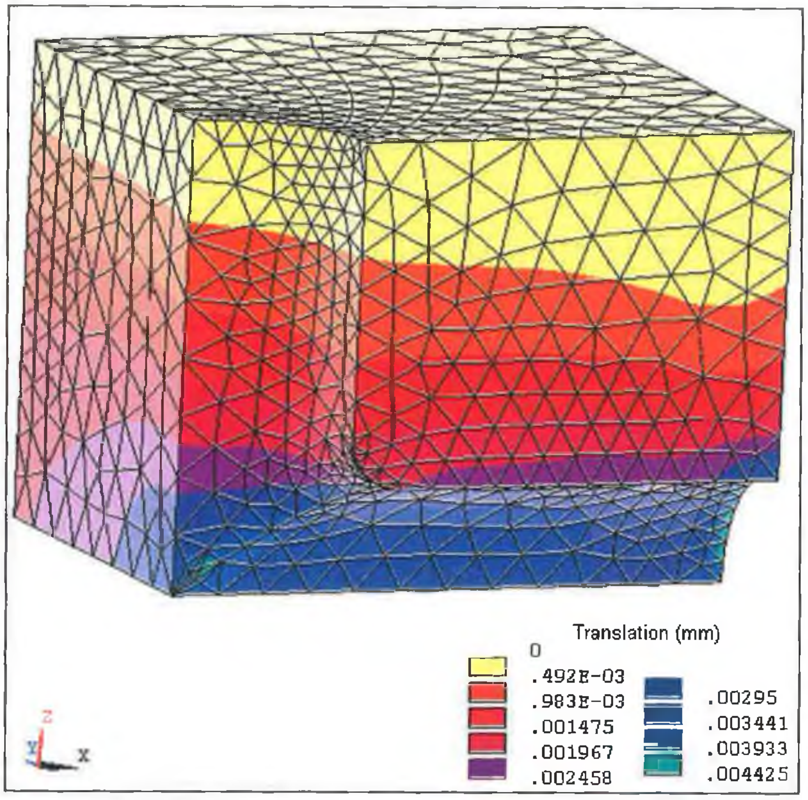

Figure 7.10. : Elastic Deformation of the Die at Full Load

7.2.3.2. Combined Pressure and Axial Load

The second simulation was run with loading pattern two which used combined internal pressure and compressive axial load applied to the tubular blank. At full load the branch height was 12mm and the maximum stress in the tube was 317 MPa. This corresponded directly with the result obtained in chapter four, in which a rigid body model was used for the die. In order to examine the development of stress in the die during the process, figures 7.11. to 7.14 show the distribution of von-Mises stress in one half of the die assembly at 25%, 50%, 75% and 100% of full load. It can be seen from the figures that the stress development is quite similar to the previous simulation as the location of maximum stress originates in the main die body and moves towards the die bend as the process continues. The stresses in this case are much higher at each stage than in the previous simulation due to friction between the die and tube and the large amount of relative sliding due to the application of compressive axial load.

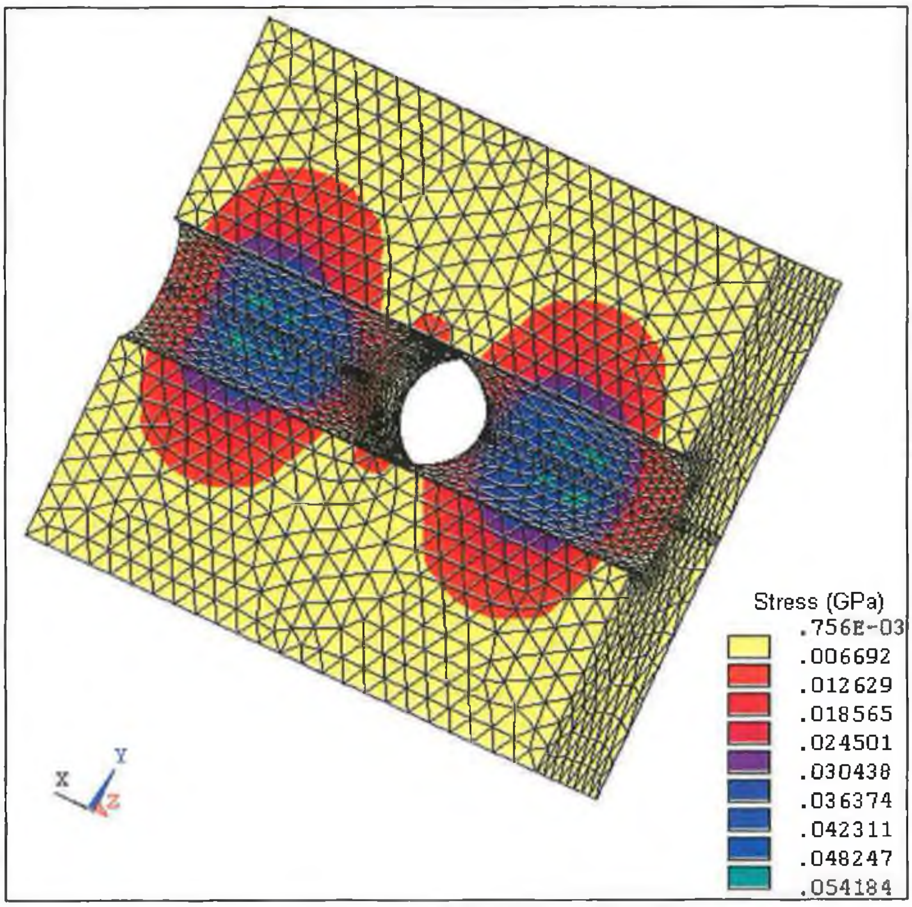

Figure 7.11. : Distribution of von-Mises Stress in the Die at 25% of Full Load

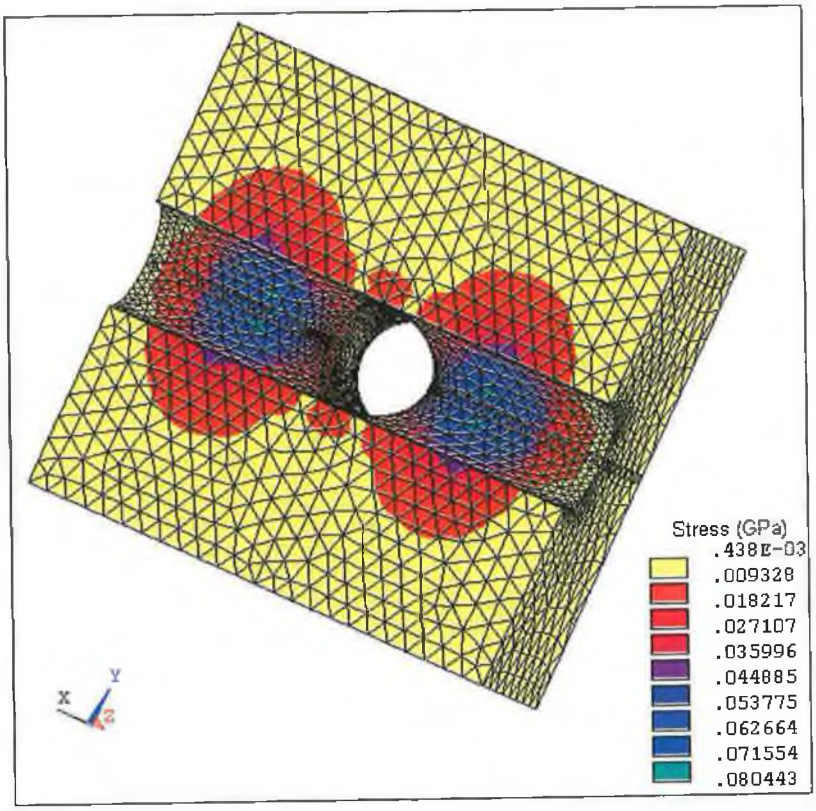

Figure 7.12. : Distribution of von-Mises Stress in the Die at 50% of Full Load

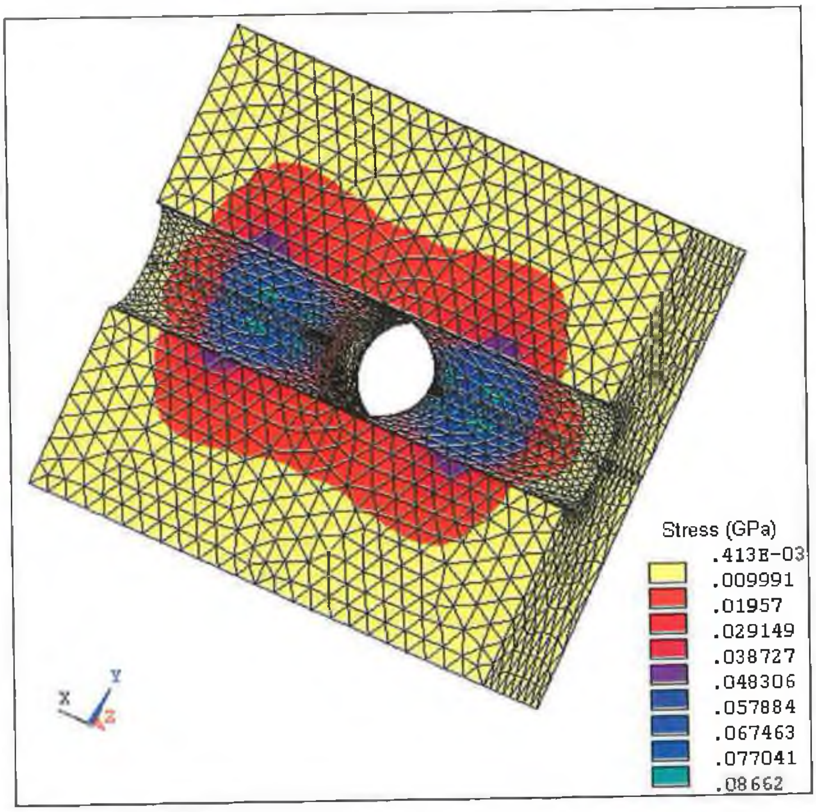

Figure 7.13. : Distribution of von-Mises Stress in the Die at 75% of Full Load

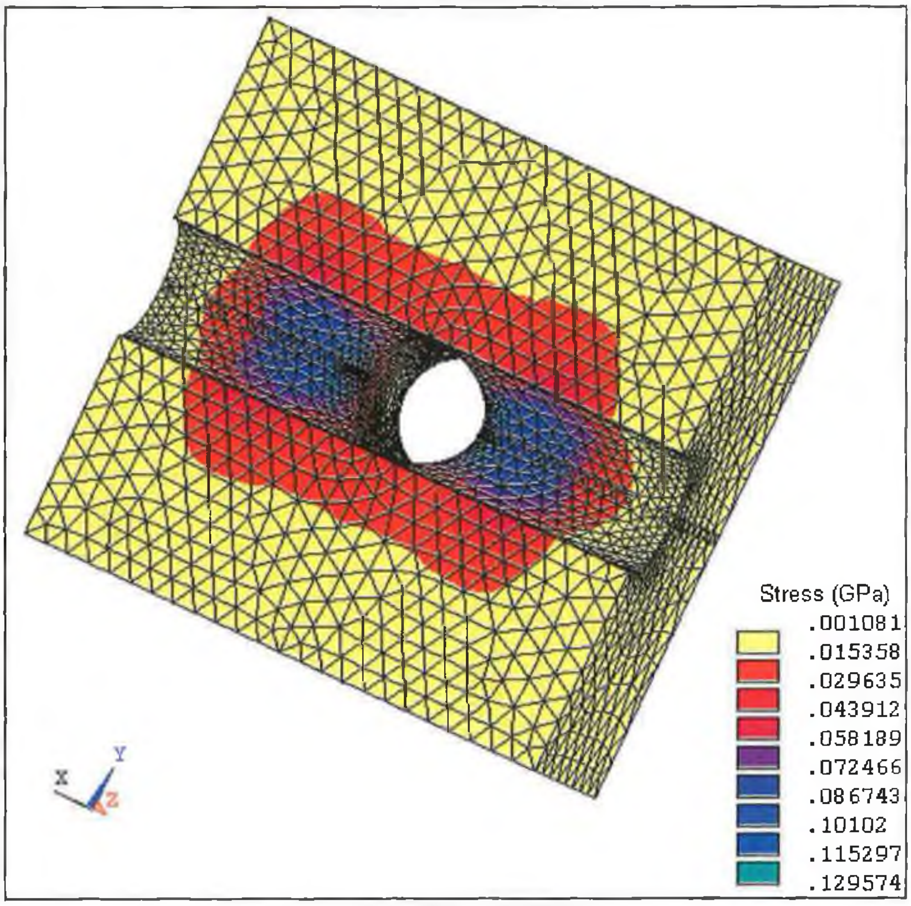

Figure 7.14. : Distribution of von-Mises Stress in the Die at 100% of Full Load

In order to provide a clearer view of the state of stress in the die at full load figure 7.15 shows the distribution of stress for one eighth of the die. It can be clearly seen from the figure that the maximum stress experienced by the die is at the die blend radius as expected. The high stress at this location can be attributed to the high pressure exerted by the tube on the die as the bulge forms and also to the large amount of relative sliding that occurs at this point. As the bulge forms material is pushed past the die radius into the bulging zone thus increasing the stress imparted on the die due to friction. In comparison to the area around the die radius, the rest of the die has experienced very little stress. This indicates that it is of most importance that a proper die blend radius is used in order to produce defect-free components as this will be the point of highest stress in the die. This result is evident in experimental analysis [30,91] and in the simulation results obtained in chapter four where the effect of altering die blend radius was investigated.

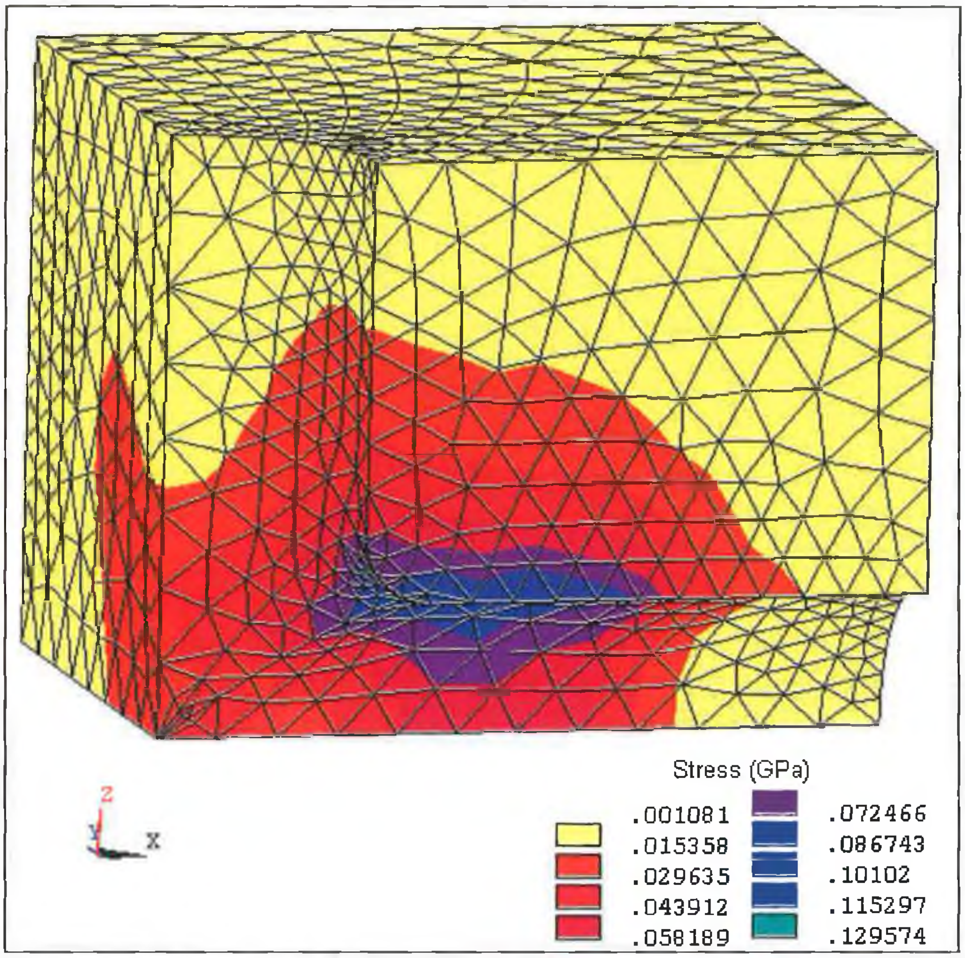

Figure 7.15. : Distribution of von-Mises Stress in the Die at Full Load

It can be seen from figure 7.15 that the maximum stress experienced by the die is 137 MPa. This is slightly higher than that obtained in the previous simulation but is still well below the yield point for steel EN21 so no permanent deformation of the die would be expected due to this loading. In order to investigate the deformation of the die during the process figure 7.16 shows the distribution of equivalent strain at full load. It can be seen from the figure that the maximum strain occurs at the region of greatest stress. In order to get a better insight into the deformation of the die figure 7.17 shows the amount of elastic deformation of the die in millimeters. It can be seen that the maximum deformation is 0.005992 mm which is not significant and thus it can be concluded that there will be no significant deformation of the die during the process when this type of loading is used.

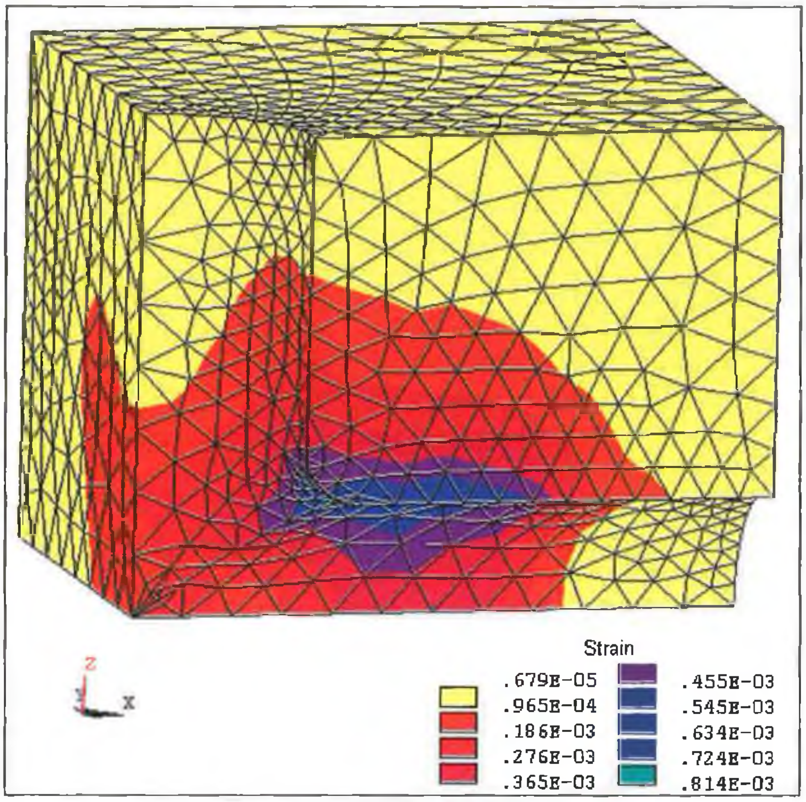

Figure 7.16. : Distribution of Equivalent Strain in the Die at Full Load

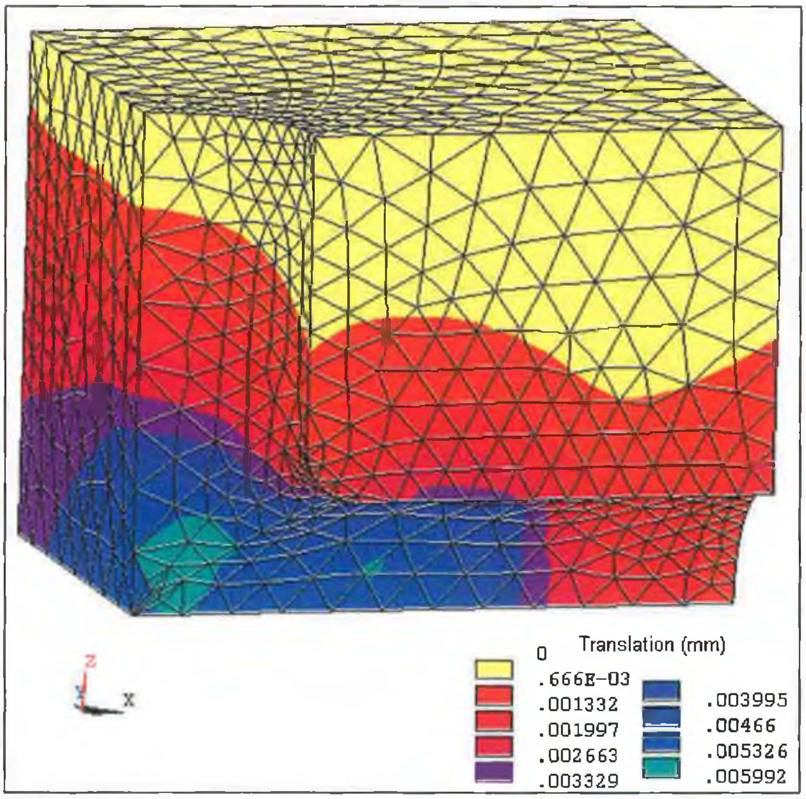

Figure 7.17. : Elastic Deformation of the Die at Full Load

7.2.3.3. The Influence of Die Elasticity

The third simulation was run using the same finite element model and loading pattern as the previous simulations but a different material model was assigned to the die. The purpose of this simulation was to investigate the effect of die elasticity on the process. The material properties assigned to the die were designed to be consistent with Aluminium 5052 an are detailed in table 7.1. In this case a linear elastic model was assigned to the die. Obviously aluminium would never be used as a candidate die material in practice, but is used here in order to have a significant difference in material properties and hence determine the effect of this change.

Property	***Value***
Density	2.68 x 10^{-6} Kg/mm^3
Young's Modulus	70 GPa
Poisson's Ratio	0.33
Yield Stress	90 MPa
Ultimate Tensile Strength	195 MPa

Table 7.1. : Material Properties for Aluminium 5052

At full load the branch height was 11.5mm and the maximum stress in the tube was 319 MPa. This was 0.5mm lower and with slightly higher stress than that obtained in the previous simulation. In order to examine the development of stress in the die during the process, figures 7.18 to 7.21 show the distribution of von-Mises stress in one half of the die assembly at 25%, 50%, 75% and 100% of full load. It can be seen from the figures that the stress development is quite similar to the previous simulation as the location of maximum stress originates in the main die body and moves towards the die bend as the process continues. The stresses in this case are slightly lower at each stage than in the previous simulation due to change in the die material properties.

In order to provide a clearer view of the state of stress in the die at full load figure 7.22 shows the distribution of stress for one eighth of the die. It can be clearly seen from the figure that the maximum stress experienced by the die is at the die blend radius as expected.

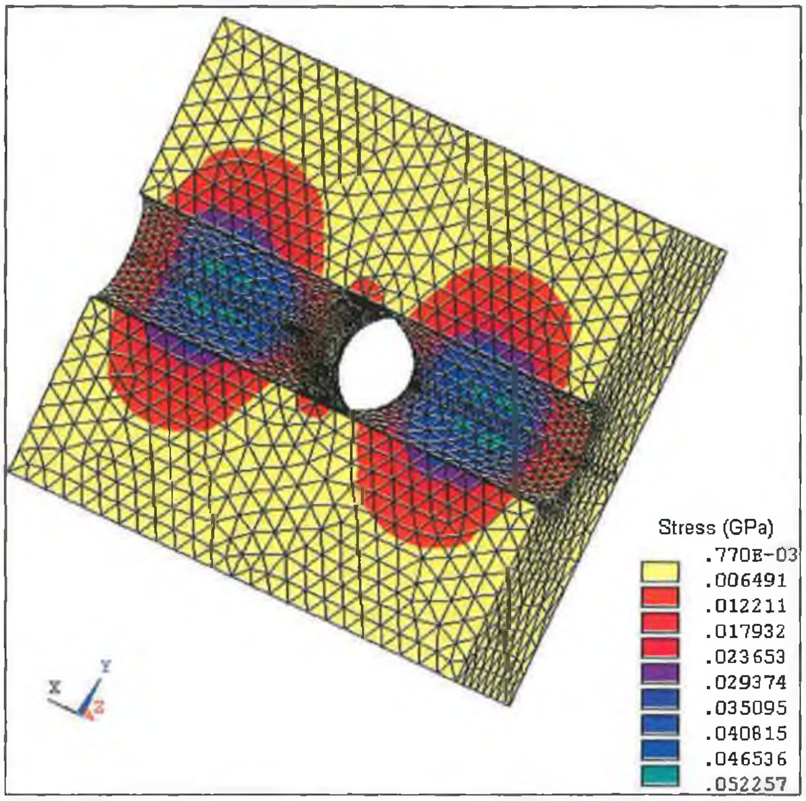

Figure 7.18. : Distribution of von-Mises Stress in the Die at 25% of Full Load

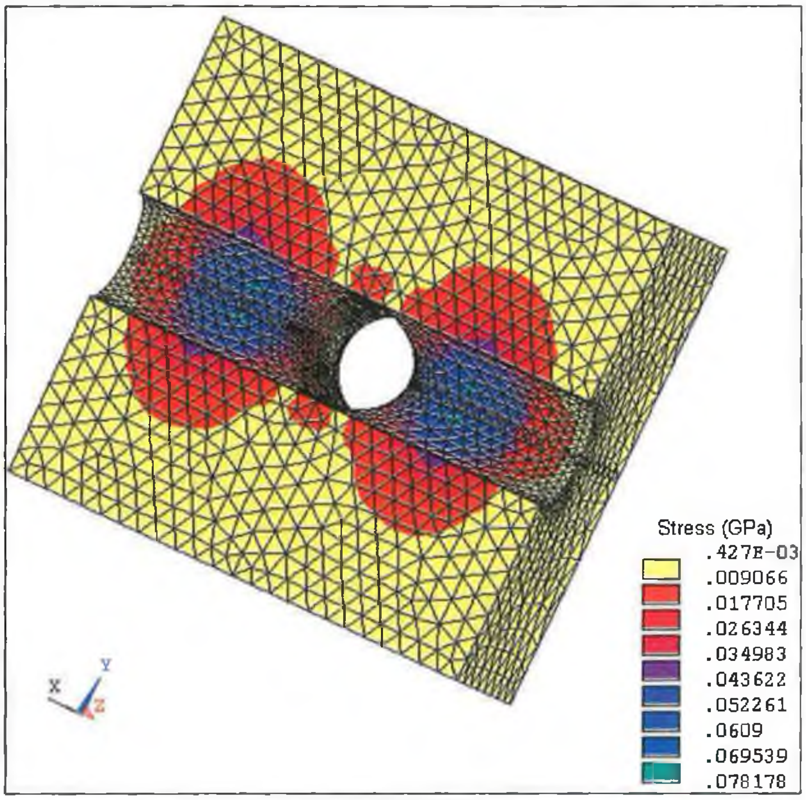

Figure 7.19. : Distribution of von-Mises Stress in the Die at 50% of Full Load

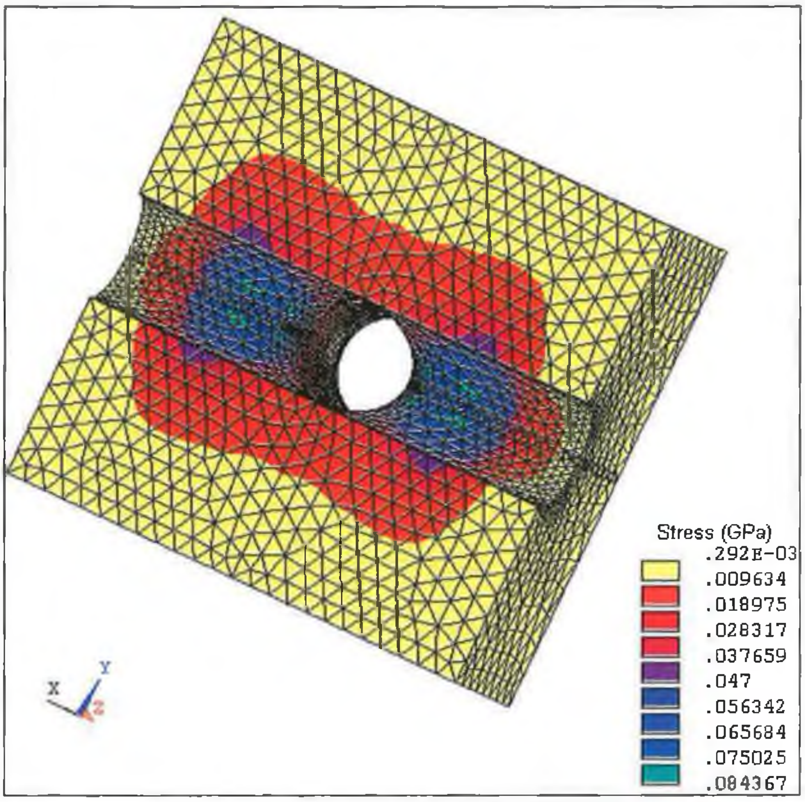

Figure 7.20. : Distribution of von-Mises Stress in the Die at 75% of Full Load

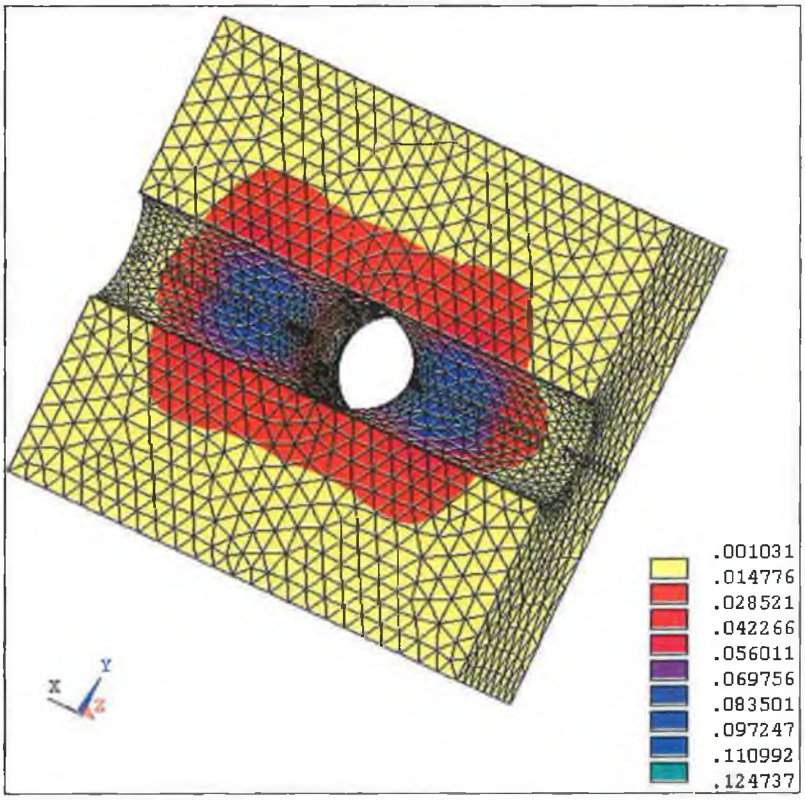

Figure 7.21. : Distribution of von-Mises Stress in the Die at 100% of Full Load

In comparison to the area around the die radius, the rest of the die has experienced very little stress. This indicates that it is of most importance that a proper die blend radius is used in order to produce defect-free components as this will be the point of highest stress in the die. This result is evident in experimental analysis [30,91] and in the simulation results obtained in chapter four where the effect of altering die blend radius was investigated.

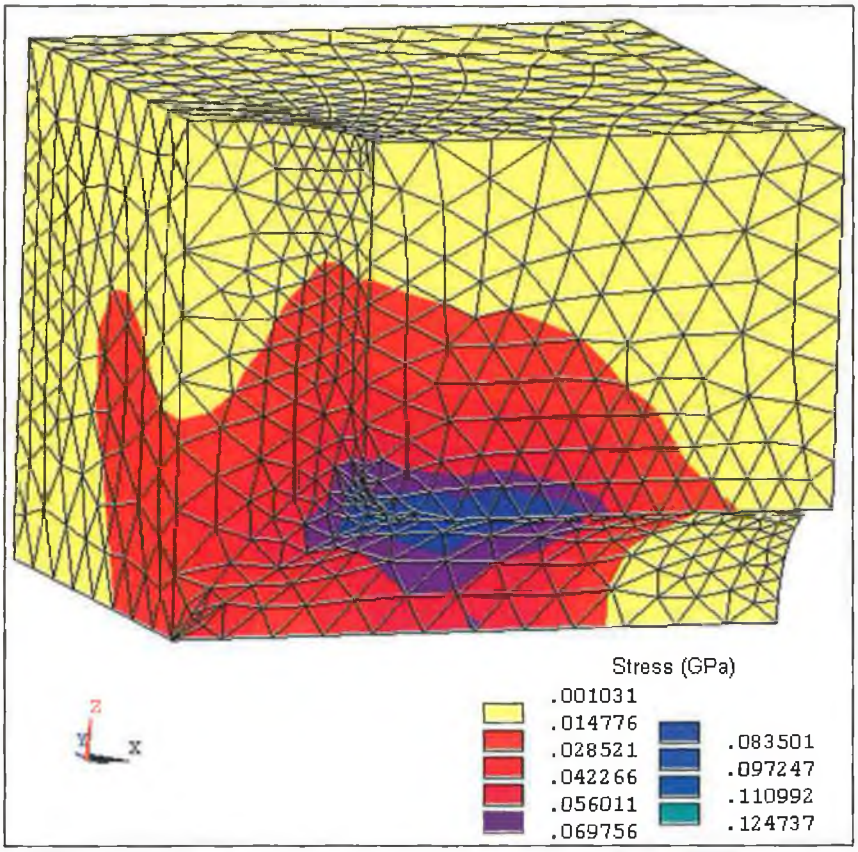

Figure 7.22. : Distribution of von-Mises Stress in the Die at Full Load

It can be seen from figure 7.22 that the maximum stress experienced by the die is 124 MPa. This is slightly lower than that obtained in the previous simulation but it should be noted, in contrast to the previous simulations, that this value is well in excess of the yield strength of the Aluminium 5052 and some plastic deformation of the die would be expected. Clearly this is unacceptable for a die design and consequently Aluminium 5052 would not be recommended as a die material for the geometry and loading used here.

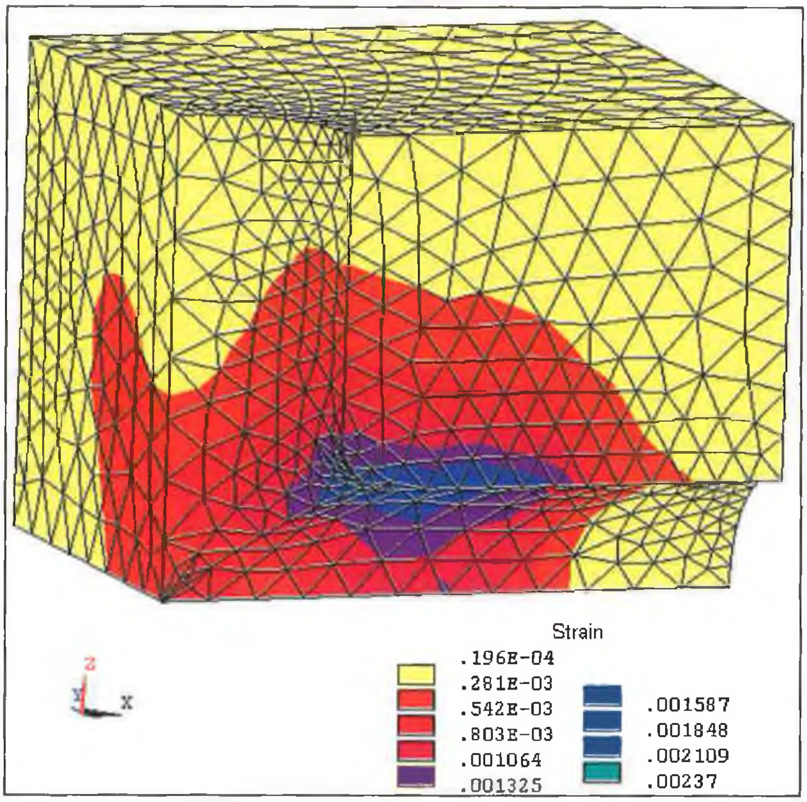

Figure 7.23. : Distribution of Equivalent Strain in the Die at Full Load

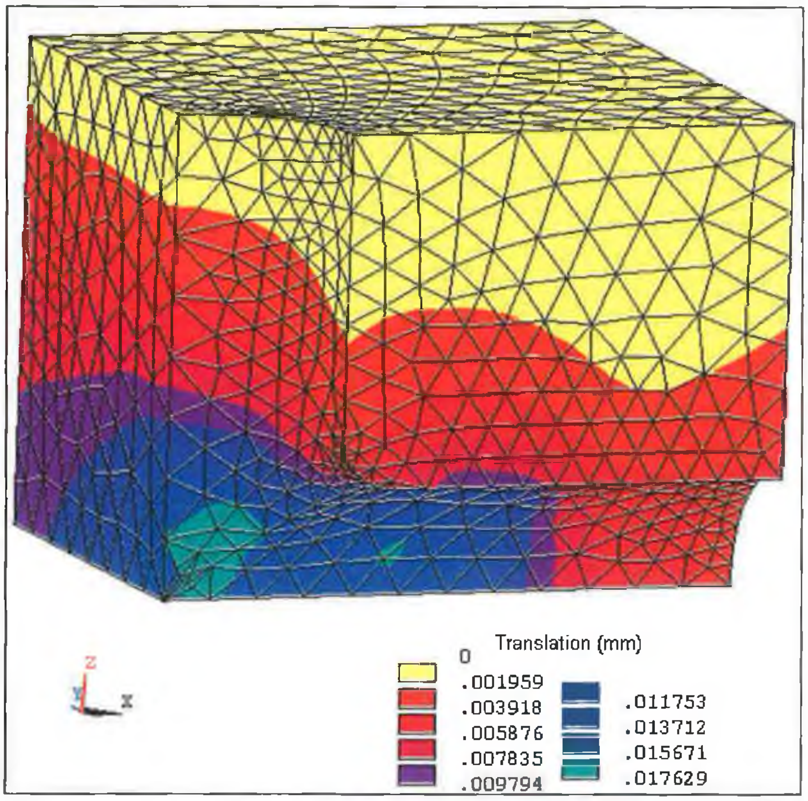

Figure 7.24. : Elastic Deformation of the Die at Full Load

Figure 7.23 shows the distribution of equivalent strain at full load. It can be seen from the figure that the maximum strain occurs at the region of greatest stress. In order to get a better insight into the deformation of the die figure 7.24 shows the amount of elastic deformation of the die in millimeters. The maximum deformation was found to be 0.017 mm. This value is almost four times that experienced in the previous simulation but is most likely inaccurate due to the fact that a linear elastic material model was used for the die. As mentioned previously the die has almost certainly undergone plastic deformation which was not taken into account by the linear elastic model. It is expected that a further analysis with an elasto-plastic material model for the die would show increased deformation.

7.3. Axisymmetric Tube Bulging with a Urethane Rod

7.3.1. Modelling, Loading and Solution

In order to analyse the behaviour of the die during a solid medium bulge forming process it was possible to use the same model that was developed in chapter 5 to analyse axisymmetric tube bulging with a urethane rod. This model has previously been validated against experimental results as detailed in chapter 5. For completeness the model is shown again in figure 7.25. The die was modelled as a linear elastic material model with the material properties assigned to model Aluminium as was used in the experimental apparatus described in chapter 5.

By taking advantage of symmetry it was possible to model one quarter of the die-tube-rod assembly and still obtain a full three dimensional solution. Accordingly the nodes at the symmetry edge of the die, tube and rod were constrained in the appropriate directions. The bottom plate of the die was not modelled, instead the nodes at the die bottom were constrained in the appropriate directions to simulate the presence of the die bottom plate. The loading pattern used in each simulation is detailed in chapter five and the results are chosen to correspond to stress distributions at particular simulation times as detailed in the results section in chapter five.

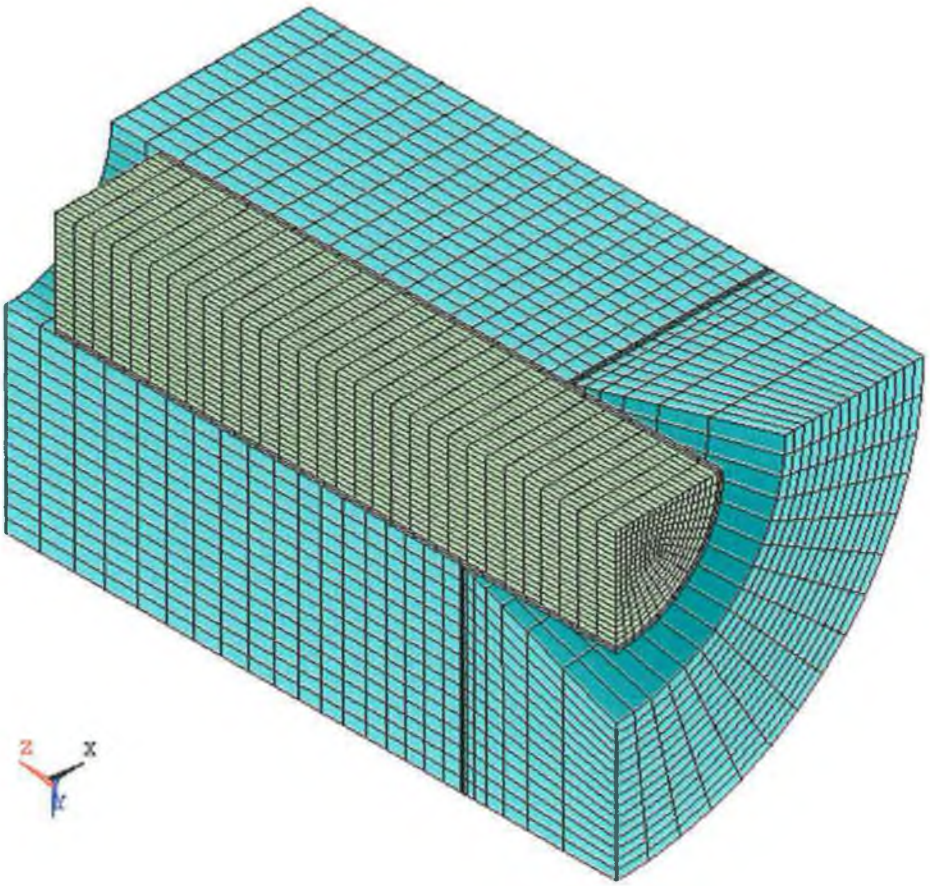

Figure 7.25. : Finite Element Model Used for Axisymmetric Die Analysis

7.3.2. Results and Analysis

7.3.2.1. First Product – Conical Bulge

In order to examine the development of stress in the die during the process, figures 7.26. to 7.29 show the distribution of von-Mises stress in the die at 40%, 60%, 80% and 100% of full load. These figures correspond directly with figures 5.35 to 5.38 in chapter five which show the corresponding stress in the tube. It can be seen that the compression of the urethane rod immediately forces the tube against the die wall, with the maximum amount of stress being experienced by the die in the main die body where there is maximum contact between the die and the tube. The region of maximum stress then moves to the die recess as the bulge begins to form and comes in contact with the die in this region.

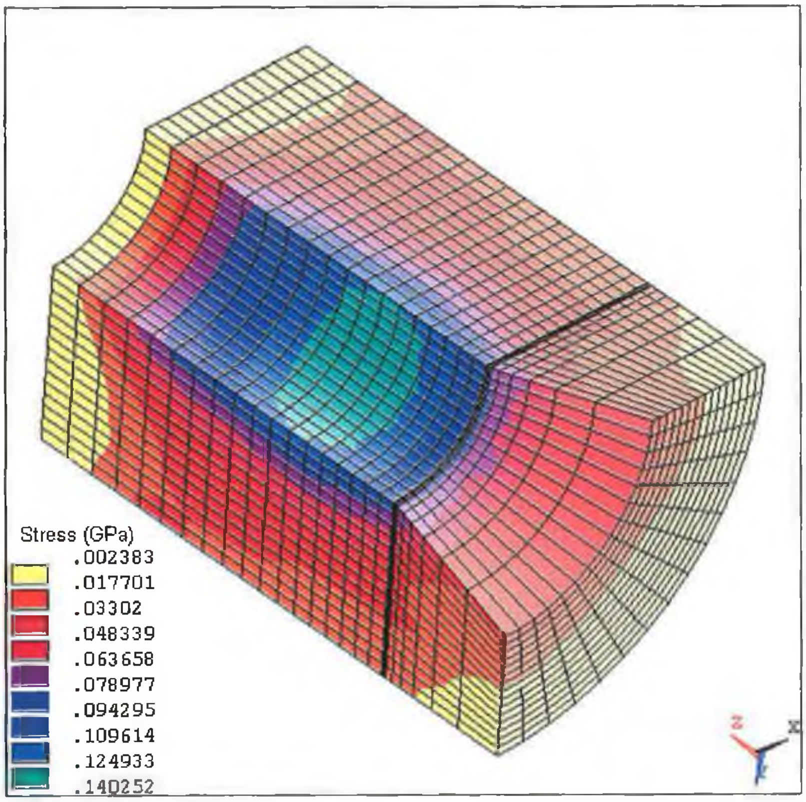

Figure 7.26. : Distribution of von-Mises Stress in the Die at 40% of Full Load

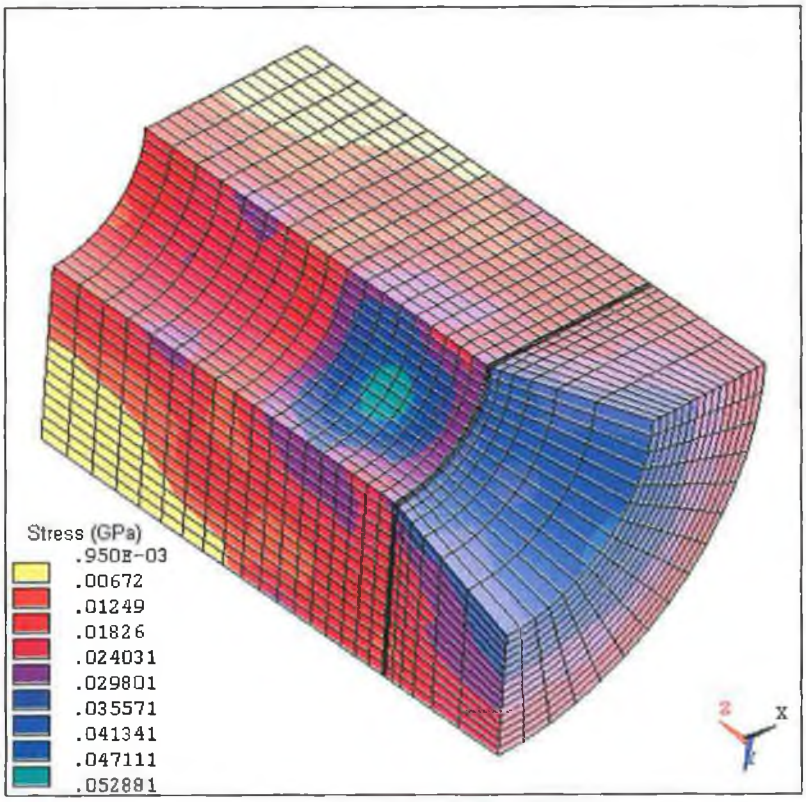

Figure 7.27. : Distribution of von-Mises Stress in the Die at 60% of Full Load

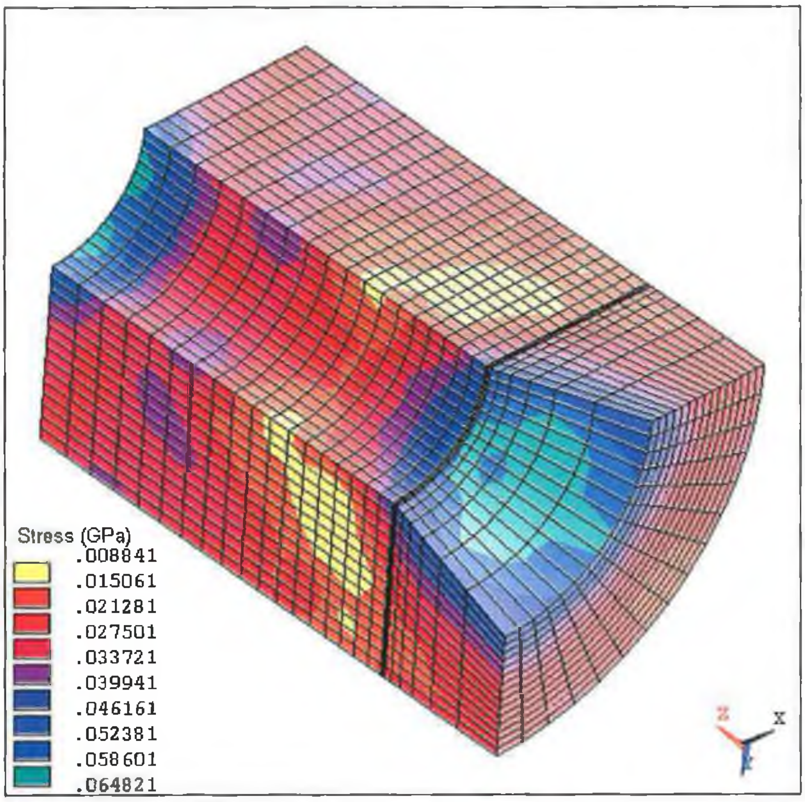

Figure 7.28. : Distribution of von-Mises Stress in the Die at 80% of Full Load

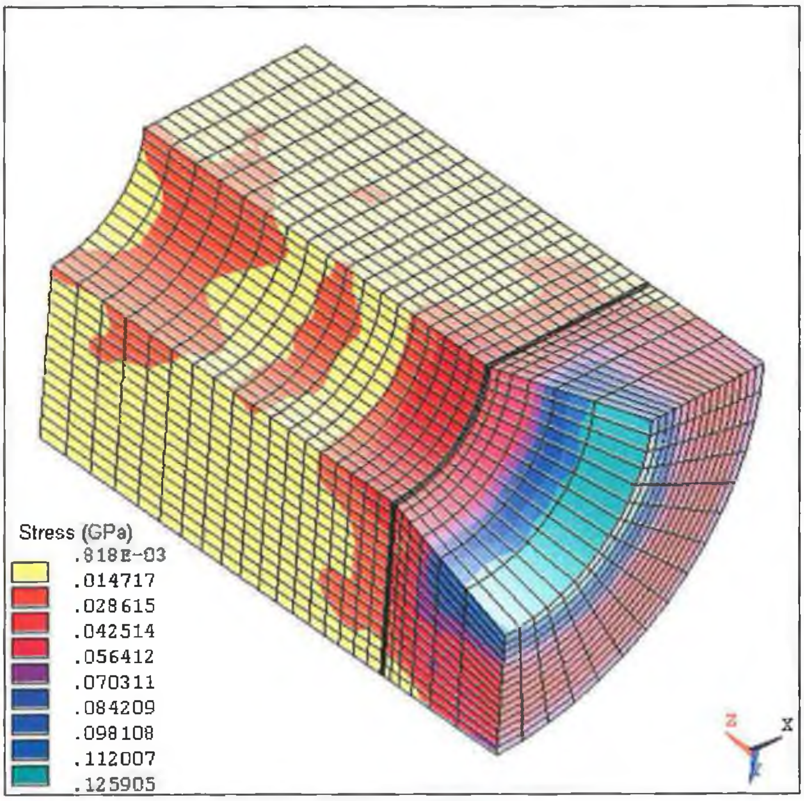

Figure 7.29. : Distribution of von-Mises Stress in the Die at Full Load

At full load the region of maximum stress is located at the bottom of the die as the bulge is completed in this region and the tube comes in contact with the die wall.

It can be seen from figure 7.29 that the maximum stress experienced by the die is 125 MPa. This is above the yield point for the aluminium material used for the die so some permanent deformation of the die could be expected due to this loading. In order to investigate the deformation of the die during the process figure 7.30 shows the distribution of equivalent strain at full load. It can be seen from the figure that the maximum strain occurs at the region of greatest stress. In order to get a better insight into the deformation of the die, figure 7.31. shows the amount of elastic deformation of the die in millimeters. It can be seen that the maximum deformation is 0.029 mm, however, as mentioned above the yield stress of the material has been exceeded and a higher deformation than predicted here would be expected.

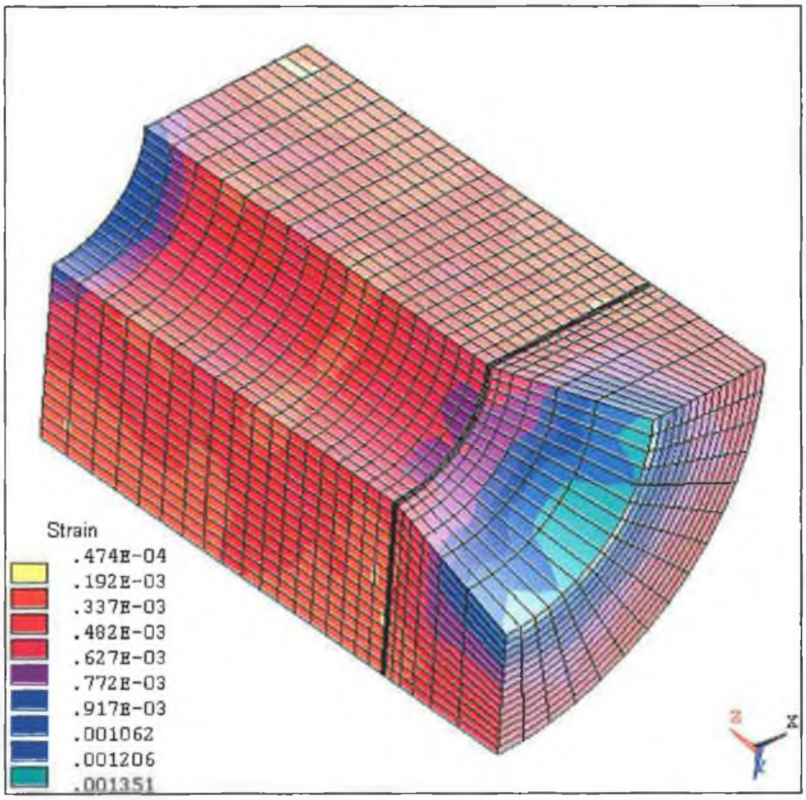

Figure 7.30. : Distribution of Equivalent Strain in the Die at Full Load

In order to investigate whether this deformation is significant the die used for this geometry was measured after completing a number of experimental tests and no measurable deformation was found. Given the geometry of the tube-rod-die arrangement used here it can be concluded that the deformation of the die is not significant and thus it can be concluded that there will be no significant deformation of the die during the process when this type of loading is used.

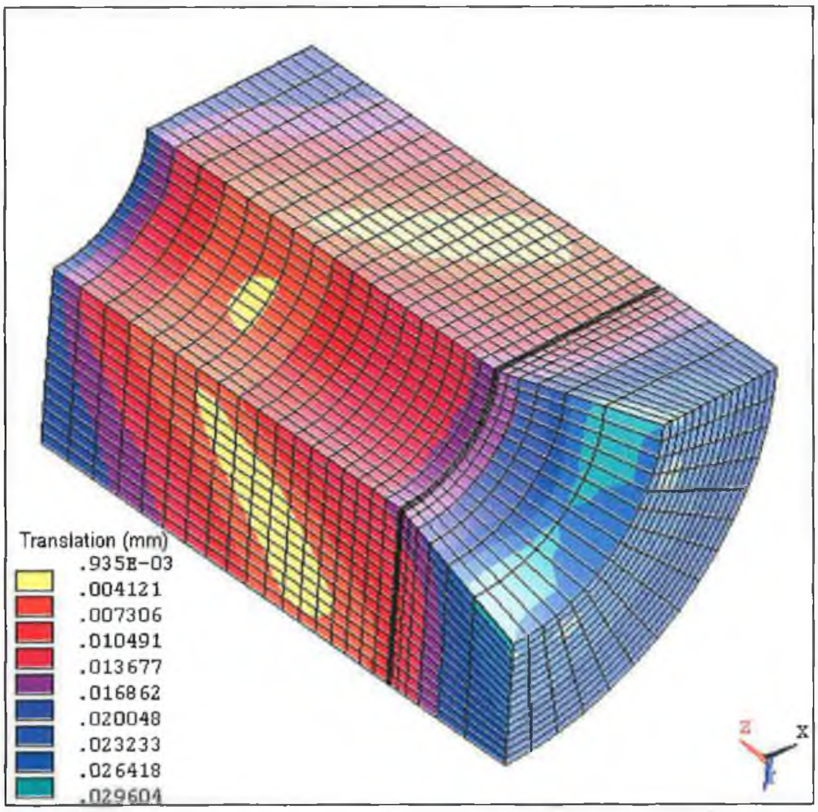

Figure 7.31. : Elastic Deformation of the Die at Full Load

7.2.3.2. Second Product – Conical Bulge with Extension

The second simulation was run to simulate the manufacture of a different product as explained in chapter five. In order to examine the development of stress in the die during the process, figures 7.32. to 7.34 show the distribution of von-Mises stress in the die at 40%, 60%, 80% and 100% of full load. These figures correspond directly with figures 5.44 to 5.48 in chapter five which show the corresponding stress in the tube. It can be seen that, similar to the previous simulation, the compression of the urethane rod immediately forces the tube against the die wall, with the maximum amount of stress being experienced by the die in the main die body where there is maximum contact between the die and the tube. The region of maximum stress then moves to the die recess as the bulge begins to form and comes in contact with the die in this region.

It is interesting to note that the distribution of stress at each stage is markedly different to the stress distribution in the previous simulation. In this case there is an increased die recess volume and hence an increased volume of tube to be bulged. There is much more movement of the tube towards the die recess in this simulation as material is pulled by the bulge formation and pushed by the urethane rod into the bulging zone. This can be seen particularly in figure 7.34 which shows the distribution of stress at 80% of full load. At this stage there is very little of the deformed tube in contact with the die recess and the situation resembles almost a free bulging scenario. Consequently there is reduced stress in the die recess and the maximum stress in this case is at the top of the die – due to friction between the tube and the main die body, as the tube tries to move towards the die recess.

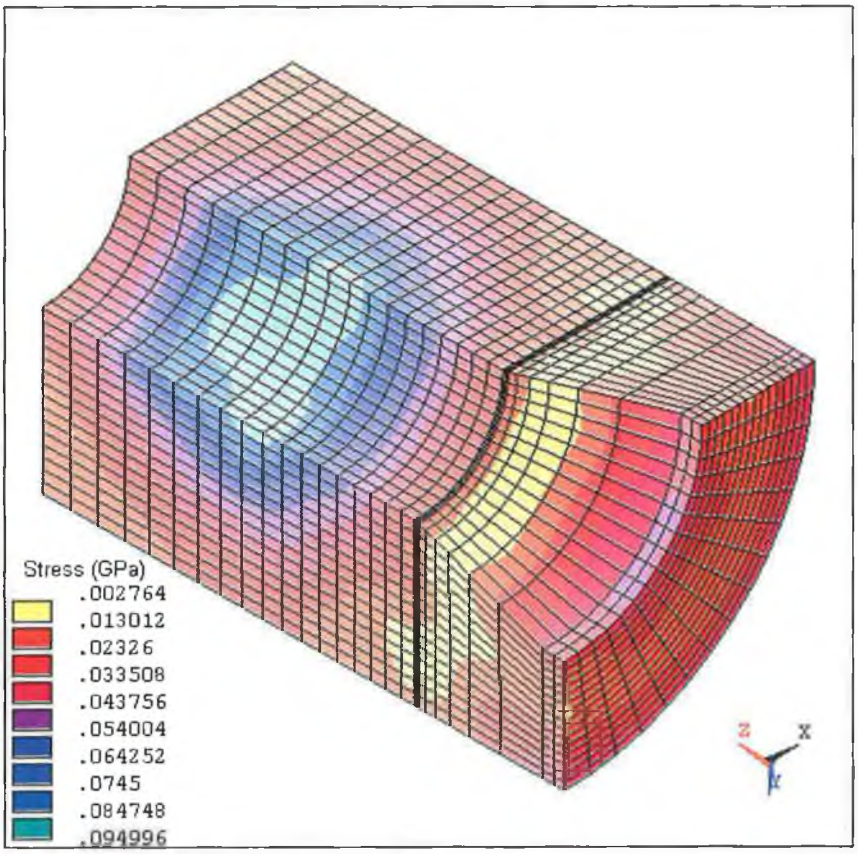

Figure 7.32. : Distribution of von-Mises Stress in the Die at 40% of Full Load

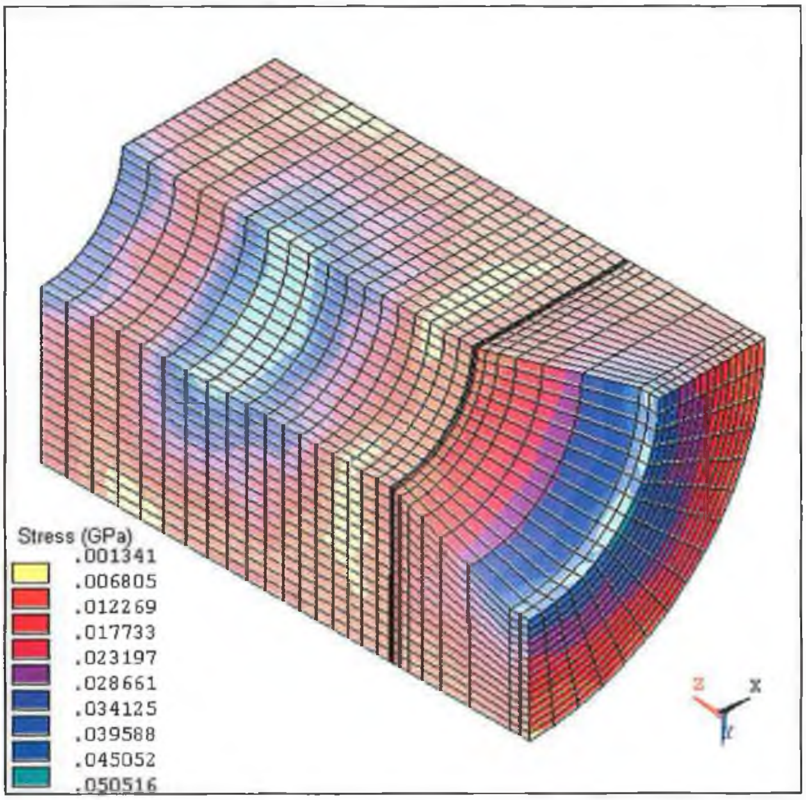

Figure 7.33. : Distribution of von-Mises Stress in the Die at 60% of Full Load

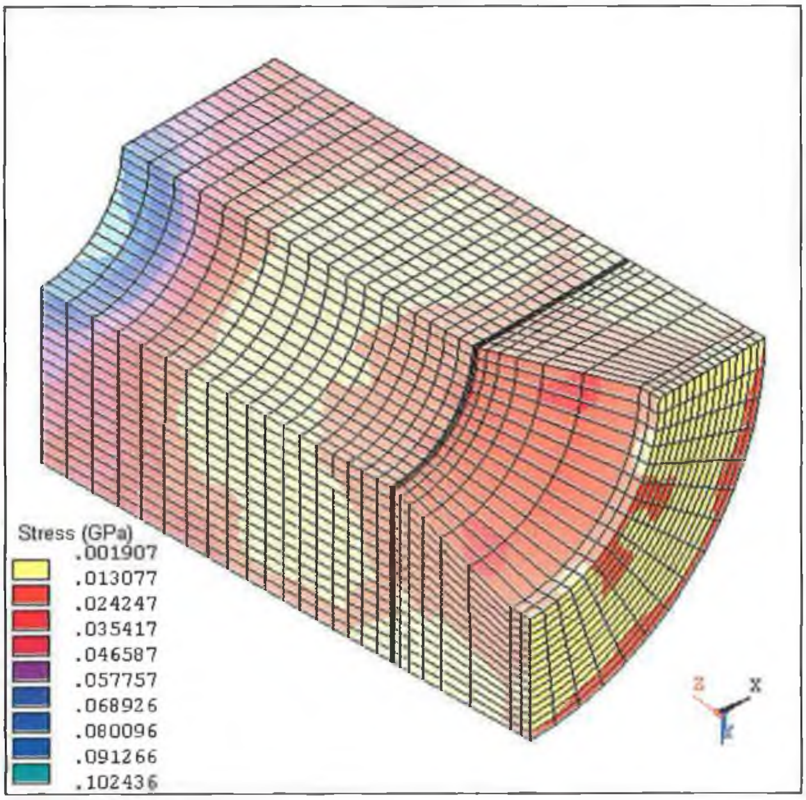

Figure 7.34. : Distribution of von-Mises Stress in the Die at 80% of Full Load

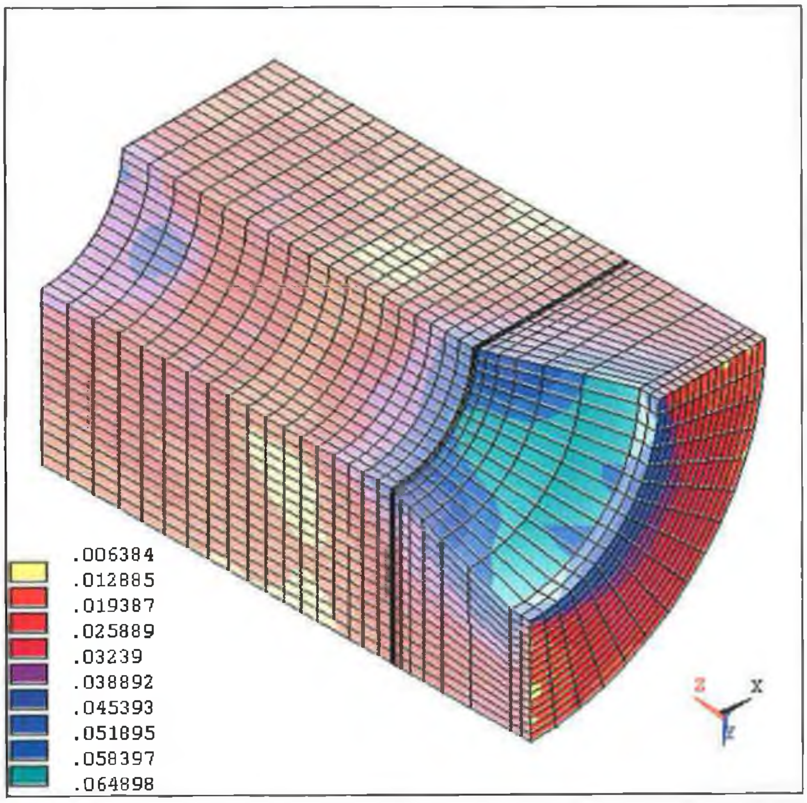

Figure 7.35. : Distribution of von-Mises Stress in the Die at Full Load

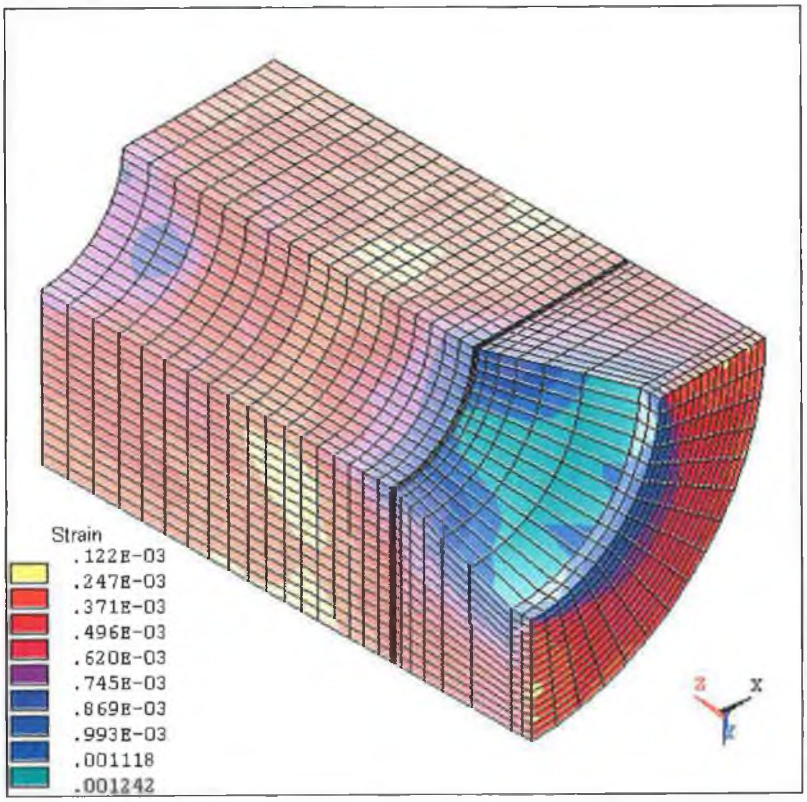

Figure 7.36. : Distribution of Equivalent Strain in the Die at Full Load

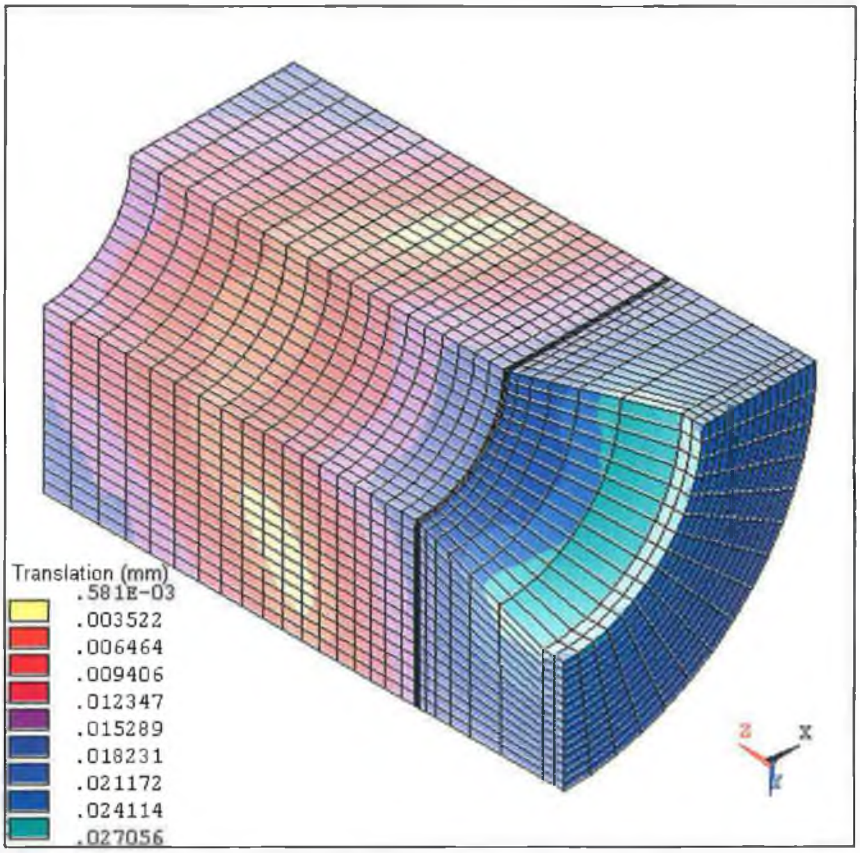

Figure 7.37. : Elastic Deformation of the Die at Full Load

It can be seen from the figures that the maximum stress experienced by the die during the process is 102 MPa at 80% of full load. This is above the yield point for the aluminium material used for the die so some permanent deformation of the die could be expected due to this loading. In order to investigate the deformation of the die during the process figure 7.36 shows the distribution of equivalent strain at full load. It can be seen from the figure that the maximum strain occurs at the region of greatest stress. In order to get a better insight into the deformation of the die, figure 7.37. shows the amount of elastic deformation of the die in millimeters. It can be seen that the maximum deformation is 0.027 mm which is slightly lower than in the previous simulation, however, as mentioned above the yield stress of the material has been exceeded and a higher deformation than predicted here would be expected.

As explained in the previous section a number of experimental tests were completed using the experimental apparatus and no measurable deformation was found. Given the geometry of the tube-rod-die arrangement used here it can be concluded that the deformation of the die is not significant and thus it can be concluded that there will be no significant deformation of the die during the process when this type of loading is used.

7.3. Summary of Chapter 7

This chapter presents the results from simulations of bulge forming using both a liquid and a solid bulging medium. The development of stress and the deformation of the die was examined in each case. The effect of die elasticity on the manufacture of cross branch components using the hydraulic bulging method was examined. The model used for the solid medium analysis has previously been validated in chapter five.

Chapter 8 : Discussion

8.1 Hydraulic Cross Branch Forming

The simulation of bulge forming by pressure load alone illustrates that the absence of a compressive load to push more material into the bulging zone does not produce very satisfactory results. The outcome of the loading pattern used in this simulation was excessive thinning of the branch tops, high stress in the bulged region and low branch heights. The highest stresses were located at the branch top and this is where failure eventually occurred, due to excessive thinning and eventually bursting. This mode of failure has been well documented in literature and the results indicate that the finite element model developed behaves in a manner that is agreeable with experimental trials.

The combination of compressive axial load with internal pressure significantly increased branch height and decreased thinning of the branch top, as illustrated in figure 4.34. The more complex loading conditions resulted in a more complex stress state in the deformed tube. The maximum stress in all simulations that utilised this combined loading was in the same location and was a combined compressive axial stress and tensile hoop stress. In all simulations the maximum stress was below the ultimate strength of the material but it is possible, with increased axial load, that a buckling failure could occur in this location.

Using the same combined loading pattern and increasing friction between the tube and the die resulted in less branch height and less stress in the formed component. Increasing friction also had the effect of increasing thinning of the branch top and increasing thickening of the main tube ahead of the punch. These results are summarised in figure 4.35. All of these effects are contrary to the production of a satisfactory component and hence are to be avoided. This suggests that when designing bulge forming operations, the designer should ensure that the friction between the die and the tube is kept to a minimum. This result is in agreement with experimental studies which examined the effect of friction on bulge forming processes [30].

Again keeping the same loading conditions but Increasing the tubular blank thickness resulted in reduced branch height and reduced stress in the formed component as indicated in figure 4.36. Increasing the thickness of the blank also has the positive effects of reducing thinning of the branch top and less thickening in the main tube. Obviously the reduced stress and thinning/thickening behaviour are very positive effects but the lower branch height is not satisfactory. The fact that the same loading conditions that were developed for the thinner tube were used here is significant. The same loading conditions were used in order to allow a direct comparison of the effects of using a thicker tube. It is obvious however that the thicker tube would be able to withstand higher internal pressure and higher axial load without failing. If higher loads are applied it is expected that the branch height could be increased. The results experienced here are in agreement with experimental trials which examined the effects of changing blank thickness in bulge forming operations [28].

As mentioned above, in all simulations the finite element model behaved in agreement with experimental investigations. The model was built to be consistent with the geometry, materials and loading conditions used by Hutchinson [30] in his experiments. As the experimental data of Hutchinson was available this allowed the finite element model to be validated against these results. Unfortunately, unsatisfactory information concerning friction conditions between the die and tube in Hutchinson's experiments were available so the simulation results from both the low friction and the high friction simulations were used. Both simulations agreed well with experimental results, with the simulation with lower friction being slightly more accurate. This shows that the finite element model developed here accurately simulates hydraulic bulge forming of cross joint components and may be used with reasonable confidence to aid in the design of bulge forming operations

8.2. Bulge Forming Using a Solid Bulging Medium

8.2.1. Cross Branch Forming Using a Soft Metal

The simulation of internal pressure loading only using a solid bulging medium illustrated that the use of a solid bulging medium allows for greater branch height, less thinning of the branch top and less stress in the formed component when compared to the hydraulic bulging process. This is as a result of the favourable conditions set up due to the use of a solid bulging medium, namely friction between the bulging medium and the tube. This friction results in some tube material being pulled into the bulging zone thus reducing thinning of the branch top which allows the process to continue and the branch height to be increased. The implications of this result for the designer is that if it is required to use pressure loading only in a bulge forming process then the solid bulging medium process should be used where possible.

It should be noted however that there are some operational disadvantages to using a solid bulging medium. If a soft metal is to be used as a bulging media then in some cases it may be required to cast the material into the tubular blank before the bulge forming process. After the bulging process is complete the only way to remove the media is to heat the tube and melt the soft metal which then can be poured out of the tube. Even though the melting point of lead (327°C) is significantly below that of copper (1083°C) it is possible that there will be some adverse effects on the tube by this process. There is also significant cost considerations in terms of the energy costs of melting and re-melting the bulging media. The use of an elastomer as a solid bulging media can remove most of these disadvantages, however, it should be noted that elastomers are only capable of producing limited deformations without using a very complex control process [31].

The simulation of combined internal pressure and compressive axial load using a solid bulging medium illustrate that in order to maximise branch height it is important that the load is applied in the proper manner. In initial simulations the load was applied to the bulging medium and tube simultaneously and resulted in a satisfactory component but with slightly reduced height when compared to the results obtained from hydraulic bulge forming. Applying an initial load to the bulging medium before applying load to the tube resulted in greater branch height with little change in stress, when compared to the results from hydraulic bulge forming. This has serious implications for bulge forming equipment design, particularly the design of the punch. If the designer requires to maximise branch height using the solid bulging medium then the punch should have an appropriate length shoulder that will allow the bulging medium to be compressed to the required level before a compressive load is applied to the tube. Further control and flexibility can be added by having a specialised punch, with its own control system, that allows the inner diameter (which compresses the bulging medium) extended independently of the outer cylinder (which compresses the tube). These results are summarised in figure 4.35.

The effect of friction between the bulging medium and the tube was investigated by varying the friction parameters used. The results obtained are summarised in figure 5.26. It was found that increased fiction has little effect on the resultant branch height but results in less stress in the formed component, more thinning of the branch top, less thickening of the main tube and a smoother stress development during the forming process. The fact that increased friction means that thinning of the branch top is increased means that it is important that friction is controlled during the process. A certain amount of friction does produce favourable conditions for forming, as mentioned earlier, but the results here suggest that if friction becomes too high then the possibilities of producing a defective component are increased.

To enable direct comparison of the results of using the hydraulic bulging method and the solid medium method, the manufacture of two components of similar height by each method was compared. When compared to a cross branch of similar height obtained by the hydraulic bulging process, it is clear that the solid medium bulging process results in far less reduction in length of the tube. Again, this is due to the favourable friction conditions between the tube and bulging medium pulling material into the bulging zone. This results in less reduction of length than the hydraulic method where the tube material is pushed into the bulging zone, which causes thickening of the tube ahead of the punch and hence reduction in length of the tube.

It was found that using the same model for the die and tube but decreasing the relative strength of the bulging media to the tube material resulted in increased bulge height with little change in the stress in the formed component, as indicated in figure 5.27. This suggests that more favourable results are obtained by using softer bulging media and is evident by the materials used in experimental analysis which tend to utilise very soft materials such as lead and solder paste [7,8].

8.2.2. Axisymmetric Tube Bulging Using a Urethane Rod

The simulation of the manufacture of the product with a conical bulge showed that the bulge initially develops in the region near the die bend. The bulge forms rapidly here but it takes almost until the end of the simulation until the bottom of the cone is formed satisfactorily. It was seen that the development of stress in the tube was highly erratic due to the fact that there is significant friction on both sides of the workpiece. It was noticed that the friction between the tube and the urethane rod had the favorable result of pushing extra material into the bulging zone thus preventing excessive thinning of the tube. The deformation mechanism that forms the bulge was found to be a combination of hoop tension and axial compression, with hoop tension being dominant.

The second simulation was designed to simulate the manufacture of a similar product but with a cylindrical extension at the end of the conical section. This geometry is representative of the type used to manufacture torchlight casings in industry. The simulation results showed that the bulge developed more rapidly than in the previous simulation, however, it again required almost the full application of load before the cylinder at the end of the conical section became evident. It was found that the development of stress was again erratic but much less erratic than in the previous simulation. The deformation mechanism that forms the bulge was, again, a combination of hoop tension and axial compression, with hoop tension being dominant.

The results of the two simulations indicate that the manufacture of the second product is much easier than the manufacture of the first product. The stress development was less erratic, the development of strain smoother and the bulge developed quicker in the second simulation than in the first. This may be a consequence of a greater volume of tube and bulging media being available in the bulging region earlier in the simulation

As mentioned earlier, the model was built to be consistent with the geometry, materials and loading conditions used in an experiment designed to validate the finite element model results. Both simulations agreed well with experimental results. This shows that the finite element model developed here accurately simulates bulge forming axisymmetric components using a urethane rod and may be used with reasonable confidence to aid in the design of bulge forming operations

8.3. Bulge Forming of Bimetallic Tubes

The simulation of bulge forming of a bimetallic tube by pressure load alone predicted that a low branch height would be obtained. The region of highest stress was confined to the outer tube and was located at the branch top and at the main tube under the branch. It is at these locations that the outer tube eventually failed due to excessive thinning.

In order to increase the branch height and hence produce a more useful component an axial compressive load was applied to the tube ends in combination with the internal pressure load. This loading did not achieve its object and, in fact, produced a component with reduced branch height. Again, failure was due to excessive thinning of the outer tube but in this case the failure was confined to the region of the main tube underneath the branch. When analysing the failure mechanisms it was found that the simulation did not continue to a point where the axial compressive load could push more material into the highly stressed area and hence prevent thinning of the outer tube.

It was initially thought that the thickness of the outer tube was influential in the early failure of the bimetallic tube so a number of simulations were carried out where the thickness of the outer tube was increased and the thickness of the inner tube decreased accordingly. The results of the simulations, however, showed that increasing the thickness of the outer tube had little effect in increasing the branch height but had considerable effect on the resultant shape of the branch, as indicated in figures 6.10, 61.4, 6.19 and 6.28. Upon investigation it was found that the contact conditions between the two tubes was influencing the failure. The contact algorithm used between the inner and outer tube effectively bonded the two tubes to each other. This meant that the compressive axial load was unable to move material into the thinning area of the outer tube without moving material into the bulging region of the inner tube. Making more material available for expansion of the inner tube increased the resultant pressure on the outer tube and effectively increased the thinning behaviour. It was found, however, that using an increased pressure load along with increasing the thickness of the outer layer could produce a satisfactory component, as indicated in figures 6.18 and 6.22.

It was found that using the same finite element model and loading conditions but decreasing the relative strength of the tube materials resulted in slightly increased branch height but still resulted in early failure of the branch.

8.4. Influence of Die Elasticity on Bulge Forming Operations

8.4.1. Hydraulic Cross Branch Forming

The use of pressure load only showed that the application of internal pressure to the tube immediately forces it against the die wall, with the maximum amount of stress being experienced by the die in the main die body where there is maximum contact between the die and the tube. It was seen that stress develops in a regular fashion in this region as the internal pressure on the die increases. Once the tube yields and the bulge begins to form the location of maximum stress moves to the region of the die bend, and is particularly concentrated at the two extremities of the die blend radius. The maximum stresses obtained showed that a die manufactured from steel EN21, as used by in experimental investigations [30], would not experience stresses beyond the elastic limit and thus no permanent deformation would be expected.

The simulation utilising combined pressure and axial loading predicted a stress development is quite similar to the pressure only simulation as the location of maximum stress originates in the main die body and moves towards the die bend as the process continues. The stresses for the combined loading pattern were much higher at each stage than in the pressure only case due to friction between the die and tube and the large amount of relative sliding due to the application of compressive axial load. The region of maximum stress was again located at the die blend radius. Again, the results indicated that steel EN21 is a suitable material for use in this bulge forming process.

The fact that the maximum stress in both simulations was found to occur at the die blend radius illustrates the importance that a proper die blend radius is used in order to produce defect-free components. This result is also evident in experimental analysis [23,43] and in the simulation results obtained in chapter four where the effect of altering die blend radius was investigated.

In order to determine the influence of die elasticity on the bulge forming process a third simulation was run whereby the material properties of the die were changed to model Aluminium 5052. The development of stress was similar to the second simulation, with the stress levels being slightly lower due to the changed material properties. In contrast to the previous simulations however, the maximum stress predicted was in excess of the elastic limit of the die material and thus some permanent plastic deformation of the die would be expected. This clearly shows the unsuitability of this material for use as a candidate die material for this bulging process.

8.4.2. Axisymmetric Bulge Forming Using a Urethane Rod

The development of stresses during the manufacture of both products showed that stress initially develops in the main die body and moves towards the die recess as the bulge grows. The stress in the die recess becomes particularly concentrated as the deformed tube touches and is subsequently pushed against the die wall. At one stage during the manufacture of the second product there is a point which resembles free bulging in which the deformed tube has very little contact with the die wall in the die recess.

In both cases the elastic limit for the die material was exceeded during the process. The levels of stress experienced were generally higher in the first simulation. The strain and deformation of the die was analysed and found to be not significant. As a linear elastic material model was used for the die in each case it is thought that the deformation may be slightly under-predicted by the model used here. The maximum deformation predicted was approximately 0.03mm which considering the geometry of the experimental apparatus used is so small as to be insignificant. The experimental apparatus was measured after a number of processes were completed and no measurable deformation could be found.

Given the experience in the previous section, which examined the die deformation during hydraulic cross branch forming, it is thought that a die made from a steel material would be able to withstand the loading used here without any permanent deformation. In this case it was required to manufacture the experimental die from aluminium due to cost constraints. The use of an aluminium die has the advantage however, that higher strains will be experienced and these can possibly be measured in future work, using strain gauges, for further validation of the model.

Chapter 9 : Conclusions

9.1. Hydraulic Cross Branch Forming

- A finite element model has been developed and validated against experimental data. The results indicate that the finite element model successfully models the hydraulic bulge forming of tubes.
- Forming by pressure load alone results in excessive thinning of the branch tops, high stress in the bulged region and low branch heights.
- Forming using pressure and axial compressive loading results in greater branch height, less thinning of the branch top and greater stress in the formed component.
- Increasing friction between the tube and the die results in less branch height and less stress in the formed component. Increasing friction also has the effect of increasing thinning of the branch top and increasing thickening of the main tube ahead of the punch.
- Increasing the blank thickness results in reduced branch height and reduced stress in the formed component. Increasing the thickness of the blank also has the positive effects of reducing thinning of the branch top and less thickening in the main tube.

From the above it can be concluded that when designing processes to bulge form cross joints that compressive axial loading should be used in combination with pressure loading where possible, friction should be kept to a minimum where maximum branch height is required and greater tube thickness should be used when seeking to reduce stress and thinning behaviour in the formed component.

9.2. Bulge Forming Using a Solid Bulging Medium

9.2.1. Cross Branch Forming Using Soft Metal

- The use of a solid bulging medium allows for greater branch height, less thinning of the branch top and less stress in the formed component when compared to the hydraulic bulging process.

- In order to maximise branch height when using combined internal pressure and axial load it is important the load is applied to the bulging medium before load is applied to the tube.
- Increasing friction between the bulging medium and the tube results in less stress in the formed component, more thinning of the branch top, less thickening of the main tube and a smoother stress development during the forming process.
- Increasing friction between the bulging medium and the tube has little effect on the resulting branch height in the formed component.
- When compared to a cross branch of similar height obtained by the hydraulic bulging process, it is clear that the solid medium bulging process results in far less reduction in length of the tube.
- Decreasing the relative strength of the bulging media to the tube material resulted in increased bulge height with little change in the stress in the formed component.

9.2.2. Axisymmetric Bulge Forming Using a Urethane Rod

- The development of stress in the deforming tube is highly erratic due to friction on both sides of the workpiece.
- The friction between the tube and the urethane rod can be advantageous, if kept under control, as it can result in more material being pushed into the deformation zone thus preventing excessive thinning of the tube.
- The simulation results indicate that the manufacture of conical bulge is more difficult than the manufacture of product with a cylinder extended from the conical section. This is thought to be a consequence of increased volume of bulging media and tube being available in the immediate deformation zone early in the process.

9.3. Bulge Forming of Bimetallic Tubes

- Failure of bimetallic tubes during bulge forming is predominantly due to excessive thinning of the outer tube at various locations, with the location been dependant on loading conditions.
- Combining axial compressive load with internal pressure loading results in reduced branch height when compared to the used of pressure load alone.

- Changing the relative thickness of the two tubes has little effect on branch height but significant effects on resultant component shape.
- Changing the relative strength of the tubes so that their yield stress is closer results in slightly increased branch height with little change in maximum stress.

9.4. Influence of Die Elasticity on Bulge Forming Operations

9.4.1. Hydraulic Cross Branch Forming

- The use of a pressure only loading results in high stress initially developing in the main die body and moving towards the die blend region as the process continues.
- The use of a combined loading pattern results in a similar development of stress in the die but with much greater stress levels.
- In all cases the maximum stress is located at the die blend radius, illustrating the importance that designers choose a correct die blend radius when designing bulge forming processes.
- The simulation results indicate that steel EN21 is a suitable die material for use in this bulge forming process. The results also indicate that Aluminium 5052 is an unsuitable material as the stress levels during the process exceed the elastic limit for the material

9.4.2. Axisymmetric Tube Bulging Using a Urethane Rod

- During this process high stress initially develops in the main die body and moves towards the die recess as the bulge forms and comes in contact with the die wall at this point.
- The maximum stress at the end of each process is located at the bottom of the die as this is the final point to come into contact with the tube.
- The results indicate that aluminium is not be a suitable material to manufacture the die due to the fact that the maximum stresses obtained exceed the material yield stress.

9.5. Thesis Contribution

Bulge forming is a manufacturing process that is becoming increasingly important as a technology that can be used to produce seamless, lightweight and near-net-shape industrial components. The understanding of the process to date has been very limited and important aspects such as stress and strain conditions in the formed component, thickening and thinning behaviour within the component and the effects of altering various process parameters have been largely unknown. As a result defects and failures in the process have been common and are of major concern to industry. Also, designers of machine tools for bulge forming processes lack sufficient understanding of the process to produce efficient designs. The simulations in this work will contribute significant knowledge in this area and will help in design of machine tools for bulge forming process and will aid in eliminating failures during the application of the technology. In particular the simulations in this work have provided:

(1) The state of stress and strain and thickening/thinning behaviour in the formed component during hydraulic cross branch forming of tubes. The simulations also identified the effects of friction, blank thickness and different loading patterns on the forming process.

(2) The state of stress and strain and thickening/thinning behaviour in the formed component during cross branch forming using a solid bulging medium. The simulations also identified the effects of varying the friction between the bulging medium and the tube, the effect of different loading patterns and the effect of varying the relative strength of the bulging medium and the tube.

(3) The state of stress and strain and thinning behaviour in the formed component during axisymmetric tube bulging using a urethane rod. The development of stress in the tube during the process was detailed and the simulations also examined the effects of varying the die geometry.

(4) The state of stress and strain and thinning/thickening behaviour in the formed component during cross branch forming of bimetallic tubes. The simulations also examined the effect of varying the relative thickness of the bimetallic layers, the

effect of varying the relative strength of the two tube materials and the effect of utilising different loading patterns.

(5) The development of stress and strain in the die during bulge forming of cross branches and axisymmetric tubes. The influence of die elasticity on the process was also examined.

9.6. Recommendations for Further Work

- Currently the optimisation of three dimensional bulge forming problems is very difficult due to lack of adequate computational power. With increasing computational power available at reasonable cost and more efficient finite element software available it should be possible to optimise most bulge forming operations in the near future. An algorithm can be adopted into the optimisation scheme which avoids failure of the tube by adjusting the pressure and axial loads, in order to produce an optimised load path. This load path can then be verified by experimental trials.

- In a similar manner the geometry of the die and tubular blank can be optimised for maximum branch height.

- The simulations in this work used the same die and blank geometry in most cases in order to allow direct comparison between results and to make clear the effect of varying different process parameters. There are many geometries and arrangements which have not been sufficiently analysed in published literature such as: T-branches and cross branches with different tube and branch diameters, long t-branches for use in tripod manufacture, angled branches etc.

- Copper was used as the tube material in all simulations in this work. It is possible to rerun the models used here to examine the results of using different tube materials, including composite materials. It is also possible to perform an optimisation on the tube material properties in order to find an ideal candidate material for each process.

References

[1] R.H. Wagoner and D. Zhou, Analysing Sheet Forming Operations – Recent Numerical and Experimental Advances, *Numerical Methods in Industrial Forming Processes*, Balkerma, Rotterdam, 1992, 123-132

[2] N. Brännberg and J. Mackerle, Finite Element Methods and Material Processing Technology, *Engineering Computations*, Vol. 11, 1994, 413-455

[3] N. Rebelo, J.C. Nagtagaal, L.M. Taylor and R. Passman, Comparison of Implicit and Explicit Finite Element Methods in the Simulation of Metal Forming Processes, *Numerical Methods in Industrial Forming Processes*, Balkerma, Rotterdam, 1992, 99-108

[4] J. Mackerle, Finite Element Methods and Material Processing Technology, *Engineering Computations*, Vol.15, 1998, 616

[5] M. Ahmed and M.S.J. Hashmi, Finite Element Analysis of Bulge Forming Applying Pressure and In-plane Compressive Load, *J. of Materials and Processing Technology*, Vol. 77, 1998, 95-102

[6] J.E. Grey, A.P. Deveraux and W.M. Parker, Apparatus for Making Wrought Metal T's, *U.S.A. Patents Office*, Filed June 1939, Patent No. 2,203,868

[7] R.E. Crawford, Solder Fittings, *Industrial Progress*, May 1948, 33-36

[8] J. Stalter, Method of Forming Complex Tubular Shapes, *UK Patent Office*, Filed March 1968, Patent No. 1,181,611

[9] J. Remmerswaal and A. Verkaik, Use of compensation forces and stress in difficult metal forming operations, *Int. Conf. of Manufacturing Technology*, ASME, 1967, 1171-1180

[10] T. Ogura and T. Ueda, Liquid Bulge Forming, *Metalworking Production,* 1968, 73-81

[11] H.A. Al-Qureshi, P.B. Mellor and S. Garber, Application of Polyurethane to the Bulging and Piercing of Thin-walled Tubes, *Advances in Mach. Tool Des. Res.* Pergammon Press, 1969, 318-338.

[12] H.A. Al-Qureshi, Comparison between the Bulging of Thin Walled Tubes Using Rubber Forming Technique and Hydraulic Forming Process, *Sheet Metal Industry*, 47, 1970, 607-612

[13] D.M. Woo, Tube Bulging Under Internal Pressure and Axial Force, *Journal of Engineering Materials and Technology*, 1978, 421-425

[14] M. Limb, J. Charkrabarty, S. Garber and P.B. Mellor, The Forming of Axisymmetric and Asymmetric Components from a Tube, *Proc. 14th International MTDR Conference*, 1973, 799

[15] M. Limb, J. Charkrabarty, S. Garber and W.T. Roberts, Hydraulic Forming of Tubes, *Sheet Metal Industries*, 1976, 418-424

[16] M. Limb, J. Charkrabarty and S. Garber, The Axisymmetric Tube Forming Process, *Int. Inst. for Prod. Eng. Research Conf.*, Tokyo, 1974, 280-283

[17] S. Kandil, Hydrostatic metal tube bulging as a basic process, *Metallurgia and Metal Forming*, 1976, 152-155

[18] W.J. Sauer, A Goetra, F. Robb and P. Huang, Free bulging of tubes under internal pressure and axial compression, *Trans. Of NAMRC VI*, SME, 1978, 228-235

[19] D.M. Woo and A.C. Lua, Plastic Deformation of Anisotropic Tubes in Hydraulic Bulging, *Journal of Engineering Materials and Technology*, 1978, 421-425

[20] D.M. Woo, Development of a bulge forming process, *Sheet Metal Industries*, 1978, 623-624 and 628

[21] V.L. Lukanov, V.V. Klechkov, V.P. Shateev and L.V. Orlov, Hydromechanical Stamping of Tees with Regulated Liquid Pressure, *Forging and Stamping Industry*, Vol. 3, 1980, 5-7

[22] A.R. Ragab, Producing superplastic tubular tee joints by thermoforming, *Proc. Int. MTDR Conf.*, 1980, 223-230

[23] T. Ueda, Differential gear casing for automobiles by liquid bulge forming processes part 1, *Sheet Metal Industries*, Vol. 60, part 3/4, 1983, 181-185

[24] T. Ueda, Differential gear casing for automobiles by liquid bulge forming processes part 2, *Sheet Metal Industries*, Vol. 60, part 4, 1983, 220-224

[25] M.S.J. Hashmi, Radial Thickness Distribution Around a Hydraulically Bulge Formed Annealed Copper T-Joint: Experimental and Theoretical Predictions, *22nd Int. M.T.D.R. conf.*, (1981) 507-516

[26] M.S.J. Hashmi, Forming of Tubular Components from Straight Tubing Using Combined Axial Load and Internal Pressure: Theory and Experiment, *Proc. Of int. conf. on dev. on drawing of metals, Metals Society,* (1983) 146-155

[27] M.S.J. Hashmi and R. Crampton, Hydraulic Bulge Forming of Axisymmetric and Asymmetric Components: Comparison of Experimental Results and Theoretical Predictions, *Proc. 25th Int. MTDR Conf.*, Birmingham, (1985) 541-549

[28] M.I. Hutchinson, R. Crampton, M.S. Ali and M.S.J. Hashmi, The Hydraulic Bulge Forming of Tubular Components – The Effect of Changing the Tube Blank Material, *Proc. 4th Nat. Conf. in Prod. Res.*, Sheffield (1988) 439-444

[29] M.I. Hutchinson, R. Crampton, W. Rushton and M.S.J. Hashmi, The Hydraulic Bulge Forming of Tubular Components – The Effect of Changing the Plungers Applying Compressive Axial Load, *Proc. 6th Irish Manufacturing Committee Conf.*, Dublin (1989) 248-254

[30] M.I. Hutchinson, Bulge Forming of Tubular Components, Ph.D. Thesis, Sheffield City Polytechnic (1988)

[31] L.A.M. Filho and H.A. Al-Quershi, Unconventional Tee Forming on Metal Tubes, *J. Eng. Ind.*, 107, 1985, 392-396

[32] F. Dohmann and F. Klass, Liquid Bulge Forming of Tubular Workpieces, *Strips Sheets Tubes*, Vol. 4, part 1, 1987, 7-10

[33] M. Murata, Y. Yokouchi, K. Onodera and H. Suzuki, The hydraulic tube bulging of a tube attached lining rubber membrane with axial compressive force, *JSME Int. J.* Series III, Vol. 32, No. 1, 1989, 118-123

[34] S. Thiruvarudchelvan and F.W. Travis, Tube Bulging with a Urethane Rod, *J. of Materials and Processing Technology,* 23, 1990, 152-209

[35] S. Thiruvarudchelvan, A Theory for the Bulging of Aluminium Tubes Using a Urethane Rod, *J. of Materials and Processing Technology,* 41, 1994, 311-330

[36] S. Thiruvarudchelvan, A Theory for Initial Yield Conditions in Tube Bulging with a Urethane Rod, *J. of Materials and Processing Technology,* 42, 1994, 61-74

[37] F. Dohmann and C. Hartl, Liquid Bulge Forming as a Flexible Production Method, *J. of Materials and Processing Technology*, Vol. 45, 1994, 377-382

[38] F. Dohmann and C. Hartl, Hydroforming – a Method to Manufacture Light Weight Parts, *J. of Materials and Processing Technology*, Vol. 60, 1996, 669-676

[39] L.A.M. Filho, J. Menezes and H.A. Al-Quereshi, Analysis of Unconventional Tee Forming on Metal Tubes, *J. of Materials and Processing Technology*, Vol. 45, 1994, 383-388

[40] S. Sheng and W. Tonghai, Research into the Bulge Forming of a Tube Under Axial-Radial Compound Forces and It's Application, *J. of Materials and Processing Technology*, Vol. 51, 1995, 346-357

[41] J. Tirosh, A. Neuberger and A. Shirizly, On tube expansion by internal fluid pressur with additional compressive stress, *Int. J. Mech. Sci.,* Vol. 38, No. 8, 1996, 839-851

[42] P.B. Mellor, Tensile instability in thin walled tubes, *J. Mech. Eng. Sci.,* Vol. 4, No. 3, 1962, 251-256

[43] B.H. Jones and P.B. Mellor, Plastic flow and instability behaviour of thin walled cylinders subjected to constant ratio tensile stress, *J. Strain Analysis*, Vol.2, 1967, 62-72

[44] R.P. Felgar, Plastic analysis of the instability of pressure vessels subjected to internal pressure and axial load, *Trans. ASME, J. Basic Eng.,* Vol. 84, 1962, 62-72

[45] N.A. Weil, Tensile instability of thin-walled cylinders of finite length, *Int. J. Mech. Sci.*, Vol. 5, 1963, 487-506

[46] K. Manabe, K. Suzuki, S. Mori and H. Nishimura, Bulge forming of thin-walled tubes by micro-computer controlled hydraulic press, *Proc. of Adv. Tech. Plasticity,* Vol. 1, 1984, 279-287

[47] A.D. Eldred, R.F. Malkin and T. Barringer, Variform – a hydroforming technique for manufacturing complex tubular components, *Technische Mitteilungen Krupp (English)*, Vol. 1, 1994, 45-50

[48] J. Hashemi, J. Rasty, S.D. Li and A.A. Tseng, Integral hydro-bulge forming of single and multi-layered spherical pressure vessels, *ASME Journals of Pressure Vessels Technology*, 1992

[49] Z.R. Wang, T. Wang, D.C. Kang, S.H. Zhang and Y. Fang, The technology of the hydrobulging of whole spherical vessels and experimental analysis, *Journal of Mech. Work. Tech.*, Vol. 18, 1989, 85-94

[50] Z.R. Wang, K. Dai, S.J. Yuan, Y.S. Zeng and X. Zhang, The development of integral hydro-bulge forming (IHBF) process and its numerical simulation, *Journal of materials processing technology,* Vol. 102, 2000, 168-173

[51] K.I. Manabe and J.I. Ozaki, Bulge forming of braided thermoplastic composite tubes under axial compression and internal pressure, *Polymer Composites*, Vol.17, 1996, 115-123

[52] D.M. Woo, The analysis of axisymmetric forming of sheet metal and the hydrostatic bulging process, *Int. J. Mech. Sci.*, Vol. 6, 1964, 303-317

[53] Y. Yamada and Y. Yokouchi, *Seisan kenku* (in Japanese), Vol. 21, No. 11, 1969, pp. 636

[54] N.M. Wang and M.R. Shammamy, On plastic bulging of a circular diaphragm by hydraulic pressure, *J. Mech. Phys. And Solid*, Vol. 17, 1969, 43-61

[55] M.F. Ilahi, A. Parmar and P.B. Mellor, Hydrostatic bulging of a circular aluminium diaphraghm, *Int. J. Mech. Sci.*, Vol.23, 1981, 221-227

[56] M.F. Illahi and T.K. Paul, Hydrostatic bulging of a circular soft brass diaphraghm, *Int. J. Mech. Sci.*, Vol.27, No. 5, 1985, 275-280

[57] H. Iseki, T. Jimma and T. Murota, Finite element method of analysis of the hydrostatic bulging of sheet metal (part 1), *Bulletin of the JSME*, Vol.17, No. 112, 1974, 1240-1246

[58] H. Iseki, T. Murota and T. Jimma, Finite element method of analysis of the hydrostatic bulging of sheet metal (part 2), *Bulletin of the JSME*, Vol.20, No. 141, 1977, 285-291

[59] S. Kobayashi and J.H. Kim, Deformation analysis of axisymmetric sheet metal forming process by the rigid plastic FEM, *Proc. of Symp. in Mechanics of Sheet Metal Forming*, Ed. D.P. Koisten and N.M. Wang, 1978, 341-363

[60] Y.J. Kim and D.Y. Yang, A rigid plastic finite element formulation considering the effect of geometric change and its application to hydrostatic bulging,*Int. J. of Mech. Sci.*, Vol. 27, No. 7/8, 1985, 453-463

[61] A.S. Wifi, FE correction matrices in metal forming analysis with application to hydrostatic bulging of a circular sheet, *IJMS*, Vol. 24, No. 7, 1982, 393-406

[62] P. Keck, M. Wilhelm, K. Lange and M. Herrmann, Comparison of different finite element methods for the simulation of sheet metal forming, *Proc. of NUMIFORM'89*, Balkema, Rotterdam, 1989, 482-488

[63] K. Lange, M. Hermann, P. Keck and M. Willhem, Application of an elasto-plastic finite element code to the simulation of metal forming process, *J. of Materials Processing Technology*, vol. 27 (1991) 239-261

[64] Y. Li, P. Hu and J. Lian, Numerical study for influences of material parameters of hydrostatic bulging of metal sheet, *Acta Mechanica Solid Sinica* (English), Vol. 6, No. 2, 1993, 134-144

[65] R.J. Cronin, J.Y. Xia, and D.T. Llewelllyu, Finite element modelling of hydraulic bulging during sheet metal forming, *Ironmaking and Steel Making*, Vol. 21, No. 1, 1994, 21-36

[66] W.B. Lee and Z.R. Ma, Prediction of the limiting shape of a die height in the hydraulic bulge forming of a circular cup, *Journal of Materials Processing Technology,* Vol. 51, 1995, 309-320

[67] M. Ahmed and M.S.J. Hashmi, Comparison of free and restrained bulge forming by finite element method simulation, *Journal of Materials Processing Technology*, Vol. 63, `997, 651-654

[68] M. Ahmed and M.S.J. Hashmi, Optimisation of bulge forming of a circular plate applying pressure and in-plane compressive load, *Proc. of the Symposium on Mechanics in Design,* Toronto, Canada, May 1996, 427-436

[69] M. Ahmed, Finite element modelling and simulation of metal flow in bulge forming, Ph.D. Thesis, Dublin City University (1997)

[70] H. Bauer, FE simulation of the production process of builder camshaft, *Numerical Methods in Industrial Forming Processes*, Balkema, Rotterdam,1992, 585-600

[71] F. Dohmann and Ch. Hartl, Finite Element Analysis of Forming Hollow Camshafts Using Internal High Pressure, Int. Conf. on Modelling and Simulation in Metallurgical & Engineering and Material Science, Beijing (1996) 640-645

[72] M. Ahmed and M.S.J. Hashmi, Three Dimensional Finite Element Simulation of Axisymmetric Tube Bulging, *Proc. Pacific Congress on Manufacturing and Management,* Brisbane, Australia, 1998, 515-521

[73] M. Ahmed and M.S.J. Hashmi, Defects in Hydraulic Bulge Forming of Tubular Components and Their Implication for Design and Control of the Process, Advanced Methods in Materials Processing Defects, M. Predeleanu and P. Gilormini (ed.), Elsevier, 1997, 197-20

[74] M. Ahmed and M.S.J. Hashmi, Finite Element Simulation of Manufacture of Metal Bellows from Tubes, *Advances in Materials and Processing Technologies*, Kula-Lumpar, Malaysia, 1998, 982-989

[75] M. Ahmed and M.S.J. Hashmi, Three Dimensional Finite Element Simulation of Bulge Forming, *Advances in Materials and Processing Technologies*, Dublin, Ireland, 1999, 153-161

[76] R. Neugebaur and M. Putz, Hydroforming – A Promising Lightweight Technology for Application in Automotive Industry, *Proc. Sheet Metal 1998,* Twente, The Netherlands, (1998) 81-88

[77] M. Kleiner, R. Kolleck, J. Rauer and T. Wediner, Die-less forming of sheet metal parts, *Proc. Sheet Metal 1998,* Twente, The Netherlands, (1998) 63-70

[78] P. Hein and F. Vollertsen, Hydroforming of sheet metal pairs, *Journal of Materials Processing Technology*, Vol. 87, 1999, 154-164

[79] E. Doege, R. Kösters and C. Ropers, Determination of Optimised Control Parameters for Internal High Pressure Forming Processes with the Finite Element Method, *Proc. Sheet Metal 1998*, Twente, The Netherlands (1998) 119-128

[80] M. Ahmed and M.S.J. Hashmi, Finite element simulation of bulge forming of an elbow of box section from a circular tube, *Journal of Materials Processing Technology*, Vol. 93, 1999, 410-418

[81] N. Asnafi, Analytical modelling of tube hydroforming, *Thin-Walled Structures*, Vol. 34, 1999, 295-330

[82] N. Asnafi and A. Skogsgardh, Theoretical and experimental analysis of stroke-controlled tube hydroforming, *Materials Science and Engineering A - Structural Materials properties microstructure and processing*, Vol. 279, Part 1-2, 2000, 95-110

[83] T. Sokolowski, K. Gerke, M. Ahmetoglu and T. Altan, Evaluation of tube formability and material characteristics: hydraulic bulge testing of tubes, *Journal of Materials Processing Technology,* Vol. 98, 2000, 34-40

[84] J. Hashemi and Q.S. Zheng, A three dimensional finite element analysis of hydrostatic bulging of an integral polyhedron into a spherical vessel, *Recent Advances in Structural Mechanics, ASME*, Vol.13, 1993, 113-117

[85] S.H. Zhang, J. Danckert and K.B. Nielsen, Integral hydro-bulge forming of pressure vessel heads, *Journal of Materials Processing Technology*, Vol. 86, 1999, 184-189

[86] S.H. Zhang, K.B. Nielsen, J. Danckert and Z.R. Wang, Numerical simulation of the integral hydro-bulge forming of non-clearance double-layer spherical vessels: deformation analysis, *Computers & Structures,* Vol. 70, 1999, 243-256

[87] S.H. Zhang, B.L. Wang, Y.L. Shang, X.R. Kong, J.D. Hu and Z.R. Wang, Three-dimensional finite element simulation of the integral hydrobulge forming of a spherical LPG tank, *International Journal of Pressure Vessels and Piping*, Vol 65, 1996, 47-52

[88] K.J. Bathe, Finite Element Procedures, Prentice-Hall International, 1996

[89] J.O. Hallquist and D.J. Benson, Explicit Finite Element Methods for Impact Engineering, *Proc. of the first Australasian Congress on Applied Mechanics*, Melbourne, 1996, 11-16.

[90] J.O. Hallquist, LS-DYNA3D Theoretical Manual, Livermore Software Technology Corporation, California, USA, 1993

[91] M. Ahmed and M.S.J. Hashmi, Estimation of Machine Parameters for Hydraulic Bulge Forming of Tubular Components, *Journal of Materials Processing Technology*, Vol. 64, (1997) 9-23

APPENDIX 1

Estimation of Failure Propagation During Bulge Forming

1. Introduction

The objective of this part of the study is to examine the failure of the tubular blank during bulge forming processes. The analyses presented in the main body of the thesis discuss the mode of failure of the various bulge forming processes simulated, but no attempt is made to illustrate these failures. This part of the study attempts to illustrate these failures by examining where the failure is initiated and how it progresses.

2. Hydraulic Bulge Forming

2.1. Failure Due to Dominance of Pressure Load

In order to examine failure due to dominance of pressure load (i.e. bursting) the pressure only loading pattern detailed in section 4.4.1. was used. In order to determine how the failure propagates with as much accuracy as possible the mesh used for the tube was refined in the area where failure was expected to occur. Figure A-1 shows the refined mesh used for the analysis.

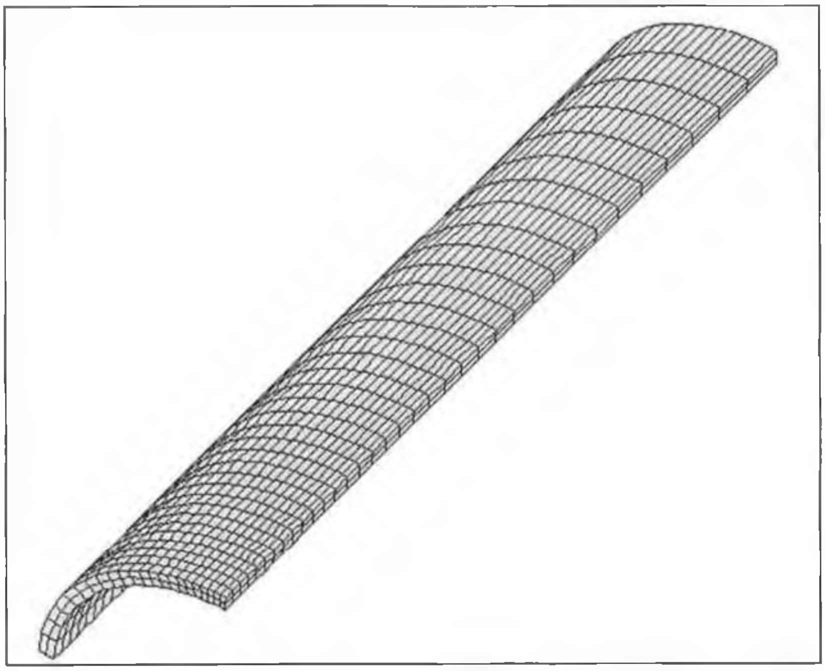

Figure A-1 : Refined Mesh Used for Failure Analysis

In order to examine the propagation of failure it was required to run the analysis past the point where failure of one node would occur. In order to do this a new tri-linear material model was used. The first two lines of the material model correspond directly with the bilinear material model previously used. The third line allows the analysis to continue past the instability strain (0.45) of the material, in order to investigate the order in which each node exceeds the instability strain. Figure A-2 shows the material model used for this analysis.

The number of time-steps used in the analysis was increased in order to determine the order in which nodes exceeded the failure strain with greater accuracy. It was found that hoop strain was the first principal strain to exceed the failure strain at each node. The propagation of failure was determined by obtaining a listing of the principal strains at each node for each time-step. Once a node exceeded the failure stain its position was noted and the subsequent time-step then examined. In this way the point of failure initiation and the subsequent path of crack development was determined.

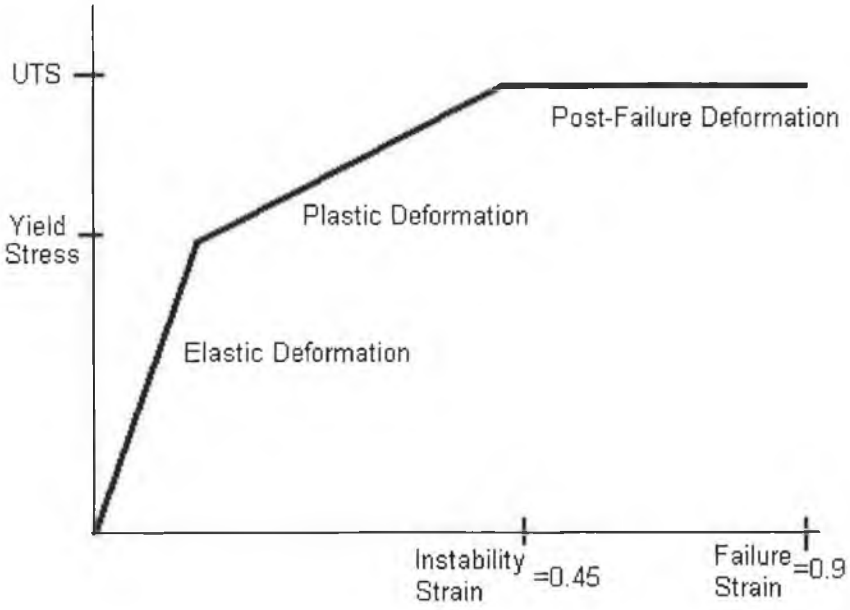

Figure A-2 : Tri-linear Material Model Used for the Failure Analysis

Figure A-3 shows a close up of the tube illustrating the order in which the first group of nodes exceeded the instability strain. The first node to fail is on the inner surface of the tube at the symmetry edges and is denoted by "1". The instability strain is then reached by two nodes in the lengthways direction of the tube, before being reached by one node in the circumferential direction of the tube. This pattern is then repeated through the thickness of the tube, as illustrated in the figure. Subsequently the failure progresses along the length of the tube at three times the rate that it progresses along it's circumference. This result indicates that failure of the cross branch due to dominance of pressure load would expect to result in a lengthways crack along the branch top. This result has been reported in experimental investigations [30] and is in agreement with the earlier analysis of strain paths of the central node of the branch top in chapter four.

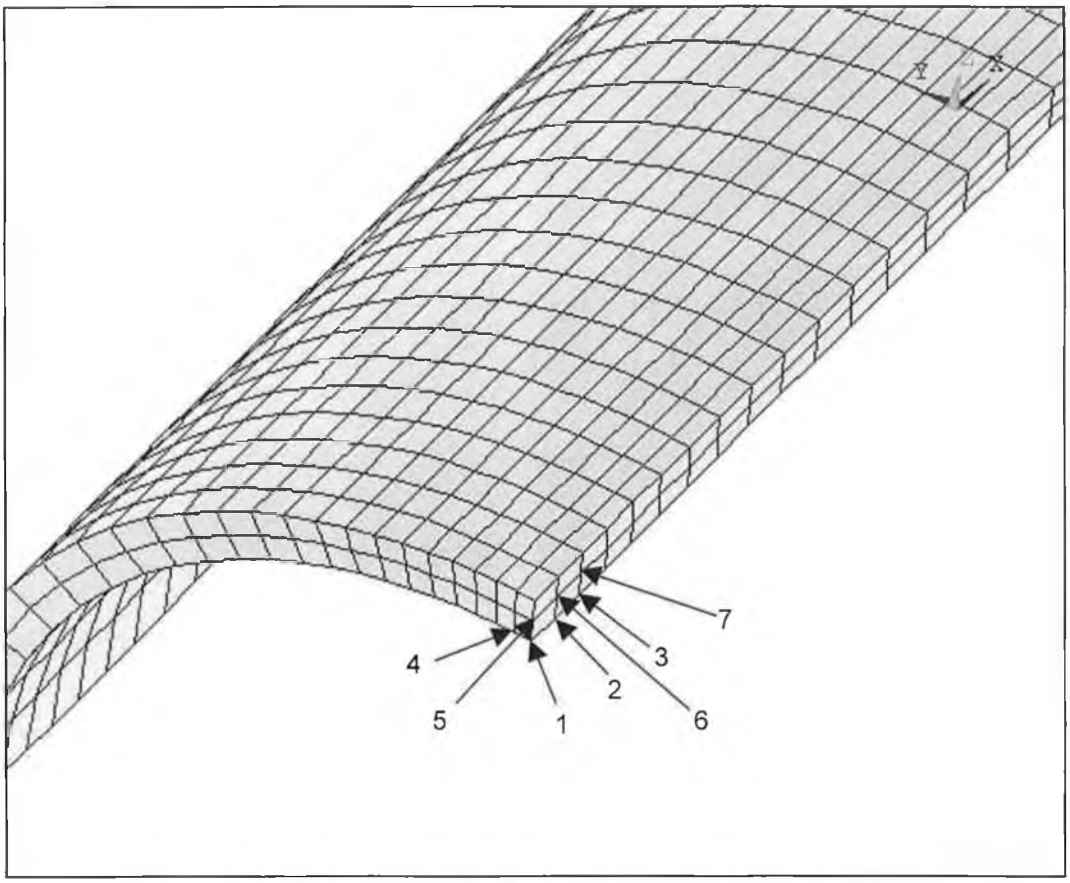

Figure A-3 : Order in Which Nodes Exceed the Failure Strain

This result is summarised in figure A-4 which shows the distribution of hoop strain in the deformed tube after the failure strain has been exceeded. In the actual forming process a crack would not progress very far as once the crack has opened the fluid supplying the internal pressure would escape and the pressure would drop dramatically. This sometimes can cause the crack to become curved as the fluid causes some extra deformation at the point where is pushes its way through. This is illustrated in figure A-5, which shows a cross branch which burst during an experimental test.

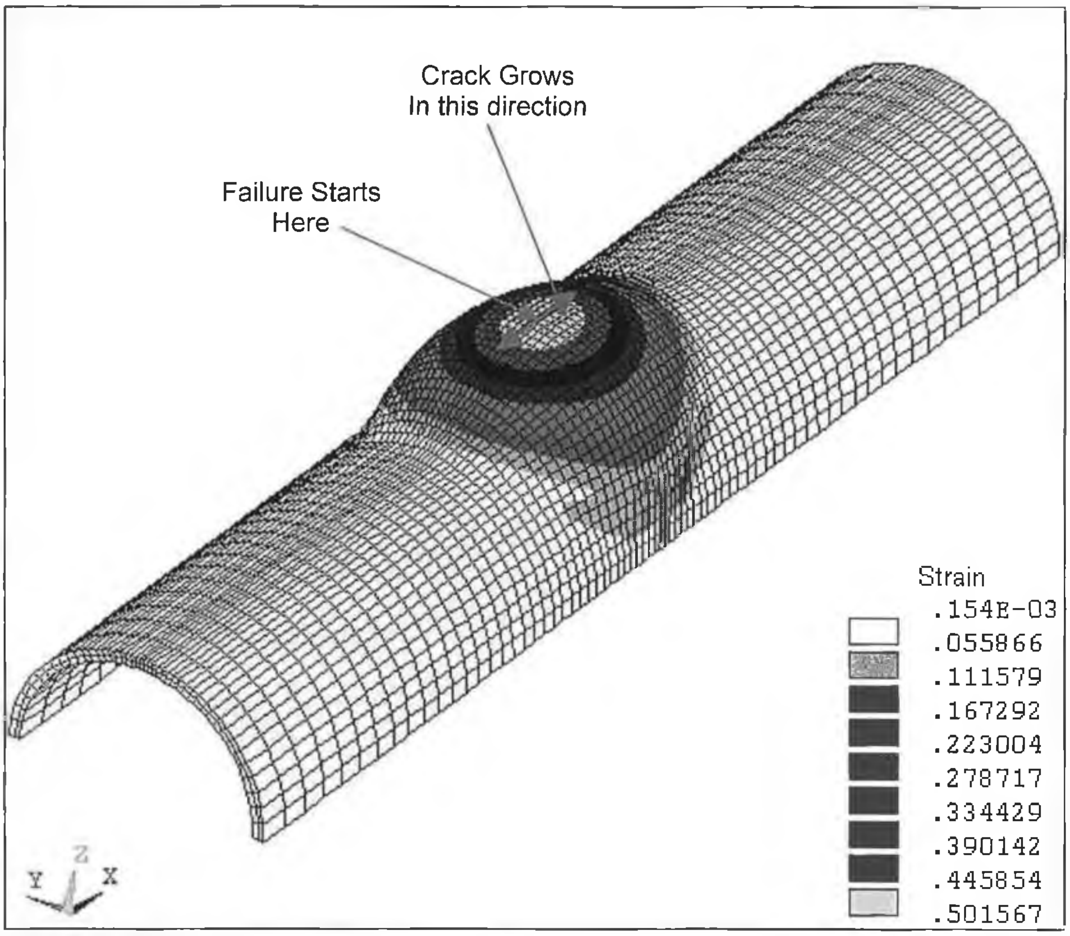

Figure A-4 : Distribution of Hoop Strain in the Tube after Failure

Figure A-5 : Bursting Failure of Cross Branch [30]

2.2. Failure Due to Prominence of Axial Load

In order to examine the post-failure deformation of a failure due to prominence of axial load the finite element model detailed in chapter four was used. The tri-linear material model detailed above was used to model the tube material. A loading pattern was developed based on experience from the simulations in chapter four which used a relatively low pressure load and a high axial displacement of the tube end.

Figure A-6 shows the buckling defect obtained. Figure A-7 shows a plan view of one half of the cross branch which allows the buckle to be seen more clearly.

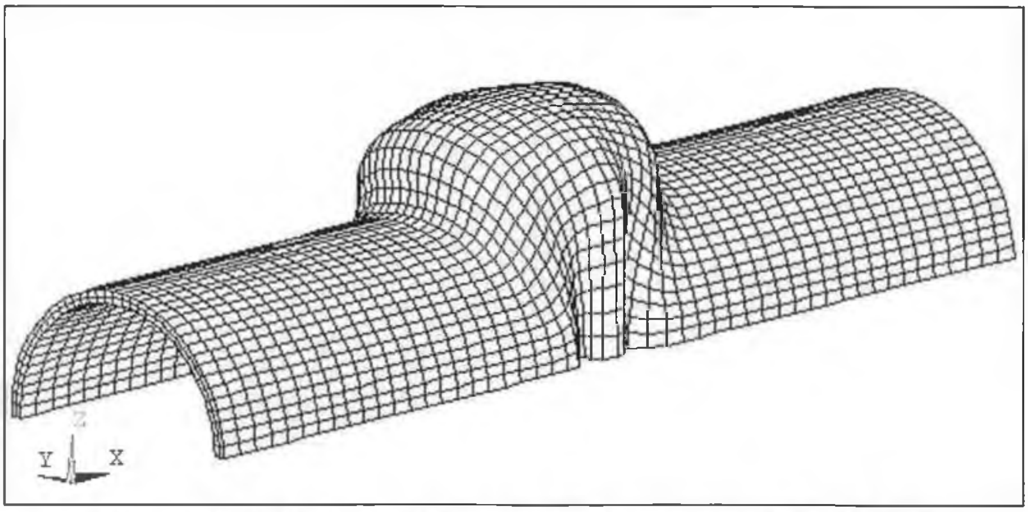

Figure A-6 : Buckling Defect due to Prominence of Axial Load

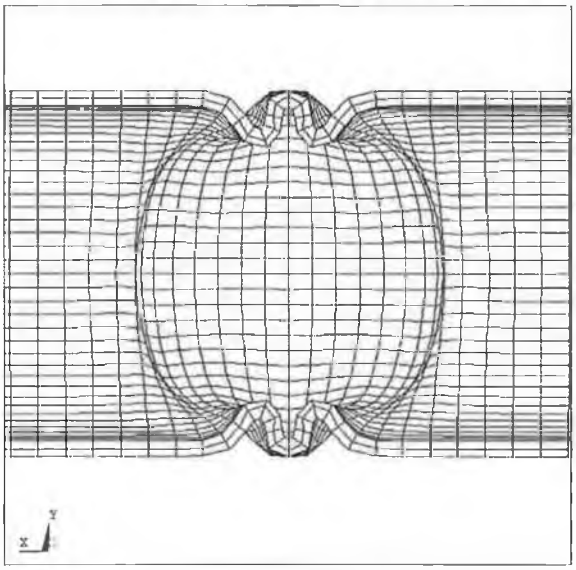

Figure A-7 : Plan View of Cross Branch Half – Illustrating Buckle Defect

3. Solid Medium Bulge Forming

3.1. Failure Due to Dominance of Pressure Load

In order to examine failure due to dominance of pressure load the pressure only loading pattern detailed in section 5.2.3.1. was used. It was found that hoop strain was the first principal strain to exceed the failure strain at each node. In order to examine the propagation of failure it was required to run the analysis past the point where failure of one node would occur. In order to do this the tri-linear material model described previously in figure A-2 was used. The propagation of failure was determined by obtaining a listing of the principal strains at each node for each time-step. Once a node exceeded the failure stain its position was noted and the subsequent time-step then examined.

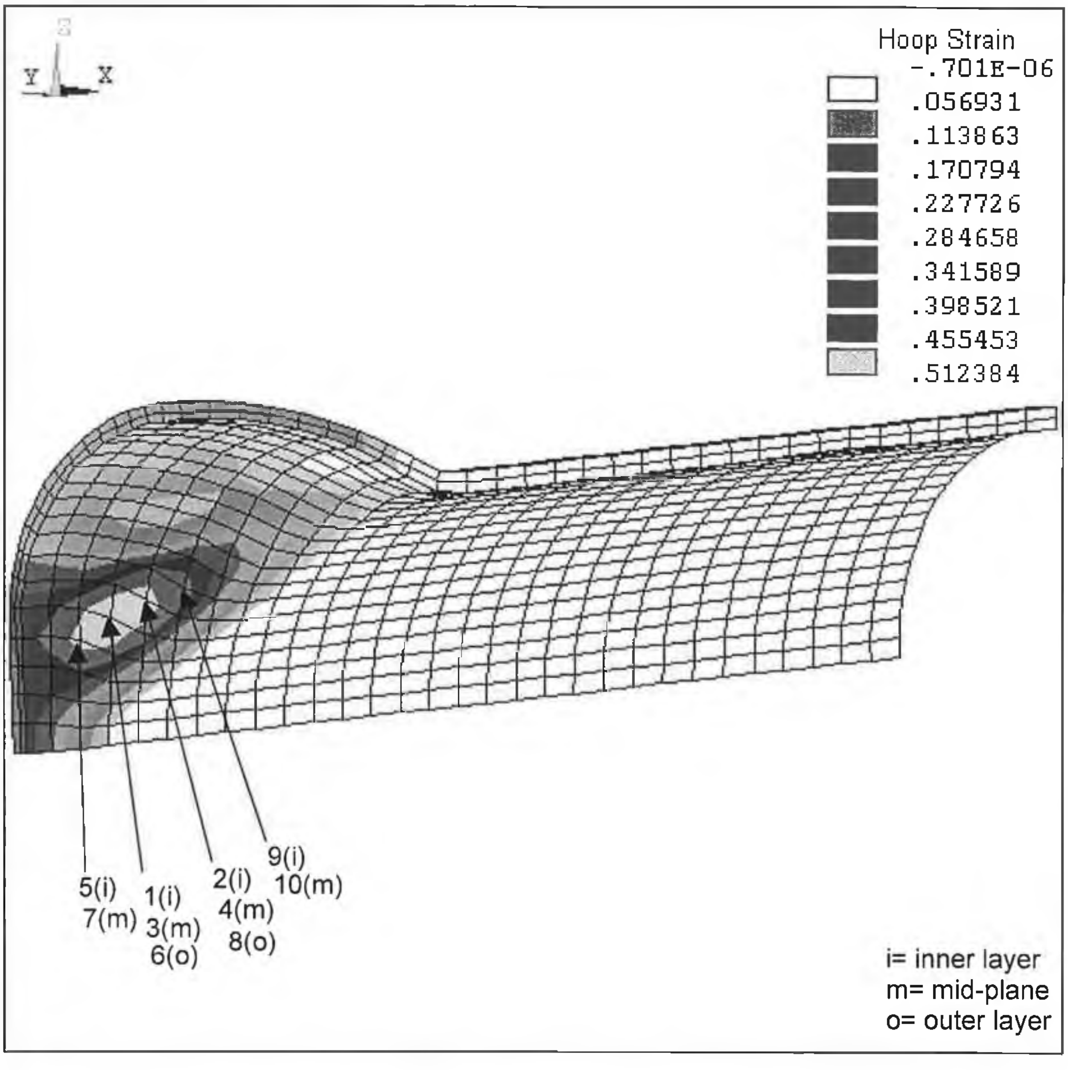

Figure A-8 : Order in Which Nodes Exceed the Failure Strain

Figure A-8 shows one eighth the tube illustrating the order in which the first group of nodes exceeded the failure strain. The first node to fail is on the inner surface of the tube at the area at which the maximum stress is experienced (as indicated in chapter 5). The failure strain is then reached by two nodes either side of this node in, before being reached by nodes in the same locations through the thickness of the tube, as illustrated in the figure. Subsequently the failure progresses around the circumference of the bulged region. Figure A-9 shows a plot of the deformed cross branch with the tube elements in which the failure strain has been exceeded in all nodes removed, clearly showing the elements of the bulging medium underneath. In the actual situation the bulging medium would begin to leak out through this hole, but, unlike the hydraulic bulging method the bulging process would continue as a significant amount of media would remain in the tube and apply internal pressure. This result indicates that failure of the cross branch due to dominance of pressure load would expect to result in crack around the bulged region which would eventually result in separation of the bulged region from the main tube.

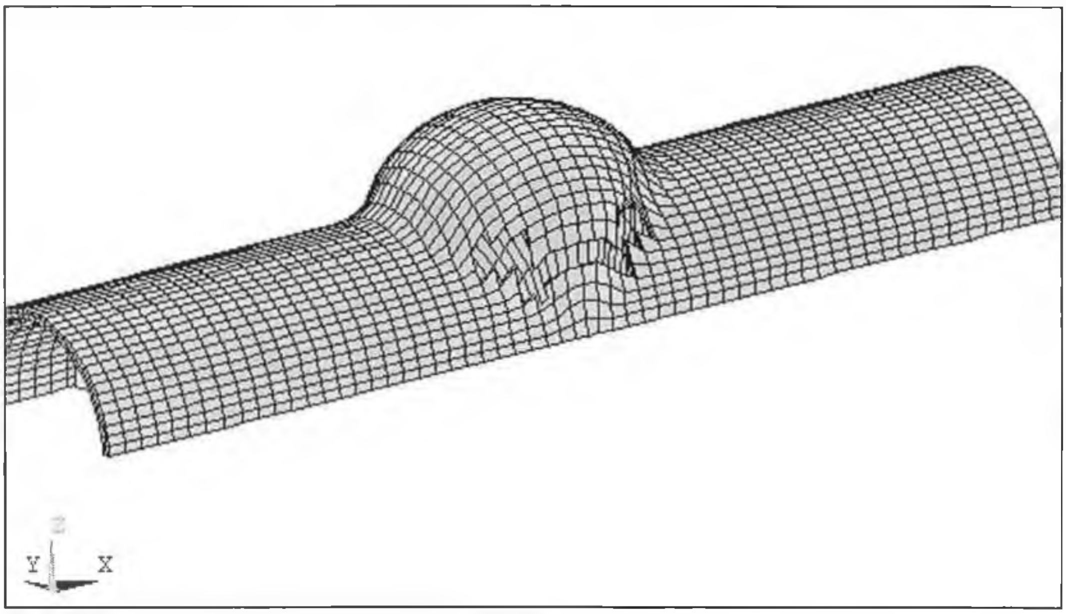

Figure A-9 : Propagation of Failure of Tube Elements

3.2. Failure Due to Dominance of Axial Load

Practically it is very difficult to produce a buckling failure when using a solid bulging media. This is because the same punch is used to apply axial displacement to the filler material and the tube. This punch is generally shouldered thus ensuring that an axial load is applied to the bulging media before any load is applied to the tube. This essentially ensures that there is always enough internal pressure to prevent buckling defects from occurring. It is possible to apply a dominant axial load to the finite element model, but as this would be unlikely to occur in reality, it was decided not to simulate a buckling failure using the solid bulging media.

3.3. Failure due to Combined Loading

In section 5.2.3.2. the results of using a combined loading pattern, where axial displacement is applied to the tube and bulging media simultaneously, are presented. Figure 5.9 shows that the area of maximum stress is located at the symmetry edge of the component directly underneath the cross branches. Consequently it is in this area that a failure would be expected to occur. This section examines the propagation of such a failure by rerunning the analysis and utilising the tri-linear material model detailed in figure A-2.

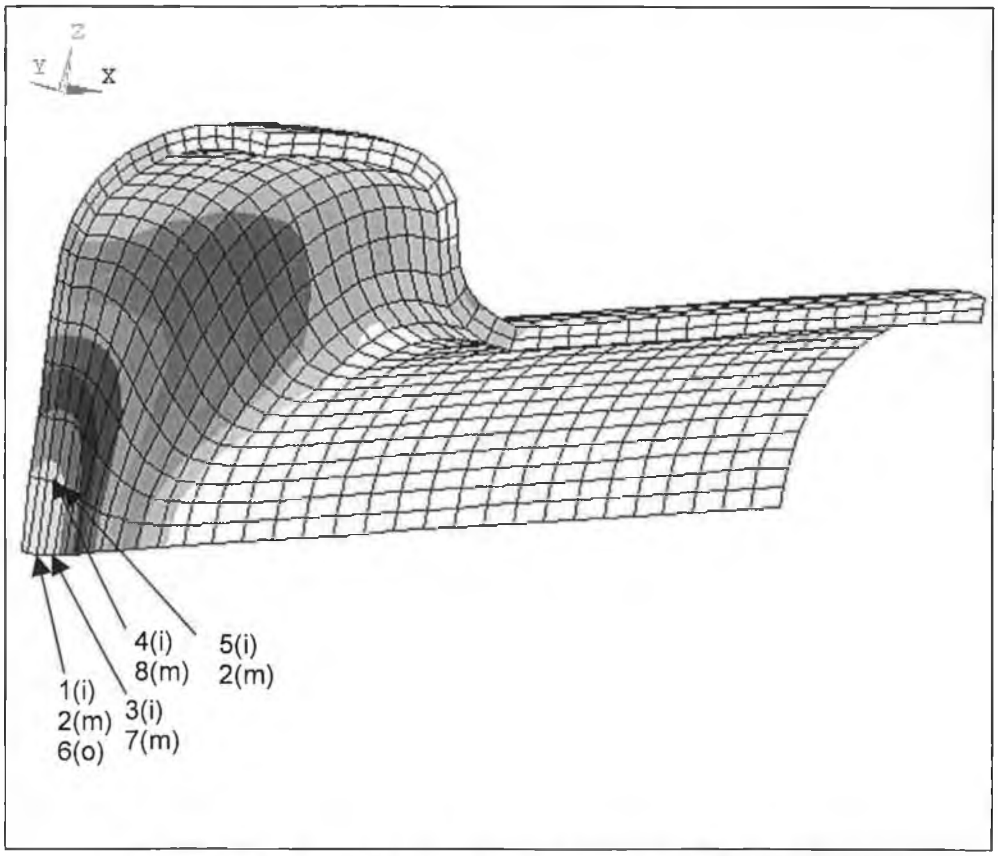

Figure A-10 : Order in Which Nodes Exceed the Failure Strain

It was found that the failure mode in the region of high stress was a combination of tensile hoop strain and compressive radial strain, which caused the elements to elongate in the hoop direction as the tube thinned. The order in which the values for hoop strain in the nodes exceeds the failure strain is shown in figure A-10. The order in which the failure strain was exceeded in the radial direction is almost exactly the same as that for the hoop direction.

The expected result of this combined thinning and elongation of the tube in the hoop direction would be the formation of a crack in the lengthways direction of the tube at this point as indicated in figure A-11.

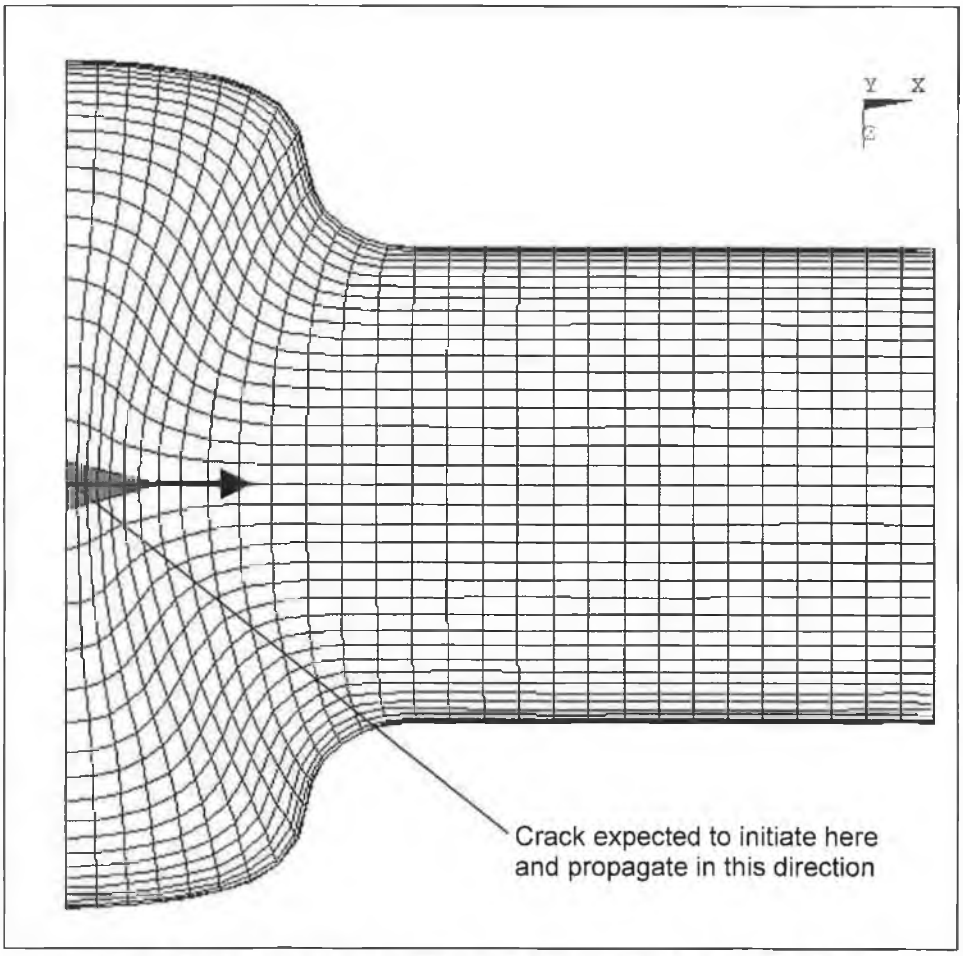

Figure A-11 : Expected Location and Direction of Growth of Crack

4. Summary

This section presents an attempt to predict the propagation of failure during the bulge forming processes simulated in the main body of this work. These predictions are limited by the functionality of the software available for the simulations, but may be seen as a 'first guess' as to how failure will propagate. Future work will concentrate on improving the finite element models to allow for the illustration of failure. This will be aided by the availability of improved software (particularly pre and post processors) in the near future.

APPENDIX 2

LIST OF PUBLICATIONS

[1] B.J. Mac Donald and M.S.J. Hashmi, Finite Element Simulation of Bulge Forming of a Cross Joint from a Tubular Blank, *Journal of Materials Processing Technology*, Vol. 103, Issue 3, 2000, 333-342

[2] B.J. Mac Donald and M.S.J. Hashmi, Three Dimensional Finite Element Simulation of Bulge Forming Using a Solid Bulging Medium, *Proc. AMS'99*, Cairns, Australia (1999) 432-436
(Also accepted for publication in *Finite Elements in Analysis and Design*)

[3] B.J. Mac Donald and M.S.J. Hashmi, Finite Element Simulation of Bulge Forming of Bimetallic Tubes, *Proceedings of the Int. Conf. on Manufacturing, IMC 2000*, Dhaka, Bangladesh (2000) 52-61

[4] B.J. Mac Donald and M.S.J. Hashmi, Finite Element Simulation of Axisymmetric Bulge Forming : Effects of the Process on the Die, *Proc. ECCOMAS 2000*, Barcelona, Spain (2000)

[5] B.J. Mac Donald and M.S.J. Hashmi, Near Net Shape Manufacture Of Engineering Components Using Bulge Forming Processes : A Review, *Proc. IMC'17*, Galway, Ireland (2000) 137-146